Biogeochemistry of the lichen-rock interface on different silica-rich rock types in the Vredefort Dome, South Africa

B Smit

orcid.org/0000-0003-2081-0679

Dissertation accepted in fulfilment of the requirements for the degree *Master of Science in Environmental Sciences* at the North-West University

Supervisor: Prof SJ Siebert

Co-supervisor: Dr. G Mahed

Graduation May 2021

24163260

DECLARATION

I declare that the dissertation submitted by me for the degree of Master of Science (MSc) in Environmental studies at the School of Geo- and Spatial Sciences, North-West University, Potchefstroom Campus, South Africa, is my own independent work and has not previously been submitted by me at another university. The study represents original work undertaken by the author and any opinion, findings or conclusions are those of the author and therefore the **Geology Subject Group** of the North-West University does not accept any liability in that regard.

Signed in Potchefstroom, South Africa

Signature:

Date: 2020/12/08

BJ Smit

ACKNOWLEDGEMENTS

All the Glory belongs to the Mighty One, my Lord Jesus Christ, for been there for me every single moment in this journey.

I would like to express my gratitude to my supervisor, Prof Stefan Siebert, whose expertise, understanding and patience added considerably to my graduate experience. I appreciate his knowledge and skills in many areas. I would also like to thank Dr. Gaathier Mahed for sharing his knowledge on geophysics, porous media, editorial work and his co-supervision in the preparation of presentations from proposal writing to the final thesis.

Very special thanks to Dr Anine Jordaan, chief subject specialist at the Laboratory for Electron Microscopy at North-West University, for her assistance during all the preparation that went into preparing the SEM samples as well as assisting me throughout all the SEM experiments. I would like to extend my appreciation to Frikkie de Beer and Lunga Bam for their expert advice analysing samples using X-ray tomography at the MIXRAD facility hosted by the National Energy Corporation of South Africa (NECSA). I recognize that this research would not have been possible without the assistance of Ricart Boneshans with various technical aspects.

In conclusion, I would also like to thank René Putter and my parents (Barnie and Eranda Smit) for the support they provided me with through my entire life, without whose love, encouragement and assistance, I would not have finished this thesis.

ABSTRACT

Land colonization by plants and their fungal and bacterial symbionts was fundamental to the evolution of terrestrial ecosystems, but how their communities influenced mineral weathering and soil development in the southern hemisphere and African environments remains largely unknown. This study considers lichen colonization on the weathering crust on silica-rich rock varieties (K-feldspar rich granite, alkali granite, sub-labile arenite, ferruginous wacke and metaconglomerate) from the ~2023 ± 4 Ma Vredefort impact crater, central South Africa, with an integrated approach using optical microscopy, X-ray micro-computed tomography (µCT) and scanning electron microscopy (SEM).

The interaction of four recurrent saxicolous lichen genera (*Acarospora* sp.pl., *Caloplaca* s. lat. sp.pl., *Buellia* sp.pl. and *Xanthoparmelia* sp.pl.) which targeted silica-rich rock varieties were explored, thus contributing to a deeper understanding of the multifaceted lichen-induced bioweathering processes that are active within impacted regions. In particular, the potential efficacy of lichen colonization on silica-rich rock degradation were investigated. The study characterized and compared the specific biomechanical and biochemical actions of each genus and documented their expected epilithic and endolithic behavior. It was investigated whether different lichen genera could explain variations in mechanisms, patterns and degree of weathering at each site.

Granitic rocks with initially low porosity became more porous as a result of impact bulking, whilst metasedimentary rocks showed a well-defined decrease in particle size and permeability, presumably related to pore collapse or impact-induced annealing. However, the heterogeneous distribution of collapsed pores, melt phases, and subsequent recrystallization, resulted in heterogeneous lichen colonization patterns. Cavities and vesicles formed during melting yielded new habitats for both cryptoendoliths and chasmoendoliths, manifested in the natural cryptoendolithic and chasmoendolithic colonization of meteor impact-shocked silica-rich rocks. The pore-fracture network serves for element transfer in the subsurface part of solid rocks and releases important nutrients that otherwise would remain bound**.** Moreover, the substrate zone where the saxicolous lichens are attached is most affected by weathering reactions and shows the highest co-occurrence of lithobiontic microorganisms.

Because of their crustose and foliose morphology, the saxicolous lichens examined here are mainly involved in combined biophysical and biochemical action, mainly on nutrient-rich, weatherable minerals. Generally, fungal hyphae were localised to the feldspar (mostly

plagioclase), mica (mostly biotite and muscovite) and amphibole (mostly Fe-hornblende) component of silica-rich rock varieties compared to quartz and iron oxides. Nevertheless, quartz and iron oxide were also weathered quite significantly. The importance of variable microtextural features, such as twinning and cleavage planes, physical micro-flaws, etch pitting and dissolution lines, seems to be prominent, inducing macro-scale effects which lead to the progressive disintegration of the substrate, with detachment and progressive incorporation of their fragments into the lichen thallus.

Major products of rock transformation *in situ* are the neoformed phyllosilicate clays (and possible amorphous silica), iron release and oxide staining along cracks, oxalate, mycogenic minerals, organic matter accumulation and abundant biofilms that are formed within the porous space in the subsurface part of solid rocks. Such secondary weathering products are mainly attributed to degradative activities, metabolite excretion and/or sorption phenomena. It is thus likely that the physical and chemical properties of the substrate, along with lichen and microorganism activity, determine weathering rates in different microenvironments and microhabitats.

Key terms

Acarospora, Biochemical weathering, Biomechanical weathering, *Buellia*, *Caloplaca*, Lichen–rock interface, Silica-rich rock varieties, Vredefort Dome, *Xanthoparmelia*

ACRONYMS USED

2D: Two-dimensional space

3D: Three-dimensional space

BSE: Back-scattered electron

CRG: Central Rand Group

cm: centimetre

dm: decimetre

EDS: Energy Dispersive Spectrometry

EPS: Extracellular Polymeric Substances

ILG: Inlandsee Lecogranofels

mm: millimetre

NECSA: National Energy Corporation of South Africa

OGG: Outer Granite Gneiss

pm: particulate matter

SAG: Schurwedraai alkali granite

SC: Schurwedraai Complex

SEM: Scanning Electron Microscope

UV: Ultraviolet

WRG: West Rand Group

µCT: X-ray micro-computed tomography

MINERAL ABBREVIATIONS USED

Ab: Albite

Amp: Amphibole

Ap: Apatite

Bt: Biotite

Chl: Chlorite

Fhb: Ferro-hornblende / Fe-Hornblende

Mag: Magnetite

Mc: Microcline

Ms: Muscovite

Kfs: K-feldspar

Pl: Plagioclase

Qz: Quartz

Sr: Sericite

Zr: Zircon

TABLE OF CONTENTS

DECLARATION ..... **I**

ACKNOWLEDGEMENTS ..... **II**

ABSTRACT ..... **III**

CHAPTER 1 GENERAL INTRODUCTION **1**

1.1 BACKGROUND **1**

1.2 PROBLEM STATEMENT **4**

1.3 RESEARCH SUBSTANTIATION **5**

1.4 RESEARCH AIMS **5**

1.5 ORGANISATION OF THE THESIS **6**

CHAPTER 2 STUDY AREA **7**

2.1 INTRODUCTION **7**

2.2 GEOLOGICAL OVERVIEW **7**

2.2.1 Archaean basement complex 9

2.2.2 Witwatersrand metasedimentary rocks 10

2.2.3 Alkali granite complex 13

2.3 VEGETATION TYPE AND CLIMATE **13**

CHAPTER 3 LITERATURE REVIEW **16**

3.1 INTRODUCTION **16**

3.2 ECOLOGY OF LICHENS **16**

3.2.1 Lichen symbiosis 17

3.2.2 Mycobionts 19

3.2.3 Photobionts 19

3.2.4 Thallus morphology and anatomy 20

3.3 LITHIC HABITATS 23

3.4 IMPACT-INDUCED LITHIC HABITATS 25

3.4.1 Physical changes 26

3.4.2 Chemical changes 27

3.5 LICHENS AS BIODEGRADERS OF ROCK SUBSTRATA 27

3.5.1 Biogeophysical weathering 30

3.5.2 Biogeochemical weathering 31

3.5.2.1 Acidolysis and complexolysis 32

3.5.2.2 Biomineralization 32

3.6 MICROBIAL ALTERATION OF HABITAT GEOCHEMISTRY 33

3.7 ANALYTICAL TOOLS USED IN LICHEN–ROCK INTERFACE STUDIES 35

3.7.1 Optical microscopy 35

3.7.2 Scanning-electron microscopy 36

3.7.3 X-ray micro computed tomography 37

CHAPTER 4 METHODOLOGY 40

4.1 INTRODUCTION 40

4.2 ALLOCATION OF HOMOGENEOUS SAMPLING UNITS 40

4.2.1 Stratification and characterisation 41

4.2.1.1 Granite of the Archaean basement complex (Unit A): 41

4.2.1.2 Quartzite of the lower Witwatersrand Supergroup (Unit B): 42

4.2.1.3 Alkali granite of the Schurwedraai Complex (Unit C): 42

4.2.1.4 Ferruginous quartzite of the upper Witwatersrand Supergroup (Unit D): 42

4.2.1.5 Metaconglomerate of the upper Witwatersrand Supergroup (Unit E): 42

4.3 SAMPLE ACQUISITION 43

4.3.1 Geological sampling 43

4.3.2 Lichen sampling 43

4.4 SAMPLE PREPARATION..... 43

4.4.1 Rock samples..... 43

4.4.2 Morphological features 44

4.4.3 Tomographic analysis..... 44

4.4.4 SEM and microprobe analysis 45

CHAPTER 5 FIELD RELATIONS 47

5.1 INTRODUCTION..... 47

5.2 DISTRIBUTION OF ROCKS AND LICHENS IN THE FIELD 47

5.2.1 Granite of the Archaean basement complex (Unit A)..... 50

5.2.2 Quartzite of the lower Witwatersrand Supergroup (Unit B)..... 52

5.2.3 Alkali granite of the Schurwedraai Complex (Unit C) 54

5.2.4 Ferruginous quartzite of the upper Witwatersrand Supergroup (Unit D)..... 56

5.2.5 Metaconglomerate of the upper Witwatersrand Supergroup (Unit E) 58

5.3 MINERAL CONTENT VARIATION 60

5.3.1 Granitic series 61

5.3.2 Siliciclastic series..... 62

5.4 PETROLOGY..... 64

5.4.1 K-feldspar rich granite 64

5.4.2 Sub-labile arenite..... 66

5.4.3 Alkali granite 69

5.4.4 Ferruginous wacke 73

5.4.5 Metaconglomerate 75

5.5 DISCUSSION 78

5.5.1 Impact of the underlying geology 78

5.5.2 Mineralogical and petrographic controls 79

5.6 SUMMARY 81

CHAPTER 6 BIOWEATHERING 82

6.1 INTRODUCTION 82

6.2 ARCHITECTURE OF LITHIC SUBSTRATE 82

6.2.1 Granitic rocks 83

6.2.2 Metasedimentary rocks of the Witwatersrand Supergroup 89

6.3 WEATHERING FEATURES AT THE LICHEN–ROCK INTERFACE 96

6.3.1 *Xanthoparmelia* 96

6.3.2 *Buellia* 106

6.3.3 *Acarospora* 112

6.3.4 *Caloplaca* 118

6.4 DISCUSSION 121

6.4.1 Rock architecture 121

6.4.2 Mechanisms of rock and mineral bioweathering 123

6.4.2.1 Characteristics of the weathering crust 123

6.4.2.2 The weathering sequence 126

6.5 SUMMARY 127

CHAPTER 7 CONCLUSIONS AND RECOMMENDATIONS 128

7.1 GEOLOGY OF THE STUDY AREA 128

7.2 BIOWEATHERING..... 129

7.3 STUDY RECOMMENDATIONS AND CLOSING NOTES 130

REFERENCES..... 132

ANNEXURES..... 161

APPENDIX A: WEATHER DATA 162

APPENDIX B: ANALYTICAL EQUIPMENT..... 165

APPENDIX C: GEOLOGICAL SURVEY DATA. 167

APPENDIX D: POINT COUNT DATA 168

APPENDIX E: SEM-EDS ANALYSIS RESULTS. 169

LIST OF TABLES

Table 1: Proposed lithostratigraphic summary for the reviewed silica-rich sedimentary deposits constituting the Archaean basement complex. 10

Table 2: Proposed lithostratigraphic summary for the reviewed siliciclastic sedimentary deposits constituting the Witwatersrand Basin. 12

Table 3: Proposed lithostratigraphic summary for the reviewed plutonic rocks constituting the alkali granite complex. 13

Table 4: A short summary of geobotanical investigations in and around the Vredefort Dome..... 15

Table 5: A short summary of the charactaristics associated with the three major growth forms associated with lichen thalli..... 22

Table 6: A general summary of the different lithic habitats associated with exposed rock surfaces..... 24

Table 7: The effects of impact cratering on the abundance and characteristics of lithophytic organisms in different lithic habitats. 25

Table 8: A short summary of relevant research on rock weathering promoted by lichens..... 28

Table 9: Summary of measurement parameters using Nikon XTH 225 ST micro-focus X-ray tomography. 45

Table 10: Records of the selected saxicolous lichen genera in the five sampling sites in the Vredefort Dome 49

Table 11: Normalised modal compositions (vol. %) of granitic rock samples..... 62

Table 12: Characteristics for the separation of primary 'wackes' and 'arenites' 64

Table 13: Petrographic features of the examined lithotypes. 80

Table 14: Major microtextural features under each lichen genus studied. 99

LIST OF FIGURES

Figure 1: Cross-sections through the Earth's crust, showing how the Vredefort impact crater, with the Vredefort Dome at its centre, formed (Reimold & Gibson, 2009). 2

Figure 2: Cutaway diagram of the Vredefort Dome today, showing how erosion of the upturned layers has produced the crescent of ridges and valleys seen in Figure 1 (Reimold & Gibson, 2009). 3

Figure 3: Simplified geological map of the Vredefort Dome, depicting the locality of the uplifted structure, and distribution of post-Transvaal syn-Bushveld intrusions. BAG: Baviaan Kranz alkali granite, SAG: Schurwedraai alkali granite, KC: Koedoesfontein Complex, LDC: Lindequesdrift Complex, RC: Roodekraal Complex, RTC: Rietfontein Complex, WW: Winddam wehrlite. 8

Figure 4: Vegetation in the Vredefort Dome. (a) View from Dwarsberg looking northeast, and showing the association of vegetation with the geology. (b) View of the Vaal River at Schurwedraai, showing dense alien invader bush along the river and native woody vegetation associated with rocky hillsides. Also note the influence of farming (white dotted circle). 14

Figure 5: Average monthly rainfall, humidity and temperature for Potchefstroom station (40 km from Dome) from 1997-2017. 15

Figure 6: A hypothetical model of fungal–algal association for lichens, showing the interactions between partners and the mechanisms that structure them. (a) Algal availability determines which algae can be contacted. (b) Fungal specificity determines the ability to form prethallus stages. (c) Fungal selectivity, dependent on ecological context, determines the final composition of observed lichens (Model by Yahr *et al*., 2006). 18

Figure 7: Common photobionts which facilitate lichenization with compatible fungal partner resulting in the formation of lichen thallus. (a) *Trentepohlia* and (b) *Nostoc*. (Micrographs by Shukla *et al*., 2014). 20

Figure 8: (a)-(b) Cross-sections of the foliose lichen thallus showing its various components. The upper cortex of fungal hyphae provides protection.

Photosynthesis occurs in the algal zone. The medulla consists of fungal hyphae. The lower cortex also provides protection. The rhizines anchor the thallus to the substrate. (Modified from Molnár & Farkas, 2010). 21

Figure 9: Most common lithic habitats found within rock substratum. Epiliths inhabit the surface of the rock; cryptoendoliths inhabit pores within the rock structure; chasmoendoliths inhabit cracks and fissures in the rock structure; hypoendoliths inhabit the undermost layer in the rock structure; euendoliths inhabit channels and grooves that were actively "bore" into the rock; and hypoliths inhabit the underside of the rock (Modified from Wierzchos *et al*., 2018). 23

Figure 10: An illustration showing common effects of lichen activity on their substratum rocks (adapted from Chen & Blume., 2002). 29

Figure 11: Microclimate dynamics for cryptogamic photoautotrophs in cold environments. Biological soil crusts and endolithic colonization form extensive near-surface biological covers in cold regions that define the critical zone of biological activity and the dry limit for photoautotrophic colonization on Earth. They occur in regions where precipitation is insufficient to sustain higher plant life. The source of moisture arises from the creation of a substrate-air thermal gradient that supports dew/frost formation. During periods of high sun angle (daytime) thawing of permafrost and soil water releases water to the critical zone (A), when the sun is at a low angle (night) the thermal differential between substrate and air results in dew formation (B) (Modified from Pointing *et al*., 2015). 31

Figure 12: Some of the main influences and effects of microorganisms on components of the built environment. There can be many dynamic interactions between the multiplicity of physical and biochemical mechanisms associated with the biodeterioration of rock- and mineral-based substrates. Biophysical mechanisms include penetration and boring; secondary mineral formation; extracellular polymeric substances (EPS) or biomass swelling or contraction; removal of lichen thalli and adhering substratum by animals and the weather; cell turgor pressure; and physical and chemical effects caused by microbial alteration of habitat geochemistry. Biochemical mechanisms include metabolite excretion (for example, H^+, CO_2); organic acids (for example, citric, oxalic); inorganic

acids (for example, sulfuric, nitric, carbonic); production of metal-complexing EPS, solvents and emulsifying agents; Fe(iii)-coordinating siderophores; redox transformations by oxidation or reduction; bioaccumulation of solubilized metal and anionic species; biomineralization and formation of carbonates, phosphates, sulfides, oxides and oxalates; and alteration of habitat geochemistry by metabolism affecting metal and anionic speciation and mobility. Biodegradation of organic substances can be achieved by extracellular enzymatic attack. Biocorrosion of metals and alloys can include sulfate reduction and metal sulfide precipitation; acid effects; redox transformations; formation of localized corrosion cells; metal complexation by exopolymers, organic acids and other metabolites; and secondary mineral formation. Micrograph scale bars, 50 µm. (illustration by Gadd, 2017a)..... 34

Figure 13: Tomographic Process at the MIXRAD facility (Illistration by Hoffman & De Beer, 2012). 38

Figure 14: Aerial photograph of the Vredefort Dome, illustrating the allocation of sampling units for rock and botanical surveys. The units are named after the predominant bedrock geology or overburden (Google Earth, 2019). 41

Figure 15: Oblique aerial photograph of the inner collar of the Vredefort Dome northwest of Parys, showing sampling unit B (arrow A) and C (arrow B) as well as the Vaal River exploiting a fault cutting the lower Witwatersrand Supergroup. The prominent Hospital Hill Subgroup quartzite (centre) is bent and offset to the north (left) on the far side of the river relative to the rocks on the west side of the river. The flat area to the left is underlain by alkali granite. (Aerial photograph by Reimold & Gibson, 2009)..... 48

Figure 16: Pictures of structural field relations associated with the granites of sampling unit A. (A) A view across the spheroidal granite boulders which roll down along gentle slopes towards the Vaal River. Note the thin exfoliation sheets and reddish iron staining on the surface of the granite. (B) A typical sample of less weathered granite displaying its heterogenenity, found scattered along the spheroidal outcrops in unit A. Note the very weak biotite foliation (white arrows). (C) Photograph of thin, grey pseudotachylitic breccia veinlets cutting the granite, confirming their pre-impact age. (Photographs by Smit, 2019). 50

Figure 17: Pictures of lichen genera reported in sampling unit A. (A) Photograph of the dominant lichen genera colonising the granite, including *Acarospora* sp.pl. (green-colored lichen assemblages) & *Xanthoparmelia* sp.pl. (gray-colored lichen assembladges). Note the thin, grey pseudotachylitic breccia veinlet (white dotted lines) cutting the granite. (B) *Xanthoparmelia* sp.pl. growing in association with vegetation including mosses and grasses. (C) *Acarospora* sp.pl. (green-colored assembladge on the left side of the geological hammer) and *Caloplaca* s. lat. sp.pl. (small irregular patches of orange-colored lichens on the right side of the hammer). (Photographs by Smit, 2019)..... 51

Figure 18: Photographs of field relations associated with sampling unit B. (A) The view across the river shows the riverine habitat associated with the landscape as well as the prominent overturned and strongly fractured quartzite of the Kommandonek ridge, on the opposite side of the river. Note the impact-formed fractures on the surface of the quartzite, which are typically open and fairly straight. (B) Photograph of herringbone cross-bedding in Hospital Hill quartzite. The darker lines are formed by oxidation (rusting) of iron-rich minerals that were deposited on small underwater sand dunes. Surface striations along the fracture planes (white arrow) are also clearly visible: these are indicative of shock deformation. The black lines indicate bedding planes. (C) Bedding-parallel pseudotachylitic breccia in Hospital Hill quartzites. (D) A typical example of a shatter cone segment showing almost parallel striations (white dotted lines) on a sample of Hospital Hill quartzite. The photo also shows an orange-brown crust due to surface oxidation (white arrows). (Photographs by Smit, 2019)..... 53

Figure 19: Pictures of lichen genera encrusting Hospital Hill quartzites in sampling unit B. (A,C) Rock surface completely covered with two dominant lichen genera, including *Buellia* sp.pl. (gray-colored lichen assembladges) and *Caloplaca* s. lat. sp.pl. (orange-colored lichen assembladges). (B) Rock surface covered with mealy and depressed *Acarospora* sp.pl. (green and brown colored assembladges) - their appearance subsequent to lichens dissolving the rock surface. (Photographs by Smit, 2019). 54

Figure 20: Panoramic view looking west over the Schurwedraai bend of the Vaal River. The flat area south of the bend is underlain by the Schurwedraai

alkali granite pluton. To the north, the buttress of the quartzites of the upper Witwatersrand Supergroup forms the highest ridges of the Vredefort Mountain Land. (Photograph by Smit, 2019)..... 55

Figure 21: Pictures of lichen genera encrusting Schurwedraai alkali granite in sampling unit C. (A,B) Rock surface completely covered with three dominant lichen genera, including *Xanthoparmelia* sp.pl. (gray to green-colored foliose lichen assemblages), *Buellia* sp.pl. (gray to white-colored crustose lichen assemblages) and *Caloplaca* s. lat. sp.pl. (orange-colored lichen assemblages). Notice the thin exfoliation sheets. (C) Several *Xanthoparmelia* sp.pl. clusters competing for space. Note the distinctive pattern of millimeter-deep depressions on the grain surface. (D) A typical sample of alkali granite displaying a hypidiomorphic granular texture, found scattered along the granitic outcrops in unit A. (Photographs by Smit, 2019)..... 56

Figure 22: Panoramic view looking north-east over the prominent ferruginous quartzite ridge of the Turffontein Subgroup in the north-western parts of the exposed arc of the vredefort Structure, Rooderand 510. (Photograph by Smit, 2019)..... 57

Figure 23: Lichens encrusting ferruginous quartzite in sampling unit D. (A) Rock surface completely covered with two dominant lichens, namely *Acarospora* sp.pl. (green colored lichen assemblages) and *Caloplaca* s. lat. sp.pl. (orange-colored lichen assemblages). (B). Rock surface displaying secondary coatings of Fe derivatives. Note the knotty appearance on the rock surface (C) A typical sample of moderately mature ferruginous quartzite displaying an orange-brown crust due to surface oxidation (white arrows). (Photographs by Smit, 2019)..... 58

Figure 24: Pictures of the field relations associated with sampling unit E. (A) Panoramic view looking north-east over the conglomerate bed of the Turffontein Subgroup in the north-western parts of the exposed arc of the Vredefort Structure, Rooderand 510. (B) Sub-angular to subrounded clasts in conglomerate hand specimen, found in the north-eastern portion of Unit E. (C) Photo showing the entrance to a mining adit in the central portion of sampling unit E. (Photographs by Smit, 2019)..... 59

Figure 25: Lichen genera encrusting metaconglomerate in sampling unit E. Rock surface covered with three lichen genera, including *Buellia* sp. (gray to white-colored crustose lichen assembladges), *Caloplaca* s. lat. sp.pl. (orange-colored lichen assembladges), and *Acarospora* sp.pl. (green colored lichen assembladges). (Photograph by Smit, 2019). 60

Figure 26: QAP modal classification of plutonic rocks. Adapted from Le Maitre (2002; Figure 2.4), after Streckeisen (1976; Figure 1a). Q=quartz, A= alkali feldspar, P = plagioclase. Alkali Fs = alkali feldspar; Qtz = quartz. 62

Figure 27: Photomicrographs of K-feldspar rich granite (sample VKA1): (A) Photomicrograph displaying a massive hypidiomorphic granular texture. Note the alteration of feldspar grains to fine-grained sericite. PPL. (B) Photomicrograph illustrating the first to second order interference colours. Note quartz grains with strongly mottled extinction patterns (mosaicism) and undulose extinction. XPL. Pl=plagioclase, Kfs=K-feldspar, Qtz=quartz, Bt=Biotite, Ilm=ilmenite. 65

Figure 28: Photomicrographs of sub-labile arenite (sample VKB1) under (A) PPL, displaying a fine-grained granoblastic polygonal texture that consists primarily of detrital quartz grains and a matrix of muscovite, and (B) the same plate under XPL, illustrating the first to second order interference colours. Note quartz displaying microcracks, undulose extinction and extensive recrystallization (white arrows). Yellow arrows are indicative of iron oxide along grain boundaries. Qtz=quartz, Ms=muscovite. 67

Figure 29: Acicular, spiky and fern-like crystallites of muscovite replacing quartz in sub-labile arenite. Notice evidence of pressure solution at quartz grain contacts. Pressure solution results in a serrated solution surface in high-strain areas (small arrows) and precipitate in low strain areas (large arrow)..... 68

Figure 30: Photomicrographs of muscovite in sub-labile arenite (sample VKB1). (A) Photomicrograph illustrating a patch of muscovite crystallites within the interstitial spaces between the quartz. Note how muscovite becomes yellowish-brown (black arrows) toward the edges due to weathering. PPL. Magnified 50 x. (B) Grain of muscovite that has been partly neocrystallized to much smaller new grains of mica with crystal faces (small white arrows).

Note the quartz grain transected by a band of new grains (large white arrow) formed by bulging (BLG)-recrystallisation. XPL. Magnified 50 x. 69

Figure 31: Photomicrographs of alkali granite (sample VKC2) under (A) PPL, displaying a medium- to fine-grained hypidiomorphic-granular texture, which is composed primarily of albite, K-feldspar, quartz and Fe-hornblende. The white arrows point to melt veins. (B) The same plate under XPL, illustrating the first to second order interference colours. Note the undulose extinction and PDF in quartz grains (top left corner). Ab=albite, Qtz=quartz, Fhb=Fe-hornblende. 70

Figure 32: Photomicrographs of the microtextures associated with alkali granite viewed under crossed polarized light (XPL). (A) Photomicrograph displaying microcline perthite. Note the well-developed tartan twinning in microcline exsolved (unmixed) from the homogeneous solid solution during cooling. (B) Photomicrograph of perthite. Note the lenticular exsolution lamellae of albite (dark grey) on K-feldspar (light grey). (C) Photomicrograph of quartz showing multiple sets of recrystallised PDF's within quartz, expressed by arrays of small fluid inclusions (black dots). Magnified 10 x..... 71

Figure 33: Photomicrographs of Fe-hornblende in alkali granite under (A) PPL, displaying aegerine (green colour) and ardfedsonite (dark blue-grey colour), and (B,C) XPL, illustrating the first to second order interference colours. Note the difference in birefringent colours of aegerine (middle second order) and ardfedsonite (lower second order). Also note the ~120° and ~60° cleavage intersections in aegerine. Yellow arrows indicate small opaque inclusions of magnetite in Fe-hornblende. Magnified 25 x. 73

Figure 34: Photomicrographs of ferruginous wacke (sample VKD1) under (A) PPL, displaying a medium- to course-grained hypidiomorphic-granular texture, which is composed of quartz in a matrix of mica and iron oxide; and (B) the same plate under XPL, illustrating the first to second order interference colours. Note quartz displaying microcracks, undulose extinction and recrystallization features (white arrows). Yellow arrows are indicative of iron oxide in the matrix. Qtz=quartz, Ms=muscovite. 74

Figure 35: Micrographs showing quartz grain features in ferruginous wacke artefacts from sampling unit D: (A) Highly deformed quartz displaying PDF's and recrystallisation, especially along the grain boundary. (B) Quartz grain with subgrain boundaries transected by bands of new grains (lower left to top right) formed by bulging (BLG)-recrystallisation. Note bulges along microcracks and grain boundaries. 75

Figure 36: Photomicrographs of metaconglomerate (sample VKE2) under (A) PPL, displaying a course- to fine-grained rock, which is composed of rounded clasts cemented by very fine grains; and (B) the same plate under XPL, illustrating the first to second order interference colours. Note quartz displaying microcracks, undulose extinction and recrystallization features. Yellow arrows are indicative of iron oxide along grain boundaries. Qtz=quartz. 76

Figure 37: Photomicrographs of different mineral phases present in metaconglomerate (sample VK5A). (A) Close-up of a quartzite clast. XPL. (B) Close-up of iron oxide. PPL. (C) Muscovite displaying middle second- to third order interference colours and perfect single cleavage. Note the small opaque inclusions of magnetite. Magnified 25 x. 77

Figure 38: Reconstructed 2D images showing the distribution of grains and void space through K-feldspar-rich granite (sample VKA2). White arrows indicate transgranular fractures penetrating deep into the rock interior. Blue arrows show intergranular fractures propagating along the grain boundaries. White dashed circles show chasmoendolithic behaviour associated with lichenized fungi and organo-mineral associations in the upper part of the weathering rind. Yellow arrows indicate Fe derivatives. Or=K-feldspar, Pl=Plagioclase, Qtz=quartz, Bt=Biotite. 84

Figure 39: Three-dimensional volume rendering of µCT data to show the distribution of *Xanthoparmelia* within K-feldspar-rich granite (sample VKA2). Note lichen thalli restricted to dark grey areas associated with plagioclase- and quartz grains. Matrix of lichen thalli has been rendered semi-transparent in shades of green..... 85

Figure 40: Reconstructed 2D images showing the distribution of grains and void space through alkali granite (sample VKC1). Note the transgranular-

(white arrows) and intergranular fractures (blue arrows) transecting the rock's microstructure. Note the initial stages of fine earth formation associated with weathering zones (white dashed circles) in the upper part of the weathering rind. Or=K-feldspar, Pl=Plagioclase, Qtz=quartz, Fhb=Fe-hornblende. 87

Figure 41: Three-dimensional volume rendering of µCT data to show the distribution of *Xanthoparmelia* within alkali granite sample (VKC1). Matrix of lichen thalli has been rendered semi-transparent in shades of green. 88

Figure 42: Reconstructed 2D images showing the distribution of grains and void space through sub-labile arenite (sample VKB2). Note the relatively sparse distribution of pores (yellow arrows) and macrocracks (white arrows). The red arrow indicates iron staining on the surface of the rock substratum (we refer here to secondary presipitate of Fe). The brightest grains were iron oxides followed by progressively less bright mica and quartz. 90

Figure 43: Three-dimensional volume rendering of µCT data to show the distribution of *Buellia* within sub-labile arenite (sample VKB2). Matrix of lichen thalli have been rendered semi-transparent in shades of green. Red arrow = iron-stained spot. 91

Figure 44: Structure of ferriginous wacke as seen by µCT (sample VKD2). (A) 2D slice showing the distribution of grains and void space in ferriginous wacke. (B) 3D volume rendering of µCT data showing structural and textural relations associated with ferriginous wacke. Matrix of lichen thalli have been rendered semi-transparent in shades of green. Red arrows = Fe-rich transgranular fractures, yellow arrow = pore filled with Fe oxides, blue arrows = deformed matrix of mica. 92

Figure 45: Three-dimensional volume rendering of µCT data to show the distribution of *Acarospora* within ferriginous wacke (sample VKD2). Matrix of lichen thalli have been rendered semi-transparent in shades of green. Note several lichen clusters competing for space. 93

Figure 46: Reconstructed 2D images showing the distribution of grains and void space through metaconglomerate (sample VKE1). Note the aggregation of pores along intergranular void space (yellow dashed circle). Red arrows

= intergranular fractures rich in Fe, green arrow = intragranular fractures, yellow arrows = in situ pores filled with Fe..... 94

Figure 47: Three-dimensional volume rendering of µCT data to show the distribution of *Caloplaca* within metaconglomerate (sample VKE1). Matrix of lichen thalli have been rendered semi-transparent in shades of green. 95

Figure 48: Interface formed by *Xanthoparmelia* thallus and granitic outcrops: *Xanthoparmelia* encrusting alkali granite (A); *Xanthoparmelia* encrusting K-feldspar rich granite (B); bulk sample of discontinuous lichen cover attached to the rough rock surface by large numbers of rhizines (C); detail of square in C, showing the dislodgement of micro-granules (white arrows) (D); surface of *Xanthoparmelia* thallus showing apothecia (white arrows) and radially arranged lobes (E); lobes overlapping like tiles on a roof (F). Fhb=Fe-hornblende, Pl=Plagioclase, Qtz=Quartz, Bt=Biotite, Ap=Apatite, Kfs=K-feldspar. 97

Figure 49: Thallus ontogeny of the foliose lichen *Xanthoparmelia*. (A) SEM images of the surface of granitic rock. Insert close ups provide detail of hyphae attached to deep rock depressions and irregular rock indentations of the rough rock surface. (B) Lichen hyphae and fungal microcolonies (yellow arrows) attached to the substrate. 98

Figure 50: Detail of thallus anatomy associated with *Xanthoparmelia*. (A) SEM close-up of lichen thalli. (B) Group of bacterial cells colonising alkali granite. (C,D) Hyphal mesh from the medulla rich in small mineral grains (white arrows) incorporated from the bedrock. 100

Figure 51: SEM image of the adhesion of *Xanthoparmelia* on alkali granite. The thallus is attached to the rock surface by rhizinae, which appear incomplete in some instances because of transversal and oblique sectioning. Loose clasts disaggregated from the alkali granite by rhizinae penetration and disruption can be observed. Red asterisks show localisation of high Ca concentrations in thallus. Pl=plagioclase, Kfs=K-feldspar, Qtz=Quartz, Fhb=Fe-hornblende. 101

Figure 52: Interface formed by *Xanthoparmelia* thallus and alkali granite. (A) Biological attack on alkali granite showing both physical and chemical decay. Note moldic porosity filled with a pedogenetic matrix (white dashed

circles). (B) Detail of square in A; showing deep etching and bio-corrosion of Fe-hornblende (white dashed circle), quartz (blue dashed circle) and K-feldspar (yellow dashed circle) grains. Note how some fungal cells are covered with mineral crystals (yellow arrows). Red asterisks indicate antiperthite. Qtz=Quartz, Fhb=Fe-hornblende, Kfs=K-feldpsar..... 102

Figure 53: Interface on K-feldspar-rich granite showing fragmentation and stripping of rock fragments, progressively incorporated into the thallus. (A) SEM image of micro-fractures radiating from a biotite grain into adjacent mineral grains, inducing rock fragmentation of plagioclase (white dashed circle) deeper down. (B) Detail of square in A, showing the distinctive patterns of etch pits and dissolution lines on biotite. Note the splitting of biotite and progressive upward incorporation of its flakes (white dashed circles) into the thallus. Note Pl=plagioclase, Kfs=K-feldspar, Bt=Biotite. ... 103

Figure 54: Detail of mycobiont growth through intercrystalline and intracrystalline porosity. (A) Deep etching and bio-corrosion of plagioclase mineral grain. (B) Highly corroded surface of biotite showing extensive etching. (C,D) Visualization of organo-mineral associations in cavities found in alkali granite. Note how fungal cells and biofilms are covered with mineral crystals. (E) Mycobiont growth through moldic porosity (top left corner) connected by mutually interecting intracrystalline fractures of quartz. Insert SEM close ups provide detail of cylindrical hyphae covered with mineral crystals (top insert) and a pyramidal crystal of calcium dehydrate (white arrow, bottom insert) through intracrystalline porosity. 104

Figure 55: Secondary weathering products on the surface of granitic rocks. (A) Secondary accumulation of nanocrystalline clay (white dashed circle) and organic matter accumulation (red asterisks) on quartz grains. (B) Mycogenic secondary mineral (white dashed circle)..... 105

Figure 56: Micrographs of the interface formed by the crustose *Buellia* thallus and the surface of sub-labile arenite (A) and alkali granite (B). SEM images of bulk samples of sub-labile arenite (C,D): continuous crust-like growth adherent or attached by hyphae throughout its underside (C); side view displaying a polygonal texture as well as the interstitial matrix (red asterisk) (D). Qtz=Quartz, Ms=Muscovite, Pl=Plagioclase, Kfs=K-feldspar Fhb=Fe-hornblende. 106

Figure 57: SEM images of bulk samples of *Buellia* encrusting sub-labile arenite. (A) Surface of *Buellia* thallus extremely rich in small mineral grains incorporated from the bedrock. (B) Detail of square in A, showing *Buellia* thallus in close contact with a colony of algae and fungi. Thallus ontogeny associated with *Buellia* (C,D,E,F): microcolonies of fungi with branching and penetrating hyphae attached to substrate (C); detail of square in C, showing tunnelling and microcolonial fungi (white arrows) on the surface of the substrate (D); lichen hyphae (white arrow) rich in small mineral grains (white arrows) incorporated from the bedrock (E); lichen hyphae etching into quartz grain (F). 107

Figure 58: Fungal growth on and in quartz grains strongly interacting with the quartzitic substrate. (A,B) Fungi (yellow arrows) and organic matter accumulation (red asterisks) along the organo-mineral interface. Also note the crystalline aggregate of calcium oxalate (yellow dashed circle). (C,D) Fungi attached to quartz grains via biologically etched pits. Note the tracks left by the hyphal growth (white arrows). 108

Figure 59: SEM image of fissures in sub-labile arenite colonized by chasmoendolithic fungi. Fungal masses can be seen deeply and widely protruding into trans- (white arrows)- and inter-granular fractures (yellow arrows). Loose clasts disaggregated from the quartzite by fungal massess can be observed in the lichen thallus, mainly at its top (upper cortex). Qtz=quartz, Ms=muscovite. 109

Figure 60: Detail of the near-surface interface of *Buellia* and quartzite. (A) SEM image displaying the fragmentation and stripping of weak parts off substrate by thallus adhering action. Arrows indicate fissures associated with the points of thallus anchorage to the lithic substrate. (B) Detail of square in A, showing organic matter accumulation (red asterisks) around quartz grains. Note the splitting of muscovite (white dashed circle) and progressive upward incorporation of its flakes) into the thallus. Qtz=quartz, Ms=muscovite. 110

Figure 61: Visualization of organo-mineral associations in cavities found in sub-labile arenite. (A) Close-up of groundmass composed mainly by intergranular microlitic laths of muscovite and equant mineral grains of Fe–Ti oxides dispersed into a micacious matrix. (B) Highly altered and dissolved

muscovite almost totally converted to a siliceous relic following the extraction of aluminium, iron and magnesium from its structure. (C,D) Secondary accumulation of clays at a point of intersecting fractures. 111

Figure 62: Interface formed by the crustose *Acarospora* thallus and the surface of ferruginous wacke on a more silica-rich (A) and iron-rich (B) patch of the substrate. SEM images of bulk samples of *Acarospora* (C,D): surface of *Acarospora* sp.pl.' thallus showing sunken apothecia (white arrows) (C); side view displaying patches of fine matrix (white dashed circles) incorporated into the thallus (D). Qtz=Quartz, Ms=Muscovite, Fe-ox=iron oxide. 112

Figure 63: Thallus ontogeny in the crustose lichen *Acarospora* (A) *Acarospora* thallus in close contact with a colony of algea and fungi. (B) Detail of square in A, showing ultrastructural details of the algal and fungal colony. (C) Surface of *Acarospora* thallus showing microcolonies of fungi with branching hyphae. (D) Detail of square in C, showing ultrastructural details of branching hyphae. (E) Colony of alga and fungi in close contact to substrate. (F) Detail of square in C, showing ultrastructural details of fungi with branching and penetrating hyphae attached to substrate. 113

Figure 64: Detail of the near-surface interface of *Acarospora* and ferruginous wacke. (A) SEM image displaying the fragmentation and stripping of weak parts off substrate by thallus adhering action. (B) Detail of square in A, showing ultrastructural detail of the progressive incorporation of fragmented quartz (white arrows) and muscovite (yellow arrows) grains into the thallus. Qtz=Quartz, Ms=Muscovite. 114

Figure 65: Detail of the near-surface interface of *Acarospora* and ferruginous wacke. (A) SEM image displaying the fragmentation and stripping of matrix-bearing muscovite by thallus adhering action. (B) Detail of square in A, showing crystalline aggregate of iron oxide and organic matter (red asterisks) along matrix. Note the accumulation of organic matter within fungal hyphae (red asterisks). Qtz=Quartz, Ms=Muscovite, Fe-ox=iron oxide. 115

Figure 66: Intensely fragmented substratum of ferrigineous wacke. (A) Physical penetration of mycobiont hyphae deep within the stone substrate

exploiting and enlarging pre-existing fractures and porosity. (B) Detail of square in A, showing chasmoendolithic hyphae deeply and widely protruding into inter- (blue arrows), and intra-granular (yellow arrows) fractures. Note the dissolution and fragmentation of quartz (white circle) and through these layers. Qtz=Quartz, Ms=Muscovite, Fe-ox=iron oxide… 116

Figure 67: Visualization of iron accumulation and organo-mineral associations in fractures and pores of ferruginous wacke. (A) Iron accumulation along transgranular fractures. (B) Dissolution of iron oxide by organic acids. (C) Endolithic fungal growth through intergranular porosity. Note how fungal cells are covered with mineral crystals. (D) Secondary iron accumulations through microfractures. (E,F) Vesicle-filling iron oxide with typical botryoidal (“bunch or cluster shaped”) habit. 117

Figure 68: Micrographs of the interface formed by the crustose *Caloplaca* thallus and the surface of metaconglomerate: lichen hyphae did not penetrate the surface of the rock but weak parts were fragmented by thallus adhering action (A,B); continuous lichen cover attached to the rock surface by hyphae (C); surface of *Caloplaca* thallus extremely rich in small mineral grains incorporated from the bedrock (D). Qtz=Quartz. 118

Figure 69: Thallus ontogeny of the crustose lichen *Caloplaca*. (A) Branching and penetrating hyphae attached to substrate. (B,C) Detail of white square (B) and yellow square (C), providing evidence of hyphae attached to the surface of the substrate. Note evidence of tunnelling (red arrows), surficial holes (yellow arrows) and the dislodgement of microgranules (white arrows)..... 119

Figure 70: Detail of the near-surface interface of *Caloplaca* and metaconglomerate. (A) Thick bio-patina with active desegregation and incorporation of mineral fragments from underlying rock substrate. (B) Detail of the near-surface interface of *Caloplaca* and metaconglomerate. (C) Traverse fracture surface of the interface between the medulla of *Caloplaca* and metaconglomerate. (D) Vesicle-filling biofilms. (E) Intragranular biological attack on iron oxide accumulation in a cavity showing both physical and chemical decay. (F) Vesicle-filling iron oxide with typical botryoidal habit… 120

CHAPTER 1

GENERAL INTRODUCTION

1.1 BACKGROUND

It is widely recognized that impact cratering is a ubiquitous geological process that is characterised by often intense and sudden deformation of immense volumes of all planetary objects with a solid surface. “Such a spectacle generally causes material from depth to be brought to the surface in the form of ejecta deposits and central uplifts, which provide a unique window into the subsurface on planetary bodies” (Osinski & Pierazzo, 2013). The effects of impact cratering have also been shown to extend far beyond the production of craters with evidence of its involvement in major biological extinctions and the ability to produce tsunamis, extreme atmospheric disturbances, and short- and longterm climate change (French, 2004). It should not be surprising, therefore, that impact cratering has played an important role throughout Earth’s history, shaping the geological landscape, affecting the evolution of life and producing economic benefits.

The Vredefort Dome in South Africa is one of the largest known terrestrial impact structures on Earth (approx. 250-300 km in diameter) and is commonly accepted to be the result of a large meteorite impact, dated around ~2023 ± 4 Ma (Kamo *et al*., 1996). The meteorite impact resulted in strong recoil of the deeper part of the crust, causing the basement granite to punch through the overlying, horizontally stacked rocks of the Dominion, Witwatersrand, Ventersdorp and Transvaal Supergroups, overturning the layers in the process (see Figure 1). At present day, only remnants of the dome’s once vast structure remain visible (Figure 2), which is evident of the varying degrees of resistance to weathering and erosion.

The dome is centered within the geologically renowned Witwatersrand Basin and is surrounded by a synclinorium which forms an outer collar surrounding the Paleo- to Meso-Archean crystalline basement core. The 45-50 km wide core consist of Archaean granitoid gneisses (~3200-3100 Ma) with subsidiary greenstone inliers as well as several ultramafic, mafic, pelithic and ironstone xenoliths, which is thought to be around ~3400-3500 Ma old (McCarthy & Rubidge, 2005; Armstrong *et al*., 2006). The 20 to 25 km wide collar consists of subvertical to partially overturned Meso-Archean to Paleo-Proterozoic supracrustal strata of the Dominion Group (~3070 Ma), followed outwards by strata of the Witwatersrand (~2950–2710 Ma), Ventersdorp (~2714 Ma) and Transvaal (~2650–2150 Ma) Supergroups (Johnson *et al*., 2006; Gibson & Reimold, 2008). The south-eastern sector of the structure is partially covered by horizontal sedimentary formations of

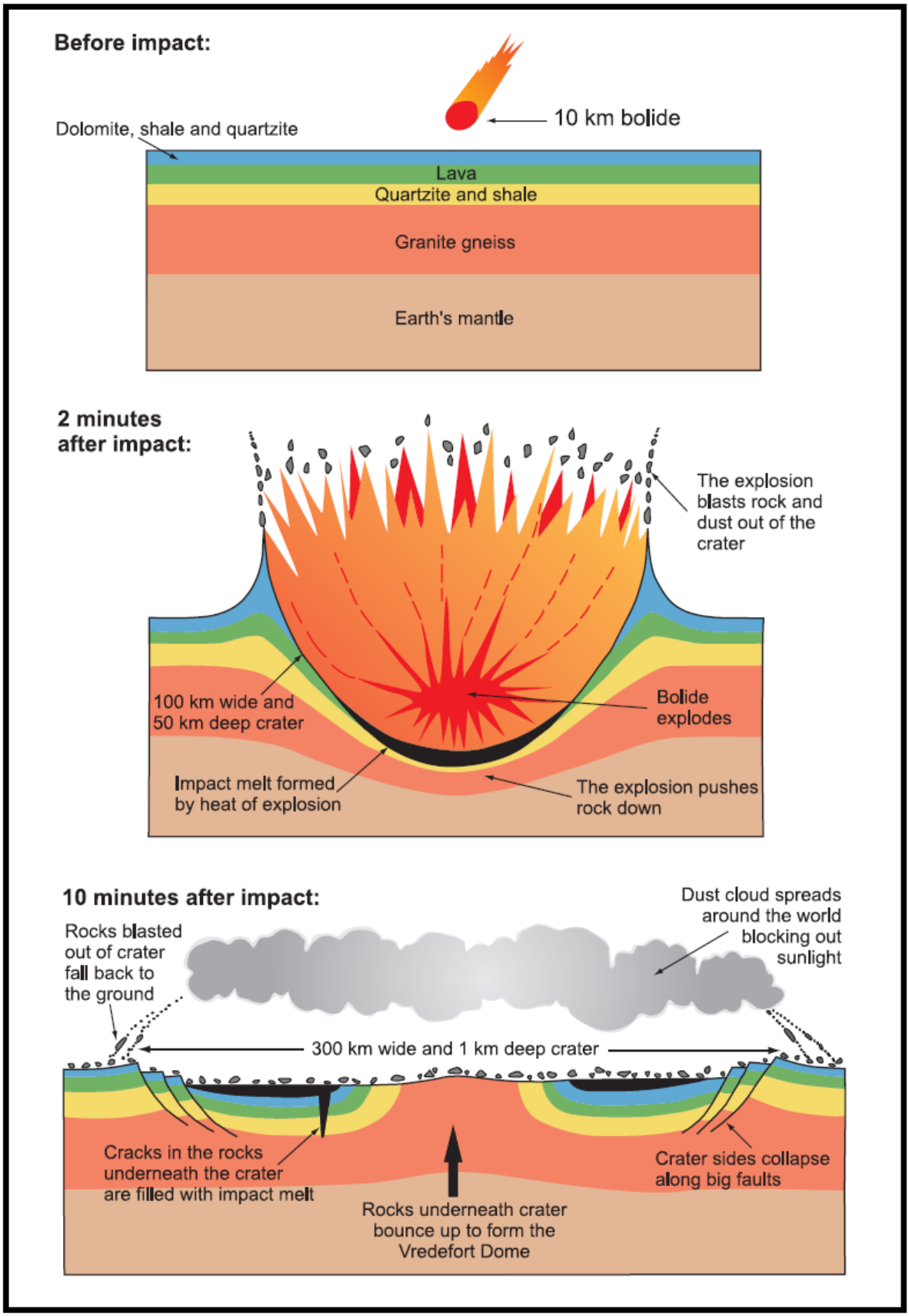


Figure 1: **Cross-sections through the Earth's crust, showing how the Vredefort impact crater, with the Vredefort Dome at its centre, formed (Reimold & Gibson, 2009).**

the Karoo Supergroup, forming the youngest group of rocks (~300 to 180 Ma) (Reimold, 2006). The Vredefort Dome also hosts several Neoarchaean (2800 Ma) to Mesoproterozoic (1000 Ma) peralkaline to ultramafic intrusive bodies that are exposed amongst its core and collar (Bisschoff, 1969, 1999; Reimold *et al*., 2000; Anhaeusser, 2004, 2006; Gibson & Reimold, 2008; Reimold and Gibson, 2009). These intrusions are broadly grouped based on their relationship to the 2023 Ma old impact deformation features of the dome (planar micro-deformation, pseudotachylite and shatter cones), and are referred to as either pre- or post-impact intrusions.

Although impact events are commonly viewed as agents of ecosystem destruction, for some microbial communities, impacts may represent an opportunity for habitat formation as some substrates are rendered more suitable for colonization when processed by impacts (Cockell *et al*., 2002). Among rock-dwelling microbial communities, lichens have been identified as the most visible components of lithic microbial ecosystems. Lichens play an important role in the biogeochemical evolution of the outer layer of the Earth, affecting the patterns and processes of

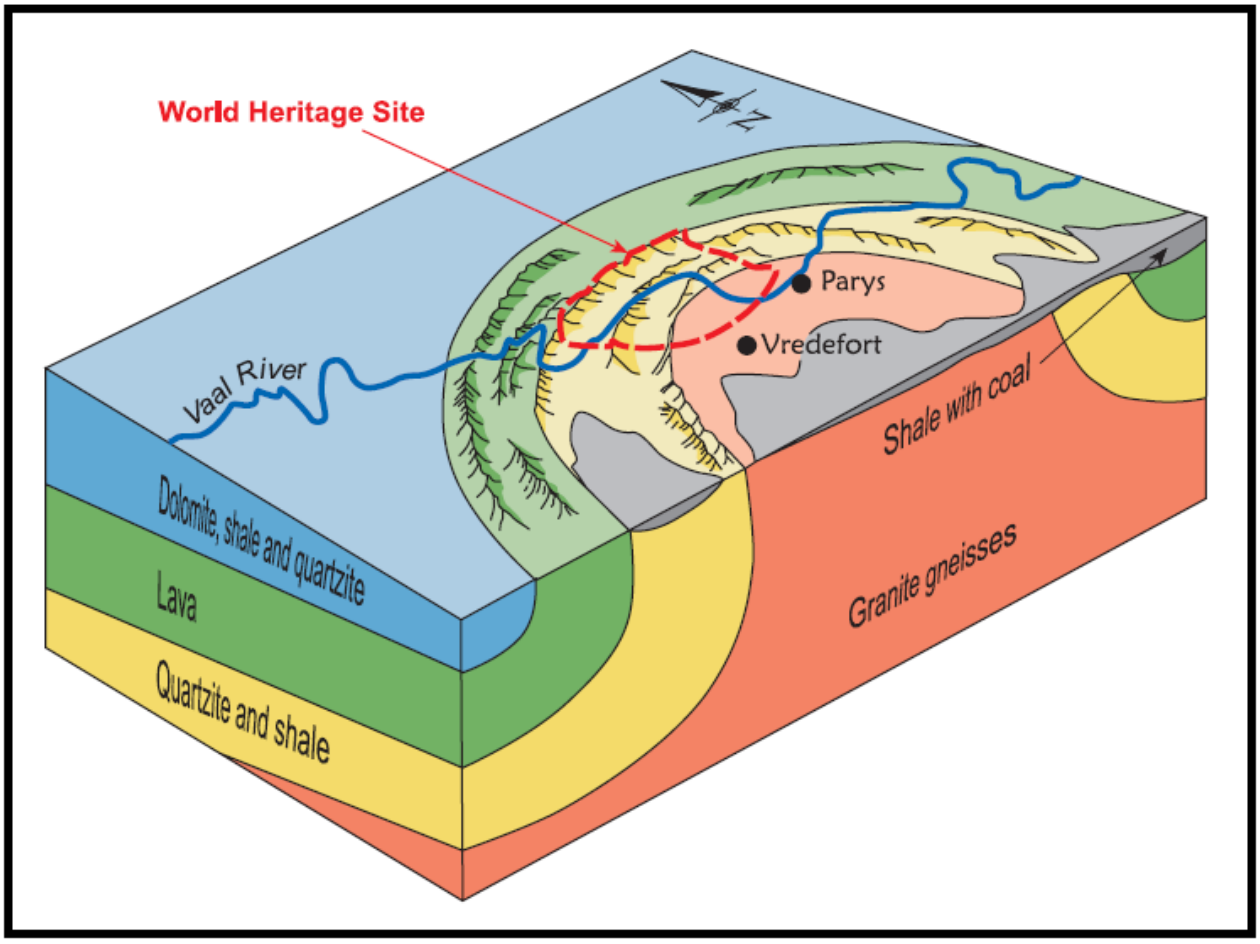


Figure 2: **Cutaway diagram of the Vredefort Dome today, showing how erosion of the upturned layers has produced the crescent of ridges and valleys seen in Figure 1 (Reimold & Gibson, 2009).**

biogeochemically important processes, such as rock weathering and the biogeochemical cycling of chemical substances (Syers & Iskander, 1973; Jones, 1988; Adamo & Violante 2000; Chen *et al*, 2000; Salvadori & Casanova-Municchia, 2016). The role of lichens in the degradation of rocks and minerals can be ascribed to their pedogenic action being both physical and chemical in nature contributing to their ability to interact with minerals, metals, metalloids and organic compounds (Gadd, 2007). On the other hand, some literature suggests that the lichens play a protective insulating role (Carter & Viles, 2005; Hall *et al*., 2005; de la Rosa *et al*., 2012).

1.2 PROBLEM STATEMENT

Studies regarding the role of lichens in the breakdown of rock surfaces is a broadly researched discipline (Adamo & Violante, 2000; Chen *et al*, 2000; Weber & Büdel, 2011; Mitchell *et al*., 2016). Despite such a rich and varied literature, only very few papers investigated the potential role of lichens in the breakdown of rock surfaces in the southern hemisphere and African environments. This is due to limited information regarding the exact nature between the geochemistry and mineralogy of the rocks, as well as the occurrence of individual lichen species and assembly of lichen communities in African environments (McKechnie *et al*., 2007).

Most of the research in southern Africa is generally limited or centred around lichen-induced deterioration of sedimentary rock types (Wessels & Schoeman, 1988; Kerr & Zavada, 1989; Wessels & Büdel, 1989; Wessels & Wessels, 1991; Wessels & Kappen, 1993; Wessels *et al*., 1995; Weber *et al*., 1996; Büdel *et al*., 2004), with little known research focusing on lichen-induced deterioration of igneous and metamorphosed (also shock-affected) rock types (Cooks & Fourie, 1989; Cooks & Otto, 1990; McKechnie *et al*., 2007). Initial observations made from these investigations indicated that lichens contribute to chemical weathering processes by chelation and mechanically by the penetration and expansion of hyphae, affecting the elemental composition of the host material. It also evidenced the distinct correlations of the habitats of some lichen species with light levels and water supply. Nonetheless, few researchers conducted a comprehensive understanding on the overall mechanisms, effects, and magnitude of effects (Favero-Longo & Viles, 2020).

By far less documented internationally, is the role of lichens in the breakdown of rock and mineral surfaces within impact craters, although different lithological units therein, outcropping are generally severely colonized by several lichen species. Previous studies conducted in the Haughton impact structure, Canada, predominately focused on the colonization of rocks by endolithic communities, thus focusing on a variety of different microbial communities (Cockell & Lee., 2002; Cockell *et al*., 2002, 2003, 2005, 2006; Fike *et al*., 2002, 2003; Cockell & Osinski,

2007; Pontefract *et al*., 2014). These studies concluded that impact-shocked rocks do offer significant refuge for endolithic communities due to increased shock state and particularly increased porosity and translucence. Another study on Loftarstone from the Lockne impact crater, Sweden, demonstrated that lichenized fungi preferentially weather the chlorite in the Loftarstone compared to feldspars and quartz (Cockell *et al*., 2007). The exact explanation for these abrupt species changes across the varying lithologies within impact craters is unclear and requires further study.

Based on these shortcomings, the Vredefort Dome in South Africa was selected as a case study to investigate the potential role of lichens in the deterioration of impact-induced rock surfaces in the southern hemisphere and African environments.

1.3 RESEARCH SUBSTANTIATION

For a biogeochemical investigation of the weathering of impact-induced rocks and minerals, lichen-encrusted rocks provide an ideal environment, where a direct relationship between lichens and their substrates can be investigated with relative ease. Such relationships may reveal important environmental and ecological characteristics regarding species adaptation to specific target lithologies within an ecosystem such as the Vredefort Dome, and as a result, provide important insight into the dynamics of important biogeochemical processes (e.g. organic and inorganic transformations, element cycling, rock and mineral transformations, mycogenic mineral formation, fungal–clay interactions, and metal–fungal interactions) within impacted regions. Understanding weathering in mixed, fractured materials may also provide insight into generalized mechanisms of how impact processing alters lithic habitats through time. Finally, the study of impact-induced rock substrate may yield important insights into possible habitats for life on other planets.

1.4 RESEARCH AIMS

The primary research aims for this study are to:

(i) Determine and discuss the petrological character of different silica-rich rock types that were identified to host abundant lichen activity.

(ii) Gain insight into microstructural characteristics (pore space and microcracks) and three-dimensional textural relationships at a pore-scale level.

(iii) Investigate the potential role of biologically mediated degradation of impact-induced silica-rich rocks by saxicolous lichens.

(iv) Identify and discuss chemical variables that correlate with changes in dominant rock types.

1.5 ORGANISATION OF THE THESIS

The body of this thesis is divided into seven chapters, starting with the Introduction here in Chapter 1 in which the background, problem statement, research substantiation, aims and organisation of thesis are presented. A description of the study area is provided in Chapter 2. This is followed by a critical review of the literature in Chapter 3, focusing on the ecology of lichens, lithic habitats, impact-induced lithic habitats, lichens as biodegradors of rock substrata, biomineralization, microbial interactions, and a description on the analytical tools used in this study. A summary of the materials and methods that were used in this study is given in Chapter 4. Chapter 5 provides details on sample collection and the determination of field relations as well as the techniques and experimental methods used during this study. Chapter 6 presents the results from the experimental tests, investigating the lichen-rock interface on different impact-induced silicate rock types in the Vredefort Dome. A concluding discussion summarising the findings as well as several recommendations for further research are given in Chapter 7. The complete set of results from the various analyses and experiments are presented in the appendices.

CHAPTER 2

STUDY AREA

2.1 INTRODUCTION

The Vredefort dome approximately 120km south-west of Johannesburg represents a respectable part (with a diameter of 190km) of the larger, 2.02 Ga Vredefort impact structure (250–300 km diameter) (Lana *et al*., 2003), and has a unique structural setting because it lies on a major lineament defined by the Great Dyke, the Bushveld Complex, the Pretoria-Johannesburg Dome, the Losberg intrusion, the Brandfort gravity anomaly and the Trompsburg Complex (Bisshoff, 1988; Stepto, 1990). It falls roughly between Potchefstroom (North West province) and the Free State towns of Parys and Vredefort (Figure 3). Adding to its importance is the accessibility of the impact structure because the surface lies below the original crater floor and it gives a full geological profile of an astrobleme. The dome is also bisected by the Vaal River - the second-largest river system in South Africa, flowing 1300 km from its headwaters in the Highveld to its confluence with the Orange River (Helgren, 1979; Gibbon, 2009). The Vaal River incised the bedrock of the Vredefort Dome and enters the dome from Parys along a major fault in the rocks of the collar (see Figure 18) before leaving the dome towards the west, again along a major fault (Reimold & Gibson, 2009).

Due to the topographic and geographical diversity of the land, fauna and flora is varied and abundant. The study area was, therefore, limited to damper areas associated with the Vaal River and its flood plains containing predominantly silica-rich rock types - the surfaces of which are regularly colonized by microbial communities (Büdel *et al*., 2004).

2.2 GEOLOGICAL OVERVIEW

During field reconnaissance (refer to Section 3.1) several silica-rich rock types were identified to be subjected to abundant lichen colonization, including granites in the Archaean Basement Complex, quartzites and metaconglomerate of the Witwatersrand Supergroup, and Alkali Granite associated with peralkalic intrusions. A wide range of different lithologies have been described under these stratigraphic units and a complete outline of each stratigraphic unit is not the scope of this chapter. However, detailed reviews are given by McCarthy *et al*. (2006), Robb *et al*. (2006) and Lana *et al*. (2004). Here, only the lithologies that were identified to host abundant lichen colonization will be discussed in further detail.

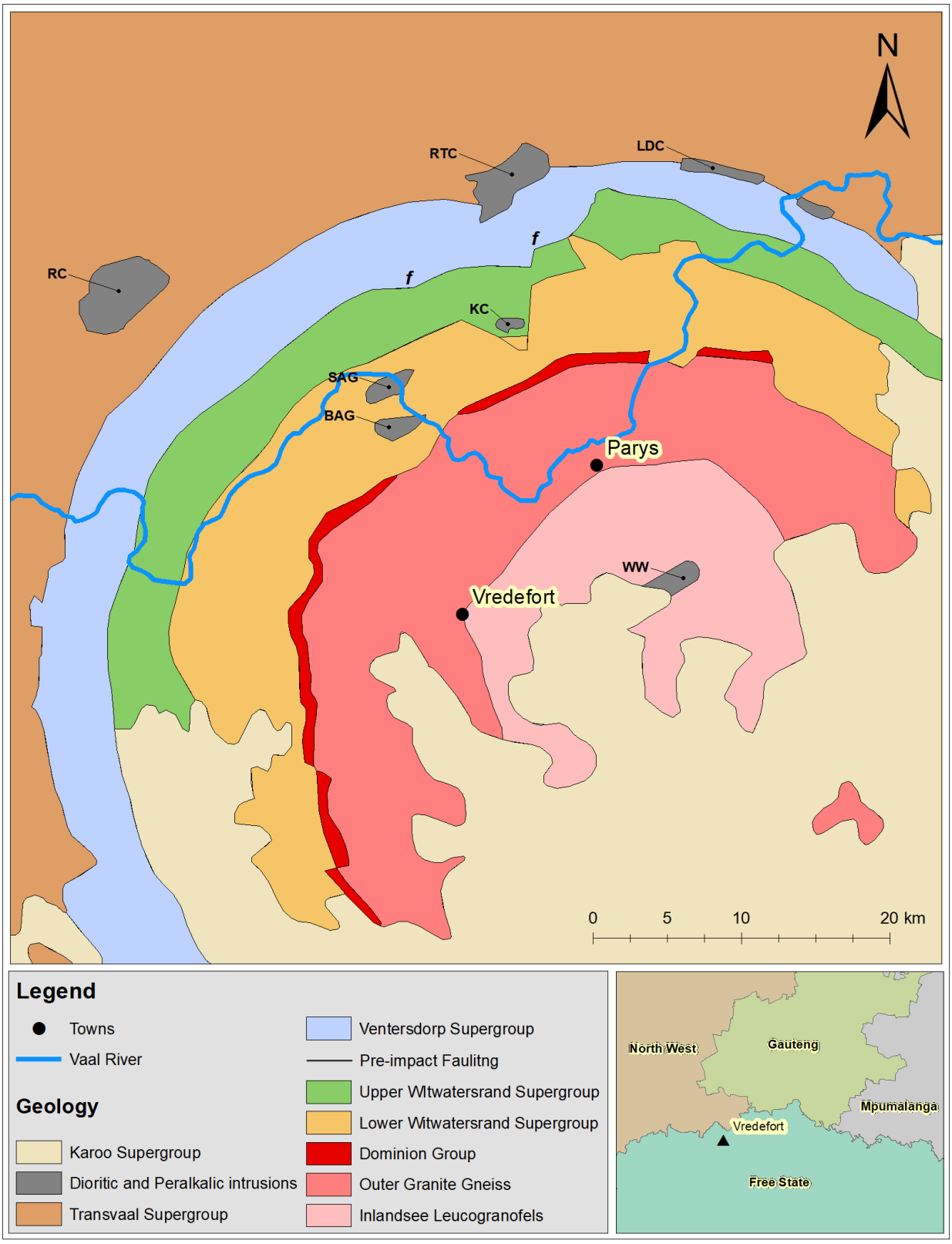


Figure 3: **Simplified geological map of the Vredefort Dome, depicting the locality of the uplifted structure, and distribution of post-Transvaal syn-Bushveld intrusions. BAG: Baviaan Kranz alkali granite, SAG: Schurwedraai alkali granite, KC: Koedoesfontein Complex, LDC: Lindequesdrift Complex, RC: Roodekraal Complex, RTC: Rietfontein Complex, WW: Winddam wehrlite.**

2.2.1 Archaean basement complex

The 3.12 to 3.10 Ma old Archaean basement complex (Outer Granite Gneiss and Inlandsee Leucogranofels in Figure 3) comprise a complex high-grade metamorphic terrane that is dominated by polyde formed, upper amphibolite- to granulite–facies migmatitic gneisses, with subsidiary small granitoid bodies and metasedimentary and metavolcanic granulite xenoliths (Stepto, 1990; Hart *et al*., 1999; Lana *et al*., 2003, 2004). In addition, a sequence of greenschist amphibolite–facies meta-komatiites and komatiitic metabasalts are exposed in the southeastern sector of the core (Anhaeusser, 2014). Stepto (1990) subdivided the basement rocks into an inner core of granulite facies gneisses termed the Inlandsee Lecogranofels (ILG, Figure 3), and an outer core of amphibolite-grade migmatitic gneisses termed the Outer Granite Gneiss (OGG, Figure 3). A general summary of the mineralogical composition of the different basement rocks is provided in Table 1.

“The terms “leucosome” and “melanosome” is used to describe the pale-colored, igneous- like, quartzofeldspathic parts of the migmatite, and the dark-colored, more mafic parts respectively” (Lana *et al*., 2003). The leucosomes and melanosomes are locally interleaved with the trondhjemitic gneiss and migmatized amphibolite xenoliths of variable size (Lana *et al*., 2004). The migmatites in the OGG is dominated volumetrically by granitic leucosomes and to a lesser extend trondhjemitic melanosomes (Table 1). The migmatites in the ILG differs from the migmatites in the OGG in that biotite is largely replaced by orthopyroxene ± clinopyroxene (i.e., more mafic), with the result that the leucosomes and melanosomes are more appropriately described as charnockitic- to enderbitic and tonalitic respectively (Table 1).

The granitic leucosomes in both the ILG and OGG commonly grade into coarse-grained schlieric and homogeneous granites that display variable foliation defined by aligned K-feldspar megacrysts in an undeformed matrix (Lana *et al*., 2003). The homogeneous granite shows a weak biotite foliation whilst the schlieric granite shows a weakly foliated matrix (plagioclase, quartz and K-feldspar), which contains biotite and K-feldspar megacrysts (Lana *et al*., 2004). Strongly foliated, nonmigmatitic, trondhjemitic and quartz dioritic gneisses occur in the northeastern sector and central parts of the dome, respectively (Lana *et al*., 2003, 2004).

The core of the dome also contains subsidiary porphyritic granodiorite, K-feldspar rich granite and magnetite-rich granodiorite (Lana *et al*., 2003, 2004). High-temperature recrystallization resulted in the advent of pseudotachylite veins and dikes in both the migmatites and gneisses of the Archaean basement complex (see Reimold & Gibson, 2009 for an overview).

Table 1: Proposed lithostratigraphic summary for the reviewed silica-rich sedimentary deposits constituting the Archaean basement complex.

Lithologies	Mineral assemblages	Retrograde + accessory minerals
Gneisses		
Trondhjemite	Plagioclase (55–60 vol%), quartz (25–30 vol%), K-feldspar (10–15 vol%), Biotite (5–10 vol%) [1,2,3]	Sericite, epidote, chlorite, sphene, ilmenite, zircon, apatite [1,2,3]
Quartz-diorite	Plagioclase (55–60 vol%), K-feldspar (30–35 vol%), quartz (5–10 vol%), clino- and orthopyroxenes (<5 vol%), biotite (<1 vol%) [1,2,3]	Biotite, chlorite, sericite, epidote, sphene, zircon, apatite [1,2,3]
Migmatite (Leucosomes)		
Granite	Plagioclase (40–50 vol%), quartz (25–35 vol%), K-feldspar (25–35 vol%), biotite (5 vol%) [1,2,3]	Sericite, epidote, chlorite, sphene, ilmenite, zircon, apatite, allanite [1,2,3]
Charnockite	Plagioclase (40–50 vol%), quartz (25–35 vol%), K-feldspar (25–35 vol%), clino- and orthopyroxenes (<5 vol%), biotite (<1 vol%) [1,2,3]	Biotite, chlorite, sericite, epidote, sphene, zircon, apatite [1,2,3]
Felsic enderbite	Plagioclase (50–60 vol%), quartz (25–35 vol%), clino- and orthopyroxenes (>5 vol%), K-feldspar (5–10 vol%), biotite (<1 vol%) [1,2,3]	
Enderbite	Plagioclase (50–60 vol%), quartz (15–25 vol%), clino- and orthopyroxenes (10–20 vol%), K-feldspar (<5 vol%), biotite (<1 vol%) [1,2,3]	Biotite, chlorite, sericite, epidote, sphene, zircon, apatite [1,2,3]
Migmatite (Melanosomes)		
Trondhjemite	Plagioclase (55–60 vol%), quartz (20–25 vol%), K-feldspar (10–15 vol%), biotite (10–15 vol%) [1,2,3]	Sericite, epidote, chlorite, sphene, ilmenite, zircon, apatite [1,2,3]
Tonalite	Plagioclase (50–55 vol%), clino- and orthopyroxenes (20–25 vol%), biotite (5–10 vol%), quartz (5–10 vol%) [1,2,3]	Biotite, chlorite, sericite, epidote, sphene, zircon, apatite [1,2,3]
Granitoids		
Porphyritic granodiorite	Plagioclase (55–60 vol%), quartz (20–25 vol%), K-feldspar (10–15 vol%), biotite (10–15 vol%) [1,2,3]	Sericite, epidote, chlorite, sphene, ilmenite, zircon, apatite [1,2,3]
Homogeneous granite	Plagioclase (40–50 vol%), quartz (30–35 vol%), K-feldspar (30–35 vol%), biotite (5 vol%) [1,2,3]	Sericite, epidote, chlorite, sphene, ilmenite, zircon, apatite, allanite [1,2,3]
Schlieric granite	Plagioclase (40–50 vol%), quartz (30–35 vol%), K-feldspar (25–30 vol%), biotite (10–15 vol%) [1,2,3]	Sericite, epidote, chlorite, sphene, ilmenite, zircon, apatite, allanite [1,2,3]
K-feldspar-rich granite	Plagioclase (40–45 vol%), quartz (20–30 vol%), K-feldspar (35–40 vol%), biotite (5 vol%) [1,2,3]	Sericite, epidote, chlorite, sphene, ilmenite, zircon, apatite [1,2,3]
Magnetite-rich granodiorite	Plagioclase (40–50 vol%), quartz (25–35 vol%), K-feldspar (25–35 vol%), biotite (5 vol%), magnetite (2–3 vol%) [1,2,3]	Sericite, epidote, chlorite, sphene, ilmenite, zircon, apatite [1,2,3]

***Sources*: [1.]Stepto, 1990; [2.]Lana *et al*., 2003; [3.]Lana *et al*., 2004**

2.2.2 Witwatersrand metasedimentary rocks

The Archaean to Mesoarchean 2.99 to 2.78 Ga (Kositcin & Krapež, 2004) Witwatersrand Supergroup is situated in the central portion of the Kaapvaal Craton of South Africa and hosts the

world's most important gold accumulation, which has yielded more than one third of all the gold ever produced on the planet (Frimmel, 2005; Hartnady, 2009; Tucker *et al*., 2016). The lithostratigraphic scheme compiled by the South African Committee for Stratigraphy (SACS, 2006) subdivided the Witwatersrand Supergroup as follows:

Upper- or Central Rand Group (~2 km thick):	Turffontein Subgroup
	Johannesburg Subgroup
Lower- or West Rand Group (~5 km thick):	Jeppestown Subgroup
	Government Subgroup
	Hospital Hill Subgroup

The Witwatersrand Supergroup contains siliciclastic rocks that were deposited in a variety of depositional environments, with only minor episodes of flood basalt volcanism accounting for less than 3% of the succession (SACS, 2006). The siliciclastic sedimentary deposits of the Witwatersrand Supergroup are composed of predominantly 'quartzites' (quartzose sandstones including arenites and wackes), metaconglomerate and metapelites (low-grade metamorphosed shales, siltstone or mudstone) (McCarthy, 2006; Smith *et al*., 2013). A general summary of the mineralogical composition of each rock type is provided in Table 2. Banded iron formation, diamictite, meta-lava and several dykes and sills are minor lithological constituents (see McCarthy *et al*., 2006 for an overview).

Deposition of the West Rand Group (WRG) took place in shallow to distal marine shelf environments (quartz arenite, shale and banded iron formation), but also in braided fluvial systems in the northwestern proximal parts of the basin (conglomerate and immature sandstone) (Maynard & Klein, 1995; Kositcin & Krapež 2004; Schmitz *et al*., 2004). Due to the preferential accumulation of strata in the northwestern parts of the depository, basin fill is distinctly asymmetric (Beukes, 1995). In the Central Rand Group (CRG), fluvial braidplain depositional environments dominate (Stanistreet & McCarthy, 1991; Catuneanu, 2001). However, minor transgressive events are reflected in the deposition of the Booysens Formation and several shallow marine quartz arenites (Bailey et al., 1990; Beukes & Nelson, 1995). "Sedimentation was controlled by deep-seated southeast-directed thrust faults along the basin margin, which lead to source area rejuvenation, uplift, erosion and recycling of older sediments in proximal areas" (Coward *et al*., 1995). The areal extent of the fluvial depositional systems waned with time, so that by upper CRG times, the depositional margin was equivalent to the tectonic margin (Myers *et al*., 1990).

Subsequently, the rocks of the Witwatersrand Basin have been altered through a series of regional metamorphic and hydrothermal events including:

(i) Pre-Ventersdorp compressive deformation and alteration (Barnicoat *et al*., 1997).

(ii) Ventersdorp-aged thermal metamorphism (lithospheric extension and high heat flow during deposition) from, or even prior to, 2714 ± 8 Ma (Armstrong *et al*., 1991).

(iii) Thaisting prior to the deposition of the Transvaal Supergroup (Myers *et al*., 1990; Roering, 1990).

(iv) Burial metamorphism of the Transvaal Supergroup (Frimmel & Minter, 2002; Meier *et al*., 2009).

(v) Thermal metamorphism related to the intrusion of the Bushveld Igneous Complex (2054 ± 1 Ma) (Scoates & Friedman, 2008; Gibson & Jones, 2002; Rasmussen *et al*., 2007).

(vi) Deformation related to the Vredefort impact event (2023 ± 4 Ma) (Kamo *et al*., 1996; Gibson & Reimold, 1999).

Although it is evident that most of the basin underwent relatively uniform, lower greenschist-facies metamorphism, there are certain parts of the basin that experienced higher grades of metamorphism, particularly around the collar of the Vredefort Dome and towards the northwest corner of the basin (Gibson & Wallmach 1995; Robb & Meyer, 1995; Frimmel, 1997; Stevens *et al*., 1997b; Gibson & Reimold, 1999). These areas are thus characterised by the addition of higher metamorphic grade minerals, such as staurolite, kyanite, sillimanite, hornblende + zoisite, hornblende + andesine, pyroxene, biotite (now commonly chloritized), andalusite, anthophyllite and cordierite (Bisschoff, 1969; Phillips & Law, 1994; Stevens *et al*., 1997a).

Table 2: Proposed lithostratigraphic summary for the reviewed siliciclastic sedimentary deposits constituting the Witwatersrand Basin.

Lithologies	Mineral assemblages	Retrograde + accessory minerals
'Quartzites'	**WRG quartzites**: quartz, feldspar (generally sericitized to various degrees) and mica (mainly muscovite) ± rock fragments (chert, shale, volcanic clasts, quartz or altered pre-existing minerals e.g. feldspar altered to quartz and mica) [1, 2, 4, 5, 6]	Chlorite, calcite, epidote, pyrite, biotite, leucoxene, tourmaline, apatite and zircon [1, 2, 4, 5, 6]
	CRG quartzites: pyrophyllite, muscovite, chlorite, chloritoid, tourmaline, quartz, pyrite and rutile ± rock fragments [1, 2, 4, 5, 6]	Kaolinite, paragonite, biotite, pyrrhotite and arsenopyrite [1, 2, 4, 5, 6]
Metaconglomerate	Chloritoid, pyrophyllite, chlorite, muscovite, pyrite, quartz, rutile and tourmaline ± rock pebbles (quartz, chert, quartzite, shale, volcanic fragments (chlorite, oxide minerals and minor recrystallized quartz) and granitic fragments (sericitized feldspar and small quartz grains contained in a matrix of clay minerals)) [5, 6, 7, 9, 10]	Feldspar (albite, microcline, K-feldspar), kaolinite, calcite, siderite, apatite, sericite and a variety of ore- and heavy minerals [5, 6, 7, 9, 10]
Metapelites	Pyrophyllite, chloritoid, quartz, chlorite, mica (muscovite and/or biotite), magnetite, amphibole, ankerite, hematite, albite and epidote. In addition, porphyroblastic cordierite-, andalusite-, biotite-, garnet-, staurolite-, magnetite- and orthopyroxene-bearing metapelites occur in the lower WRG and core of the Vredefort Dome [3, 8, 9, 10, 11]	Kaolinite, tourmaline, rutile, pyrite, andalusite, kyanite, carbonate, zircon, ilmenite, monazite, allanite, apatite, titanite, and pyrrhotite [3, 8, 9, 10, 11]

***Sources*: [1.]Pegg, 1950; [2.]Fuller, 1958; [3.]Phillips, 1988; [4.]Law *et al*., 1990; [5.]Meyer *et al*., 1990; [6.]Phillips & Law, 1994; [7.]Robb & Meyer, 1995; [8.]Stevens *et al*., 1997a; [9.]McCarthy, 2006; [10.]Guy *et al*., 2010; [11.]Nwaila *et al*., 2017**

2.2.3 Alkali granite complex

Several small, chemically related, alkali granitic bodies have intruded into the subvertical to overturned supracrustal collar rocks of the Vredefort Dome (Elsenbroek, 1991; Walraven & Elsenbroek, 1991; Graham *et al*., 2005). Amongst these intrusions are the Schurwedraai Complex (SC) that represents a younger suite of post-Transvaal syn-Bushveld intrusions (2.5 Ga, Graham *et al*., 2005) in the inner north-northwest sector of the collar of the dome through which the Vaal River flows (Salminen *et al*., 2009).

The SC is composed of two related plutons cutting across the strike of the WRG namely: a) the Schurwedraai pluton (SAG in Figure 3) that was forcefully injected along the plane of a strike fault, and b) the Baviaan Kranz pluton (BAG in Figure 3) intrusive into the Government Reef Subgroup (Bisschoff, 1969, 1973). These plutons have a peralkaline to peraluminous composition, consisting of alkali granite and nepheline syenite (i.e., mariupolite) (Table 5). Both lithologies are extensively transected by pseudotachylitic breccia veining (<0.05 mm up to 10 cm), and they also display abundant multiply striated joint surfaces and shatter cones, confirming their pre-impact age (Bisschoff, 1973, 1988). In areas where the alkali granite contains large numbers of nepheline syenite xenoliths, the granite grades into quartz alkali syenite, containing up to 5% quartz due to the assimilation of quartzite along contact areas (Graham *et al*., 2005).

Table 3: Proposed lithostratigraphic summary for the reviewed plutonic rocks constituting the alkali granite complex.

Lithologies	Mineral assemblages	Retrograde + accessory minerals
Alkali granite	Plagioclase, -albite (43%); K-feldspar, -microcline (22%); quartz (25%); aegirine/riebeckite/arfvedsonite (9%); mica, -Fe-rich biotite to Mg-rich lepidomelane (1%) [1, 2, 3, 4,]	Zircon, apatite, magnetite, ilmenite, chalcopyrite [1, 2, 3, 4]
Quartz alkali syenite	Plagioclase, -albite (59%); K-feldspar (19%); aegirine/arfvedsonite (20%); quartz (2%) [1, 2, 4, 5]	Zircon, apatite, magnetite, ilmenite, chalcopyrite [1, 2, 4, 5]
Nepheline syenite	Nepheline (25%); plagioclase, -albite (55%); K-feldspar, -microcline (15%); aegirine (4%); hornblende, Na-mica and sodalite [1, 2, 3, 4, 5]	Magnetite, ilmenite, zircon and sphene [1, 2, 3, 4, 5]

***Sources*: [1.] Bisschoff, 1969; [2.] Bisschoff, 1973; [3.] Walraven & Elsenbroek, 1991; [4.] Bisschoff, 1999; [5.] Graham *et al*., 2005**

2.3 VEGETATION TYPE AND CLIMATE

"The unique geo-diversity of the Vredefort Dome, along with its related soil, topography, and microclimate, as well as the proximity of the Vaal River, produced distinct conditions under which

different plant communities have established themselves" (Boneschans *et al*., 2015). In addition to these natural influences, human influences, such as farming (Figure 4b) and mining activities (refer to Figure 27C), also contributed to the establishment of the current biological diversity of the dome (Balkwill, 2009).

The area is characterised by rocky hills and ridges, with higher densities of woody vegetation on the south-facing slopes (Figure 4). The rocky outcrops are covered predominantly with elements of Upland (Temperate) Subhumid Mountain Bushveld, whilst the flat areas with deep soils are covered by Moist Cool-Temperate Grassland (see Balkwill, 2009 for an overview). Several regional studies supportively concluded from vegetation studies in the area that there is a clear correspondence between the distribution of vascular plant communities in the dome and specific geological formations (see Table 4). These studies, however, predominantly focused on vascular plant communities with very few of them applying approaches to sample non-vascular plants.

The area receives summer rainfall with very dry winters and frequent frost (especially on the south facing slopes), but less common on the ridges and hills. As displayed in Figure 5, summers are hot and wet with average temperatures between 14°C and 27°C whilst winters are cold and dry with average temperatures between 5°C and 14°C. For corresponding statistical data, refer to Appendix A.

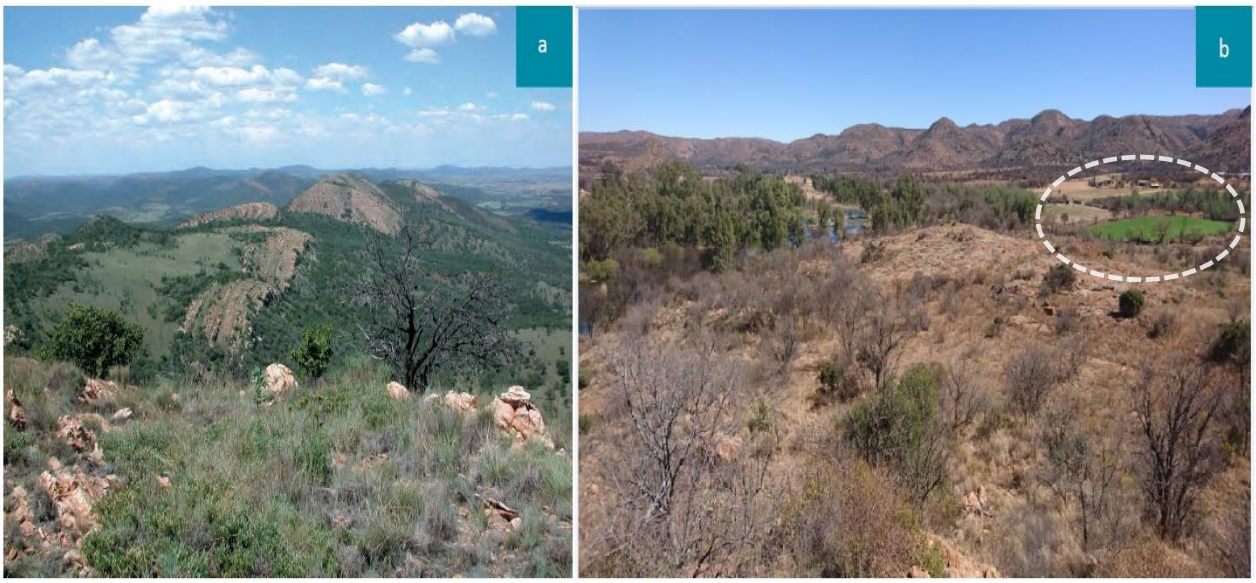


Figure 4: **Vegetation in the Vredefort Dome. (a) View from Dwarsberg looking northeast, and showing the association of vegetation with the geology. (b) View of the Vaal River at Schurwedraai, showing dense alien invader bush along the river and native woody vegetation associated with rocky hillsides. Also note the influence of farming (white dotted circle).**

Table 4: A short summary of geobotanical investigations in and around the Vredefort Dome.

Lithologies	Vegetation unit + indicator species
Quartzite	Gold Reef Mountain Bushveld vegetation unit including: *Celtis africana*, *Combretum molle*, *Nuxia congesta, Senegalia caffra* and *Searsia magalismontana* [1,2,3]
Alkali granite	Vredefort Dome Granite Grassland including: *Diospyros lycioides* subsp. *lycioides*, *Protea caffra*, *Searsia pyroides*, *Vachellia karroo, Sporobolus fimbriatus*, and *Ziziphus mucronata* [1,3,4,7]
Andesitic outcrops	Andesite Mountain Bushveld vegetation unit including: *C. africana*, *S. caffra*, *V. karroo*, *Zanthoxylum capense* and *Z. mucronata* [2,3]
Shales	Andesite Mountain Bushveld and Gold Reef Mountain Bushveld vegetation units (see above) [2,3]
Diorite	*Senegalia caffra* and *Vachellia robusta* [1,2,7]
Ultramafic outcrops	*Vachellia karroo* [5,6,7]
Lower lying alluvial soil habitats	Central Free State Grassland vegetation unit: *Vachellia karroo* and *Z. mucronata* [3,6]

***Sources*: [1.]Mogg, 1961; [2.]Bezuidenhout & Bredenkamp, 1988; [3.]Mucina & Rutherford, 2006; [4.]Balkwill, 2009; [5.]Boneschans *et al*., 2015; [6.]Boneschans, 2018; [7.]Siebert *et al*., 2018.**

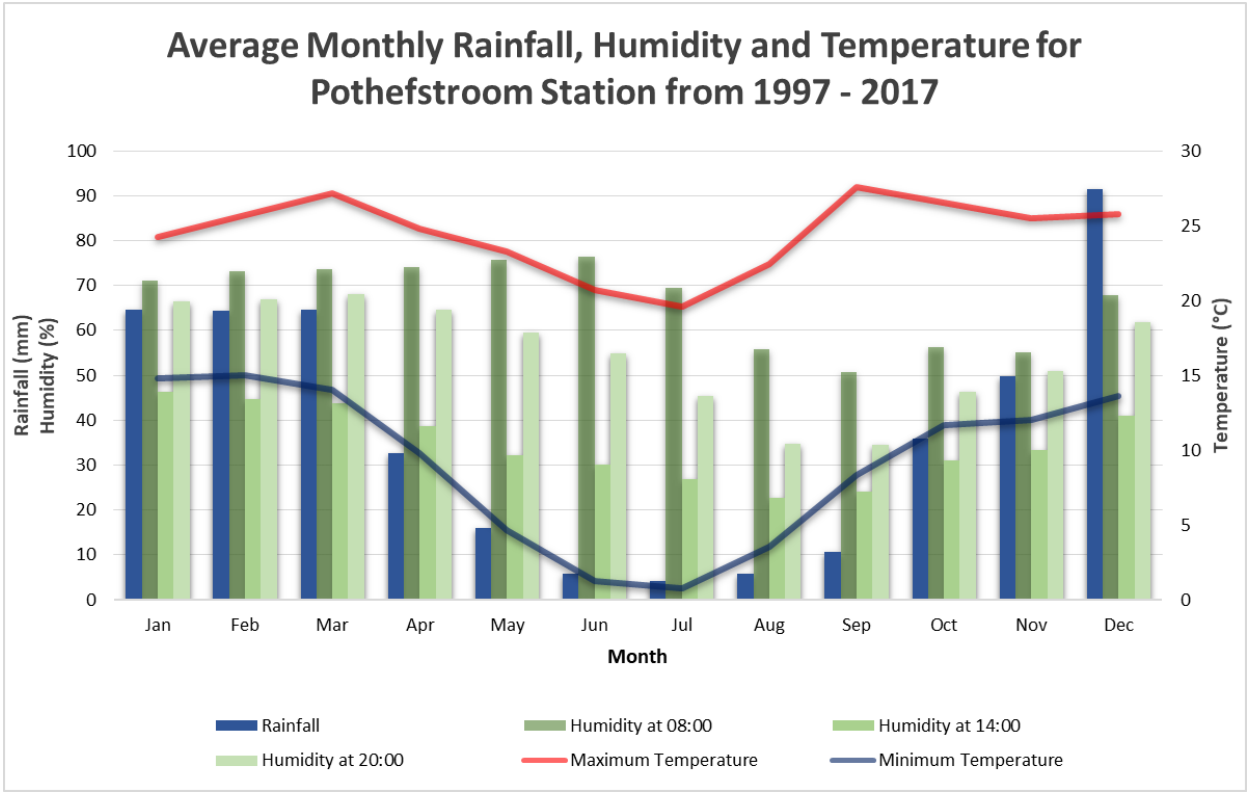


Figure 5: Average monthly rainfall, humidity and temperature for Potchefstroom station (40 km from Dome) from 1997-2017.

CHAPTER 3

LITERATURE REVIEW

3.1 INTRODUCTION

This literature review is comprised of four sections. In order to define the ecological characteristics that are associated with lichens, the first section considers lichen symbiosis and thallus morphology and anatomy. A wide range of different ecological characteristics has been investigated, but a complete outline of lichen ecology is not the scope of this section. Detailed reviews thereof are given by Purvis (2000) and Nash (2008). Secondly, to understand the relationship between impact cratering and lithic habitats, an overview is provided of different lithic habitats and the effects that impact events may impose on these lithic habitats. Thirdly, the review covers the deteriorative potential of lichens to draw attention to their involvement in the biogeochemical evolution of the outer layer of the Earth. The review concludes with an overview of the analytical tools that were used in this study.

3.2 ECOLOGY OF LICHENS

Lichens are by definition stable symbiotic associations between a nutritionally specialized fungus, referred to as the mycobiont; and one or more photosynthetic partner(s), referred to as the photobiont, most often either a green alga and/or a cyanobacterium (Honegger, 2009). This diverse group of plant-like organisms possess diverse range of ecological tolerances, influencing the geochemistry of the land, atmosphere and ocean (Burford et al., 2003a; Adams et al., 2012; Kenrick et al., 2012; Mitchell et al., 2016). Hence, they are regarded amongst the most successful forms of symbiosis and account for more than 20% of the global fungal biodiversity, populating 8-12 % of Earth's surface (Honegger, 2012).

In the terrestrial environment, lichens are of fundamental importance, playing important roles in the biogeochemical evolution of the outer layer of the Earth (Asplund & Wardle, 2017). Their involvement in several key Earth systems can be summarised as follows:

(i) Lichens contribute substantially in the determination of several soil and vegetation parameters including chemistry, hydrology and temperatures (Longton, 1997; Cornelissen *et al*., 2001, 2007; Kurina & Vitousek, 2001; Sedia & Ehrenfeld, 2006).

(ii) Lichens affect metabolic activity of microbes involved in biogeochemical cycles, with effects from the small to the global scale (Bashkin, 2003; Nash, 2008).

(iii) Lichens are responsible for the biogenic transformation and differentiation of elements in the environment, and the release of gaseous metabolites as well as liquid metabolites and decay products (Gadd, 2007; Nash, 2008; Shukla *et al*., 2014).

(iv) Lichens generally promote weathering and erosion by means of biodeterioration (Adamo & Violante, 2000; Chen *et al*., 2000; Bjelland & Thorseth, 2002).

(v) Lichens play an important role in biogeochemical cycling of metals, e.g. Na, Mg, Ca, Mn, Fe, Cu, Zn, Co and Ni; as well as in the mobilization and immobilization of non-essential metals, e.g. Cs, Al, Cd, Hg and Pb (Burford *et al*., 2003a; Gadd *et al*., 2007).

(vi) Lichens tend to accumulate trace elements and other heavy metals of environmental concern, including radionuclides that form metal–organic biominerals (Purvis *et al*., 2004; Haas & Purvis, 2006; Gadd *et al*., 2007; Nash, 2008; Shukla *et al*., 2014).

(vii) Lichens sometimes play a protective insulating role, preventing weathering and erosion (Carter & Viles, 2005; Hall *et al*., 2005; de la Rosa *et al*., 2012).

(viii) Lichens both facilitate and compete with vascular plants, thus affecting vegetation succession (Honegger, 1991; Lange *et al*., 1998; Sedia & Ehrenfeld, 2003, 2005).

(ix) Lichens provide a staple food to mammals with important feedbacks to soils and biota (Helle & Aspi, 1983; Danell *et al*., 1994; Kojola *et al*., 1995).

(x) Lichens facilitate water retention and the sorption of organic compounds (e.g. nutrients) and ions (e.g. metal ions) (Wierzchos *et al*., 2015; Asplund & Wardle, 2017).

(xi) Lichens can chemically react with minerals and accelerate dissolution and therefore participate in the biomobilization of elements, biomineralization phenomena and clay mineral transformation processes (de los Ríos et al., 2014; Asplund & Wardle, 2017).

3.2.1 Lichen symbiosis

Although the nature of lichen symbiosis is widely debated and deserves further investigation, most researchers refer to lichens as a classic case of mutualism, where all the partners gain benefits from the association (Nash, 2008; Honegger, 2009). This is evidenced by its desiccation tolerance which is greater in the lichen symbiosis than in its isolated partners. Lichens also produce characteristic secondary metabolites and bioactive compounds as a result of symbiosis, which seldom occur in the isolated partners (Elix & Stocker-Wörgötter, 2008). Lichens can also be regarded as an example of controlled parasitism, because the mycobiont does sometimes seems to obtain most of the benefits and the photobiont may grow more slowly in the lichenized state than when free-living (Tripathi & Joshi, 2019). It is, however, much more complex since there are different fungi from the dominant mycobiont that might have a commensalistic, saprophytic/saprobic or parasitic relationship with the lichen, which may play functional roles for

the symbiosis, cause extensive damage to the thallus or result in complete death of the thallus. Fungal symbionts have also been found resembling endophytes (i.e., endolichenic fungi) which appear similarly ubiquitous in asymptomatic thalli of lichens, wherein they associate primarily with photobionts (Arnold *et al*., 2009; U'Ren *et al*., 2012). Although they have been characterized from a limited number of lichen species and geographic areas, current evidence suggests that like endophytes, endolichenic fungi are horizontally transmitted, form highly localized infections, and represent at least five classes of nonlichenized Pezizomycotina, dozens of families, and large numbers of previously unknown species (U'Ren *et al*., 2012).

“Variation in the fungal–algal symbiotic associations may be explained by multiple interacting factors, such as fungal specificity, algal availability, mode of transmission and fungal selectivity” (Yahr *et al*., 2006). In their research, Yahr *et al*. (2006) indicates that there is ecological specialization for a particular lichen relationship and a site, and that this selectivity is complex and environmentally dependent. Therefore, they presented a working model (Figure 6) that combines algal abundance, fungal specificity and selectivity, thus, retaining variations in symbiotic composition across landscapes.

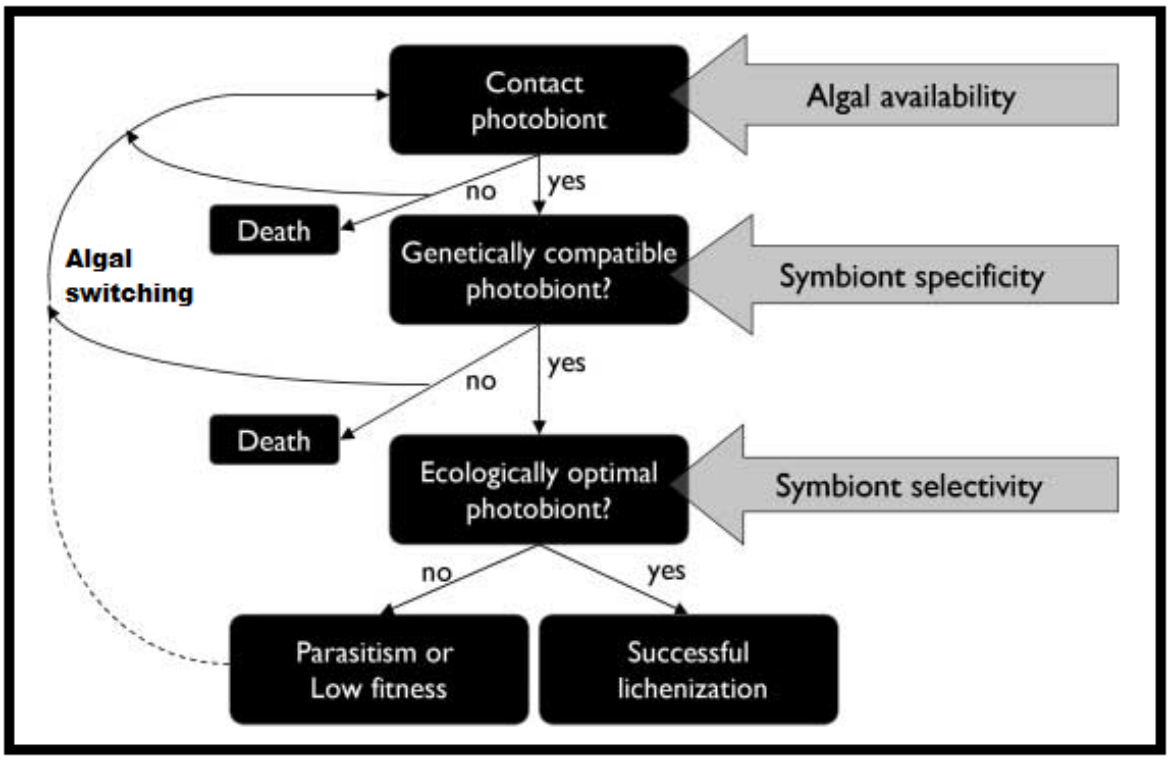


Figure 6: **A hypothetical model of fungal–algal association for lichens, showing the interactions between partners and the mechanisms that structure them. (a) Algal availability determines which algae can be contacted. (b) Fungal specificity determines the ability to form prethallus stages. (c) Fungal selectivity, dependent on ecological context, determines the final composition of observed lichens (Model by Yahr *et al*., 2006).**

3.2.2 Mycobionts

Lichen-forming fungi (mycobionts) are a polyphyletic, taxonomically heterogeneous group of nutritional specialists and estimates of species vary from 17 000 to approximately 20 000 in over 1 000 genera (Hawksworth, 2001; Scherrer *et al*., 2002; Yahr *et al*., 2006; Lücking *et al*., 2009; Nelsen *et al*., 2011). Lichen-forming fungi belong to several unrelated lineages within the kingdom Fungi, specifically the phyla Ascomycota and subordinately Basidiomycota, hence, they are termed ascolichens and basidiolichens (see Honegger, 2012 for an overview).

In general, lichen-forming fungi host an internal photosynthetic cell population from which they receive their source of carbon in the form of simple sugars. The mycobiont uses these sugars to meet its own basic energy needs and complex structural building, which accommodates and enhances the operation of the photobiont (St. Clair & Seaward, 2004; Zambare & Christopher, 2012; Shukla et al., 2014). Mycobionts also regulate the quality and quantity of light reaching the photobiont, produce secondary metabolites (Figure 7) which protect the algal partner, deliver water and mineral nutrients to the photobiont, promote gas exchange, effectively neutralize some groups of potentially toxic airborne elements and chemically control herbivores (St. Clair & Seaward, 2004; Honegger, 2008; Shukla *et al*., 2014). Moreover, mycobionts are considered the principal actors of lichen biogeochemical interaction with rock substrates, although a remarkable role by photobionts has also been demonstrated (Cockell *et al*., 2003; Gadd, 2007).

3.2.3 Photobionts

Thus far, only little more than 100 species of lichen photobionts in 50 genera have been reported. The most frequent photobionts include: 1) *Trebouxia* and *Trentepohlia* (Figure 7), that are of eukaryotic nature and belong to the green algae, and 2) *Nostoc* (Figure 7), that are of prokaryotic nature and belong to the oxygenic photosynthetic bacteria (cyanobacteria) (Friedl & büdel, 2008; Lücking *et al*., 2009; Shukla *et al.,* 2014). About 85 % of lichens have green algae as symbionts, approximately 10 % have cyanobacteria as symbionts, and approximately 3-4 % of lichens (so-called cephalodiate species) have both green algae and cyanobacteria as symbionts (Adams *et al*., 2012; Honegger, 2008, 2012).

The role of the photobiont in lichens is straightforward – to provide the fungal partner with fixed carbon through photosynthesis (St. Clair & Seaward, 2004). The carbon is furnished in the form of simple sugars, which is a common and widespread mode of nutrition. The mode of activation of CO_2 uptake varies depending on whether the photobiont is prokaryotic or eukaryotic. Lichens containing green algae can begin photosynthesis after elevated humidity alone, whereas lichens

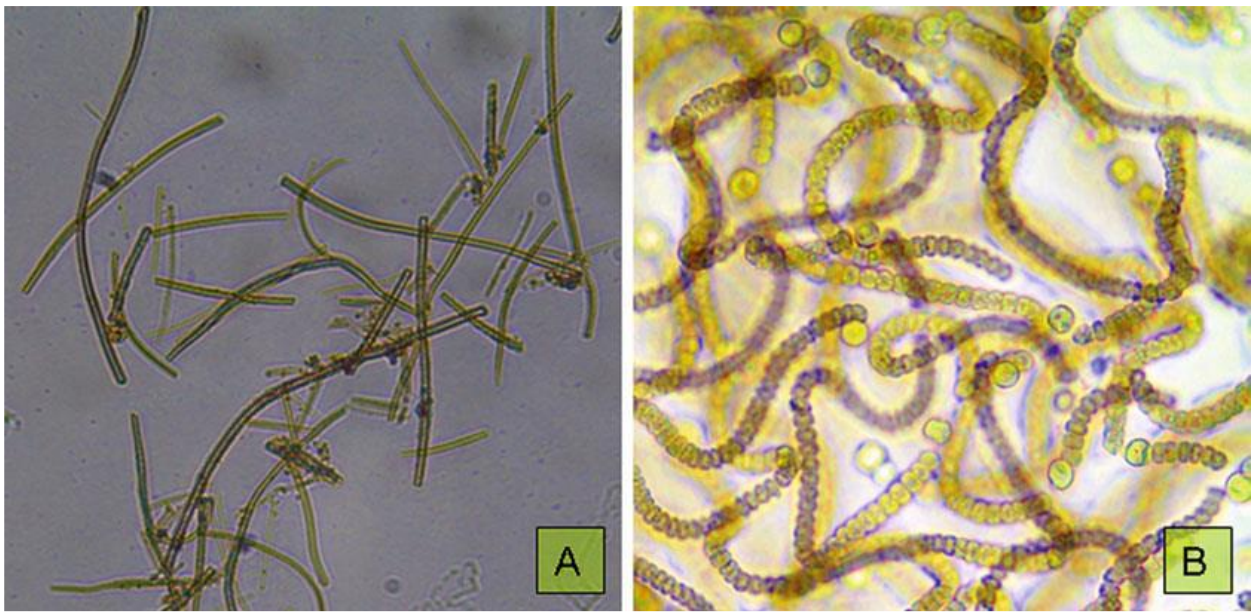


Figure 7: **Common photobionts which facilitate lichenization with compatible fungal partner resulting in the formation of lichen thallus. (a) *Trentepohlia* and (b) *Nostoc*. (Micrographs by Shukla *et al*., 2014).**

containing cyanobacteria can only begin photosynthesis when wetted, thus requiring liquid water for recovery (Lange *et al*., 1993). The type of carbohydrate released by the alga is determined by the photobiont. In the case of green algal lichens, polyols (especially sugar alcohols) move to the fungus as carbohydrates, whereas in the case of cyanolichens, glucose moves to the fungus as carbohydrates (Kranner *et al*., 2008).

3.2.4 Thallus morphology and anatomy

Lichen thalli refer to the fungal body (vegetative tissue) and are the product of a complex hyphal polymorphism (see Scherrer *et al*., 2002 for an overview). The thallus is composed of a dense network of fungal hyphae (± 90% of the thallus volume) with one or more photosynthetic partner(s) (Figure 8). The gross morphology, chemistry and colour of lichen thalli is primarily determined by the mycobiont (exhabitant) with partial contribution from the photobiont (inhabitant) (Shukla *et al*., 2014). The influence of the photobiont on lichen morphogenesis is much more prevalent in the developing stages of the thallus when considering that the characteristic thallus of a lichen is only determined after the establishment of the symbiosis (Adams *et al*., 2012; Muggia *et al*., 2013).

Most lichens are complex in structure with an internally stratified thallus (heteromerous thalli), which are characterized by the differentiation of conglutinated zones (usually as peripheral cortex) and gas-filled thalline areas (as internal medulla and algal layer). The main subdivisions within heteromerous thalli are therefore into upper cortex, photobiont layer, medulla and lower cortex

(see Figure 8). Other lichens are simple in structure with an undifferentiated thallus (homoiomerous) that is characterized by evenly distributed symbiotic phenotypes (Jahns, 1973; Büdel & Scheidegger, 2008; Honegger, 2012).

Several morphological and physiological adaptations of the thallus structure give lichens a distinct ecological advantage over vascular plants that are at their physiological limits under similar environmental conditions. Nevertheless, some vascular plants have adaptations approaching that of lichens. These adaptations enable lichens to tolerate severe environmental conditions, such as extremes of temperature, ultraviolet (UV) radiation and desiccation (Kappen, 2000; Gadd, 2011; Pontefract *et al*., 2014; Meslier *et al*., 2018). The morphological structure of the thallus is optimized for water uptake and/or loss within a specific habitat. The water relations that are related to the mycobiont–photobiont contact site is key in understanding the function of mycobiont–photobiont interactions (Honneger, 2007), such as:

- continuously fluctuating water contents from full hydration to desiccation;
- the full recovery of metabolic activity after rehydration;
- the main fluxes of solutes in the apoplastic continuum, which are passively driven by wetting and drying cycles; and
- active uptake of soluble carbohydrates, which is assumed to take place at the immediate mycobiont– photobiont contact sites.

The anatomical structure of the thallus on the other hand follows principles that allow positive net photosynthesis under a given habitat moisture regime. This is achieved by actively positioning the photobiont cells throughout the thalli in a manner that secures adequately illuminated, optimal

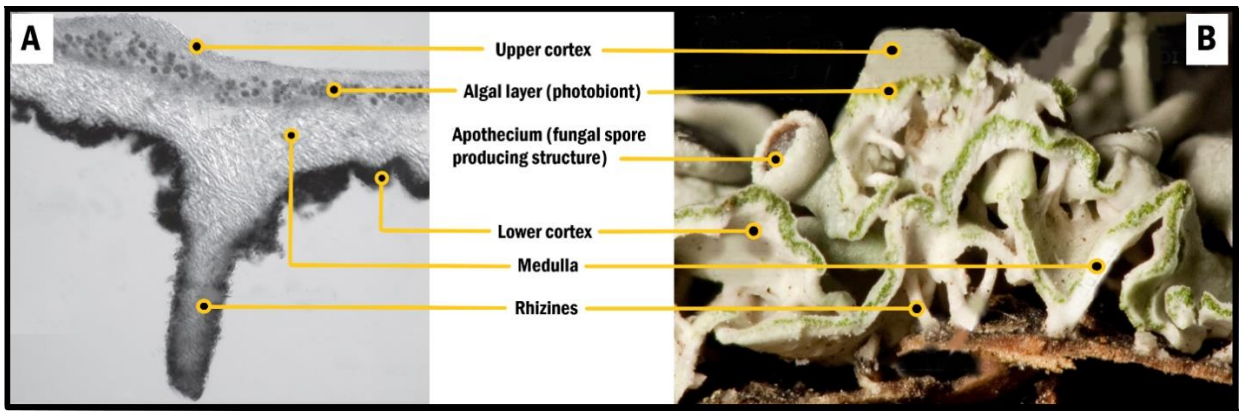


Figure 8: **(a)-(b) Cross-sections of the foliose lichen thallus showing its various components. The upper cortex of fungal hyphae provides protection. Photosynthesis occurs in the algal zone. The medulla consists of fungal hyphae. The lower cortex also provides protection. The rhizines anchor the thallus to the substrate. (Modified from Molnár & Farkas, 2010).**

Table 5: A short summary of the charactaristics associated with the three major growth forms associated with lichen thalli.

Growth form	Typical Structure	Diagnostic features	Attachment to substratum	Example
Crustose	Crust-like	• An estimated 50 % of all lichen-forming ascomycetes forms crustose thalli • Crustose lichens usually grow on (episubstratic) or within (endosubstratic) the substratum. • Crustose lichens never possess a lower cortex and the photobionts occur in a distinct layer below an upper mycobiont cortical layer • The ability of crustose lichens to restrict water loss to the upper, exposed surface only enables them to tolerate and inhabit extreme habitats such as bare, exposed rock surfaces • Crustose lichens grow relatively slowly (≤1.0 mm/year) compared to other growth forms, such as foliose (1.0–2.5 mm/year) and fruticose lichens (2.0–6.0 mm/year) • Variation of the basically crustose type is abundant, and the following subtypes can be distinguished: leprose/powdery-, endolithic-, endophloeodic-, squamulose-, peltate-, pulvinate-, lobate-, effigurate- and suffruticose crust	This growth type is firmly and closely attached to the substrate via the entirety of the lower surface of the thallus, most often by means of a crust-like growth adherent or attached by hyphae throughout its underside. Hence, thalli generally grow radially outwards from the point of establishment (nucleation).	 *Candellariella* sp.
Foliose	Leaf-like	• Only one out of four lichen-forming ascomycetes (approx. 25 % of species) produces foliose thalli • The thalli of foliose lichens typically spread and expand horizontally outwards and are often divided into lobes (see example), which show various degrees of branching • Many foliose thallus margins consist of individual marginal lobes exhibiting radial growth and periodically divided; this division can give lobules of equal or different size and the result is a complex structure • Certain foliose lichens do not remain adhered to the substratum and have hygroscopic movement, i.e. the thalli are able to roll up and expose lower cortices in dry conditions, while the thalli unroll and expose their upper surface to the sunlight when they take up water • The photobionts within foliose lichens occur in a layer below an upper cortex with a discrete cortex below, separate from the substratum on which it grows • Variation of the basically foliose type include lobate-, inflated- and circular thalli	Foliose thalli are characterized as internally stratified thalli that are attached to the substratum by large numbers of rhizines, which are clusters of fungal hyphae that extend from the underside of the thallus and penetrate the substratum.	 *Physcia stellaris*
Fruticose	Branched tree-like, shrubby, pendulous	• Some groups of fruticose thalli have dorsiventrally aligned thalli, but the predominant share possesses radial symmetric thalli • Thallus lobes, which are planar or cylindrical in shape, always extrude from the substrate surface and their branching pattern varies considerably among various systematic classes and within a singular genus • The photobiont can be found in a layer inside the outer cortex	Fruticose thalli are also characterized as internally stratified thalli and usually attach to the substratum at the base by basal disc or holdfast.	 *Ramalina fastigiata*

***Sources*: Jahns, 1973; Viles, 1995; Honegger, 2007; Büdel & Scheidegger, 2008; Zambare & Christopher, 2012; Shukla et al., 2014**

conditions for gas exchange and access to water and dissolved nutrients (Büdel & Scheidegger, 2008; Honegger, 2012). Due to the complexity and immense variety of the morphology and anatomy of different lichen thalli, lichens are traditionally divided into three major growth forms: these are the crustose, foliose and fruticose thalli (Table 5). Intermediate growth forms are usually arbitrarily placed in that group to which the majority of closely related species belong (Büdel & Scheidegger, 2008). “These groupings may not be consistent with lichen taxonomy, since lichens with similar growth forms are not necessarily related by ancestry” (Büdel & Scheidegger, 2008). Lichen growth forms are categorised mainly based on their morphology (overall habit) without direct reference to ecological adaptations (Shukla et al., 2014). Their distribution thus reflects competition and adaptation to abiotic environmental conditions (mainly water relations).

3.3 LITHIC HABITATS

Lichens, as well as other lithobionts, commonly occupy lithic habitats that formed as a result of biotic–abiotic relationships on, under or within rocks (Figure 9). These rock-dwelling organisms preferentially occupy cavities or protected areas on the surface of the rock substrate (epilithic), whilst others hide within the rock interior (endolithic habitat) or on the underside of the rock substrate (hypolithic habitat). A general summary of the different lithic habitats associated with exposed rock surfaces is provided in Table 6.

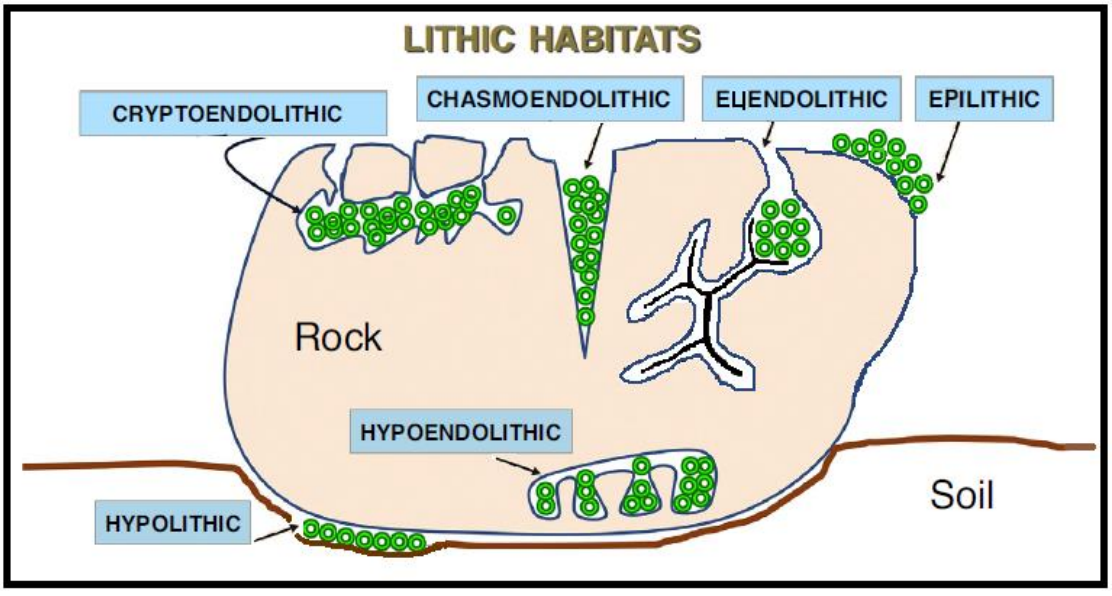


Figure 9: **Most common lithic habitats found within rock substratum. Epiliths inhabit the surface of the rock; cryptoendoliths inhabit pores within the rock structure; chasmoendoliths inhabit cracks and fissures in the rock structure; hypoendoliths inhabit the undermost layer in the rock structure; euendoliths inhabit channels and grooves that were actively “bore” into the rock; and hypoliths inhabit the underside of the rock (Modified from Wierzchos *et al*., 2018).**

Table 6: A general summary of the different lithic habitats associated with exposed rock surfaces.

Name of habitat	Description of habitat	Development of habitat	Common host substratum	Common colonizers
Epilithic	Habitats on top of any stable substrate	Epilithic habitats develop on any surface that is not toxic and that are able to provide adequate nutrients and water required by epilithic organisms to establish initial attachment and colonization	Any rock type that is not toxic	Representatives from all three domains of life, *Bacteria*, *Archaea* and Eukarya (e.g. algae and fungi)
Cryptoendolithic	Pores within the interior of the rock	Development is dependent upon a balance between an increase in porosity and the expansion of interconnected pore spaces within the rock matrix	Sandstones and limestones, which are sufficiently translucent and porous for cryptoendolithic colonization	Lichen-dominated eukaryotic communities and cyanobacterial-dominated prokaryotic communities
Chasmoendolithic	Fissures and cracks within the rock that are formed by a diversity of processes including aeolian- and fluvial weathering as well as freeze-thaw events	Develop on weathering crusts (surface of rocks) or the surface of contiguous cracks or fractures that connect the surface of the rock to the interior of the rock in which PAR is available	Any rock type that is not toxic	Lichen-dominated eukaryotic communities and cyanobacterial-dominated prokaryotic communities
Hypoendolithic	Habitats in pore spaces located on the underside of the rock making contact with the underlying soil and exterior environment through narrow fissures	Develop in pores that are positioned in an instance where transmitted light filtering through the rock substrate could be sufficient for photosynthesis and adequate liquid water and/or higher relative humidity values is achievable	Rocks which are sufficiently translucent with a stable supply of water and nutrients	Phototrophic eukaryotes and prokaryotes
Euendolithic	Channels and grooves that were actively "bore" into the rock	Euendoliths enter the substrate via a small opening from which they expand laterally, producing channels and grooves that comply closely with the outlines of their bodies, which at a finer scale leave etch marks that comply with and reflect the crystalline composition of the rock. These euendoliths dissolve the substrate by producing organic acids	Rocks which are sufficiently translucent with a stable supply of water and nutrients	Microborers (phototrophs and heterotrophs) and/or Macroborers (specialized sponges, various groups of worms, phoronids and sipunculids, and other invertebrates)
Hypolithic	Habitat on the underside of the rock substrate (basal surfaces)	Development requires that the rock is translucent or that spaces are created around the edges of the rock for light to penetrate to its underside	Rocks which are sufficiently translucent with a stable supply of water and nutrients	Phototrophic eukaryotes and prokaryotes

***Sources*: Friedmann, 1982; Bell, 1993; Al-Thukair et al., 1994; de la Torre et al. (2003); Cowan & Ah Tow, 2004; Cockell et al. (2005); Cockell & Osinski, 2007; Omelon, 2008; Wong et al., 2010; Cowan et al., 2011; Khan et al., 2011; Tribollet et al., 2011; Wierzchos et al., 2011, 2012b, 2015, 2018; Chan et al., 2012; de los Ríos et al., 2014; Makhalanyane et al., 2015**

It is well documented that endolithic habitats provide long-term stable environmental conditions for life through the provision of adequate resources (water, light, and nutrients, above all) and effective protection from incident lethal UV- and PAR radiation, extreme temperature fluctuations, wind ablation, freeze–thaw events and excessive evapotranspiration, thus assuring efficient gas exchange (Fike *et al*., 2003; Cowan & Ah Tow, 2004; Walker & Pace, 2007; Cockell *et al*., 2013; Wierzchos *et al*., 2012b, 2015, 2018; Archer *et al*., 2016; Meslier *et al*., 2018). "The bioreceptivity (capacity to harbour life) of rocks to lithic colonization is mainly determined by the micromorphological, structural, physical, and mineralogical properties of the substratum" (de los Ríos *et al*., 2014). This includes the rock's mineral composition, pore structure, permeability, water retention capacity, pH, climatic exposure, nutrient sources, and presence of chemical compounds (Guillitte, 1995; Omelon *et al*., 2007; Walker & Pace, 2007; Kelly *et al*., 2011).

3.4 IMPACT-INDUCED LITHIC HABITATS

Impact events generally have far-reaching consequences for several biogeochemically important processes, influencing living organisms' habitats, their distribution and their associated biogeochemical cycles (refer to Table 7). "This may be attributed to the generation of pressures

Table 7: The effects of impact cratering on the abundance and characteristics of lithophytic organisms in different lithic habitats.

Name of habitat	General effects of impact
Cryptoendolithic	Impact-induced fractures and pore space is likely to increase interior space for colonization in many rock types. However, photosynthetic endoliths require light penetration. Impact alteration of rock translucence may change availability of habitat.
Chasmoendolithic	Impact-induced fractures and fissures are likely to make an increase in chasmoendolithic habitat a common occurrence in impact structures.
Euendolithic	Increase in pore space caused by shock or changes in density of rock and rock chemistry (e.g., heterogeneous carbonate melts) could plausibly affect the ease with which microorganisms can actively penetrate into rocks.
Epilithic	The habitat on the surface of rocks will generally be unaffected by impact. However, two possible modes of change in suitability for colonization could be: 1) changes in weathering rates caused by mineralogical changes e.g., melting, could cause changes in the abundance of surface attachment sites (e.g., caused by changes in surface roughness); or 2) changes in macronutrient availability might change suitability of rock surfaces for microbial biofilm formation.
Hypolithic	The habitat on the underside of rocks will generally be unaffected by impact. A possible instance in which hypolithic habitat availability could be changed would be alterations in the translucence of rocks (for example, the formation of impact glasses in desert settings), which would alter suitability of underside of rocks for photosynthetic hypoliths.

***Sources*: As summarized by Cockell *et al.* (2005).**

and temperatures that can vaporize, melt, shock metamorphose, and/or deform a substantial volume of the pre-impact target sequence, rendering the target lithology more heterogeneous after impact" (Cockell *et al*., 2005). Hence, target lithology is usually characterised by the heterogenous distribution of collapsed pores, melt phases, and subsequent recrystallization in which diverse geochemical sources of nutrients are brought into close proximity (Cockell & Osinski, 2007; Cockell *et al*., 2013; Pierazzo & Melosh, 2013). The primary focus regarding impact-induced lithic habitats is divided into two main facets, encompassing both the physical and chemical changes to lithic habitats. This section will, therefore, discourse from both a physical and chemical viewpoint.

3.4.1 Physical changes

Impact bulking, i.e. the fracturing of rock (increased porosity and permeability), signifies one of the most important effects that impacts impose on the pre-impact target sequence (Cockell *et al*., 2002, 2005). Another important effect evolves around impact vesiculation, i.e. the selective shock-induced volatilization of some of the less refractory mineral phases present (Cockell *et al*., 2003). "Both bulking and vesiculation result in an increase in surface area (living space), either by growth along surfaces or by water transport, and allow for living organisms to move within the rock matrix" (Pesonen *et al*., 1999). It also increases the flow of fluids into the target material, which could increase the availability of electron donors and acceptors and alter the oxidation state of metals (Cockell *et al*., 2013). The latter is likely to have a significant effect on the bioavailability of redox pairs and nutrients in post-impact lithic habitats. Increased translucency is, furthermore, directly related to bulking and vesiculation which plays a critical role in rendering the rocks amenable to colonization (Cockell & Osinski, 2007).

On the other hand, pore collapse or impact-induced annealing (impact melting) can render post-impact target material less conducive to life, as is seen in some sedimentary lithologies with high porosities (Cockell, 2011; Pontefract *et al*., 2014). This may be caused by the re-orientation of the grains into a more closely packed configuration, reducing the bulk porosity and possibly the interconnectedness (permeability) of the target material. Low shock pressures ($\leq$ 10 GPa) generally causes pore collapse, whilst an increase in pressure exposure (10-35 GPa) usually causes vesiculation of the rocks, generating interconnected spaces that allow for the infiltration of water and nutrients (Cockell & Osinski, 2007; Pontefract *et al*., 2014). At shock pressures higher than approximately 35 GPa, solid glass is formed, which impede colonization, although potentially still accessible to some euendolithic microorganisms.

3.4.2 Chemical changes

Many impact structures are the sites of localized concentrations of metals and other elements, which is associated either with the impact event itself or with impact-produced deformation of the target rocks (French, 2004). There is also the possibility of new minerals (e.g. evaporites) being formed within and around impact craters as a result of impact processing (Cockell, 2011). The enhancement of elements within impact structures could be beneficial to biota or in some cases they might plausibly be detrimental to biota (Cockell *et al*., 2013). Two mechanisms are known to possibly be responsible for the enhancement of elements within an impact structure namely the:

- impact-redistribution of elements present in the pre-impact environment at high concentration (Reimold *et al*., 2005), and
- localized concentration of elements in the impact hydrothermal system (Ames *et al*., 2006).

Thus far, three basic types of ore deposits have been distinguished within impact structure settings namely: (1) progenetic (i.e., pre-impact) deposits that already existed in the target regions prior to an impact event, but may have become accessible as a direct result of the impact; (2) syngenetic (syn-impact) deposits that owe their existence directly to the impact process, and (3) epigenetic (immediately post-impact) deposits that result from impact-induced thermal/hydrothermal activity (Cockell *et al*., 2013). The Vredefort impact structure represents the most prominent example of progenetic (i.e., pre-impact) deposits, in which gold- and uranium deposits, which already existed in the target regions prior to the impact event, became accessible as a direct result of the impact (Reimold *et al*., 2005).

3.5 LICHENS AS BIODEGRADERS OF ROCK SUBSTRATA

“Rocks and minerals represent a vast reservoir of elements, many of them are essential to life” (Gadd *et al*., 2007). This is evident as living organisms take up these elements selectively for the synthesis of biological macromolecules and energy capture (e.g. C, N, H, O, P, S), for the transmission of information (e.g. Na, K, Ca), for catalysis (e.g. Fe, Cu, Zn, Mo), for transfer of electrons (e.g. Fe), and for building solid structures (e.g. Ca, P, Si) (Chapin & Eviner, 2004; Prasad *et al*., 2006; Gadd *et al*., 2007). Their release is a natural phenomenon that occurs via weathering of rock substrate - a process dictated by a complex and interactive combination of physical-, chemical-, and biological induced weathering processes which are not mutually exclusive and act cooperatively (Chen *et al*., 2000). For the purpose of this study, we only focus on biological induced weathering processes, in particular lichen induced rock weathering.

Plenty of papers have dealt with various aspects of bioweathering promoted by lichens (summarised in Table 8). Two synergistic actions by which lichens degrade mineral substrates are biomechanical- and biochemical weathering (Figure 10). Both of these mechanisms induce and accelerate weathering of their rock substrate, contributing to the preliminary phases of soil formation and cation mobilization (Seaward, 1997; Adamo & Violante, 2000; Chen *et al*, 2000; Bjelland & Thorseth, 2002; Büdel *et al*., 2004; St. Clair & Seaward, 2004; Favero-Longo *et al*., 2011; Vingiani *et al*., 2013; Shukla *et al.,* 2014; Mitchell *et al*., 2016). The nature and rate of lichen

Table 8: A short summary of relevant research on rock weathering promoted by lichens.

Weathering of various rocks and minerals caused by lichen colonization	Syers & Iskander, 1973**;** Jones, 1988**; Wessels & Schoeman, 1988; Cooks & Fourie, 1989**; **Wessels & Büdel, 1989; Cooks & Otto, 1990**; **Wessels & Wessels, 1991**; Adamo *et al*., 1993; **Wessels & Kappen, 1993**; Ascaso & Wierzchos, 1994, 1995; **Wessels *et al*., 1995**; Barker & Banfield, 1996; Barker *et al*., 1997; Bjelland & Thorseth, 2002; Chen & Blume, 2002; de los Ríos *et al*., 2002, 2005a, 2005b; Jie & Blume, 2002; Souza-Egipsy *et al*, 2000; Arocena *et al*., 2003, 2007; Bungartz *et al*, 2004; Bjelland & Ekman, 2005; **McKechnie *et al.,* 2007**; Favero-Longo *et al*, 2011; Guglielmin *et al*., 2011
The detection of organic and mineral by-products of lichen activity	Jones *et al*., 1981; Ascaso *et al*., 1990; Wierzchos & Ascaso, 1994, 1996; Adamo *et al*, 1997; Edwards *et al*., 1997; Prieto *et al*., 1997; Lee & Parsons, 1999; Adamo & Violante, 2000; Culberson & Culberson, 2001; Souza-Egipsy *et al*, 2002; Arocena *et al*., 2003; Giordani *et al*., 2003; Wierzchos *et al*., 2003; Favero-Longo *et al*., 2005; Molnár & Farkas, 2010; Mahaney *et al*, 2013; Gadd *et al*., 2014
Biogeochemical transformations of rocks, minerals, metals and radionuclides by fungi	Burford *et al*., 2003a, 2003b, 2006; Gadd, 2007, 2010, 2011, 2017, 2017b; Gadd *et al*., 2007; Gorbushina, 2007; Fomina *et al*., 2004, 2010
Laboratory studies associated with the weathering of rocks and minerals induced by lichens and lichen compounds	Jacks, 1953; Johnston, 1959; Smith, 1962; Henderson & Duff, 1963; Schatz, 1963; Haynes, 1964; Syers, 1964; Iskandar & Syers, 1971, 1972; Williams & Rudolph, 1974; Ascaso & Galvan, 1976; Mast & Drever, 1987; Hawksworth, 1988; Song & Huang, 1988; Ganor & Lasaga, 1994; Varadachari *et al*., 1994
The quantification of lichen-induced weathering rates on various rock types	Viles, 1987; Broadbent, 1990; Brady *et al*., 1999; Aghamiri & Schwartzman, 2002; Stretch & Viles, 2002
The role of different environmental conditions on the behaviour and degree of rock/mineral weathering	Prieto *et al*., 1999; Kidron, 2002; Edwards *et al*., 2004; Hall *et al*., 2005, 2008; Jorge-Villar & Edwards, 2010
Biodeterioration of building stones and stonework especially in archeological contexts and for cultural heritage preservation and restoration	Danin & Caneva, 1990; Warscheida & Braams, 2000; Lisci *et al*., 2003; Silva & Prieto, 2004; de los Ríos *et al*., 2004, 2005a, 2009; Lee & Yi, 2007; Begonha, 2009; Salvadori & Casanova-Municchia, 2016
The potential role of biologically-mediated degradation of rocks by lichens versus abiotic weathering	Barker & Banfield, 1996; Brady *et al*., 1999; Guglielmin *et al*., 2005; Scarciglia *et al*., 2012

* **Articles in bold represent work done in South Africa.**

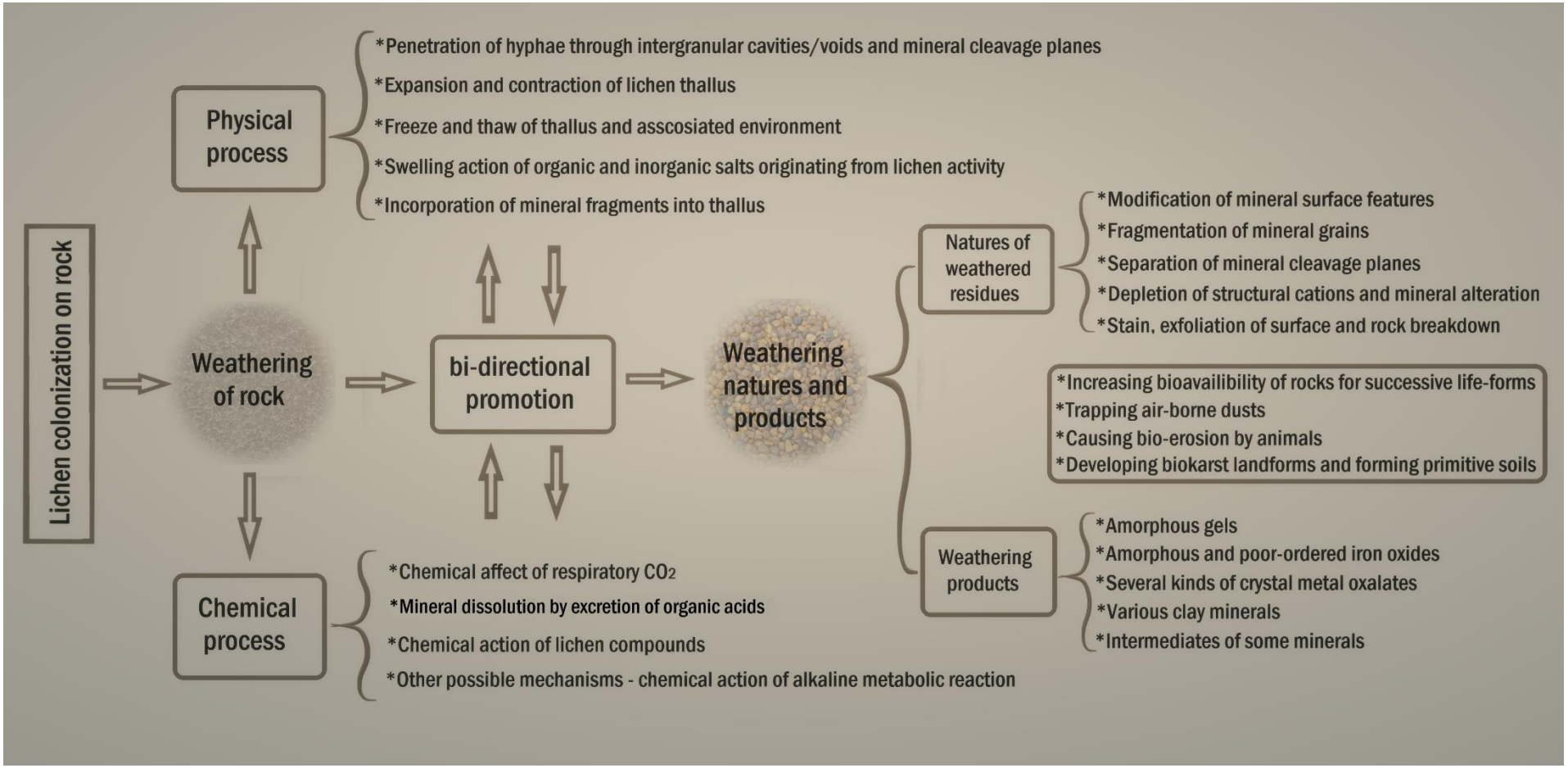


Figure 10: **An illustration showing common effects of lichen activity on their substratum rocks (adapted from Chen & Blume., 2002).**

induced rock weathering is dictated by several factors including: 1) the physiological differences among lichen species; 2) the physico-chemical attributes of the rock, including elemental composition, molecular structure, cementing agents, density, porosity, pH and nature of origin; and 3) local and regional climatic patterns (St. Clair & Seaward, 2004; Favero-Longo & Viles, 2020).

3.5.1 Biogeophysical weathering

Biogeophysical weathering refers to the mechanical action of lichen thalli on the rock and is especially dominant in the early stages of lichen colonization. Biomechanical processes (Figure 10) influence the microstructure properties (microfractures, surface spalls and porosity) of the host rock through tensile stresses, thus, leading to extensive disaggregation and fragmentation of the lithic surface immediately below the lichen crust (Adamo & Violante, 2000; Chen *et al*., 2000; Chen & Blume, 2002; St. Clair & Seaward, 2004; Guglielmin *et al*., 2011).

Fungal hyphae generally penetrate mineral matter via points of weakness (fractures, cavities/voids and mineral cleavage planes), but in some cases by direct tunnelling or boring (Gadd, 2017a). Expansion and contraction of fungal hyphae generally succeed hyphal penetration. This mechanism is caused by wetting and drying cycles and subsequent expansion or contraction of biomass, which ultimately lead to the fragmentation and exfoliation of the rock and its component minerals (Jorge-Villar & Edwards, 2010; Weber & Büdel, 2011). The expansion and contraction capabilities of the thallus is furthermore enhanced due to the medulla (Figure 8) of lichens being an excellent hygroscopic substance with a great water holding capacity (Chen *et al*., 2000).

Freeze and thaw cycles are an additional aspect of physical weathering arising from thermal variations between substrates and air, especially in cold environments (Chen *et al*., 2000; Pointing *et al*., 2015). This occurs both during vaporization of permafrost during warmer temperatures and dew/frost deposition at colder temperatures (see Figure 11). This phenomenon affects microstructure properties (interconnected fractures or pores) of the substrate, resulting in the disintegration and subsequent colonisation of freshly exposed minerals along grain boundaries (Adamo & Violante, 2000).

The mechanical disruption of substrate rock may also be prompted by the crystallization of secondary salts, especially various oxalates, originating from the reactions of organic and inorganic acids excreted by organisms with mineral substrate (Chen *et al*., 2000). “Such salts are often highly water soluble and, thus are hydrated, resulting in an increased water content of

porous mineral materials" (Sand, 1997). It can be expected, therefore, that the presence of salts within pores and cracks of rocks exert sufficient pressure to separate mineral grains or rock fragments. Finally, hyphal interpenetration of the substrate particles and thallus swelling and shrinking also contributes to the *in-situ* dislodgement and movement of granules, which can be engulfed by the thallus (Wierzchos & Ascaso, 1994, 1996; Adamo & Violante, 2000; McKechnie *et al*., 2007).

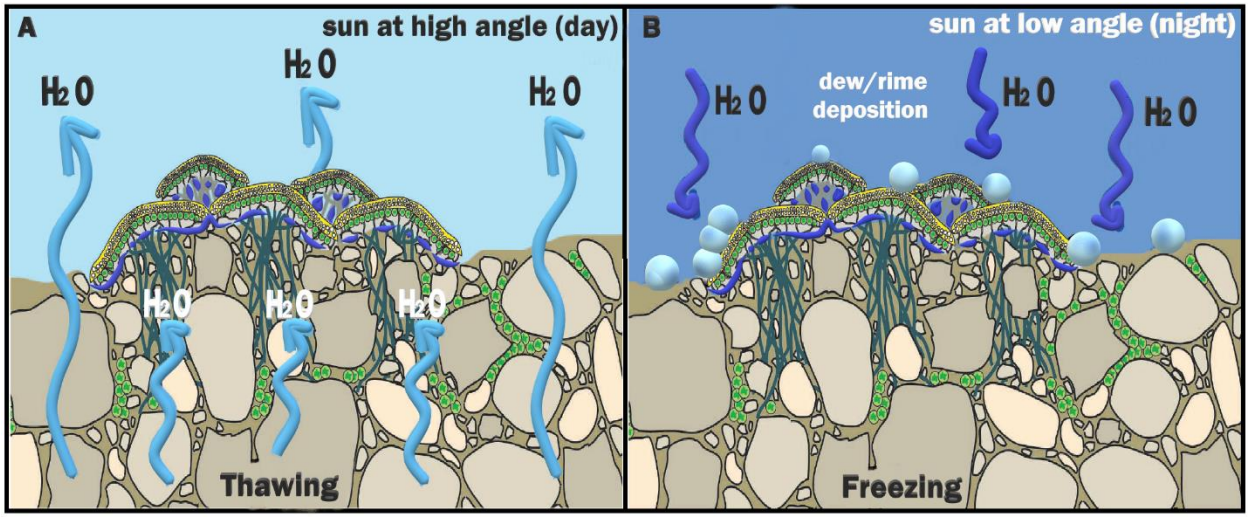


Figure 11: **Microclimate dynamics for cryptogamic photoautotrophs in cold environments. Biological soil crusts and endolithic colonization form extensive near-surface biological covers in cold regions that define the critical zone of biological activity and the dry limit for photoautotrophic colonization on Earth. They occur in regions where precipitation is insufficient to sustain higher plant life. The source of moisture arises from the creation of a substrate-air thermal gradient that supports dew/frost formation. During periods of high sun angle (daytime) thawing of permafrost and soil water releases water to the critical zone (A), when the sun is at a low angle (night) the thermal differential between substrate and air results in dew formation (B) (Modified from Pointing *et al*., 2015).**

3.5.2 Biogeochemical weathering

All the processes involved in biomechanical weathering of rocks by lichens are strongly connected with biochemical processes that affect habitat geochemistry (e.g. changes in pH, redox potential, porosity, water retention, aerobic/anaerobic transitions). Biochemical processes (Figure 10) are characterized by the solubilization of minerals and insoluble metal compounds; these affect the corresponding excretion of H^+, CO_2, organic acids, siderophores, and other metabolites, which produces pitting, etching or dissolution (Banfield *et al*., 1999; Gadd, 2010; Gadd, 2017a). "Fungi can solubilize minerals and metal compounds through several mechanisms, including acidolysis, complexolysis, alkalinolysis, redoxolysis, and by metal accumulation in the biomass" (Gadd, 2007). Amongst these mechanisms, acidolysis and complexolysis represent the primary fungal

impact on mineral dissolution (Gadd *et al*., 2007). Another important component of bioweathering is biomineralization, which refers to the process by which living organisms produce secondary organic and inorganic minerals – see 2.5.2.2.

3.5.2.1 Acidolysis and complexolysis

As suggested by many authors, acidolysis (or proton-promoted dissolution) occurs when fungi acidify their microenvironment as a result of the excretion of protons and organic acids and the formation of carbonic acid resulting from respiratory CO_2 (Wierzchos & Ascaso, 1996; Gadd *et al*., 2007; Weber & Büdel, 2011). Lichens can also excrete metal-complexing metabolites (e.g. carboxylic acids, amino acids, siderophores and phenolic compounds), which are associated with complexolysis or ligand-promoted dissolution (Gadd *et al*., 2007). Of the suite of organic acids produced by fungi, carboxylic acids are the most significant bioweathering agent with strong chelating properties. “Their dominant effect is attributed to the presence of hydrogen ions and the formation of cation-complexes, i.e. proton-promoted and oxalate-promoted mechanisms” (Chen & Blum, 2002).

It is furthermore suggested that organic compounds which are abundant in lichens, also referred to as lichen acids although not all of them are in fact acids, can dissolve and decompose rock-forming minerals by complexing structural metallic cations (Iskandar & Syers, 1972; Ascaso and Galvan, 1976). However, this process has not been conclusively demonstrated in field studies (Chen *et al*., 2000). Finally, some authors suggest that alkaline metabolic products are believed to stimulate the dissolving of lichen compounds and therefore accelerate the weathering of minerals (Berthelin, 1983; Prieto *et al*., 1997; Sand, 1997). The specific absorption and uptake of some elements by lichens would result in the acceleration of solubilization of the related element-bearing minerals (Chen *et al*., 2000).

3.5.2.2 Biomineralization

“Biomineralization refers to the processes by which living organisms produce secondary organic and inorganic minerals through metabolism-independent and -dependent processes, such as metabolite excretion and oxidation or reduction of a metal species” (Beimforde, 2011). Moreover, the process of biomineralization may be important in the weathering crust as precipitation of secondary minerals may increase soil aggregation and release dissolved cations (e.g. Si^{4+}, Fe^{3+}, Al^{3+} and Ca^{2+}) (Gadd *et al*., 2007). Depending on physicochemical conditions, secondary precipitates may exhibit a variety of crystalline forms (tetragonal, bipyramidal, platelike,

rhombohedral or needles) with relatively low molecular weight, the products of which accumulate in the cortex or in the medullary layer as extracellular tiny crystals on the outer surfaces of the hyphae (Gadd *et al*., 2007; Nash, 2008; Molnár & Farkas, 2010). Some of the most common secondary metabolites include oxalates, carbonates, phosphates, and oxides; these products contributing to physical disruption, mineral dissolution, staining and discolouration, and rock coating development (Adamo & Violante, 2000; Gadd, 2007, 2010, 2017; Gorbushina 2007; Fomina *et al*. 2010; de los Ríos *et al*., 2014).

Of the suite of secondary metabolites, oxalates have been identified as the most frequent forms of secondary mineral precipitates, resulting from the reaction of oxalic acid with the minerals of the rock substrates (Chen *et al*., 2000). Calcium oxalate are the most common forms of oxalate in nature, which act as a reservoir for calcium and influences phosphate availability (Gadd *et al*., 2007). “Fungi can also produce other metal oxalates with a variety of different metals and metal-bearing minerals, including Ca, Cd, Co, Cu, Mg, Mn, Sr, Zn, Ni and Pb” (Chen *et al*., 2000; Gadd, 2007, 2010; Gadd *et al*., 2014). It is, furthermore, noted that oxalate excretion has been reported to be induced or enhanced by NO^{3-} in contrast to NH^{4+}, and the presence of HCO^{3-}, Ca^{2+}, and some toxic metals (copper, aluminium) or minerals (pyromorphite, zinc, phosphate) (Arvieu *et al*., 2003; Casarin *et al*., 2003; Clausen & Green, 2003; Fomina *et al*., 2004).

Fungi are also known to precipitate a variety of other secondary minerals and reduced forms of metals and metalloids in and around fungal hyphae (Gadd, 2011). “This phenomenon immobilizes metals and limits their bioavailability, whilst releasing nutrients, such as sulphate and phosphate, if these are mineral components” (Gadd, 2007). Finally, due to silicate dissolution, which releases important nutrients that otherwise would remain bound, many lichens and free-living fungi contribute to the genesis of secondary clays. (Banfield *et al*., 1999; Chen *et al*., 2000; Gadd, 2017b). It is also important to keep in mind that some clays might be derived from extraneous sources in the form of wind-borne dust trapped by lichen thalli (Adamo & Violante, 2000).

3.6 MICROBIAL ALTERATION OF HABITAT GEOCHEMISTRY

“Rocks and minerals are the most fundamental earth materials with which microbes interact at all scales, from macroscopic to microscopic” (Dong, 2010). The distribution of subsurface microbes is controlled by multiple interacting factors, including porosity, temperature, pressure, energy and nutrient availability, and rates of geohydrologic processes (Horsfield *et al*., 2007). The mineral–microorganism interface is best charactarised by diverse metal-mineral-microbe interactions that are important in natural biosphere processes, influencing habitat geochemistry (e.g. changes in

pH, redox potential, porosity, water retention, aerobic/anaerobic transitions), biogeochemical cycling of elements, mineral formation, mineral deterioration, and chemical transformations of metals, metalloids and radionuclides (see Figure 12). Microbes also serve as a food source for animals, primarily gastropods and echinoderms, which periodically remove layers from the rock substrate (Viles, 1995).

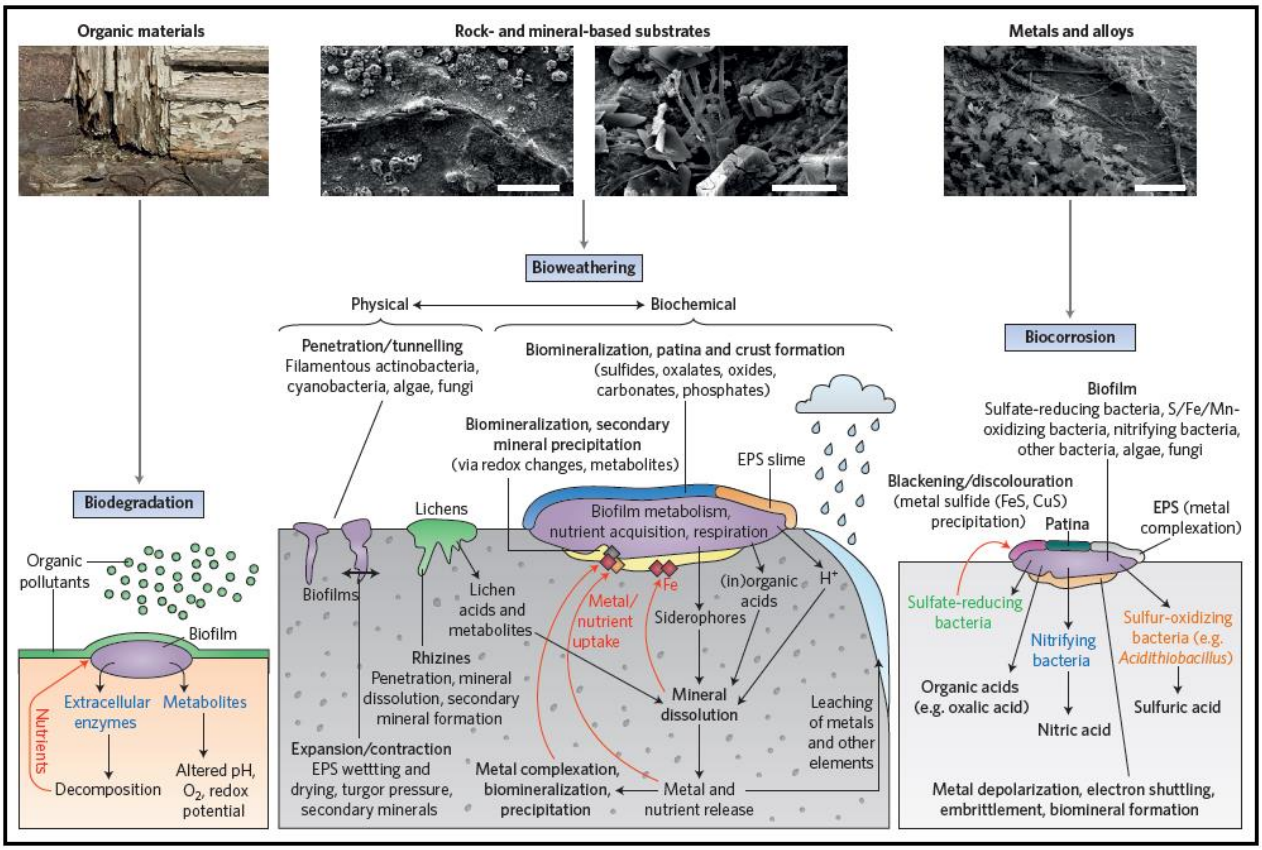


Figure 12: **Some of the main influences and effects of microorganisms on components of the built environment. There can be many dynamic interactions between the multiplicity of physical and biochemical mechanisms associated with the biodeterioration of rock- and mineral-based substrates. Biophysical mechanisms include penetration and boring; secondary mineral formation; extracellular polymeric substances (EPS) or biomass swelling or contraction; removal of lichen thalli and adhering substratum by animals and the weather; cell turgor pressure; and physical and chemical effects caused by microbial alteration of habitat geochemistry. Biochemical mechanisms include metabolite excretion (for example, H^+, CO_2); organic acids (for example, citric, oxalic); inorganic acids (for example, sulfuric, nitric, carbonic); production of metal-complexing EPS, solvents and emulsifying agents; Fe(iii)-coordinating siderophores; redox transformations by oxidation or reduction; bioaccumulation of solubilized metal and anionic species; biomineralization and formation of carbonates, phosphates, sulfides, oxides and oxalates; and alteration of habitat geochemistry by metabolism affecting metal and anionic speciation and mobility. Biodegradation of organic substances can be achieved by extracellular enzymatic attack. Biocorrosion of metals and alloys can include sulfate reduction and metal sulfide precipitation; acid effects; redox transformations; formation of localized corrosion cells; metal complexation by exopolymers, organic acids and other metabolites; and secondary mineral formation. Micrograph scale bars, 50 µm. (illustration by Gadd, 2017a).**

Atmosphere-exposed microbial communities or ‘subaerial biofilms’ (association of microbial communities) may produce extracellular polymeric substances (EPS) which have certain structural and protective functions within lithobiontic communities, such as helping to maintain structure, acting as a protective barriers (protection against water stress and UV and PAR radiation) and facilitating water retention and the sorption of organic compounds (e.g. nutrients) and ions (e.g. metal ions) (Chan *et al*., 2012; Wierzchos *et al*., 2015; Makhalanyane *et al*., 2015). Additionally, EPS also chemically react with minerals and accelerate dissolution, and therefore participate in the biomobilization of elements, biomineralization phenomena and clay mineral transformation processes (de los Ríos *et al*., 2007, 2014; Rossi & De Philippis, 2015).

3.7 ANALYTICAL TOOLS USED IN LICHEN–ROCK INTERFACE STUDIES

Optical microscopy is traditionally used as a starting point to provide a first level of information on the mineralogical and textural characteristics of different rock types. This method is subject to the shortcomings of human error and lack of statistically reliable data, which in turn has led to the development of more sophisticated methods of analysis. Modern biogeochemistry of the lichen-rock interface involves the application of qualitative and quantitative tools such as: (a) scanning-electron microscopy (SEM) in secondary emission mode (SEM-SE); (b) SEM in back-scattered electron emission mode (SEM-BSE); (c) transmission electron microscopy (TEM); (d) FT-Raman microscopy; (e) infrared spectroscopy (IR); (f) X-ray diffraction (XRD); (g) energy dispersive X-ray spectrometry (EDS); (h) X-ray photoelectron spectroscopy (XPS) and (i) Mössbauer spectroscopy (see Chen *et al*., 2000 for an overview).

Although these techniques continuously provide new and interesting observations, there is a need to explore other techniques that allow for the non-destructive, direct observation of the lichen-rock interface. “This permits observation of a wider surface area with a high spatial resolution, allowing the study from macro- to submicroscopic range and the possibility of instantaneous qualitative and quantitative *in situ* microanalysis of the inorganic constituents” (Wierzchos & Ascaso, 1996). One of the most promising tools, complementary to other techniques, is X-ray computed tomography (X-ray CT) that represents a promising alternative to traditional time consuming and error prone laboratory procedures (Ketcham & Carlson, 2001). Here, only the techniques most relevant to this study will be discussed in further detail.

3.7.1 Optical microscopy

In order to examine the microtextural and mineralogical features in the thin section of targeted

silica-rich rock varieties with higher resolution, an optical microscope is used. The modal abundance of different rock types could also be determined by performing point counts on a thin section. “Point counting represents the quantification of the mineral components and the percentages of each phase present in a thin section, which is conducted through mechanical or electromechanical devices attached to a microscope” (Larrea *et al*., 2010). This requires measurements to be made at regular positions on the sample where the device specifies the mineral to which the respective grid point and its local neighborhood belongs. By counting the number of points found for each mineral, the percentages that these values represent overall the counted points can be determined. Concerning the statistically correct number of counts required for quantitative examinations, the image to be manipulated must contain between 1500 and 5000 points (Larrea *et al*., 2010).

3.7.2 Scanning-electron microscopy

Scanning-electron microscopy (SEM) is a non-destructive technique that allows for quantitative chemical analysis of materials and the generation of high-resolution images and mineral maps (Gottlieb *et al*., 2000; Fandrich *et al*., 2007). SEM provides the opportunity to investigating surface morphology and perform analyses of selected point locations on the specimen. SEM devices generally require measurements to be undertaken in a vacuum in which primary electrons are focused into a small-diameter electron probe that is raster scanned over the specimen in order to generate a variety of signals at the surface of the specimen (Clarke & Eberhardt, 2002). This action stimulates the emission of low-energy secondary electrons (SE that are used to determine morphology and topography on specimens), high-energy backscattered electrons (BSE that are used for rapid phase discrimination based on variations in chemical composition), diffracted backscattered electrons (EBSD that are used to determine crystal structures and orientations of minerals), photons (characteristic X-rays that are used for elemental analysis and continuum X-rays), visible light and heat (Clarke & Eberhardt, 2002; Egerton, 2016). Depending on the type of detector (secondary-, backscattered-, or X-ray detector, Figure), the detected signal is converted to an image of the sample’s surface topography.

The two signals most often used to produce images are secondary electrons (SEs) and backscattered electrons (BSEs) (Egerton, 2016). SEM in back-scattered electron emission mode (SEM-BSE) has clear advantages over other techniques (e.g. LM, SEM-SE and TEM) due to the possibility of continuous observation from the macro- to submicroscopic scale (Wierzchos & Ascaso, 1994). This enables mineralogical characterisation which includes liberation status, association, grain size distribution and texture (Nwaila, 2014). SEM-BSE also permits the

characterization of the different ecological niches and the spatial organization of lithic ecosystems (Wierzchos & Ascaso, 2001; Ascaso & Wierzchos, 2003, de los Ríos *et al*., 2003, 2005a, 2005b, Wierzchos *et al*., 2003, 2005). Furthermore, SEM-EDS is especially useful in the qualitatively or semi-quantitatively determination of chemical compositions, crystalline structures and crystal orientations (Egerton, 2016).

3.7.3 X-ray micro computed tomography

X-ray micro-computed tomography (μCT) is a non-destructive technique that allows geophysical rock properties to be calculated based on the identification and quantification of features such as pores or minerals in the reconstructed gray-value images (Ketcham and Carlson, 2001; Cnudde & Boone, 2013). This state-of-the-art imaging technique produces two-dimensional images (‘‘slices’’) and comprises of voxels making the volume elements, which reveal the interior of an object as if it had been sliced open along the image plane for viewing (Denison *et al*. 1997; Koeberl *et al*., 2002). “The grey scale levels or values within each slice correspond to the X-ray attenuation coefficient for the input X-ray spectrum, a quantity that depends strongly on rock density and also on atomic number” (Duliu, 1999). In addition, it can accurately capture the pore space's 3D tortuosity to reliably predict permeability.

Basically, the device consists of four different functional units; a lead-lined cabinet, an external control module, an external chiller and PCs with acquisition software, 3D virtual image reconstruction and visualisation and analysis software. The X-ray tube directs X-rays from different orientations to an object and calculates the intensity reduction along a sequence of linear paths. “This decrease is characterized by Beer's Law, which describes intensity reduction as a function of X-ray energy, path length, and material linear attenuation coefficient” (Nwaila, 2014).

A specialized algorithm is used to reconstruct the distribution of X-ray attenuation in the volume being imaged. Three equations have been proposed based on the fundamentals of Beer’s law and the nature of material (Denison *et al*., 1997; Ketcham & Carlson, 2001; Koeberl *et al*., 2002):

$$I = I_0 \exp[-\mu x] \qquad \text{Eq. 1}$$

$$I = I_0 \exp\left[\sum_i (-\mu_i x_i)\right] \qquad \text{Eq. 2}$$

$$I = \int I_0(E) \exp\left[\sum_i (-\mu_i(E) x_i)\right] dE \qquad \text{Eq. 3}$$

Where: I_0: X-ray intensity

I: final X-ray intensity

μ: material's linear attenuation coefficient (unit 1/length)

x: length of the X-ray path

i: increment

E: X-ray energy

Equation 1 is referred to as the basic equation for attenuation of a monoenergetic beam through a homogeneous material. “If the scan object is composed of a number of different materials, equation one is modified to form equation two where each increment mirrors a single material with attenuation coefficient μ_i over a linear extent x_i” (Nwaila, 2014). The attenuation coefficient is a strong function of X-ray energy and therefore requires the equation to be resolved over the range of the X-ray energy spectrum utilised, which is represented by equation 3. Since the majority of reconstruction strategies solve for a single attenuation value at each spatial position, this calculation is usually not solved properly. This complicates absolute calibration and may lead to beam-hardening artifacts, which consequently result in changes in image grey values caused by preferential attenuation of low-energy X-rays (see Hoffman & De Beer, 2012 for an overview).

The object under investigation is fixed on the sample manipulator in the micro-focus X-ray cabinet to ensure that no movement of the sample occurs during scanning (Figure 13). The sample is then horizontally optimized, normally for maximum enlargement of the sample to obtain optimal

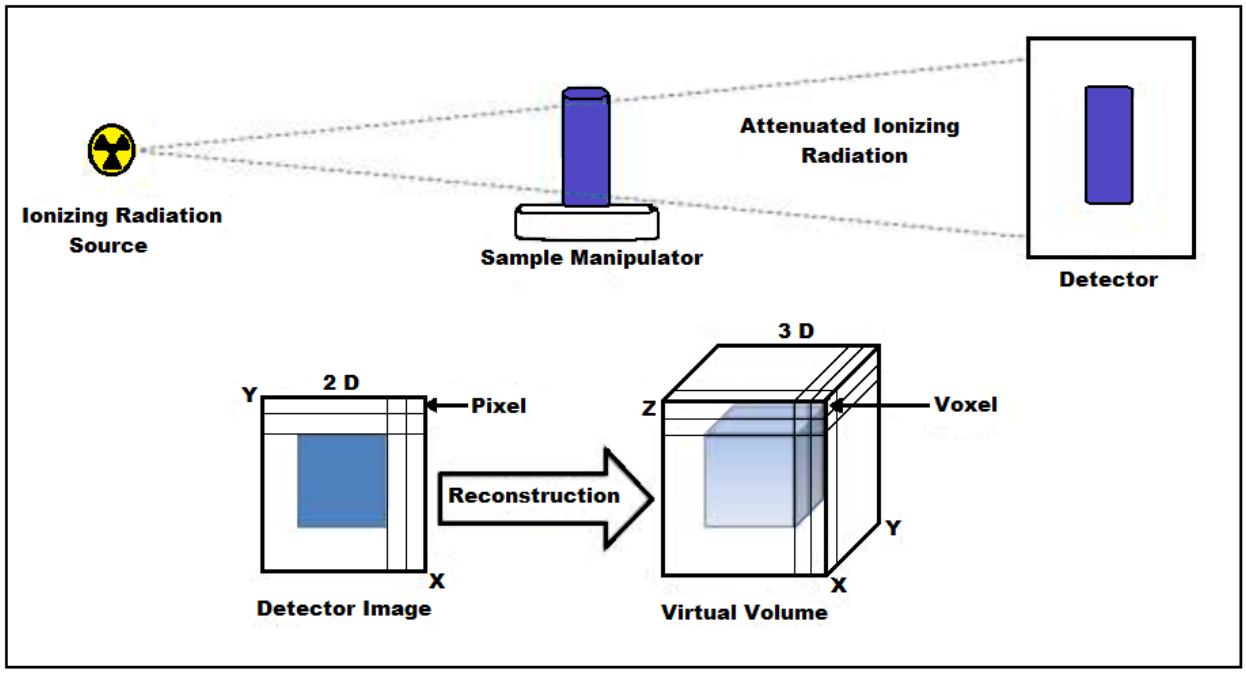


Figure 13: Tomographic Process at the MIXRAD facility (Illistration by Hoffman & De Beer, 2012).

spatial resolution (Cnudde & Boone, 2013; Shearer *et al*., 2016). “This adjustment also ensures that the sample is horizontally included in each 2D radiograph at all angles of rotation and for correct normalization during the tomography reconstruction process” (Hoffman & De Beer, 2012).

The X-ray source (most commonly X-ray-, synchrotron- or gamma-ray emitter) and detector that measures X-ray intensity attenuation along multiple beam paths, remain stationary. Different configurations of the X-ray source, sample manipulator and detector can be used to create X-ray CT scanners optimised for imaging objects of various sizes and compositions (Mees *et al*., 2003). Although X-ray CT uses a state-of-the-art imaging technique, there are still some limitations (see Cnudde & Boone, 2013 for an overview).

CHAPTER 4

METHODOLOGY

4.1 INTRODUCTION

This chapter is subdivided into three sections describing the experimental methods used in this study. Section 4.2 provides details on the stratification of the study area into homogeneous sampling units. Section 4.3 describes the methodology that was used for representative sampling at each sampling unit. In section 4.4, a description will be given on the procedure that was used for the laboratory scale spectroscopic and tomographic experiments.

4.2 ALLOCATION OF HOMOGENEOUS SAMPLING UNITS

In order to identify areas where silica-rich rock outcrops will most likely be colonized by lichens, a geological survey was performed, utilising the geological map (scale 1:50000) of the Council for Geoscience (Bisschoff, 1999), and the detailed map (scale 1:10000) of Bisschoff (1969). The average bedding orientation were taken where possible, along with GPS coordinates, altitude, and the approximate distance from the Vaal River (Appendix C1).

Emphasis was put on integrating the geomorphology of the site with the floristic and physiognomic characteristics of the supported vegetation to stratify the study area for sampling following the geobotanical approach described in Heshmatti & Squire (1995). Therefore, data from the geological survey was used to divide the area into five homogeneous sampling units (Figure 14). Each unit was selected according to, a) the absence and presence of specific groups of silica-rich rock types (ranging from crystalline to metamorphic rock types), b) the key lichen community present, and c) the geographical position of the outcrop with reference to the Vaal River.

By rather dividing each unit subjectively according to rock type and their related key lichen assembladge, as opposed to random stratification, a corresponding geochemical and ecological gradient is more clearly established for sampling. As a result, each proposed unit represents an area of a specific silica-rich rock and dominant lichen genera. By sampling within the allocated homogeneous units, changes in the mineralogical and chemical composition of the bedrockgeology can be correlated with changes in vegetation characteristics. Ultimately by correlating these variations, the effect of each rock type on specific vegetation features can be determined.

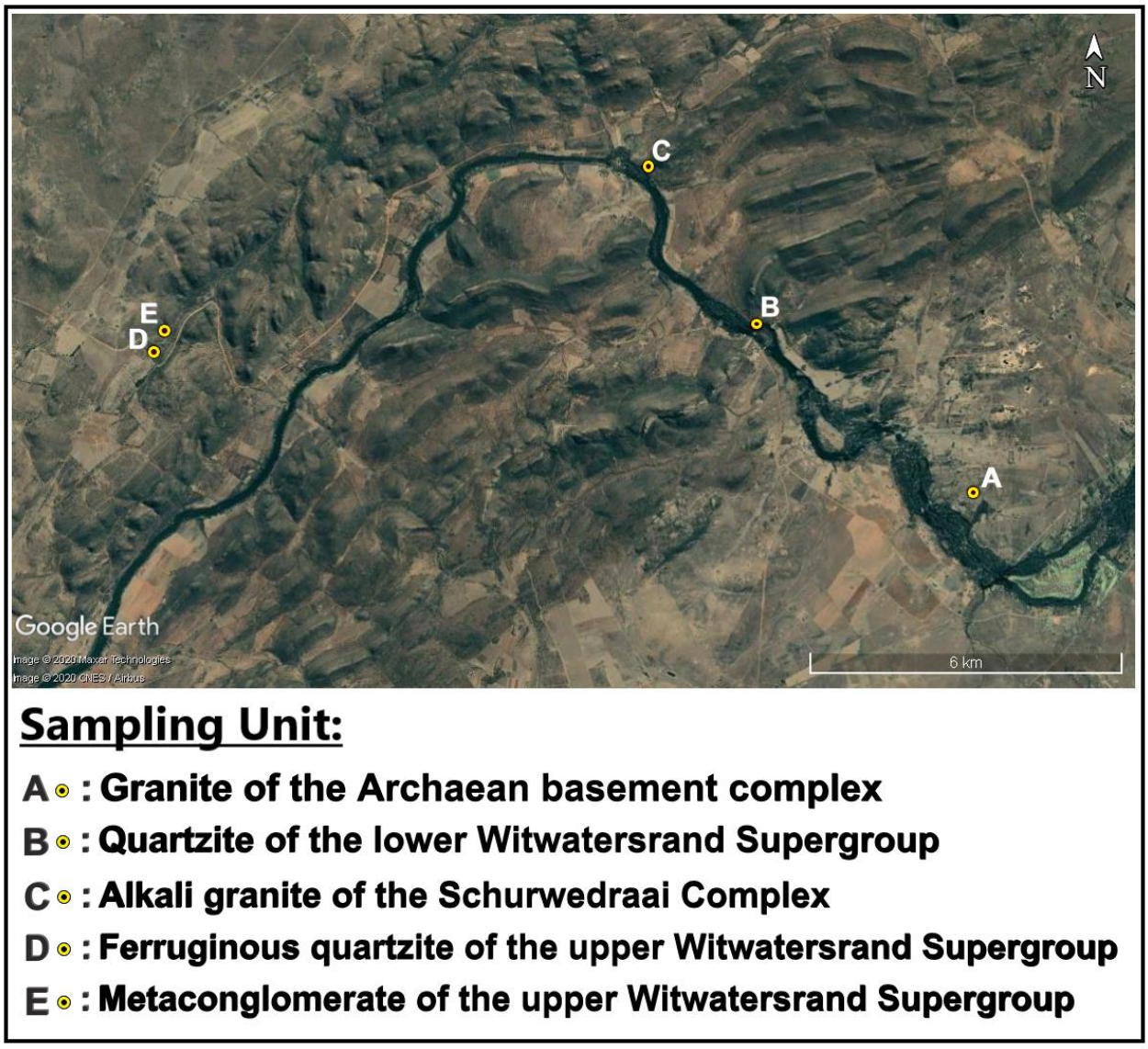


Figure 14: **Aerial photograph of the Vredefort Dome, illustrating the allocation of sampling units for rock and botanical surveys. The units are named after the predominant bedrock geology or overburden (Google Earth, 2019).**

4.2.1 Stratification and characterisation

The study area was stratified into the following sampling units (Figure 14):

4.2.1.1 Granite of the Archaean basement complex (Unit A):

This area is largely dominated by granitic outcrops along the flood plains of the Vaal River in the Archaean basement complex. The related soils are shallow and rocky. Lichen colonization is mainly sparse and dominated by *Xanthoparmelia* sp.pl. and *Acarospora* sp.pl.

4.2.1.2 Quartzite of the lower Witwatersrand Supergroup (Unit B):

Sampling unit B is dominated by quartzitic outcrops – the area which also marks the point were the Vaal River enters the dome from Parys along a major fault in the rocks of the collar (Figure 15). The soil is similarly shallow and rocky. Lichen community mainly comprises *Buellia* sp.pl. and to a lesser extend *Caloplaca* s. lat. sp.pl. and *Acarospora* sp.pl.

4.2.1.3 Alkali granite of the Schurwedraai Complex (Unit C):

The Schurwedraai pluton consists of alkali granite and nepheline syenite along the Vaal River where it cuts across the strike of the rocks of the Witwatersrand System (refer to Figure 15). The area follows the outcrop pattern of the alkali granite intrusion, which is primarily peralkaline to peraluminous in composition. The soil is similarly shallow and rocky, but nonetheless hosts higher densities of lichen species compared to unit A and B, particularly *Xanthoparmelia* sp.pl., *Buellia* sp.pl., and *Caloplaca* s. lat. sp.pl.

4.2.1.4 Ferruginous quartzite of the upper Witwatersrand Supergroup (Unit D):

Ferruginous quartzite together with metaconglomerate (unit E) form part of the Turffontein Subgroup. The most prominent outcrops of ferruginous quartzite occur within the outer arc of a very wide arcuate valley, which has been incised at the contact between the Witwatersrand and Ventersdorp Supergroups (refer to Figure 3). Due to a lack of access to the properties at which the Turffontein quartzite cuts accros the Vaal River, samples could only be taken further away from the river (approx. 2.8km from the river) at higher alltitudes with respect to those from other sampling units (±1450m compared to ±1350m). The soil cover is slightly thicker. Lichen community mainly comprises *Acarospora* sp.pl. and to a lesser extend *Caloplaca* s. lat. sp.pl.

4.2.1.5 Metaconglomerate of the upper Witwatersrand Supergroup (Unit E):

Sampling unit E is dominated by conglomerate beds – individual conglomerate beds are lenticular and never persist for long distances along strike. The individual thicknesses and frequency of the conglomerate beds are, therefore, highly variable. As is the case with unit D, samples could only be taken at higher alltitudes (±1450m). The soil cover is similarly slightly thicker, but nonetheless hosts higher generic abundance of lichens compared to sampling unit D, particularly *Buellia* sp.pl., *Caloplaca* s. lat. sp.pl. and *Acarospora* sp.pl.

4.3 SAMPLE ACQUISITION

4.3.1 Geological sampling

Based on the visual presence of biotic crusts, fragments of weathered silica-rich rocks were collected. The samples, consisting of intact biotic crusts of recognizable (colour-based) lichen genera and the weathered surface layer of silica-rich rock varieties, were collected across the five sampling units selected under section 4.2. Sample numbers and corresponding coordinates are provided in Appendix C1. Rock blocks of about 3 to 4 dm in diameter and 5 to 8 cm in thickness were detached from lichen-encrusted silica-rich rock boulders along pre-existing joints using a geological hammer. They were subsequently split into smaller rock fragments with visible signs of lichen colonization, to minimize effects of disturbance possibly caused during rock sampling.

Analytical techniques were used to determine the morphology, *in situ* chemical composition and mineralogy of the mineral accumulations. The morphology and *in situ* chemical composition were determined using a FEI Quanta FEG 250 SEM (Appendix B3) equipped with energy dispersive system (SEM-EDS) while the mineralogy was determined using a Nikon Eclipse 50iPOL polarizing microscope (Appendix B1).

4.3.2 Lichen sampling

The sampling of saxicolous lichens was carried out in conjunction with geological sampling from the 10 samples collected under section 4.3.1. As the study area is subjected to frequent trampling by grazing livestock, site selection was dependent upon the availability of lichen rich patches in the landscape. Out of the 10 marked areas, 6 spots that clearly showed growth of single lichen colonies, were selected for lichen identification (Figure 14). For the purpose of this study, lichens were only identified at the genus level. Data on macroscale environmental variables (approximate distance from Vaal River, elevation, etc.) were taken for each sampling unit.

4.4 SAMPLE PREPARATION

4.4.1 Rock samples

At the Geology laboratory, North-West University, the samples were sorted and labelled. The material for petrological analyses were prepared firstly by cutting off any weathered surfaces into stone slabs (± 50mmx30mm) using a diamond saw cutter, to ensure that fresh samples are used.

The stone slabs were then mounted onto an optical glass slide using an epoxy with a birefringence close to that of the optical glass and grounded to an approximate thickness of 30 µm. At this thickness most minerals become more or less transparent, allowing their study with a Nikon Eclipse 50iPOL polarizing microscope (Appendix B1) at the Geology laboratory, North-West University. The determination of mineral abundances was achieved by making use of a point counter (results thereof is given in Appendix D1).

4.4.2 Morphological features

Bulk samples of the thallus sections were investigated in water, K and lactophenol cotton-blue under a stereomicroscope in reflected light in order to identify the diagnostic anatomy and cellular structure of each lichen. In particular, their growth morphology, reproductive organs (apothecia and perithecia), surface features and color of thallus were examined and integrated with taxonomic keys of classification. This comparison allowed us to determine the taxonomic genus and classify them according to Fryday (2015).

4.4.3 Tomographic analysis

A tomographic analysis was carried out on targeted silica-rich rock varieties representing a wide range in composition as well as grain- and pore sizes. Here the focus was away from nano-scale characterization, mainly because the main interest was in linking micro-scale processes. Hence, the need to consider sample volumes that are large enough to be representative of the material as a whole.

To prevent biased results and ensure that as many measurements as possible can be correlated directly with one another, tomographic analysis was carried out on the same blocks of resin-embedded rock samples prepared for SEM examination (see section 4.4.4). Selected samples were analysed using a Nikon XTH 225 ST micro-focus X-ray tomography system at the MIXRAD facility hosted by NECSA (refer to Appendix B3). The scanning parameters for all samples in this study are detailed in Table 9.

Imaging optimisation was required to generate an accurate representation of the rock structure, essential for subsequent processing. After image acquisition of packed bed volumes, reconstruction of the projection images was performed using VGSTUDIO MAX 3.4 software in order to correct artefacts present in the reconstructed files to produce more representative volumes. In addition, 3D volume rendering was used to examine the surface of each silica-rich rock under investigation - a factor of importance for bioencrustation.

Table 9: Summary of measurement parameters using Nikon XTH 225 ST micro-focus X-ray tomography.

System Characteristic		Value
X-ray source	Potential	180 KV
	Current	60 (μA)
	Voxel size	~17 μm
	Beam Angle	25°
	Filter	0.25 mm Cu
Translation table	Axis movement (directions)	5
	Sample Movement in Horizontal Plane (mm)	200
	Sample Movement in Vertical Plane (mm)	300
	Sample Movement in Beam Direction (mm)	610
	Rotation accuracy	1/1000th of a degree
	Tilt	0°
	Number of projections	1000
Detector	Type	Perkin Elmer
	Dynamic Range	16 bit
	Physical Size (mm)	400 x 400
	Pixel Size (Micron)	200 x 200

4.4.4 SEM and microprobe analysis

Polished blocks of resin-embedded rock samples were prepared for scanning electron microscopy (SEM) to prevent section smearing. Selected lichen-encrusted rock fragments were immediately fixed in 70% ethanol for at least 24 hours; dehydrated in an increasing ethanol series (80 %, 90 %, 100 %, and 100 %) for 30 min; and embedded in LR White resin (i.e., hydrophilic acrylic resin of low viscosity) following the protocol described in Wierzchos & Ascaso (1994). Blocks of resin-embedded rock samples were then ground down on a 220-grit silicon carbide lap for 5 minutes to reveal a suitable transverse section through each sample and lapped on a 500-grit lap for 10 minutes then 220-grit lap for 20 minutes. Grinding and lapping were carried out using water, 9 μm diamond suspension, and 3 μm diamond suspension respectively; to prevent

a build-up of mineral dust during polishing that can cause undercutting and may also result in contamination of the lichen.

Both the blocks of resin-embedded rock samples and bare rock fragments were vapor fixed in osmium tetroxide (OsO_4) and sputter-coated with carbon-palladium. Sections were mounted with double sided tape on aluminium stubs and examined in a FEI Quanta FEG 250 SEM utilising a back-scattered electron (BSE) detector, operated at 2 kV. SEM-EDS was used for semi-quantitatively determination of chemical compositions, crystalline structures and crystal orientations (Egerton, 2016). The basic working principle of SEM is shown in the schematic diagram of Appendix B2.

CHAPTER 5

FIELD RELATIONS

5.1 INTRODUCTION

Published literature and site geology of the Vredefort Dome revealed a general shortage of structural, petrological and geochemical knowledge with regards to silica-rich rock varieties that are subjected to abundant lichen activity. As a result, it was unclear if there is a correspondence between the distribution of saxicolous lichens in the dome and specific geological formations. Hence, the geological features of each sampling unit had to be assessed and the full extent and relationship of the targeted silica-rich rock varieties needed to be documented.

The justification, ultimately, was to provide an improved understanding of the microhabitats and chemical microenvironments supporting saxicolous lichens growing on silica-rich rock varieties, to better understand the preferences and distribution of lichens in the Vredefort Dome. Specific objectives for this facet of the larger study were to (i) describe field relations and physical characteristics associated with each sampling unit (section 5.2) and, (ii) determine and discuss the mineralogical- and petrographical characteristics of targeted silica-rich rock varieties (section 5.3 and 5.4 respectively).

5.2 DISTRIBUTION OF ROCKS AND LICHENS IN THE FIELD

The field survey evidenced that various genera of saxicolous lichens colonise the surface of rock outcrops throughout the 40 to 50 km wide central core of the dome as well as in parts of the 20 to 25 km wide collar of up- to overturned layers. Broady speaking, the extent of lichen cover seemed to be affected mostly by the physico-chemical attributes of the rock, the aspect of the outcrop, the presence of shade from taller vegetation, as well as the position of the outcrop with regards to the Vaal River. As the ecology of the different genera were not the focus of this study, the above observations were not verified by means of specific surveying techniques and analytical methods. The relation of the sampling sites to the geology, as well as the Vaal River, is shown in Figure 15.

At a local scale, the majority of lichen genera seemed to be restricted to silica-rich rock types. Nonetheless, certain lichen genera were unaffected and showed a higher abundance on mafic- and ultramafic outcrops. In particular, granites of the Archaean Basement Complex, quartzite and metaconglomerate of the Witwatersrand Supergroup, and Alkali Granite associated with

peralkalic intrusions were identified to host abundant lichen activity. Preference was, therefore, given to silica-rich rock varieties - the bioreceptivity (capacity to harbour life) of which generally favours bioencrustation (e.g Büdel *et al*., 2004; Walker & Pace, 2007).

In the dome the prevailing direction of rain is from the southwest, while the predominant average hourly wind direction is from the north and the in-fall direction of the sun's rays is from the East. The cool and moister slopes are therefore facing toward the southeast**,** with the result that denser lichen covers are found on the south facing parts of outcrops, and in the shade where the evaporation rate is lower than in the open. This also explained denser lichen cover in the damp areas associated with the Vaal River and its flood plains.

Saxicolous lichen assemblages were quantitatively analysed for frequency of taxa (identified at the genus level) visually recognized as dominant through the whole area and thus selected as observation target. In particular, two lichen growth forms, foliose and crustose, were encountered. Species of the crustose genera *Acarospora* sp.pl. and *Caloplaca* s. lat. sp.pl. were recorded as the dominant lichens encrusting silica-rich rock varieties in the dome, followed by *Buellia* sp.pl.



Figure 15: **Oblique aerial photograph of the inner collar of the Vredefort Dome northwest of Parys, showing sampling unit B (arrow A) and C (arrow B) as well as the Vaal River exploiting a fault cutting the lower Witwatersrand Supergroup. The prominent Hospital Hill Subgroup quartzite (centre) is bent and offset to the north (left) on the far side of the river relative to the rocks on the west side of the river. The flat area to the left is underlain by alkali granite. (Aerial photograph by Reimold & Gibson, 2009).**

Table 10: Records of the selected saxicolous lichen genera in the five sampling sites in the Vredefort Dome

Genus	Family	Growth form	Morphological features	Sites									
				Unit A Altitude: ±1370m (450-480m)		Unit B Altitude: ±1340m (30-50m)		Unit C Altitude: ±1360m (100-120m)		Unit D Altitude: ±1450m (2780-2800m)		Unit E Altitude: ±1440m (2800-2850m)	
				VK1A	VK1B	VK2A	VK2B	VK3A	VK3B	VK4A	VK4B	VK5A	VK5B
Xanthoparmelia sp.pl.	Parmeliaceae	Foliose	The *Xanthoparmelia* sp.pl. recorded in the dome is predominantly blackish-grey to greenish-grey in color, with a lobate thallus composed of subirregular to sublinear lobes that grow radially and branch, and lacking isidia and soralia.	D1	D1	-	-	D1	D1	-	-	-	-
Acarospora sp.pl.	Acarosporaceae	Crustose	The *Acarospora* sp.pl. recorded in the dome is green in color and exhibits an effigurate thallus with radially arranged and long marginal lobes. It strongly adheres onto the substratum.	D2	D2	D3	D3	x	x	D1	D1	D2	D2
Caloplaca s. lat. sp.pl.	Teloschistaceae	Crustose	*Caloplaca* s. lat. sp.pl. is orange in color and also exhibits an effigurate thallus with radially arranged and long marginal lobes. It strongly adheres onto the substratum.	x	x	D2	D2	D2	D2	D2	D2	D1	D1
Buellia sp.pl.	Caliciaceae	Crustose	The *Buellia* sp.pl. recorded in the dome predominantly exhibits a white-gray rimose-areolate thallus with areoles partially encompassing apothecia, and strongly adhering onto the substratum. Rimose-areolate thallus is generally accompanied by the development of a carbon black ring or outer margin (exciple) around the fruiting body disc (apothecium).	-	-	D1	D1	D2	D2	-	-	D1	D1
Species richness (no of taxa)				3	3	3	3	4	4	2	2	3	3

D1, dominant taxon within microhabitat; D2, primary co-dominant taxon within microhabitat; D3, secondary co-dominant taxon within iacrohabitat; x, present at site; values in parentheses indicate the distance of each sampling unit from the Vaal River.

and the foliose *Xanthoparmelia* sp.pl. Per each plot, taxon richness (i.e. number of the selected lichen genera), growth form diversity, and associated morphological features (see Table 10) were surveyed. Though there was no significant linear relationship between altitude and saxicolous lichen genera diversity, a gradual decrease in number of sampling units containing saxicolous lichens was observed with increasing altitude (Table 10).

5.2.1 Granite of the Archaean basement complex (Unit A)

Unit A is situated in the north-western portion of the Archaean basement complex and comprises a complex high-grade metamorphic terrane that is dominated by granitic outcrops. The granites

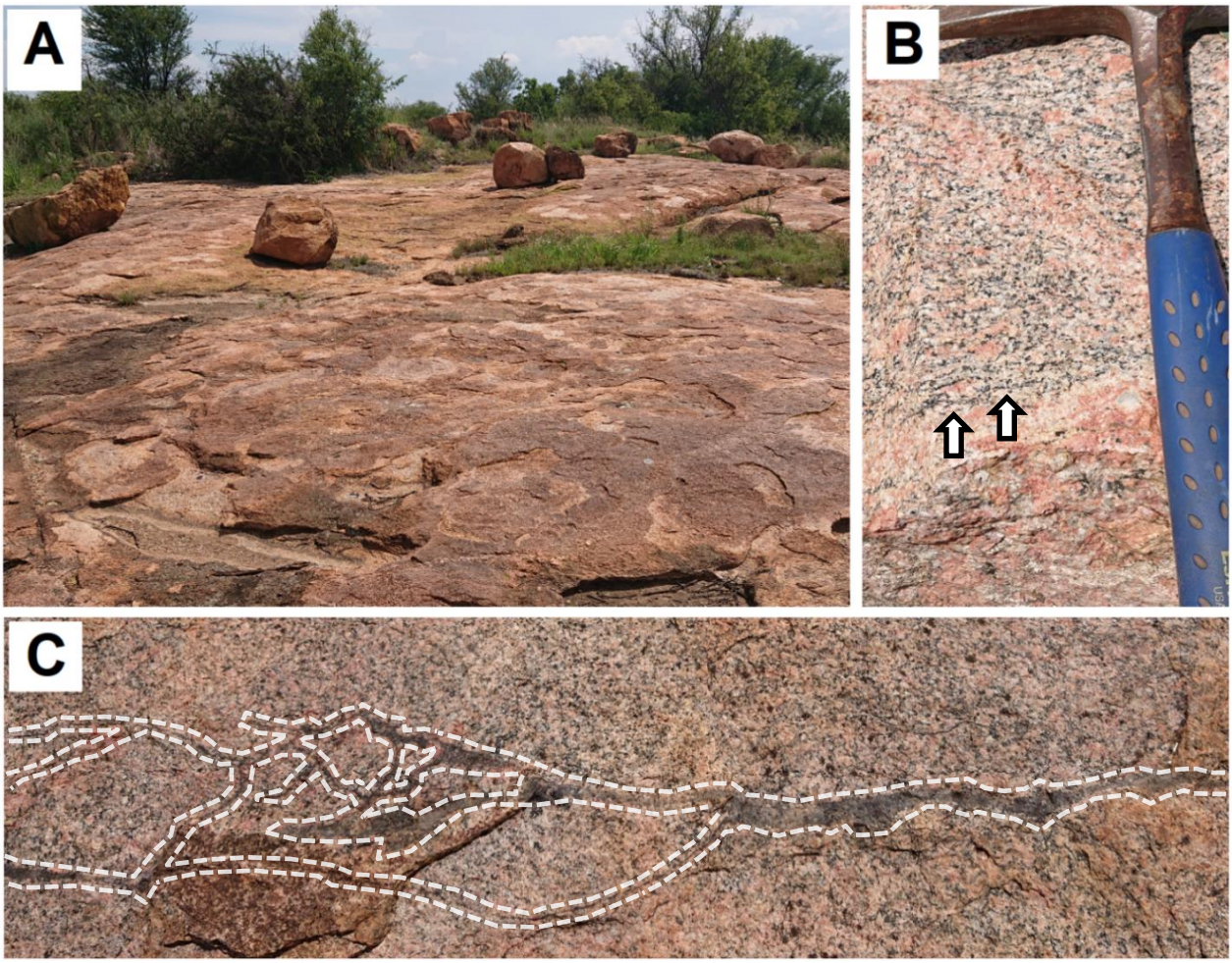


Figure 16: **Pictures of structural field relations associated with the granites of sampling unit A. (A) A view across the spheroidal granite boulders which roll down along gentle slopes towards the Vaal River. Note the thin exfoliation sheets and reddish iron staining on the surface of the granite. (B) A typical sample of less weathered granite displaying its heterogenenity, found scattered along the spheroidal outcrops in unit A. Note the very weak biotite foliation (white arrows). (C) Photograph of thin, grey pseudotachylitic breccia veinlets cutting the granite, confirming their pre-impact age. (Photographs by Smit, 2019).**

are charactarised as a heterogeneous medium- to fine grained phase of the rock in which plagioclase feldspar slightly dominates over pink alkali feldspar and quartz, and the dark minerals are biotite (Figure 16B). Although no preferred orientation of crystals is evident, biotite does seem to show a very weak preferred orientation pattern (Figure 16B).

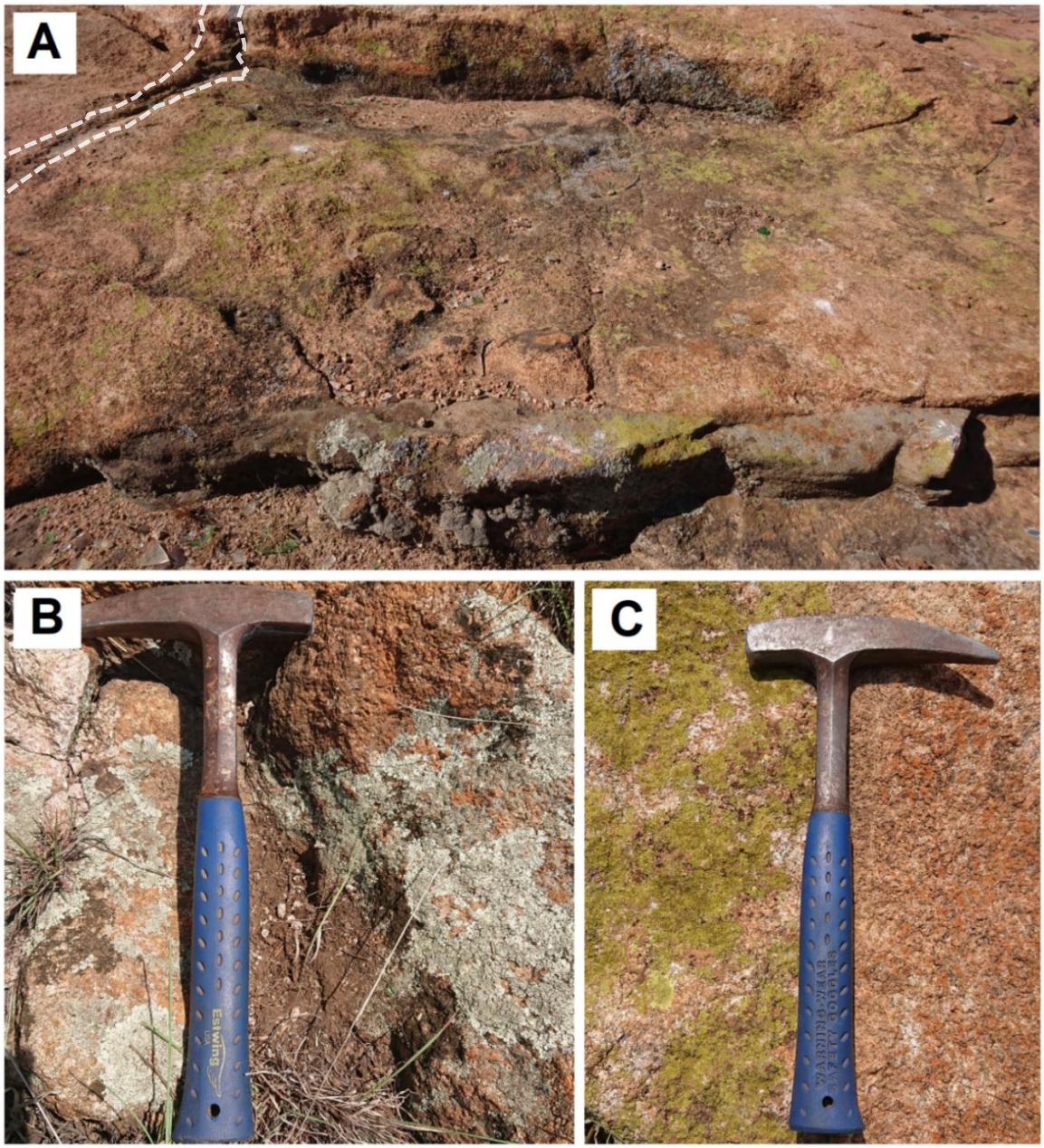


Figure 17: **Pictures of lichen genera reported in sampling unit A. (A) Photograph of the dominant lichen genera colonising the granite, including *Acarospora* sp.pl. (green-colored lichen assemblages) & *Xanthoparmelia* sp.pl. (gray-colored lichen assembladges). Note the thin, grey pseudotachylitic breccia veinlet (white dotted lines) cutting the granite. (B) *Xanthoparmelia* sp.pl. growing in association with vegetation including mosses and grasses. (C) *Acarospora* sp.pl. (green-colored assembladge on the left side of the geological hammer) and *Caloplaca* s. lat. sp.pl. (small irregular patches of orange-colored lichens on the right side of the hammer). (Photographs by Smit, 2019).**

The granitic outcrops are also extensively transected by thin, grey veinlets of pseudotachylitic breccias (Figure 16B and 17A), which are established markers for impact-related deformation (Elsenbroek, 1991; Gibson & Reimold, 1999; Reimold, 2006). Subspherical boulders and core-stones are characteristic of the landscape, which frequently exhibit a moderately-weathered outer shell, with millimetre to centimetre - thick exfoliation sheets or flakes (Figure 16A), often widely encrusted by lichens (e.g. Figure 17A). These spheroidal boulders represent the inner, unweathered, or less-weathered portions of saprolite and are derived from spheroidal weathering (Migoń & Lidmar-Bergstroöm, 2001).

The dominant saxicolous lichen assemblage recorded from unit A included three main taxa (Table 10). *Xanthoparmelia* sp.pl. was identified as the dominant lichen taxon colonising these granitic outcrops, followed by *Acarospora* sp.pl. as the primary co-dominant taxon. Small irregular patches of *Caloplaca* s. lat. sp.pl. could also be observed, but not frequently.

5.2.2 Quartzite of the lower Witwatersrand Supergroup (Unit B)

Sampling unit B is set in a riverine habitat (Figure 18A) in the northwestern sector of the collar where the Vaal River enters the dome from Parys along a major fault in the rocks (refer to Figure 15). The largest portion of exposed strata is dominated by metamorphosed quartzite of the Hospital Hill Subgroup, the lowermost part of the lower Witwatersrand Supergroup (see Figure 3). This quartzite represents the oldest bedrock lithology of the study area and is charactarised as a hard homogeneous fine-grained phase of the rock, which often exibits well-defined and well-exposed dip slopes (see geological survey data, Appendix C1).

Despite the rock being made up almost entirely of light-coloured and sometimes glassy quartz, its distinguishing feature is the presence of a pale green chromiferous mica which gives the rock a characteristic green tint. According to Fuller (1958), the mica tends to concentrate in narrow bands and is associated with detrital chromite. The bedding is intensely deformed and displays common impact related deformation, including impact-formed fractures (Figure 18A and 19B), bedding-parallel pseudotachylitic breccia (Figure 18C), and shatter cones (Figure 18D). The observed shatter cones commonly display a partially conical form, with an almost planar fracture surface.

Herringbone crossbedding (Figure 18B) was observed throughout unit B, which evidences that these were indeed old beach sand moving in opposing directions, now lithified and turned on-end by the Vredefort doming event (Reimold & Gibson, 2009). Ripple marks were also exposed in the

unit cutting across the Vaal River but not as frequently. Species of three of the selected lichen genera were recorded from unit B (Table 8). *Buellia* sp.pl. was dominant on the Hospital Hill quartzite followed by *Caloplaca* s. lat. sp.pl. and *Acarospora* sp.pl. as the primary and secondary co-dominant components respectively (refer to Figure 19).

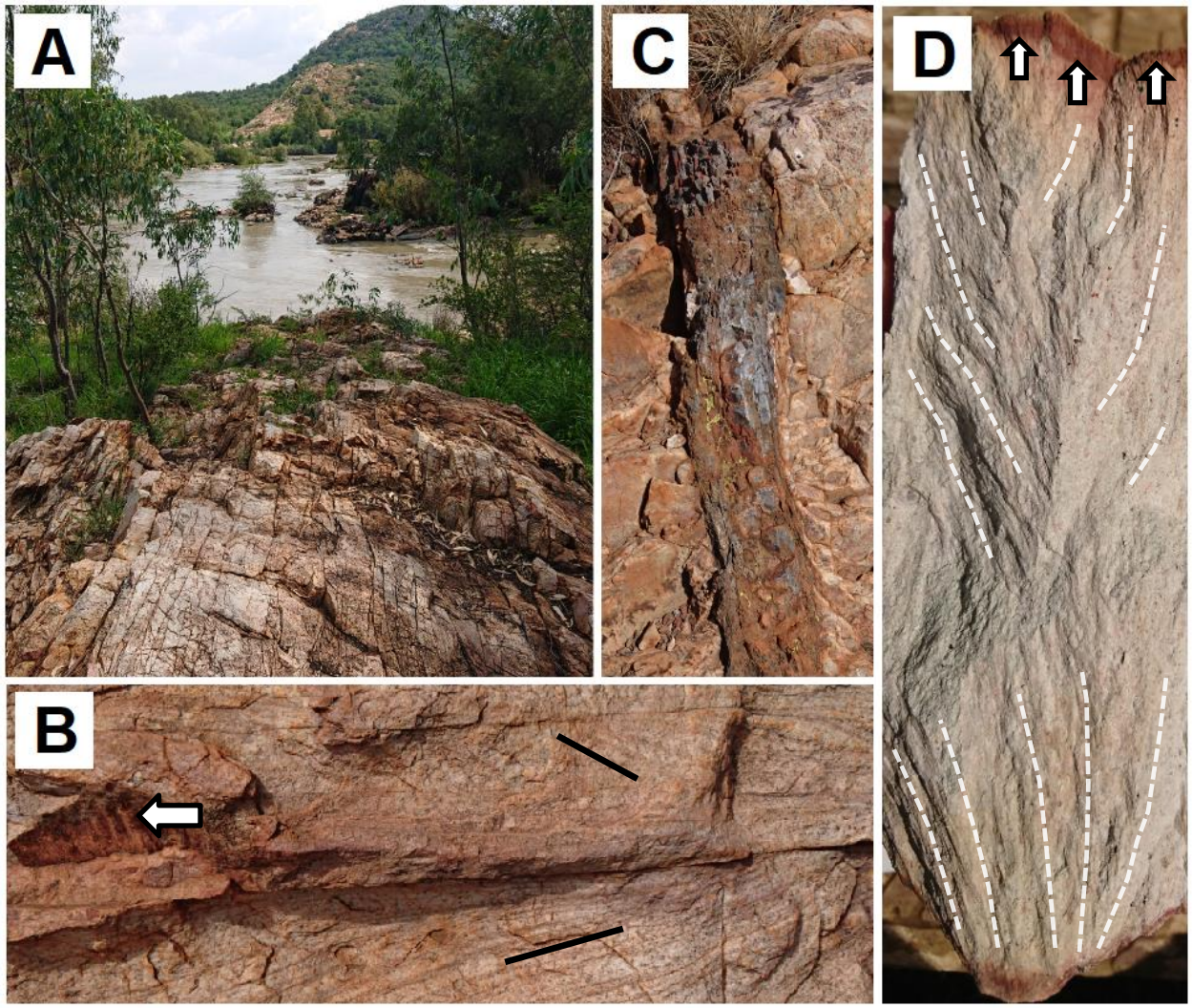


Figure 18: **Photographs of field relations associated with sampling unit B. (A) The view across the river shows the riverine habitat associated with the landscape as well as the prominent overturned and strongly fractured quartzite of the Kommandonek ridge, on the opposite side of the river. Note the impact-formed fractures on the surface of the quartzite, which are typically open and fairly straight. (B) Photograph of herringbone crossbedding in Hospital Hill quartzite. The darker lines are formed by oxidation (rusting) of iron-rich minerals that were deposited on small underwater sand dunes. Surface striations along the fracture planes (white arrow) are also clearly visible: these are indicative of shock deformation. The black lines indicate bedding planes. (C) Bedding-parallel pseudotachylitic breccia in Hospital Hill quartzites. (D) A typical example of a shatter cone segment showing almost parallel striations (white dotted lines) on a sample of Hospital Hill quartzite. The photo also shows an orange-brown crust due to surface oxidation (white arrows). (Photographs by Smit, 2019).**

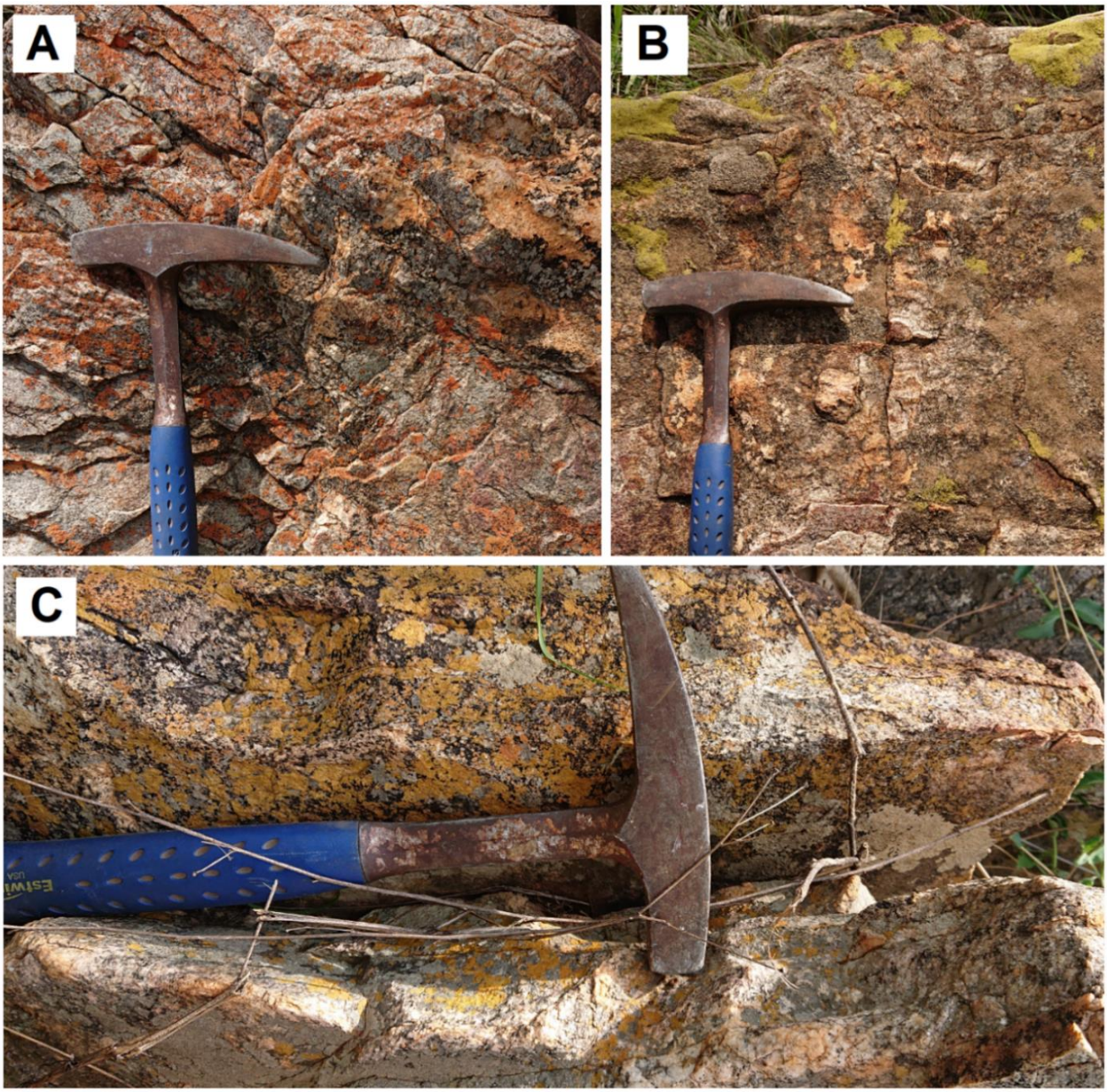


Figure 19: **Pictures of lichen genera encrusting Hospital Hill quartzites in sampling unit B. (A,C) Rock surface completely covered with two dominant lichen genera, including *Buellia* sp.pl. (gray-colored lichen assembladges) and *Caloplaca* s. lat. sp.pl. (orange-colored lichen assembladges). (B) Rock surface covered with mealy and depressed *Acarospora* sp.pl. (green and brown colored assembladges) - their appearance subsequent to lichens dissolving the rock surface. (Photographs by Smit, 2019).**

5.2.3 Alkali granite of the Schurwedraai Complex (Unit C)

Sampling unit C is situated in the northwestern collar of the Vredefort Dome and comprises a small alkali granitic body (3 to 4 km in length) along the Vaal River where it cuts across the strike of the rocks of the Witwatersrand System (refer to Figure 15). The Schurwedraai alkali pluton forms subhorizontal outcrops trending roughly northeasterly (Figure 20). The outcrop surfaces dip towards the east at a low angle. It bears a passing resemblance to the granites in the core of the

dome; however, there are several significant differences. It has a more heterogeneous - but nonetheless medium- grained size with more feldspar (mainly albite and K-feldspar) and slightly less quartz, and the dark minerals are amphibole (Figure 21D). The quartz-albite-K-feldspar ratio varies considerably from one locality to the next, in the northeastern section of the Schurwedraai pluton the quartz content falls below 5% (Graham *et al*., 2005; de Waal *et al*., 2008). In this area nepheline syenite xenoliths are common in the granite.

Pre-impact lithological heterogeneities are absent in the complex and pre-impact textural and structural features are scarce in contrast to the granites and gneisses of the Archaean basement complex and the metasedimentary collar strata. Nevertheless, alkali granite is extensively transected by pseudotachylitic breccia (from a few millimeters to about 1.5 m wide, or as networks up to 6 m wide), and they also display multiply striated joint surfaces and shatter cones, confirming their pre-impact age.



Figure 20: **Panoramic view looking west over the Schurwedraai bend of the Vaal River. The flat area south of the bend is underlain by the Schurwedraai alkali granite pluton. To the north, the buttress of the quartzites of the upper Witwatersrand Supergroup forms the highest ridges of the Vredefort Mountain Land. (Photograph by Smit, 2019).**

Specimens of the four selected genera were recorded from unit B, and consequently the highest diversity of lichen genera among the studied rocks (Table 8). *Xanthoparmelia* sp.pl. was dominant, followed by *Buellia* sp.pl. and *Caloplaca* s. lat. sp.pl. as the primary co-dominant taxa (refer to Figure 21). Small irregular patches of *Acarospora* sp.pl. could also be identified but not as frequently.

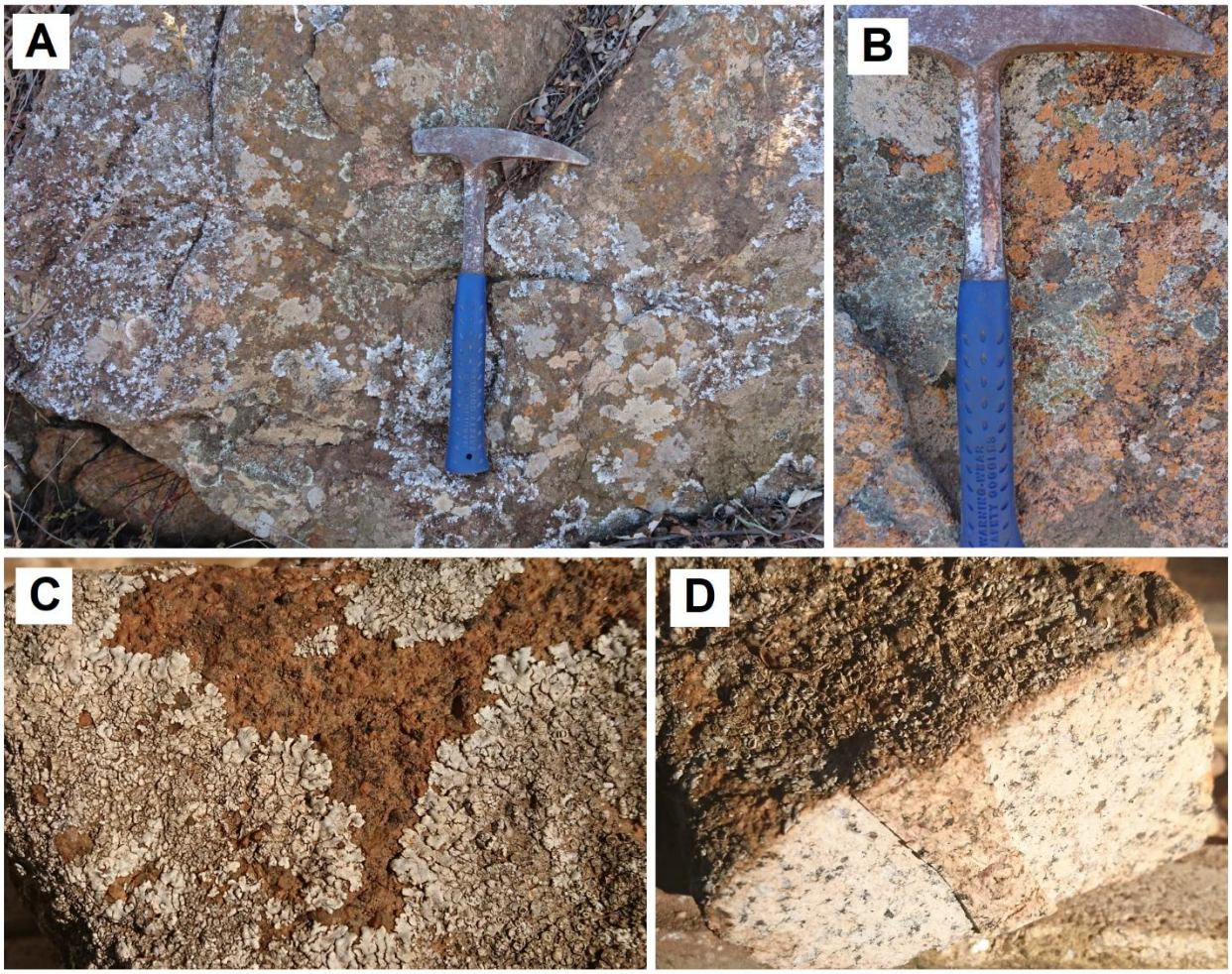


Figure 21: **Pictures of lichen genera encrusting Schurwedraai alkali granite in sampling unit C. (A,B) Rock surface completely covered with three dominant lichen genera, including *Xanthoparmelia* sp.pl. (gray to green-colored foliose lichen assemblages), *Buellia* sp.pl. (gray to white-colored crustose lichen assemblages) and *Caloplaca* s. lat. sp.pl. (orange-colored lichen assemblages). Notice the thin exfoliation sheets. (C) Several *Xanthoparmelia* sp.pl. clusters competing for space. Note the distinctive pattern of millimeter-deep depressions on the grain surface. (D) A typical sample of alkali granite displaying a hypidiomorphic granular texture, found scattered along the granitic outcrops in unit A. (Photographs by Smit, 2019).**

5.2.4 Ferruginous quartzite of the upper Witwatersrand Supergroup (Unit D)

Sampling unit D is situated in the north-western sector of the collar on the farm Rooderand 510. The largest portion of exposed strata is dominated by ferruginous quartzite (i.e. the Buffelskloof Formation of Els & Mayer, 1992) of the Turffontein Subgroup, which forms part of the upper Witwatersrand Supergroup (see Figure 3). Sampling unit D, along with sampling unit E, were positioned furher away from the Vaal River (approx. 2.8km from the Vaal River) at higher alltitudes (Figure 22).



Figure 22: **Panoramic view looking north-east over the prominent ferruginous quartzite ridge of the Turffontein Subgroup in the north-western parts of the exposed arc of the vredefort Structure, Rooderand 510. (Photograph by Smit, 2019).**

The ferruginous quartzite forms prominent outcrops that are texturally moderately mature (Figure 23C). It is a hard, medium to coarse-grained phase of the rock which consists primarily of quartz grains in a deformed matrix. In addition, the ferruginous quartzite often exibits scattered pebbles – the frequency of which increases towards the top where thin lenticular conglomerates and layers of single pebbles are found (Bisschoff, 1999). The bulk of the formation weathers to brown and buff colours due to the presence of a fine clastic matrix with a variable content of iron oxides. Secondary ferrous coatings are also common on outcrop surfaces – these ferrous coatings seemed to be avoided by lichens (Figure 23B).

Only species of two of the surveyed lichen genera were recorded from unit D, and consequently the lowest diversity of lichen genera among the studied rocks (Table 8). *Acarospora* sp.pl. were identified as the dominant lichen colonising these quartzitic outcrops followed by *Caloplaca* s. lat. sp.pl. as the primary- co-dominant taxon.

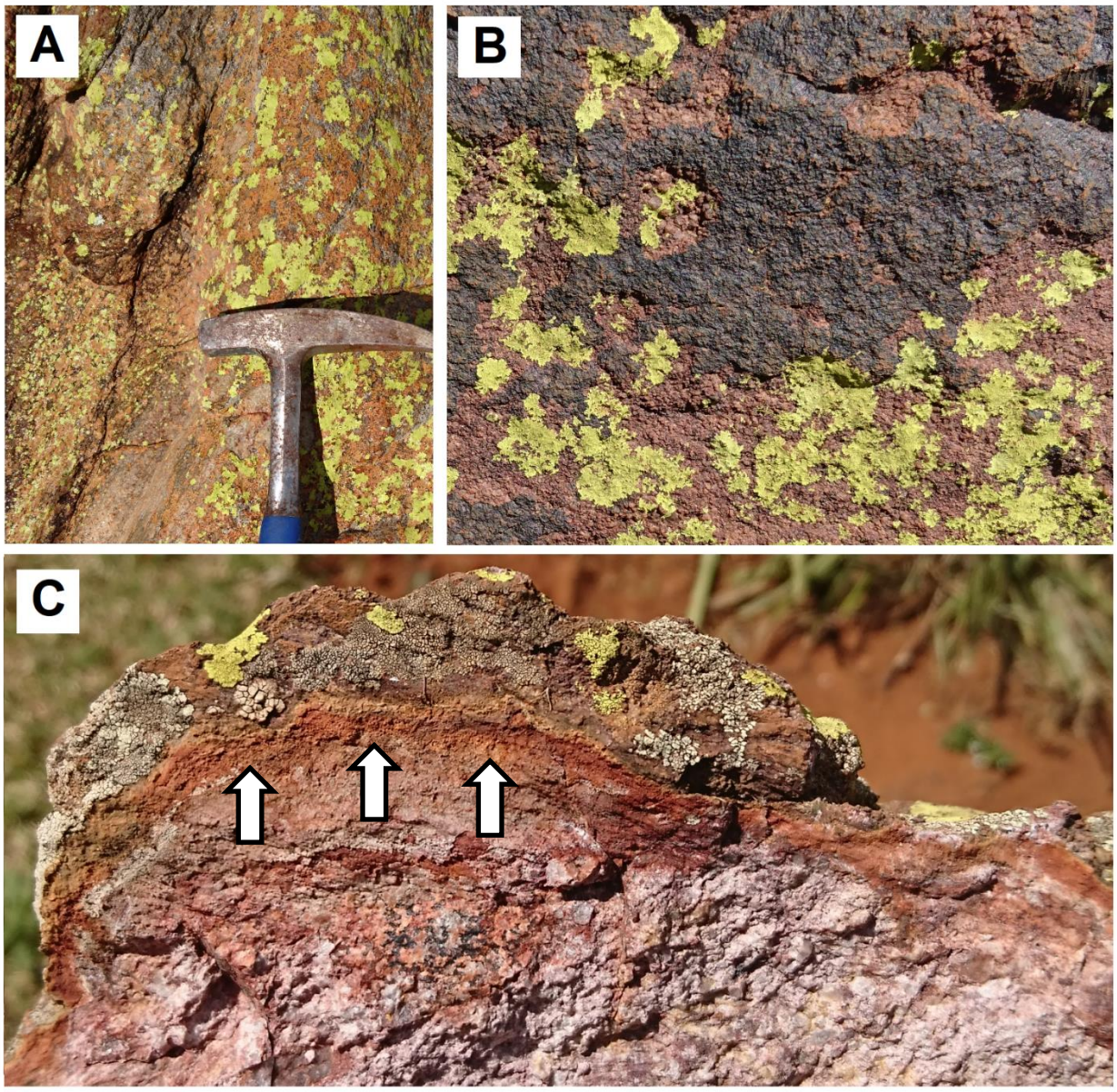


Figure 23: **Lichens encrusting ferruginous quartzite in sampling unit D. (A) Rock surface completely covered with two dominant lichens, namely *Acarospora* sp.pl. (green colored lichen assemblages) and *Caloplaca* s. lat. sp.pl. (orange-colored lichen assemblages). (B). Rock surface displaying secondary coatings of Fe derivatives. Note the knotty appearance on the rock surface (C) A typical sample of moderately mature ferruginous quartzite displaying an orange-brown crust due to surface oxidation (white arrows). (Photographs by Smit, 2019).**

5.2.5 Metaconglomerate of the upper Witwatersrand Supergroup (Unit E)

Sampling unit E is also situated on the farm Rooderand 510 and consists of interbedded conglomerate (i.e. the Rooderand Formation of Els & Mayer, 1992) – the individual thicknesses and frequency of which are highly variable. These conglomerate beds, which disconformably overlie the ferruginous quartzite of unit D, are lenticular and never persist for long distances along

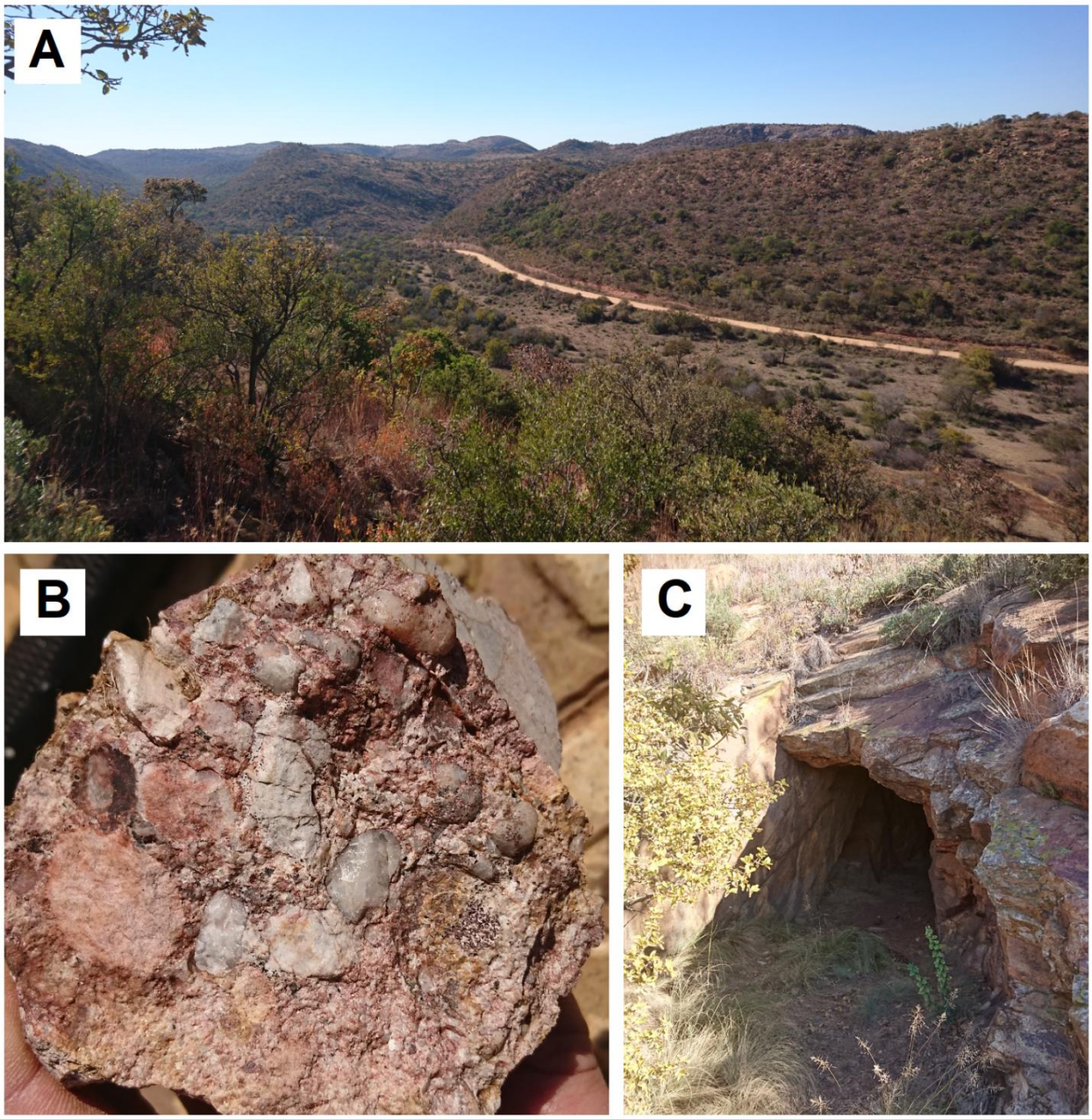


Figure 24: **Pictures of the field relations associated with sampling unit E. (A) Panoramic view looking north-east over the conglomerate bed of the Turffontein Subgroup in the north-western parts of the exposed arc of the Vredefort Structure, Rooderand 510. (B) Sub-angular to subrounded clasts in conglomerate hand specimen, found in the north-eastern portion of Unit E. (C) Photo showing the entrance to a mining adit in the central portion of sampling unit E. (Photographs by Smit, 2019).**

strike. It comprises a succession of arenaceous and rudaceous sediments deposited during a period charactarised by a marked increase in the supply of coarse clastic material to the basin (Bisschoff, 1999). The presence of scattered pebbles (Figure 24B), the lenticular nature of conglomerates, and an estimated high clay-matrix content supports the notion of deposition under fluvial conditions. Numerous small, inclined prospect tunnels (Figure 24C) found along the

outcrop of the conglomerate horizon in unit E, bear witness to the fact that much of the near-surface, oxidised zone of the conglomerate beds was prospected by various companies and individual operators.

The dominant saxicolous lichen assemblage recorded from unit E (Table 8) consisted of *Acarospora* sp.pl. and *Xanthoparmelia* sp.pl., followed by *Caloplaca* s. lat. sp.pl. as the primary co-dominant taxon (refer to Figure 25).



Figure 25: **Lichen genera encrusting metaconglomerate in sampling unit E. Rock surface covered with three lichen genera, including *Buellia* sp. (gray to white-colored crustose lichen assembladges), *Caloplaca* s. lat. sp.pl. (orange-colored lichen assembladges), and *Acarospora* sp.pl. (green colored lichen assembladges). (Photograph by Smit, 2019).**

5.3 MINERAL CONTENT VARIATION

The mineral percentages determined by means of point counts were used in order to classify the rocks on the International Union of Geological Sciences (IUGS) classification diagram (Figure 26). Accessory minerals that occur below 2 vol. % was confirmed petrographically (section 5.4) and were not detected by the percentage analysis. This factor relates to a small degree of error when the mineralogical composition is recalculated to mode percentages based on volume (Appendix D1). Nevertheless, due to their low concentration in substrate (<2 vol. %), this error was permissibly small.

Samples were classified according to the classification schemes and recommendations set forth by the IUGS Subcommission on the Systematics of Igneous Rocks (Le Maitre, 2002) and the reconstructive approach to the classification of Witwatersrand metasedimentary rocks (Law *et al*., 1990). In order to retain nomenclatural unity within the Vredefort Dome, samples were classified as metamorphic only when the secondary mineral phases are extensively predominant over primary ones.

The classification of samples in the following discussion will be dealt with according to their established relative age and field relationships. Granitic samples from the Archaean basement complex and the Schurwedraai alkali pluton are classed first, followed by the samples of the Witwatersrand metasedimentary rocks. The latter samples were compiled into a felsic series and siliciclastic series and will be named based on the primary minerals normalised weight percentages (Tables 11 & Appendix D1).

5.3.1 Granitic series

Rocks of the felsic series comprise primarily of plagioclase (~40 to 45 vol. %), K-feldspar (~22 to 38 vol. %), quartz (~22 to 28 vol. %) which dominates over small quantities of biotite (~4 to 6 vol. %) or Fe-hornblende (~8 to 9 vol. %). Minor to accessory minerals include Ilmenite, apatite, muscovite, zircon and chlorite.

Samples VKA1 and VKA2, which was taken near the north-western portion of the Archaean basement complex, contains a greater amount of quartz (~26 to 28 vol. %) and K-feldspar (~35 to 36 vol. %) with subordinate biotite (~35 to 36 vol. %) and Ilmenite, apatite and zircon are minor constituents. Samples VKC1 and VKC2, which was taken along the Schurwedraai alkali pluton (Figure 3), where the highly weathered outcrops of felsic rocks were encountered (Figure 16), contained a lower amount of quartz (~22 to 24 vol. %) and microcline (~22 to 24 vol. %). Muscovite and clinochlore, however, were scarcely observable.

Samples were classified based on their felsic mineral content (Table 11), applying the QAP scheme as illustrated in Figure 26. In contrast with the recommendations of the IUGS (Le Maitre, 2002), the albite endmember (An_{0-5}) of the plagioclase series was normalised together with microcline as part of the the alkali feldspar component (A). This decision was made to synchronise the classification methods applied by previous authors including Bisschoff (1969, 1999) and Elsenbroek (1991), as referenced by de Waal *et al*. (2008) and Graham *et al*. (2005). Samples VKA1-2 and VKC1-2 were therefore respectively classified as K-feldspar rich granite and alkali granite.

Table 11: Normalised modal compositions (vol. %) of granitic rock samples.

Sample	Quartz	K + Na-feldspar	Plagioclase feldspar
VKA1	26	$36_{(An<5)}$	$38_{(An>5)}$
VKA2	28	$35_{(An<5)}$	$37_{(An>5)}$
VKC1	24	$76_{(An<5)}$	$0_{(An>5)}$
VKC2	22	$78_{(An<5)}$	$0_{(An>5)}$

(An<5) = Microcline + Albite; (An>5) oligoclase to andesine

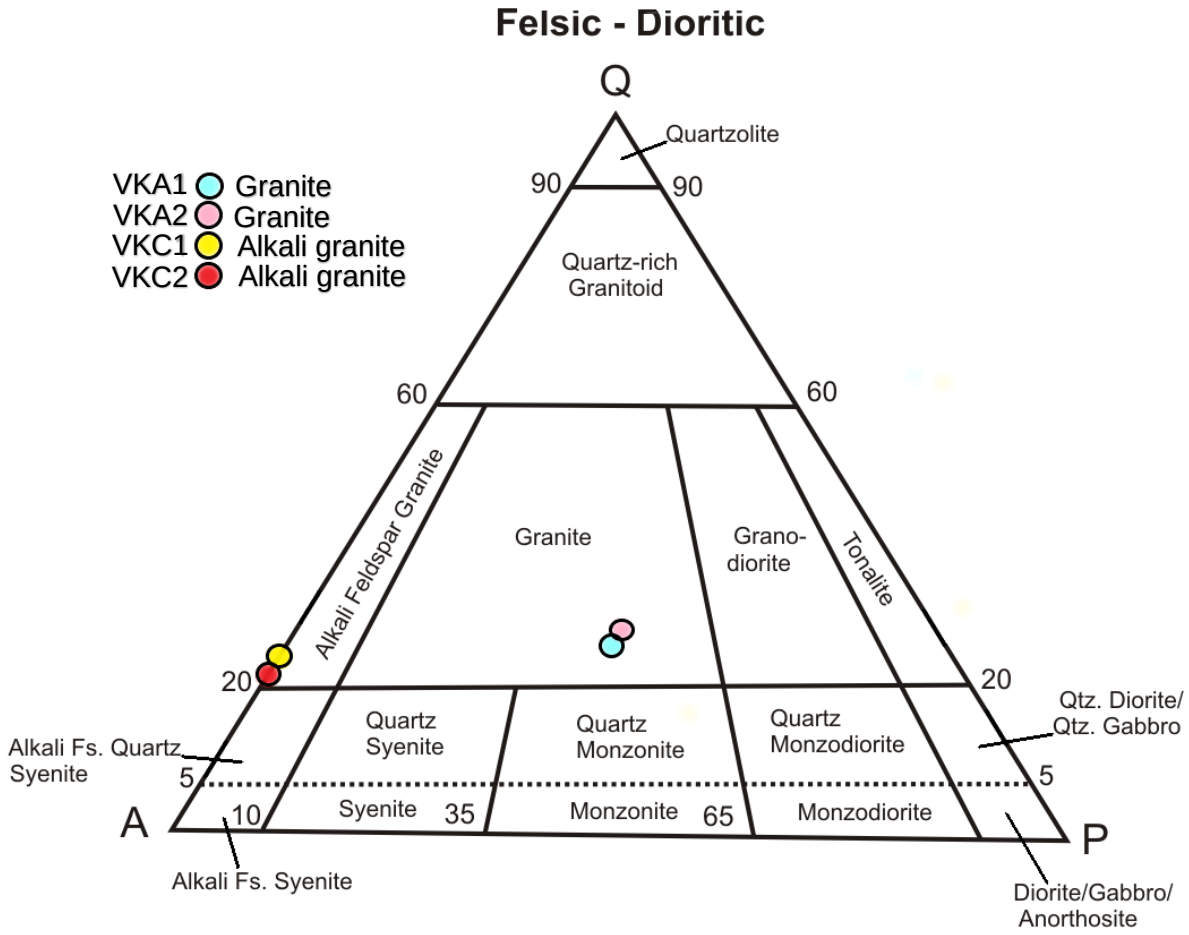


Figure 26: QAP modal classification of plutonic rocks. Adapted from Le Maitre (2002; Figure 2.4), after Streckeisen (1976; Figure 1a). Q=quartz, A= alkali feldspar, P = plagioclase. Alkali Fs = alkali feldspar; Qtz = quartz.

5.3.2 Siliciclastic series

Standard classifications of unaltered sedimentary rocks are not applicable to Witwatersrand metasedimentary rocks (we refer here to Witwatersrand 'quartzites', metaconglomerate and

metapelites) because of pervasive fluid alteration related to diagenesis and metamorphism of the original detrital assemblage (Kamo *et al*., 1996; Bisschoff, 1999; Gibson & Reimold, 1999). Although regional metamorphism and pervasive alteration have converted all the original sedimentary rocks of the Witwatersrand Basin into slates, schists, quartzites and metaconglomerates, the textures, sedimentary structures and bulk rock composition still allow the original nature of most of the metasediments to be determined (Law *et al*., 1990).

Law *et al*. (1990) proposed a reconstructive approach to the classification of Witwatersrand 'quartzites' and other sedimentary sequences with secondary, diagenetic or metamorphic, mineral assemblages. The proposed scheme differs from classification schemes for unaltered sedimentary rocks in that it recognizes post-depositional alteration and metamorphism of the original detrital assemblage. Following the classification scheme of Law *et al*. (1990), Witwatersrand 'quartzites' have been subdivided into 'arenites' and 'wackes' based on original matrix, stratification, and sorting (Table 12).

Within the 'wacke' and 'arenite' fields further subdivisions are defined based on quartz content. Sediments with an excess of 95% quartz are classified as quartz arenites irrespective of the initial composition of the matrix material. Furthermore, within the 'arenite' field, sub-labile arenites contain in excess of 75% quartz, whereas labile arenites contain less than 75% quartz. 'Labile' fields are further subdivided into 'feldspathic' or 'lithic' arenites based on the dominant labile component. An excess of feldspathic over lithic fragments thus defines the field of 'feldspathic' arenites while an excess of lithic over feldspathic fragments is indicative of the field of 'lithic' arenites. Within the 'wacke' field, quartz wackes contain less than 85% quartz and less than 5% feldspathic and/or lithic fragments. The field of labile wackes is subdivided into 'feldspathic' and 'lithic' fields according to the dominant labile component.

Sample VKB1 and VKB2, which was taken from the northwestern sector of the collar were the Vaal River enters the dome from Parys along a major fault in the rocks (refer to figure 15) tentatively classified as quartzite (synonymous with Hospital Hill quartzite of Bisschoff, 1969), and display the typical characteristics as specified to confirm this deduction. The samples are generally silica-rich in composition, comprising primarily quartz (~82 to 83 vol. %) in a deformed matrix (~17 to 18 vol. %). Other accessory minerals include iron-oxide and rutile. Based on their well-sorted sediments, fine-grained recrystallized texture, and corresponding high silica content (> 75 wt. % quartz), samples VKB1 and VKB2 are verified as sub-labile arenites.

Samples VKD1 and VKD2, which was taken from the north-western sector of the collar on the farm Rooderand 510, tentatively classified as ferruginous quartzite, display the typical

characteristics as specified to confirm this deduction. The samples often exibits scattered pebbles and are generally iron-rich in composition, although quite variable, comprising primarily of quartz (~71 to 73 vol. %) in a deformed matrix (~27 to 29 vol. %) of muscovite and iron oxide. Other accessory minerals include rutile and monazite. Based on their moderately sorted sediments, altered minerology, and corresponding high iron content, the samples VKD1 and VKD2 are verified as ferruginous wacke.

Samples VKE1 and VKE2, which was also taken from the north-western sector of the collar on the farm Rooderand 510 and tentatively classified as metaconglomerate. These samples display the typical characteristics as specified to confirm this deduction and comprise a substantial fraction of rounded to subangular gravel-size clasts (~72 to 74 vol. %), most often quartz or quartzite clasts, in a deformed matrix (~16 to 18 vol. %). Other accessory minerals include rutile and zircon. Based on their poorly sorted sediments and corresponding high rounded to subangular gravel-size clasts content, the samples VKE1 and VKE2 are verified as metaconglomerate.

Table 12: Characteristics for the separation of primary 'wackes' and 'arenites'

Wacke	Arenite
1) > 15% matrix required but not diagnostic	1) <15% original matrix required
2) massive (no evidence of stratification)	2) stratified or cross-stratified (deposition by traction currents)
3) sorting of quartz grains and clasts extremely poor	3) moderately to well sorted

5.4 PETROLOGY

Petrographical descriptions of selected thin sections (Appendix C1) will be discussed in accordance with the relative age and name specified in section 5.3. Thin sections of 10 samples were made and studied under a petrographic microscope (see Appendix B1). The mineral abbreviations used in the supplementary photomicrographs are explained on page vii.

5.4.1 K-feldspar rich granite

K-feldspar rich granite (Figure 30) represents a feairly homogeneous coarse- to medium-grained hypidiomorphic-granular rock composed of plagioclase, K-feldspar, quartz and biotite. Chlorite, Ilmenite, apatite, and zircon were identified as minor or accessory minerals (Appendix E1).

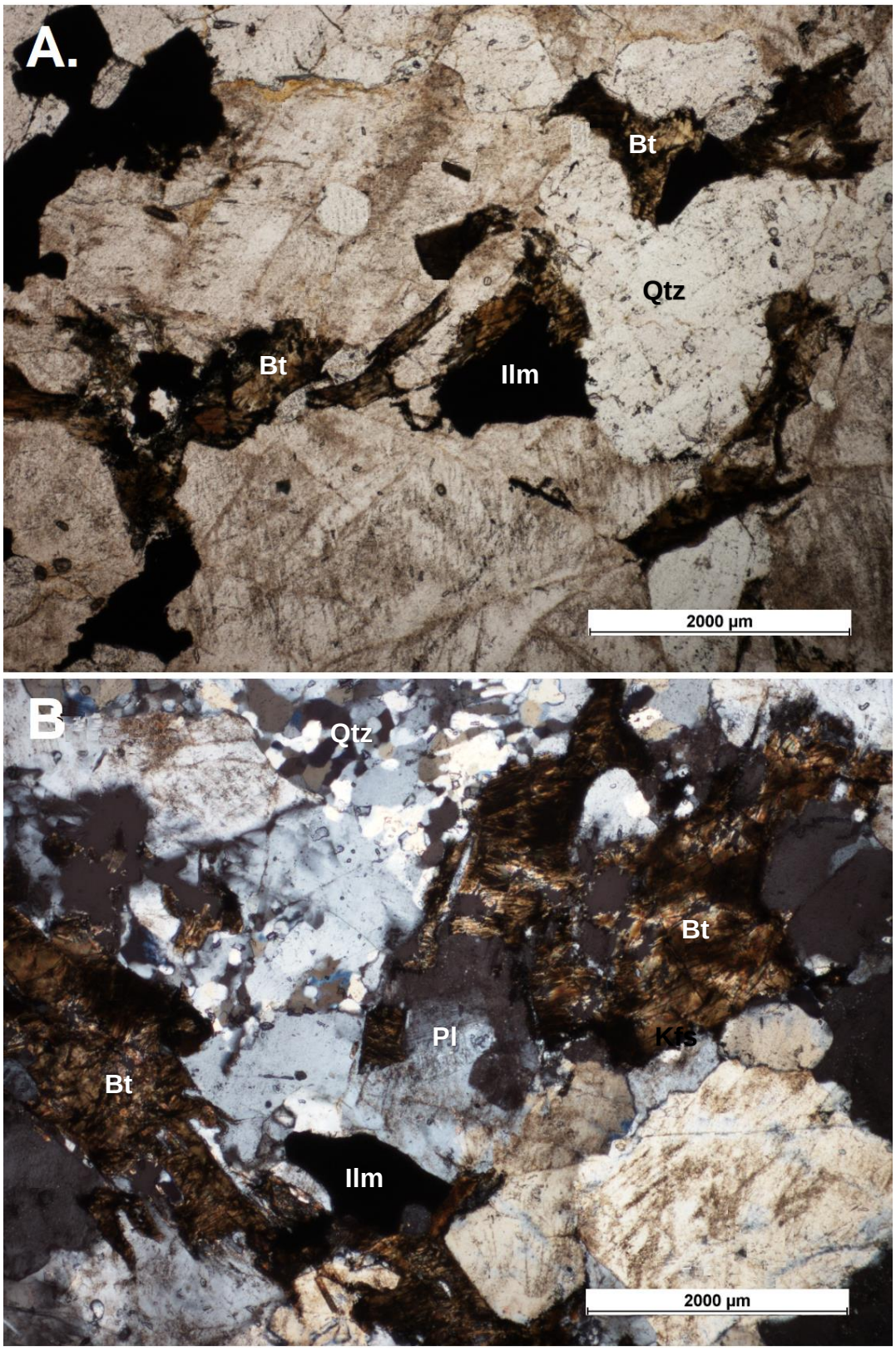


Figure 27: **Photomicrographs of K-feldspar rich granite (sample VKA1): (A) Photomicrograph displaying a massive hypidiomorphic granular texture. Note the alteration of feldspar grains to fine-grained sericite. PPL. (B) Photomicrograph illustrating the first to second order interference colours. Note quartz grains with strongly mottled extinction patterns (mosaicism) and undulose extinction. XPL. Pl=plagioclase, Kfs=K-feldspar, Qtz=quartz, Bt=Biotite, Ilm=ilmenite.**

The feldspar of these rocks ranges from plagioclase through to K-feldspar. Plagioclase is the most prominent mineral and occurs as large anhedral to subhedral grains (1000 to 6000 µm) which display a darker first order grey interference colour (Figure 27B). K-feldspar grains have a larger grain size (2000 to 8000 µm) than the plagioclase feldspar and is generally more euhedral and irregularly shaped. K-feldspar displays a light first order grey interference colour. The feldspar grains are easily distinguished from quartz because feldspars are cloudier due to incipient alteration to fine-grained minerals (Figure 27A).

Quartz occurs mostly as subhedral- to anhedral grains (100 to 4000 µm), which seldom display fracturing. Quartz is typically the clearest mineral in the granite because it is not very susceptible to alteration to fine-grained minerals. Undulose extinction are regularly seen in quartz grains, which is the result of “recovery” - it involves the organization of dislocations (line defects) into regular arrays (subgrain boundaries), forming subgrains in deformed crystals (Vernon, 2019). Mosaicism (Figure 27B) is also a common feature found in quartz. “Mosaicism respresents a typical shock effect that display a strongly irregular extinction pattern (mottled extinction pattern) originating from the formation of differently orientated blocks within the crystal structure” (Winter, 2010). Fluid inclusions could also be identified in quartz grains, but not as frequently.

The biotite shows pleochroism (light brown to dark brown) and has a grain shape ranging from subhedral to euhedral (500 to 4000 µm) with a platy habit. Biotite does also show kink bands in several of the samples. Ilmenite seems to occur interstitially between biotite and feldspar grains. These ilmenite grains have subhedral to euhedral grain shapes (500 to 4000 µm).

5.4.2 Sub-labile arenite

The sub-labile arenite of sampling unit B represents a fine-grained rock of granoblastic polygonal texture consisting primarily of detrital quartz grains oriented within a deformed matrix; matrix includes fine-grained intergrowths of micas and quartz in addition to other phases which cannot be identified as having granular precursors, such as secondary clays (Figure 28). Iron-oxide, chlorite and rutile were identified as minor or accessory minerals (see SEM-EDS data in Appendix E2).

The quartz mostly shows equant to rounded grain shapes (100 to 1000 µm) which commonly display microcracks. Quartz grains also seem highly deformed with evidence of undulose extinction and fluid inclusions. There is complete contact between grains, and sutured boundaries are well developed obscuring the original grain shapes. Pressure solution is also evident (Figure

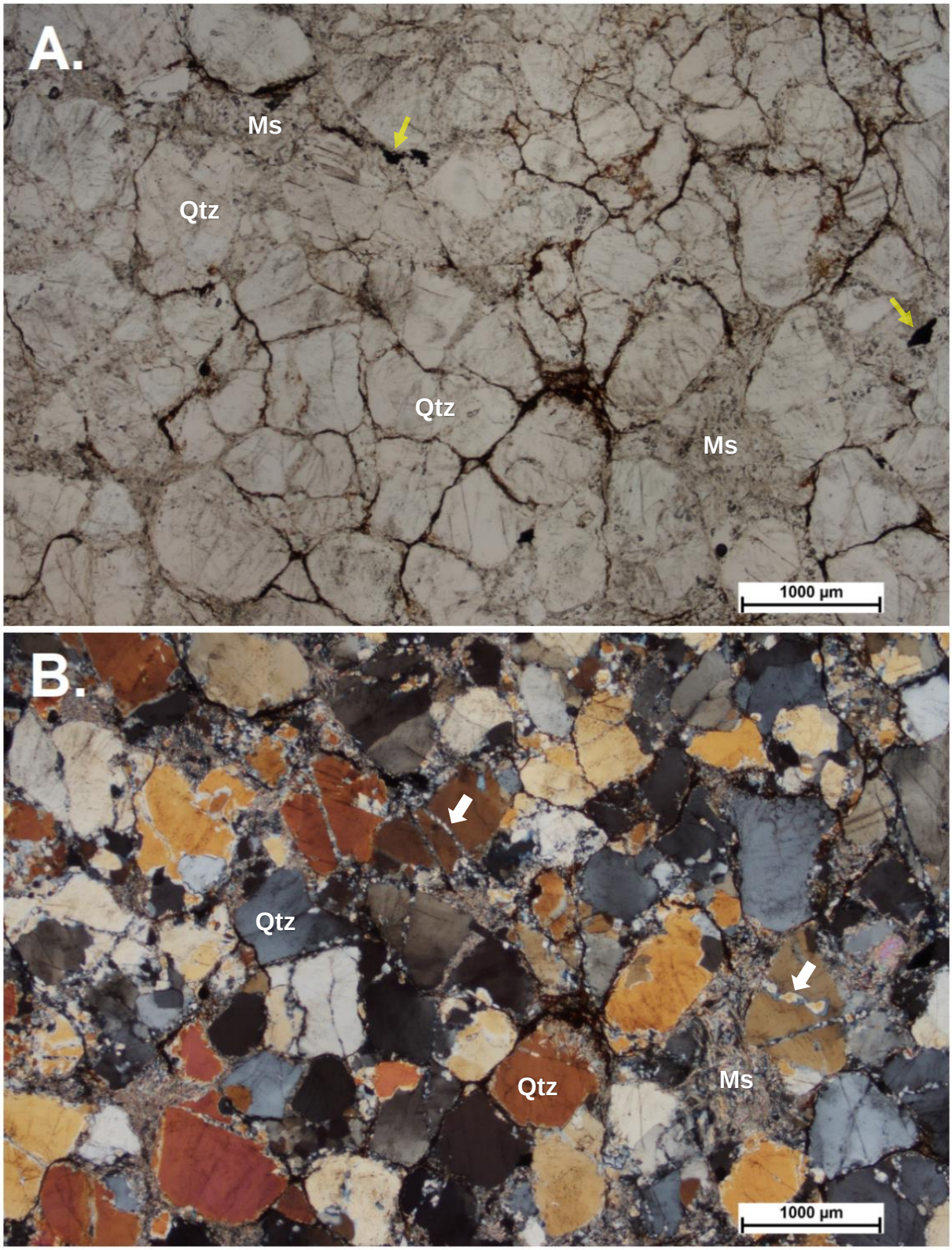


Figure 28: **Photomicrographs of sub-labile arenite (sample VKB1) under (A) PPL, displaying a fine-grained granoblastic polygonal texture that consists primarily of detrital quartz grains and a matrix of muscovite, and (B) the same plate under XPL, illustrating the first to second order interference colours. Note quartz displaying microcracks, undulose extinction and extensive recrystallization (white arrows). Yellow arrows are indicative of iron oxide along grain boundaries. Qtz=quartz, Ms=muscovite.**

29) – a process that requires intergranular fluid to be effective. Grain contacts at a high angle to σ_1 (the shortening direction) become highly strained and have higher energy. Acording to Winter (2010), the material at these contacts dissolves more readily as a result of the higher energy and produces higher concentrations of dissolved species at these locations which, in turn, sets up an activity gradient so that dissolved species migrate from high activity to low activity places (which are also low strain places) where the material precipitates.

Quartz grains also show evidence of recrystallization - a process that involves the movement of grain boundaries or the development of new boundaries, both of which produce a different configuration of grains (with high-angle orientation differences from neighbors), not subgrains. For a more detailed explanation, see the summaries of metamorphic textures and deformation mechanisms by Passchier & Trouw (2005) and Vernon (2019).

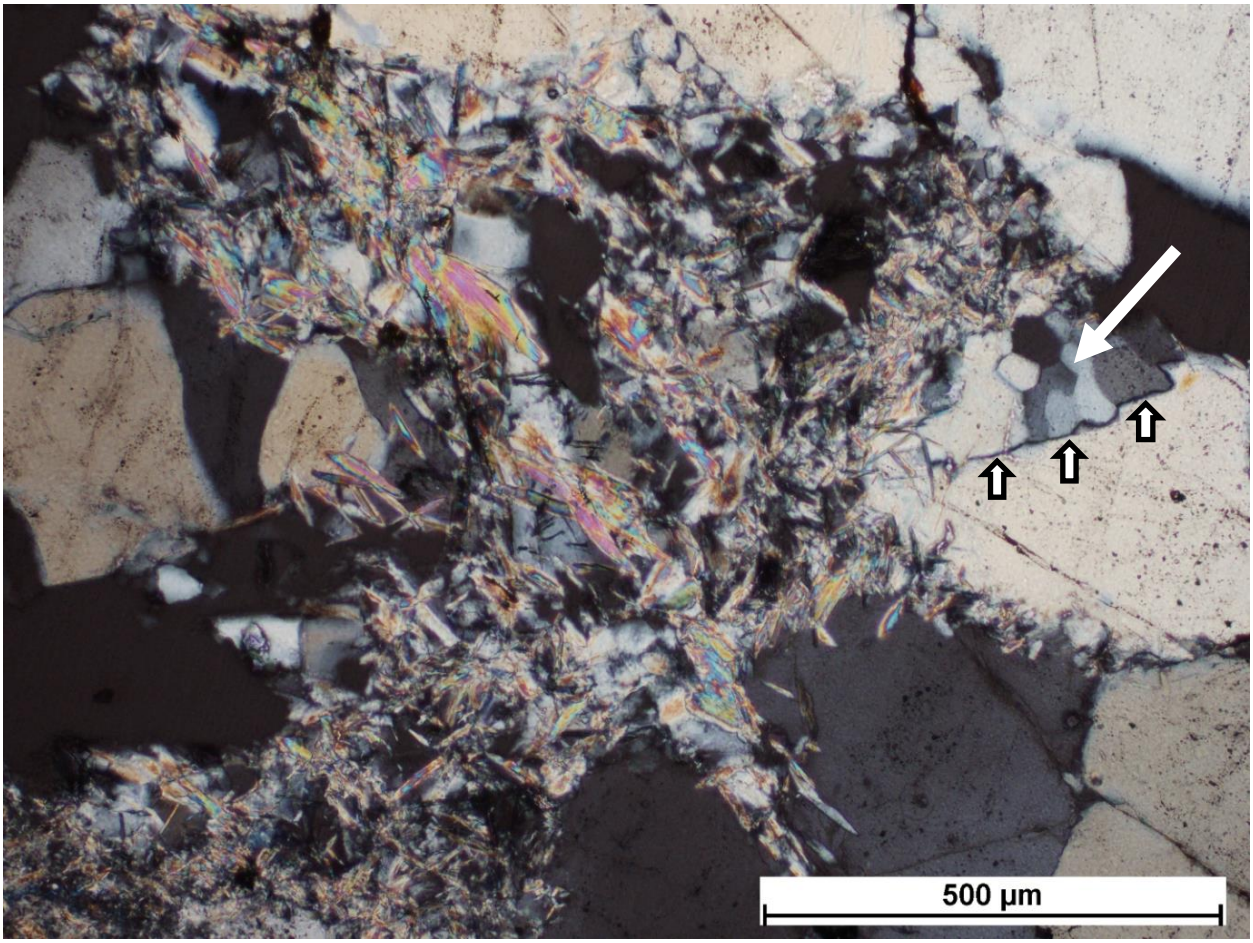


Figure 29: **Acicular, spiky and fern-like crystallites of muscovite replacing quartz in sub-labile arenite. Notice evidence of pressure solution at quartz grain contacts. Pressure solution results in a serrated solution surface in high-strain areas (small arrows) and precipitate in low strain areas (large arrow).**

Muscovite occurs mostly as patches of fine (10 to 500 µm) acicular (needle-like) grains within the interstitial spaces between the quartz. Muscovite shows middle third order interference colours (Figure 30B) and a perfect basal cleavage. Muscovite also shows a change in colour during weathering, resulting in brown, yellow colours toward the edges while the centre remains unchanged (Figure 30A). This phenomenon also results in a decrease in birefringence, resulting in grey, yellow interference colours toward the edges.

Furthermore, clear interlocking aggregates of quartz grains sometimes contain patches of green "nests" of mica in which there are one or two grains of chromite. This gives the rock a characteristic green tint in certain areas - the intensity of the green colour of the mica increases as the amount of associated chromite becomes greater (Frankel, 1939).

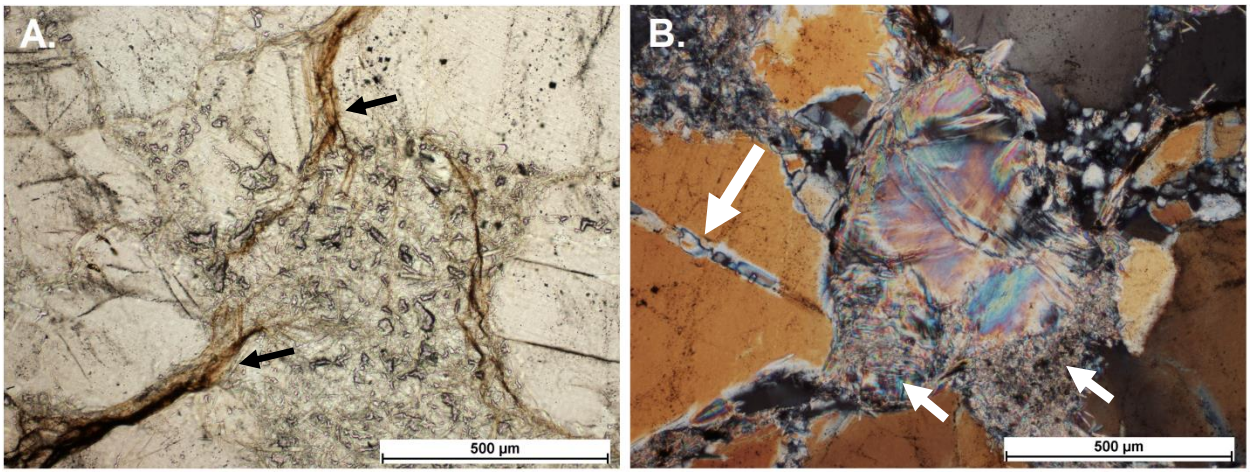


Figure 30: **Photomicrographs of muscovite in sub-labile arenite (sample VKB1). (A) Photomicrograph illustrating a patch of muscovite crystallites within the interstitial spaces between the quartz. Note how muscovite becomes yellowish-brown (black arrows) toward the edges due to weathering. PPL. Magnified 50 x. (B) Grain of muscovite that has been partly neocrystallized to much smaller new grains of mica with crystal faces (small white arrows). Note the quartz grain transected by a band of new grains (large white arrow) formed by bulging (BLG)-recrystallisation. XPL. Magnified 50 x.**

5.4.3 Alkali granite

Alkali granite represents a heterogeneous medium- to fine-grained hypidiomophic-granular rock composed primarily of quartz, albite, K-feldspar, Fe-hornblende (aegirine/arfvedsonite) which dominates over small quantities of Fe-rich biotite to Mg-rich lepidomelane (Figure 33). Small irregular patches of chlorite, apatite, magnetite, ilmenite and zircon could also be identified but not as frequently.

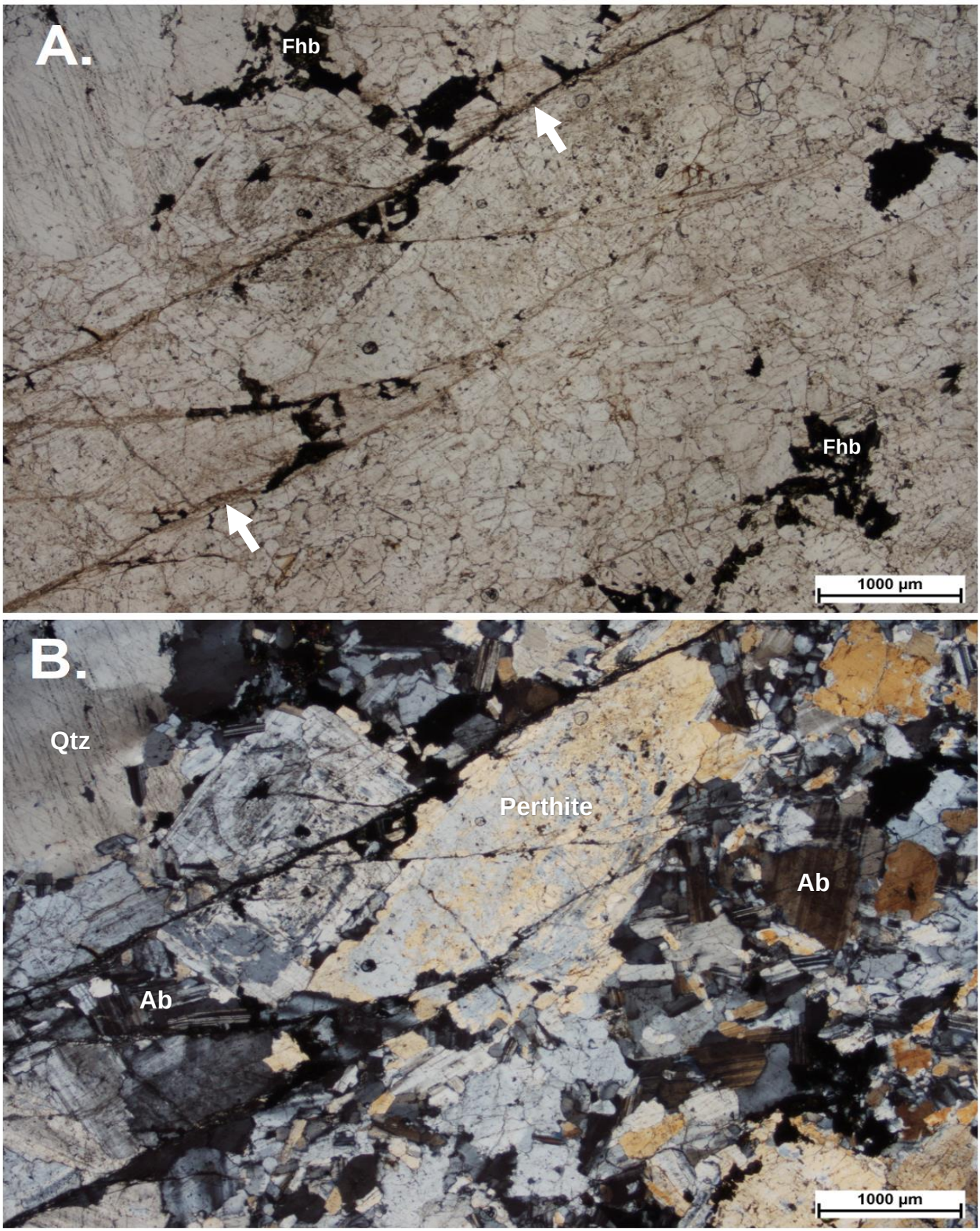


Figure 31: **Photomicrographs of alkali granite (sample VKC2) under (A) PPL, displaying a medium- to fine-grained hypidiomorphic-granular texture, which is composed primarily of albite, K-feldspar, quartz and Fe-hornblende. The white arrows point to melt veins. (B) The same plate under XPL, illustrating the first to second order interference colours. Note the undulose extinction and PDF in quartz grains (top left corner). Ab=albite, Qtz=quartz, Fhb=Fe-hornblende.**

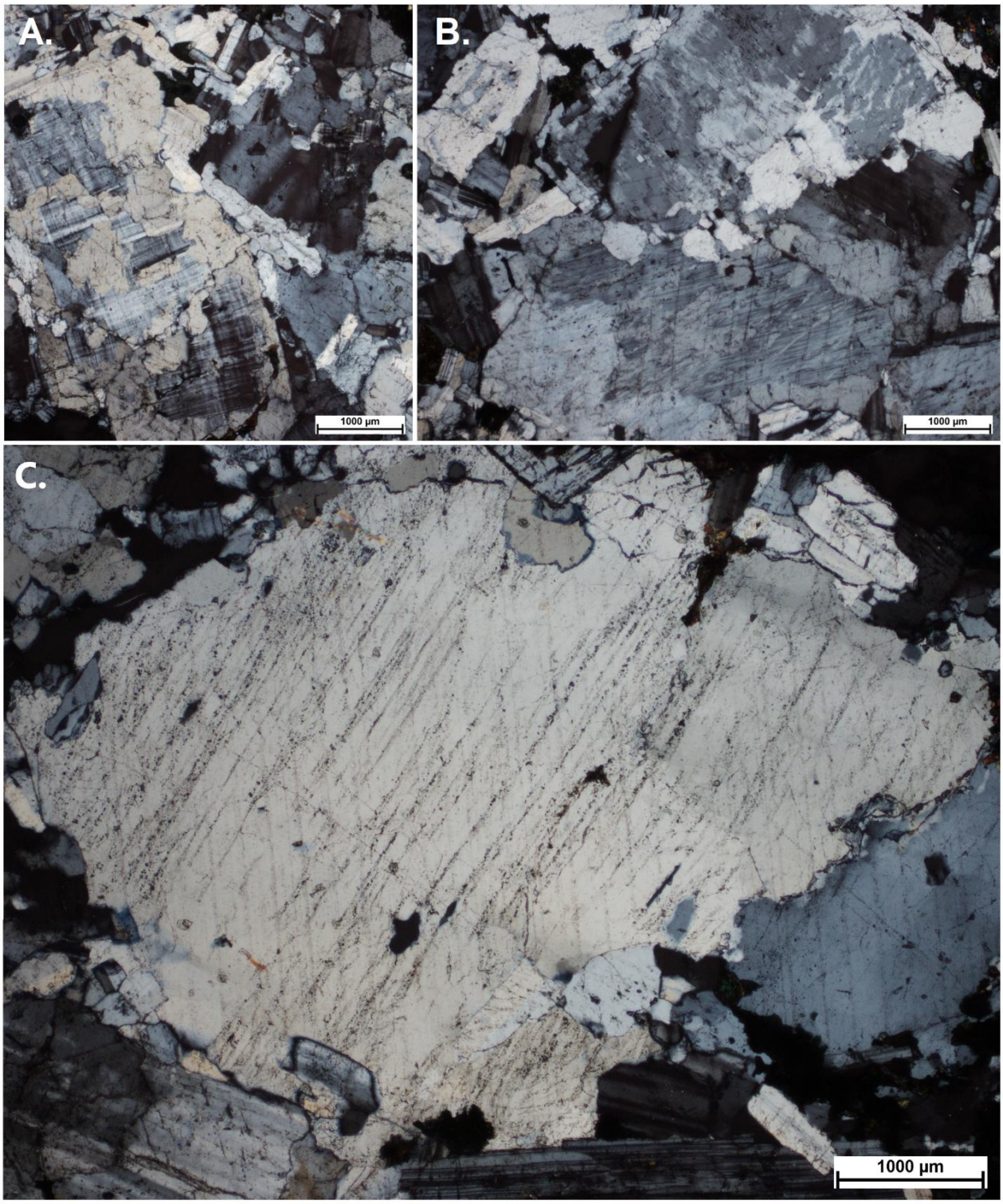


Figure 32: **Photomicrographs of the microtextures associated with alkali granite viewed under crossed polarized light (XPL). (A) Photomicrograph displaying microcline perthite. Note the well-developed tartan twinning in microcline exsolved (unmixed) from the homogeneous solid solution during cooling. (B) Photomicrograph of perthite. Note the lenticular exsolution lamellae of albite (dark grey) on K-feldspar (light grey). (C) Photomicrograph of quartz showing multiple sets of recrystallised PDFs within quartz, expressed by arrays of small fluid inclusions (black dots). Magnified 10 x.**

The feldspar of these rocks ranges from albite and microcline, which is free from exsolved lamallae, through perthite to microcline perthite. These crystals are frequently weakly zoned. Albite is the most prominent feldspar and occurs as anhedral to subhedral grains (500 to 2000 µm), which are mostly tabular. K-feldspar grains have a larger grain size (1000 to 4000 µm) than the plagioclase feldspar and is generally more euhedral and irregularly shaped.

The amount of perthite seems to exeed antiperthite by far. The perthite has a larger grain size (1000 to 5000 µm) than the albite and is generally more euhedral and irregularly shaped, with grain boundaries that appear serrated and often altered to fine minerals. A lighter first order yellow to light gray interference is shown by the K-feldspar host grains, while albite lamellae can be differentiated by their dark gray interference colour. These long, wispy albite lamellae (Figure 32B) result from chemical mixing involving the separation of K-rich and Na-rich segregations (Winter, 2010). Microcline perthite on the other hand, frequently display cross-hatched patterns (Figure 32A), which comprise of lamellar twins according to albite and pericline laws (Klein & Duttrow, 2008).

Quartz grains are mostly equant to rounded (100 to 300 µm) and seldomly display fracturing. Planar deformation features (PDF's, Figure 32C) are commonly observed in quartz grains – PDF's represent shock produced microstructures whose development correlated with relatively low shock pressures involving only partial and localized deformation of the host crystal (Pickersgill, 2014). PDF's generally occur as multiple sets of closed, extremely narrow (typically <2–3 µm), parallel planar regions where the original PDF planes are replaced by arrays of small fluid inclusions (Figure 31 & 32). These fluid inclusions are produced when the original amorphous material in the planar deformation feature planes is recrystallised back to quartz (Pickersgill, 2014).

Fe-hornblende grains are anhedral to subhedral (100 to 500 µm) and occur mainly within the interstitial spaces between the albite, microcline and quartz. In particular, aegerine and ardfedsonite were identified according to their optical properties. Their pleochroism respectively is as follows: X = lavender blue, Y = blue green, Z = greenish grey, or X = blackish blue, Y = light green, Z = yellowish brown. The birefringent colours of aegerine are typically up to middle second order whilst ardfedsonite' are typically up to lower second order (Figure 33C). In some of the aegerine grains, the ~120° and ~60° cleavage intersections are visible (Figure 33B). The Fe-hornblende grains also frequently contain small opaque inclusions of magnetite (Figure 33).

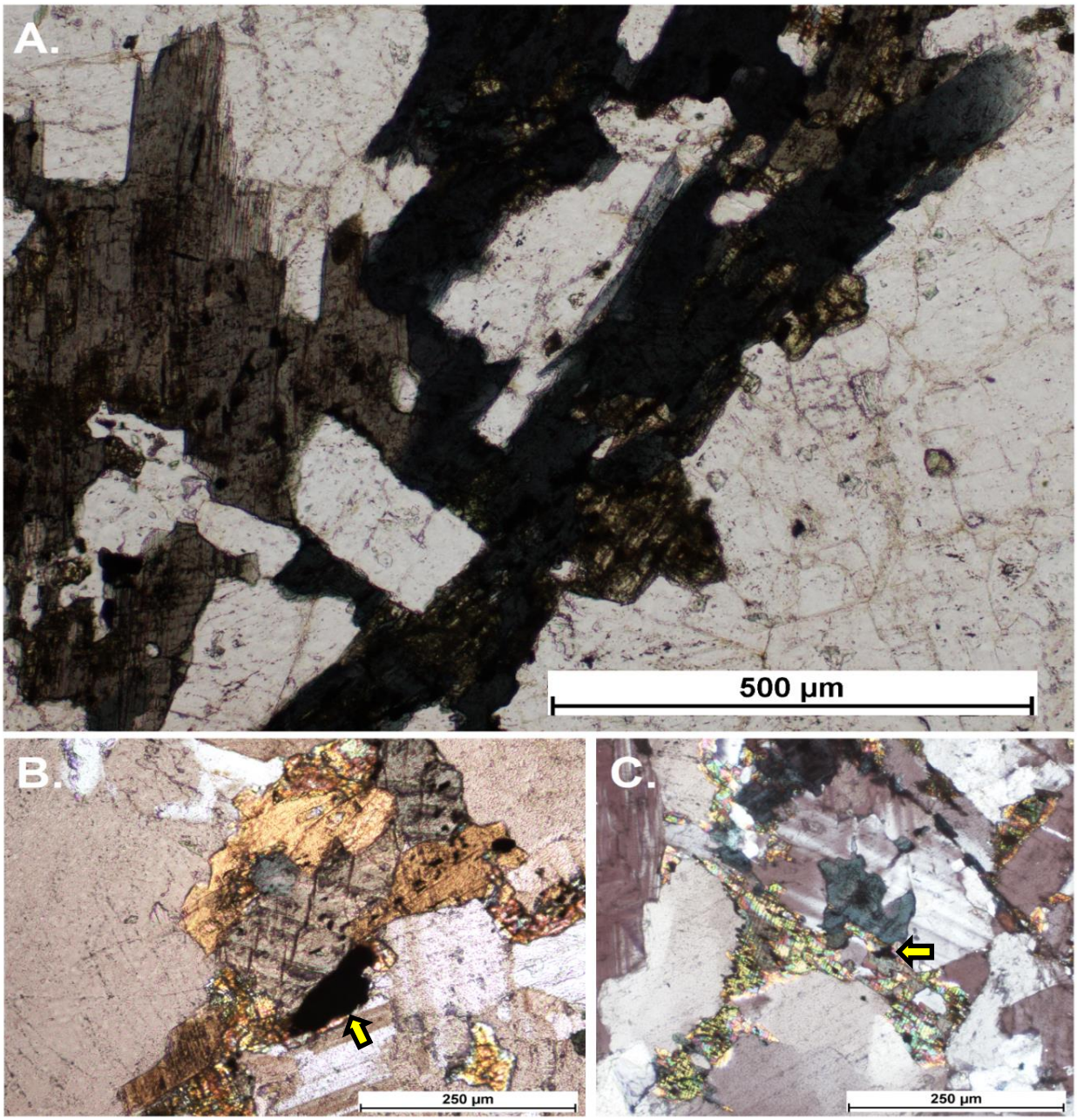


Figure 33: **Photomicrographs of Fe-hornblende in alkali granite under (A) PPL, displaying aegerine (green colour) and ardfedsonite (dark blue-grey colour), and (B,C) XPL, illustrating the first to second order interference colours. Note the difference in birefringent colours of aegerine (middle second order) and ardfedsonite (lower second order). Also note the ~120° and ~60° cleavage intersections in aegerine. Yellow arrows indicate small opaque inclusions of magnetite in Fe-hornblende. Magnified 25 x.**

5.4.4 Ferruginous wacke

Petrologically, the ferruginous wacke bears a passing resemblance to the sub-labile arenite; however, there are several significant differences. The ferruginous wacke has a coarser and more heterogenous, but nonetheless granoblastic texture, in which quartz are oriented within a more

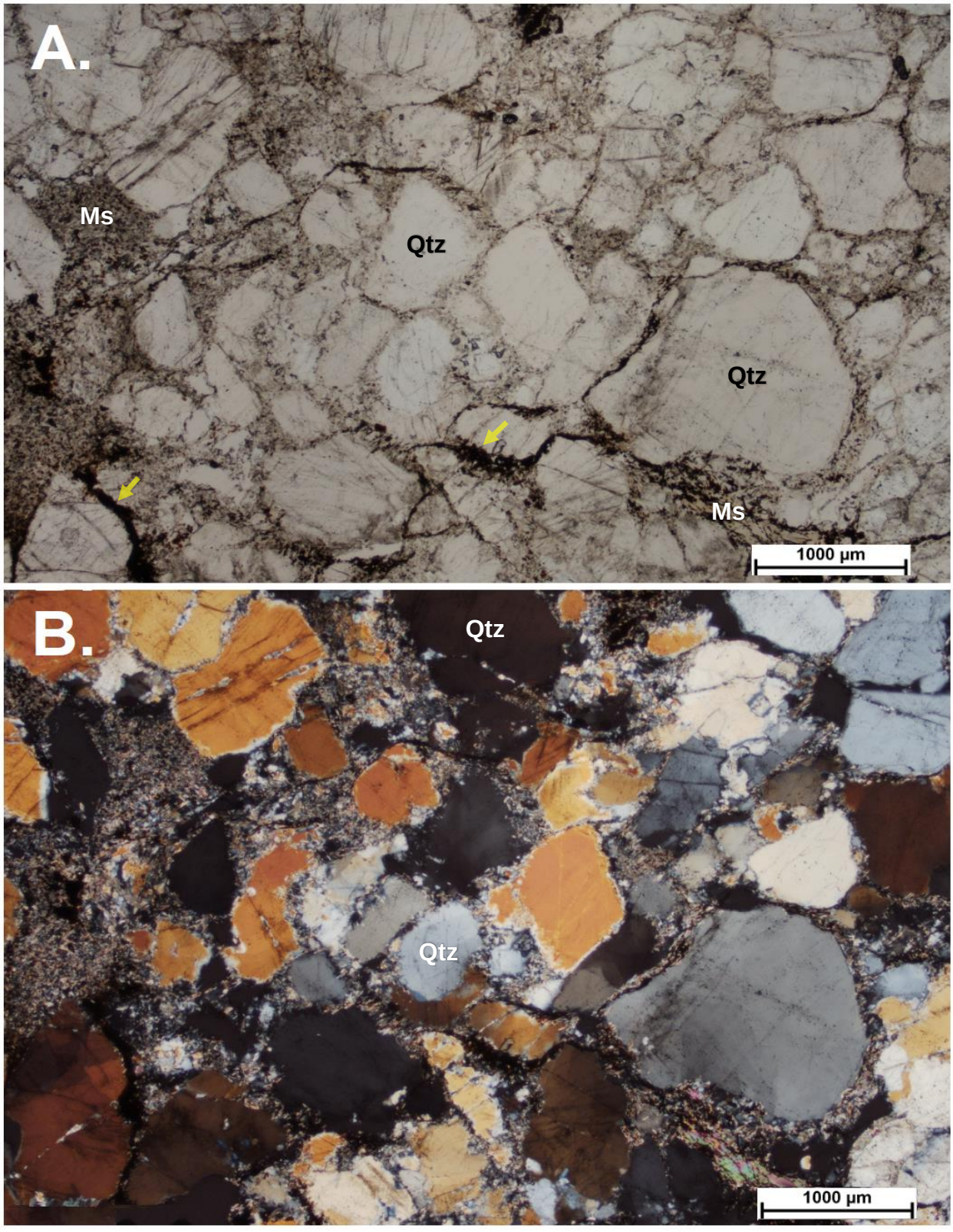


Figure 34: **Photomicrographs of ferruginous wacke (sample VKD1) under (A) PPL, displaying a medium- to course-grained hypidiomorphic-granular texture, which is composed of quartz in a matrix of mica and iron oxide; and (B) the same plate under XPL, illustrating the first to second order interference colours. Note quartz displaying microcracks, undulose extinction and recrystallization features (white arrows). Yellow arrows are indicative of iron oxide in the matrix. Qtz=quartz, Ms=muscovite.**

porous matrix of muscovite and iron oxide (Figure 34). Rutile, chlorite and monazite were identified as accessory minerals (see SEM-EDS data in Appendix D4).

The quartz mostly shows equant to rounded grain shapes (100 to 4000 µm) which commonly display microcracks (Figure 34A). There is complete contact between grains, and sutured boundaries are well developed obscuring the original grain shapes. Quartz grains are highly deformed with evidence of undulose extinction, planar deformation features, fluid inclusions and recrystallization (Figure 35A). Quartz grains also display buldging recrystallization, which is characterized by bulges and small recrystallized grains along grain boundaries and, to some extent, microcracks (Figure 35B).

The matrix of these rocks consists of muscovite and iron oxide. Muscovite is generally the most prominent mineral in the matrix and occurs as fine acicular grains, which shows middle second order interference colours (Figure 34B). Iron oxide occurs as fine acicular grains, especially along grain boundaries (Figure 34A).

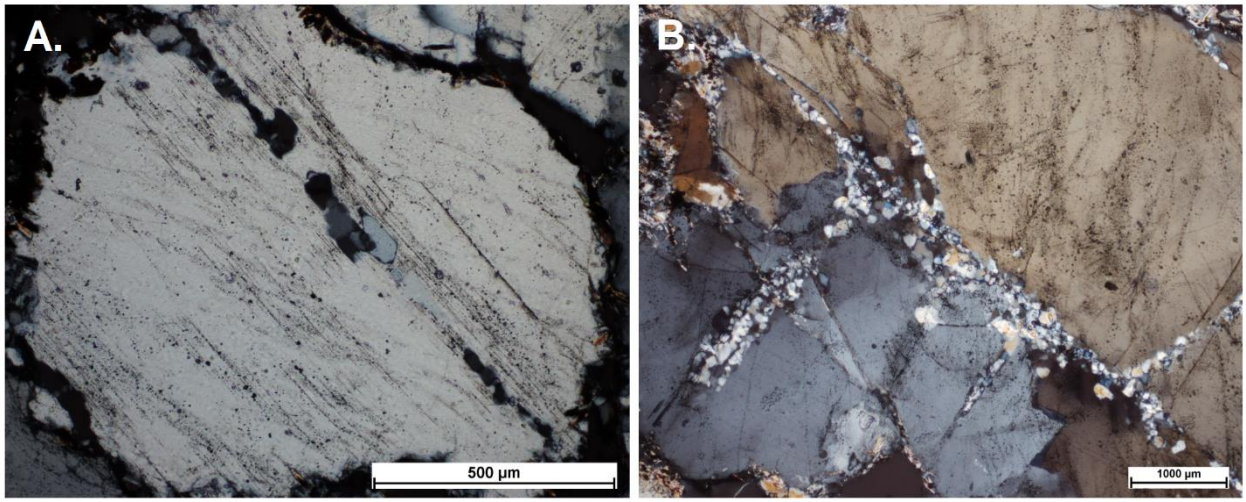


Figure 35: **Micrographs showing quartz grain features in ferruginous wacke artefacts from sampling unit D: (A) Highly deformed quartz displaying PDF's and recrystallisation, especially along the grain boundary. (B) Quartz grain with subgrain boundaries transected by bands of new grains (lower left to top right) formed by bulging (BLG)-recrystallisation. Note bulges along microcracks and grain boundaries.**

5.4.5 Metaconglomerate

The metaconglomerate of sampling unit E represents a poorly sorted coarse- to fine-grained rock which consists primarily of a substantial fraction of rounded to subangular gravel-size clasts in a matrix of finer grained sediments, which fills the interstices between the clasts (Figure 36). SEM-EDS data (Appendix E5) confirmed that most of the pebbles and larger clasts are either quartz or

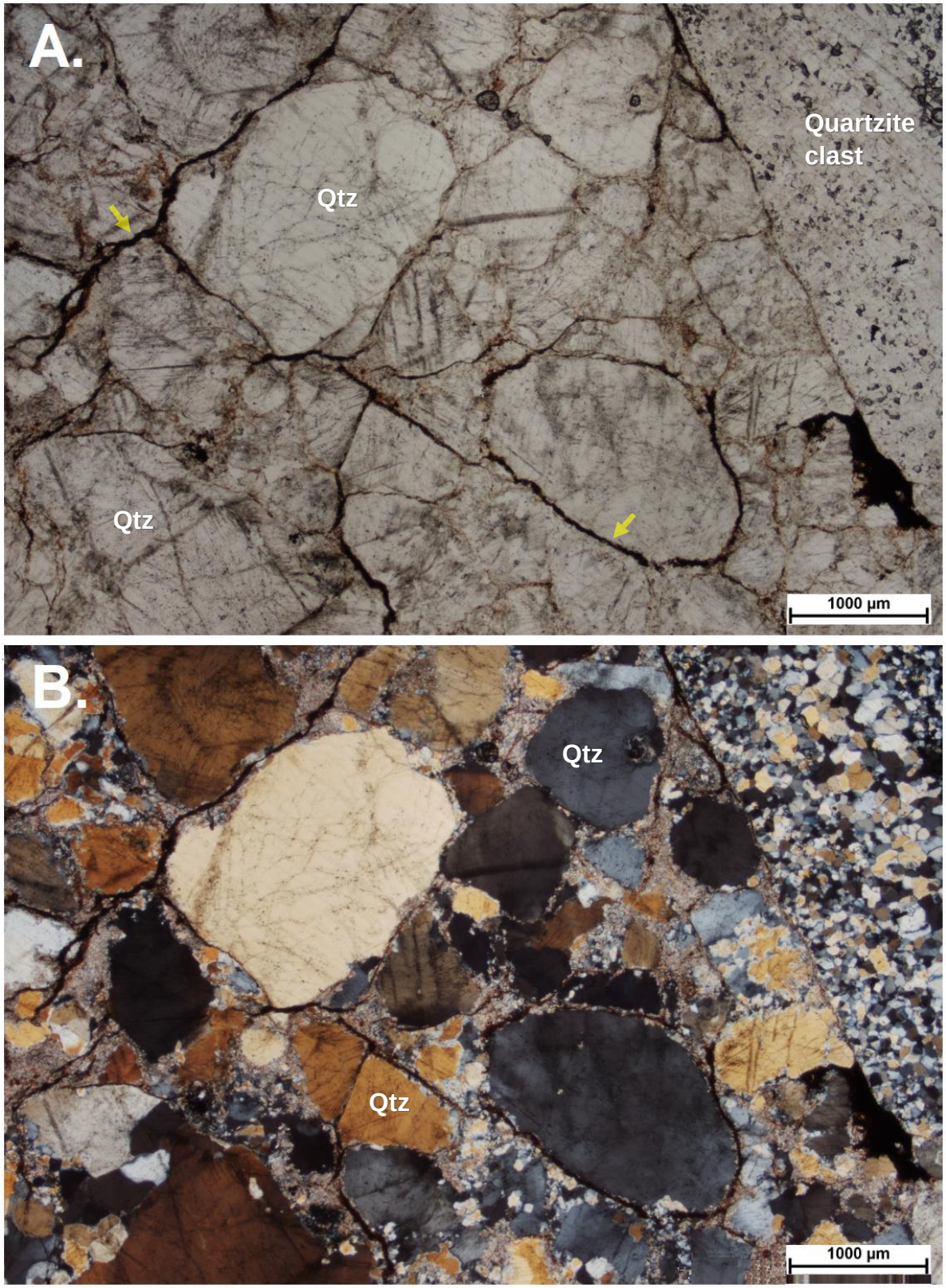


Figure 36: **Photomicrographs of metaconglomerate (sample VKE2) under (A) PPL, displaying a course- to fine-grained rock, which is composed of rounded clasts cemented by very fine grains; and (B) the same plate under XPL, illustrating the first to second order interference colours. Note quartz displaying microcracks, undulose extinction and recrystallization features. Yellow arrows are indicative of iron oxide along grain boundaries. Qtz=quartz.**

quartzite, whilst the fine-grained matrix consists primarily of muscovite and clay minerals. Rutile and zircon were identified as accessory minerals. Due to the variety of mineral phases that constitutes metaconglomerate, it is characterised as the most heterogeneous among the silica-rich rock varieties studied.

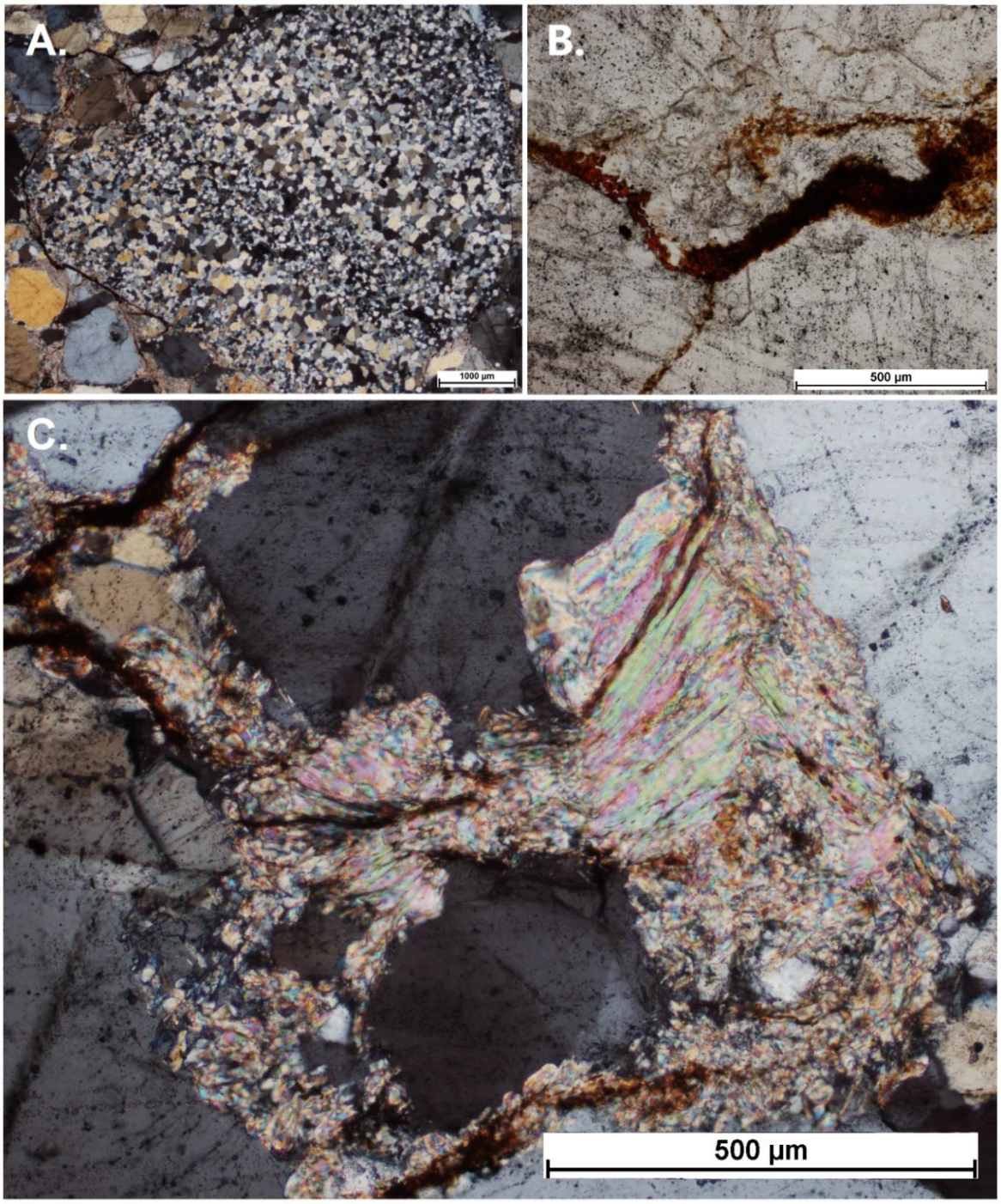


Figure 37: **Photomicrographs of different mineral phases present in metaconglomerate (sample VK5A). (A) Close-up of a quartzite clast. XPL. (B) Close-up of iron oxide. PPL. (C) Muscovite displaying middle second- to third order interference colours and perfect single cleavage. Note the small opaque inclusions of magnetite. Magnified 25 x.**

The quartz and quartzite clasts mostly show equant to rounded grain shapes with sutured boundaries obscuring the original grain shapes. These clasts are commonly deformed with evidence of of undulose extinction, microcracks, fluid inclusions and recrystallization (Figure 36). As mentioned, the matrix consists primarily of muscovite, clay minerals and iron oxide (Figure 37B). Muscovite is generally the most prominent mineral in the matrix and occurs mostly as fine acicular grains, which shows middle second to third order interference colours (Figure 37C). Clay minerals were to fine to be identified. Due to weathering, matrix bearing minerals are regularly altered to iron oxide, especially along grain boundaries (Figure 37B).

5.5 DISCUSSION

The Vredefort Dome is recognized as a prominent feature with a considerable geological record, which produced distinct conditions under which different lichen communities have established themselves. In order to interpret the results of the geological and petrological analysis, the following discussion will aim to describe the effect of the underlying geology on the supported vegetation, as well as petrographic and mineralogical controls. In particular, I aim to determine if the targeted silica-rich rock varieties from a chemically differentiated series can cause measurable changes in the related lichen assemblage. A detailed classification of each lichen species encrusting targeted silica-rich rock varieties and related interpretation of biological controls falls beyond the scope of this study.

5.5.1 Impact of the underlying geology

Whilst the relationship between the distribution of vascular plant communities in the Vredefort Dome and specific geological formations is quite well documented (Table 4), our knowledge on bioweathering, induced by lichens, is rather limited. In correspondence with the topography and geological association, the study area was selectively divided into sampling units representing possible lichen-rock relationships (section 3.2; Figure 17). From the presented results, the following deductions can be made with regards to the geology and general field relations:

The K-feldspar rich granite (Sampling Unit A) comprises of plagioclase, K-feldspar, quartz and biotite, which dominate over accessory amounts of apatite, chlorite, ilmenite and zircon (Appendix D1). Feldspars and biotite provide abundant sources of nutritional elements including Na, K, Mg, Al, Ca, Fe and P, although they are not evenly distributed as a result of fractional crystallisation and subsequent deformation. *Xanthoparmelia* sp.pl. was identified as the dominant taxon

colonising K-feldspar rich granite followed by *Acarospora* sp.pl. as the primary co-dominant taxon. Small irregular patches of *Caloplaca* s. lat. sp.pl. could also be identified but not as frequently.

The exposed sub-labile arenite ridges (Unit B) were primarily composed of detrital quartz grains in a micacious matrix, which dominates over small quantities of iron-oxide, chlorite and rutile. The muscovite and iron oxide provide some source of K, Al and Fe (Appendix D2); however, these amounts are presumed to be less compared to granitic rocks**.** The arenites of unit B contain the least amount of mafic minerals, as well as feldspars, and thus their derived soil products can be expected to illustrate lower nutritive capabilities, since quartz does not contribute any nutritional elements and weathers far less rapidly compared to mafic silicates and feldspars (Boggs, 2010). *Buellia* sp.pl. were identified as the dominant taxon colonising sub-labile arenite followed by *Caloplaca* s. lat. sp.pl. and *Acarospora* sp.pl. as the primary and secondary co-dominant taxa, respectively.

The felsic intrusion of alkali granite (Unit C) is composed primarily of albite, K-feldspar, muscovite, Fe-hornblende which dominates over small quantities of Fe-rich biotite to Mg-rich lepidomelane. Due to the dominance of feldspar, as well as higher amounts of Fe-hornblende, alkali granite are the most concentrated sources of Na, K and Fe (Appendix D3). They also potentially provide a source of Ca and Mg; the latter element also being provided by Mg-rich lepidomelane. Here, *Xanthoparmelia* sp.pl. was the dominant taxon, followed by *Buellia* sp.pl. and *Caloplaca* s. lat. sp.pl. as the primary co-dominant taxa. Small irregular patches of *Acarospora* sp.pl. could also be identified but were not as frequent.

The thin successions of ferruginous wacke (Unit D) and metaconglomerate (Unit E) are positioned furher away from the Vaal River (approx. 2.8km from the Vaal River) at higher alltitudes (±1450m compared to ±1350m) and are primarily composed of detrital quartz grains and/or scattered pebbles in a deformed matrix. The frequency of scattered pebbles increases towards the top where thin lenticular conglomerates and layers of single pebbles are found (Bisschoff, 1999). The matrix contributes minor sources of mica and Fe-oxide**,** which can relate to increased concentrations of Mg, Na, K, Al, Ca, and Fe (see Appendix D4 and D5). Accessory amounts of rutile, zircon and monazite could also be identified.

5.5.2 Mineralogical and petrographic controls

Variance in the dominant rock types and the corresponding mineralogy are shown in Table 13. These chemical variables are expected to cause specific environmental gradients and/or

deficiencies to occur, which clearly influence the distribution and extent of lichen colonization as evident by the species richness associated with different silica-rich rock varieities in the dome (Table 10). In the surveyed plots, foliose lichens (we refer here to *Xanthoparmelia* sp.pl.) were found to be confined to granitic outcrops whilst crustose lichen assemblages (*Acarospora* sp.pl., *Caloplaca* s. lat. sp.pl. and *Buellia* sp.pl.) showed less preference, occupying both granitic- and metasedimentary rock types.

Based on the data obtained, granitic rocks are more felsic and contain abundant feldspars and mica. Feldspars and mica are generally more prone to weathering and they represent repositories of most of the total content of nutrient cations (e.g. Mg, Na, K, Al, Ca, and Fe) which are very slowly released during weathering. Subsequently, the surface of granitic outcrops showed evidence of severe surface erosion. By comparison, the metasedimentary rocks consist primarily of silicate minerals, which show an exceptional high resistance against weathering. Metasedimentary rocks are therefore less prone to weathering, which in turn decreases macronutrient availability – a factor of importance for bioencrustation. Hence, less frequent colonisation by lichen assembladges was noted on metasedimentary rocks. Nevertheless, the presence of muscovite and clay minerals in the rock matrix still provides sufficient concentrations of nutrients to enable lichen colonisation, albeit less frequently.

From the above findings, it is arguable (although it should be demonstrated by surveying more plots, as replicates for each lithology) that petrographic and mineralogical controls play a key role in the development of weathering products, cumulatively propagating their effects to the macro-

Table 13: Petrographic features of the examined lithotypes.

Lithotype	Code	Minerals	Microstructure	Grain size
K-feldspar- rich granite	VKA1	Pl, Kfs, Qtz, Bt	homogeneous, hypidiomophic-granular	up to centimetric
Sub-labile arenite	VKB1	Qtz, Ms	granoblastic-polygonal, matrix-supported, with micasious cement	submillimetric
Alkali granite	VKC2	Pl, Kfs, Qtz, Fhb	heterogeneous, hypidiomophic-granular	up to centimetric
Ferruginous wacke	VKD1	Qtz, Ms, Fe-ox	homoclastic, granoblastic, matrix-supported, with muscovite and iron oxide cement	up to millimetric
Metaconglomerate	VKE2	Pebbles/clasts (incl. quartz and quartzite), Ms	heteroclastic, granoblastic, matrix-supported, with muscovite and iron oxide cement	up to centimetric

Pl=plagioclase, Kfs=K-feldspar, Qtz=quartz, Bt=Biotite, Ms=muscovite, Fhb=Fe-hornblende, Fe-ox=iron oxide

scale. Some of the microtextures described in impacted silica-rich rocks (e.g. planar deformation features and recrystallization features) are well-known markers for impact-related deformation (Gibson and Reimold, 1999; Reimold, 2006) and confirm that these rocks are indeed of pre-impact occurrence, hence, they are older than 2023 ± 4 Ma years (Kamo *et al*., 1996).

5.6 SUMMARY

From the re-evaluation of field relations and geology, it can be concluded that targeted silica-rich rock varieites in the Vredefort Dome were colonised by a variety of lichen taxa, here identified at the genus level, in particular *Acarospora* sp.pl., *Caloplaca* s. lat. sp.pl., *Buellia* sp.pl., and *Xanthoparmelia* sp.pl. This observation supports previous reports in the Haughton- and Lockne impact structures (Cockell & Lee., 2002; Cockell *et al*., 2002, 2003, 2006, 2005, 2007; Fike *et al*., 2002, 2003; Cockell & Osinski, 2007; Pontefract *et al*., 2014), which argues that impact-shocked rocks do not prevent lichen colonization. This may have to do with increased shock state and particularly increased porosity and translucence.

Due to slight variances in chemical composition and mineral stability, it was believed that weathering of different silica-rich rocks will cause similar chemical gradients to occur within the related microenvironments. Changes in the dominant rock types of each sampling unit are also expected to have similar effects on the colonization and abundance of particular lichen genera. Here, it was possible to provide clear support from the chemical and physical characteristics of the variety of rock types on why these geological formations would be able to support a lichen flora (see Table 10). In particular, foliose lichens preferencially occupied felsic rock types, whilst crustose lichens did not show any preference in terms of minerology, encrusting both granitic- and metasedimentary rock types.

Apart from chemical variables related to the geology, lichen colonization also correlated with microenvironments that provide long-term stable environmental conditions for life through the provision of adequate resources (water, light, and nutrients, above all) and effective protection from environmental extremses (e.g. lethal UV- and PAR radiation, extreme temperature fluctuations, gusts of wind and rain, and excessive evapotranspiration). Hence, the largest quantity of lichen genera was observed on rock outcrops in close proximity to the Vaal River and its flood plains, especially on shaded slopes where the evaporation rate is lower than in the open. Denser lichen cover was also observed on rocks that are characterized by weathering, e.g. granitic rocks that are highly weathered and more porous, thus facilitating access into the rock.

CHAPTER 6

BIOWEATHERING

6.1 INTRODUCTION

The geological data (Chapter 5) revealed that abrupt environmental gradients do occur across the identified sampling units of the Vredefort Dome. The aim of this chapter is to determine the rock bioreceptive characteristics of targeted silica-rich rock varieties (i.e. that which influences the distribution of saxicolous lichens); and to demonstrate the degree of ichen-rock interaction of four taxa in relation to environmental gradients. The latter includes the characterization of biomechanical and biochemical actions that the selected lichen genera impose on the targeted rock- and mineral surfaces.

Specific objectives for the bioweathering facet of this study were to (i) provide valid insights into the microstructural characteristics (pore space and microcracks) and three-dimensional textural relationships of targeted silica-rich rock varieties (section 6.1); and (ii) characterise and compare the lithic behaviour of four recurrent saxicolous lichen taxa on targeted silica-rich rock varieties with different structure–texture characteristics, paying attention to their association with specific components of rocks and structural spaces on the rock surface (section 6.2).

6.2 ARCHITECTURE OF LITHIC SUBSTRATE

Lichens in lithic habitats are integrated within a complex ecological entity, or ecosystem. “The dynamics of this integration are driven by multiple relationships involving not only the biological components but also the lithic substrate in which they are found” (de los Ríos *et al*., 2014). Here we interpret µCT observations of the micromorphological, structural, physical, and mineralogical properties associated with targeted silica-rich rock varieties collected over several locations (distance from Vaal River, altitude). In particular, the key parameters porosity and permeability were of high interest to predict the rock bioreceptive characteristics.

It is noteworthy that permeability estimates based solely on observations derived from the reconstructed gray-value images can lead to a significant over-estimate of permeability (e.g. Nehler, 2017). Nevertherless, it does provide useful information of the rock geometry and time-resolved changes on the micro-scale under *in-situ* conditions. This contributes to the improvement of multiphase permeability prediction in impact-induced media and provides a better understanding of trapping mechanisms or changes in the rock bioreceptive characteristics as

permeability-porosity relationships varies. In addition, three-dimensional (3D) volume rendering of high-resolution µCT data provides valid insight into the establishment and development of lichen populations - an important theme in ecology.

Geological data suggested some relationship between the distribution of lichens belonging in certain genera in the dome and specific geological formations. Foliose lichens of genus *Xanthoparmelia* seemed to target crystalline rock types (we refer here to granitic varieties) whilst crustose lichens of genera *Buellia*, *Caloplaca* and *Acarospora* showed less preference colonising both metasedimentary- and crystalline rock types (see Table 10). Hence, the primary focus regarding rock architecture is divided into two main facets, encompassing both granitic- and metasedimentary rock types. This section will, therefore, discourse from both a granitic and metasedimentary viewpoint.

6.2.1 Granitic rocks

K-feldspar rich granite (sampling unit A) is a medium- to fine-grained rock composed primarily of K-feldspar, plagioclase, quartz, and biotite (refer to section 5.4). In µCT-scanned images, iron oxide appears in a brighter colour compared with biotite, feldspar and quartz because it had the highest density (Figure 41). But it was difficult to differentiate quartz and plagioclase minerals using µCT techniques, as there is no noticeable difference between quartz and plagioclase densities.

From a structural perspective, K-feldspar rich granite exhibits a well-developed pore-fracture network (Figure 38). Large transgranular fractures (affecting more than one grain) can be seen emerging from the outer edge, penetrating deep into the rock interior. Smaller intergranular fractures (along the grain boundaries) were also found propagating along the grain boundaries and between the same mineral grains with different crystallographic orientations. Intragranular fractures cannot be resolved by µCT, however, SEM data did confirm that intragranular fractures have formed within some of the feldspar, quartz, and biotite crystals. These fractures serve as a uniform network that provides sufficient permeability to allow microorganisms not merely to invade the rock along any surface-related fractures, but also to expand and grow through the rock spaces, forming coherent chasmoendolithic behaviour as observed in µCT (Figure 38).

“The alteration of mechanical properties in granite with increasing pressures and temperatures occurs due to thermally-induced microcracks and the substantial coalescence of these microcracks into macrofractures” (Avanthi Isaka *et al*., 2019). These fractures allow the penetration of water which in turn enhances rock fracturing and disintegrating through wetting and

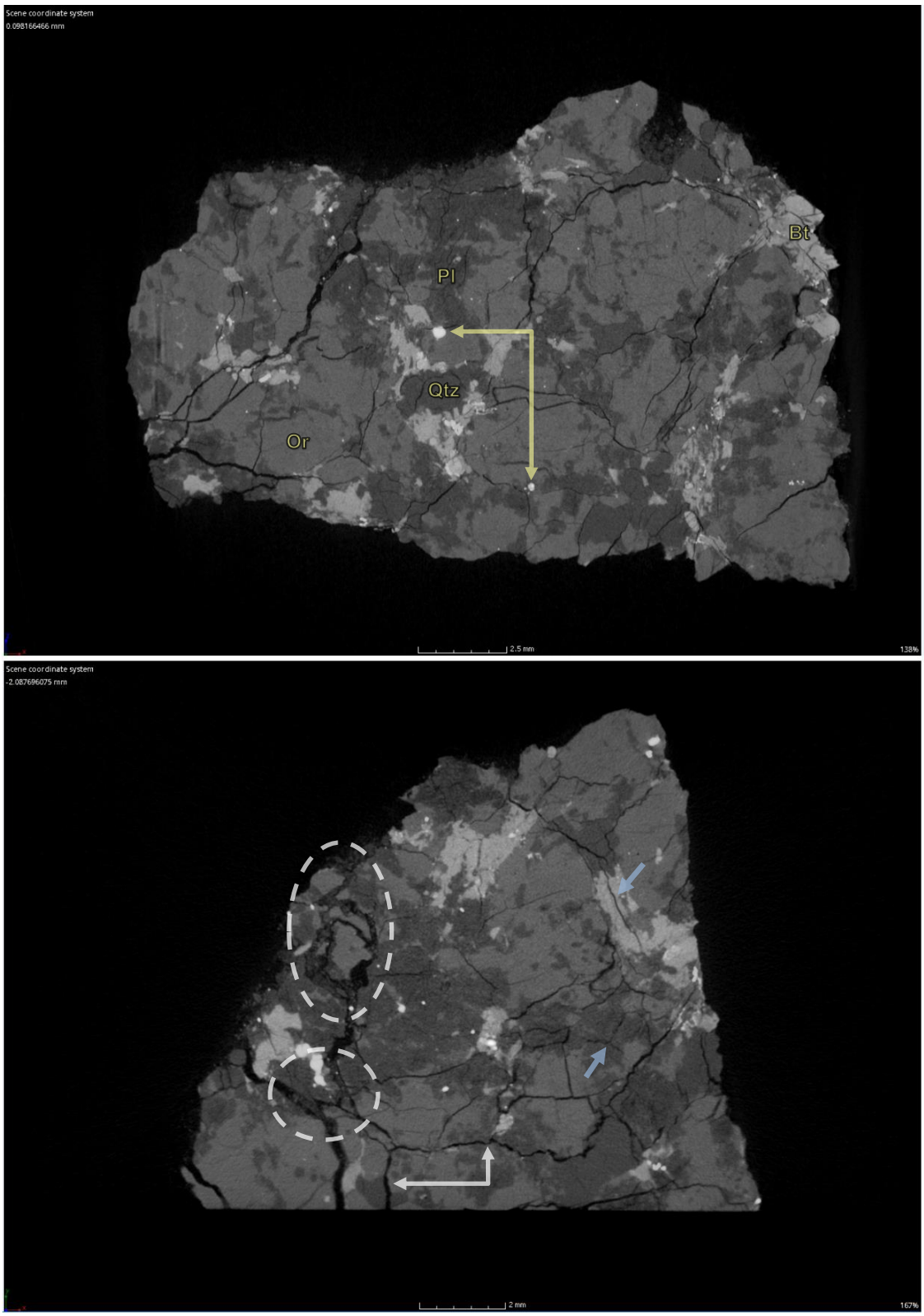


Figure 38: **Reconstructed 2D images showing the distribution of grains and void space through K-feldspar-rich granite (sample VKA2). White arrows indicate transgranular fractures penetrating deep into the rock interior. Blue arrows show intergranular fractures propagating along the grain boundaries. White dashed circles show chasmoendolithic behaviour associated with lichenized fungi and organo-mineral associations in the upper part of the weathering rind. Yellow arrows indicate Fe derivatives. Or=K-feldspar, Pl=Plagioclase, Qtz=quartz, Bt=Biotite.**

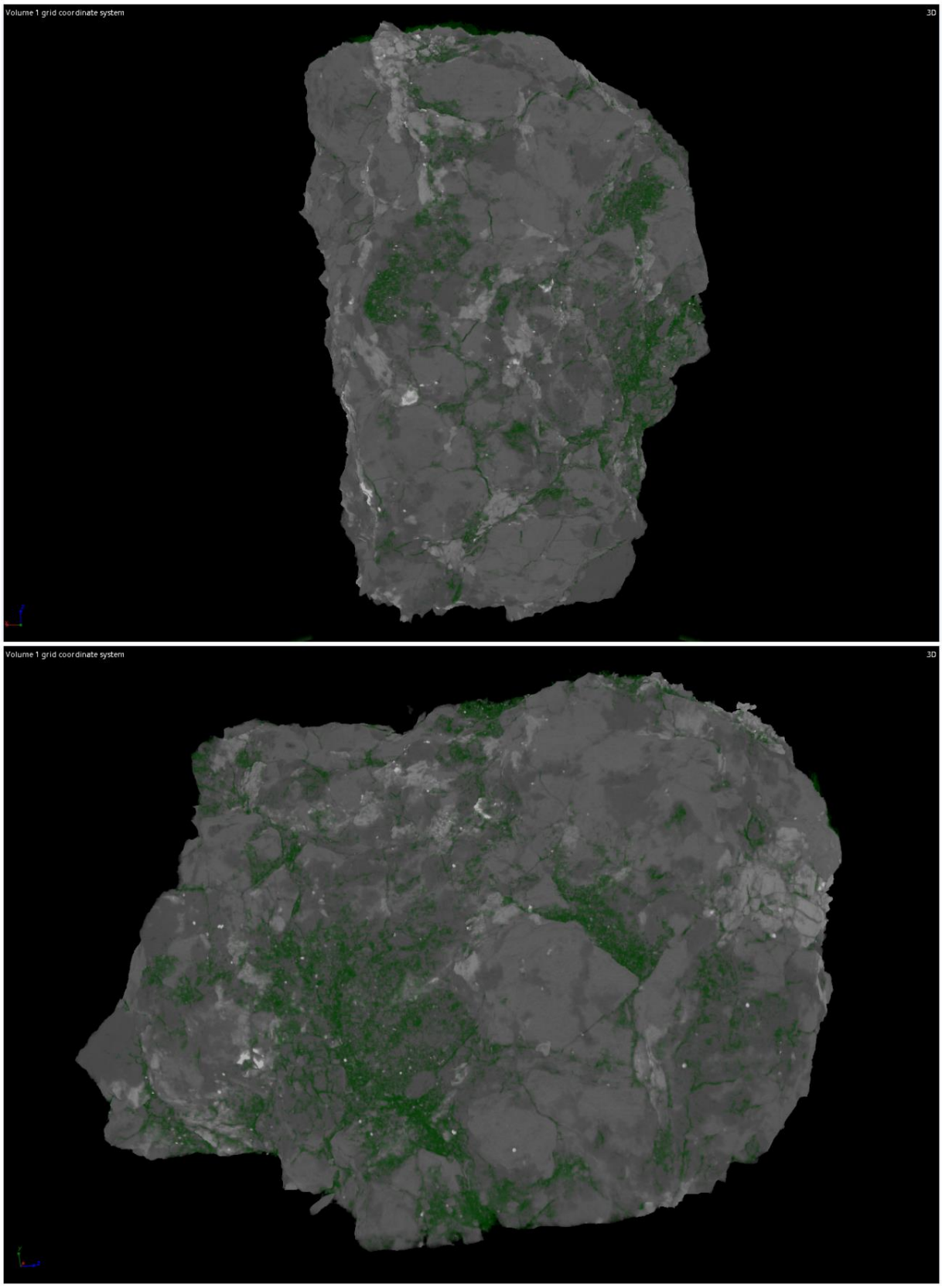


Figure 39: **Three-dimensional volume rendering of µCT data to show the distribution of *Xanthoparmelia* within K-feldspar-rich granite (sample VKA2). Note lichen thalli restricted to dark grey areas associated with plagioclase- and quartz grains. Matrix of lichen thalli has been rendered semi-transparent in shades of green.**

drying cycles, gradually widening and deepening pre-existing joints. Fractures also help to channel light down which increases the penetrability of photosynthetically active radiation - a factor of importance for the colonization of shocked rocks (Cockell *et al*., 2002, 2013). Chasmoendolitic behaviour (Figure 39) and evidence of weathering zones with indications of organo-mineral associations formed in points of intersection between fractures. Biological and mineral components were intermixed in this field, but biological components predominated. According to SEM-EDS data (Appendix D), such areas have a higher content of Fe, C, Si, Al, K, Ca, and Mg.

3D volume rendering of µCT data revealed regions of lichen thalli that are part of the interconnected pore-fracture network and separates them from either unconnected pore regions or higher density non-organic sample components, such as mineral phases (Figure 39). Most lichens seem to develop on parts of periphery that are easily accessible, but also shielded from extreme weather conditions, for example deep rock depressions, subcircular concavities, sharp steps or indentations and open fractures that are physically linked to the surface of the rock. Lichen thalli also showed selectivity with respect to mineral composition, with thalli encrouchment restricted to the areas around plagioclase- and quartz grains (Figure 39)**,** as well as inclusions of biotite, albeit less frequently.

By comparison, the alkali granite of sampling unit C, also a medium to fine grained rock, shows a slightly higher proportion of plagioclase than K-feldspar and with a higher quartz content. Moreover, the dark minerals represent Fe-hornblende. In µCT-scanned images, scattered fragments of iron oxides are the brightest grains followed by progressively less bright Fe-hornblende, plagioclase, quartz, and K-feldspar (Figure 40).

Like K-feldspar rich granite, alkali granite seems to have collapsed and fractured during impact, creating a much broader cracking network and increasing contact between large-scale fractures and pores (Figure 40). As previously alluded to, these fractures connect zones depleted in nutrients and water at the center of endolithic systems and layers at the top and bottom. Initial stages of in situ fine earth formation (i.e. that what actualy transforms rock to soil) have been observed in pocket-like microzones enriched with organic material (Figure 40).

Simply looking at the 3D volume rendering (Figure 41), the surface of alkali granite is characterised by denser covering of lichen assemblage (we refer here to foliose lichens). This may have to do with alkali granite having a slightly higher iron content compared to K-feldspar rich granite as well as a broader cracking network and increased contact between large-scale fractures and pores. Here, no directional preference of attack by thalli was discernible.

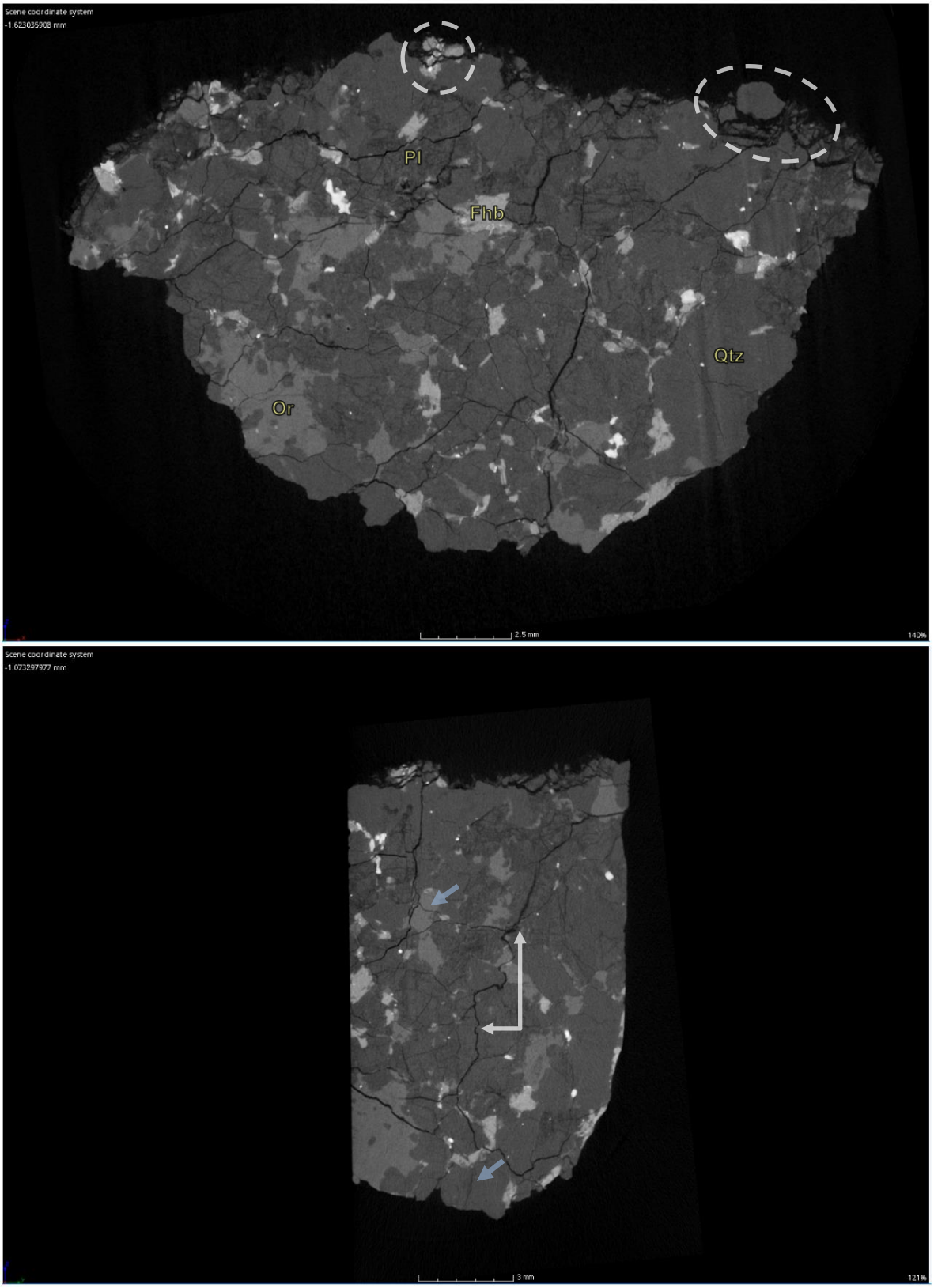


Figure 40: **Reconstructed 2D images showing the distribution of grains and void space through alkali granite (sample VKC1). Note the transgranular- (white arrows) and intergranular fractures (blue arrows) transecting the rock's microstructure. Note the initial stages of fine earth formation associated with weathering zones (white dashed circles) in the upper part of the weathering rind. Or=K-feldspar, Pl=Plagioclase, Qtz=quartz, Fhb=Fe-hornblende.**

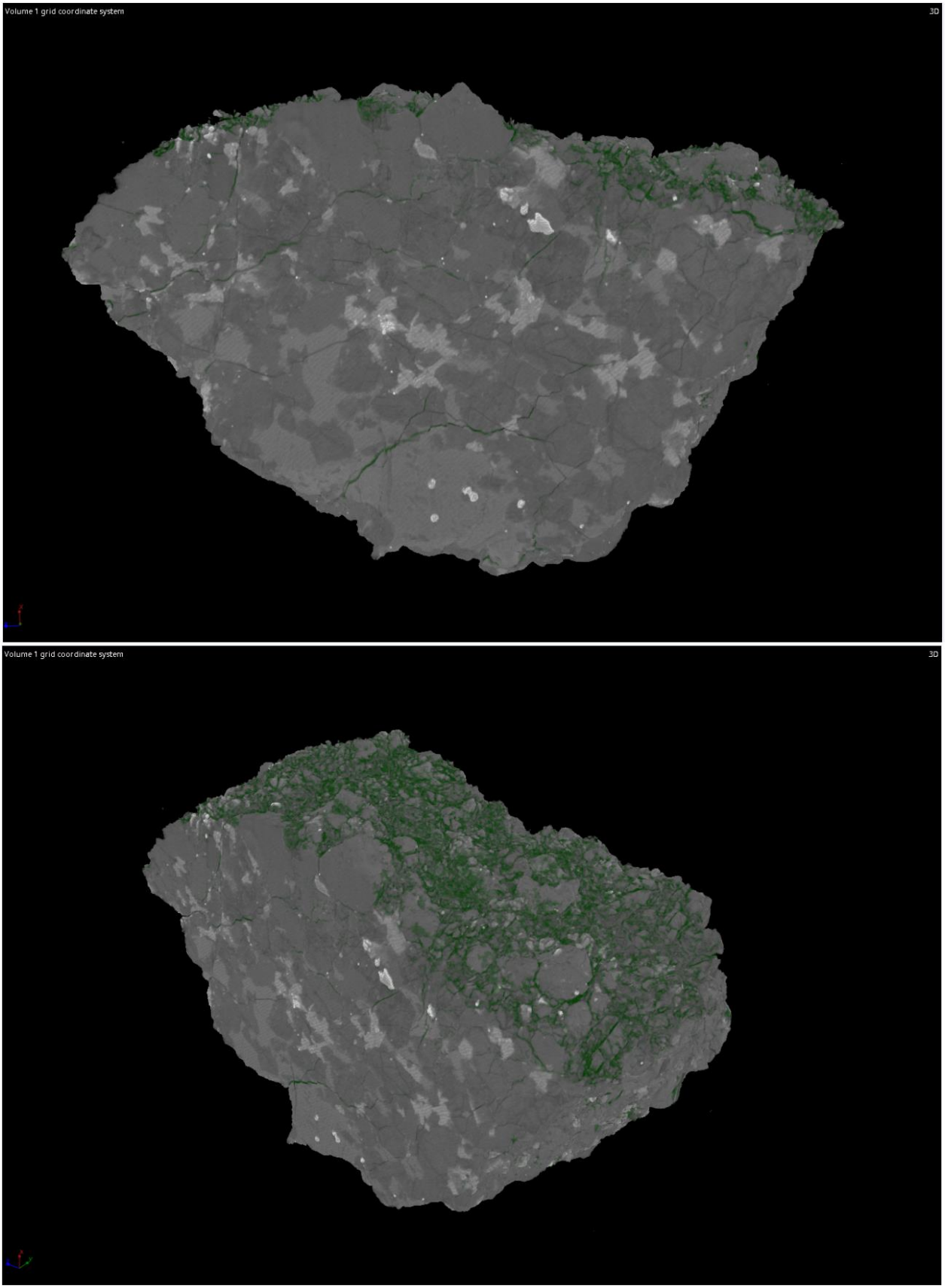


Figure 41: **Three-dimensional volume rendering of µCT data to show the distribution of *Xanthoparmelia* within alkali granite sample (VKC1). Matrix of lichen thalli has been rendered semi-transparent in shades of green.**

6.2.2 Metasedimentary rocks of the Witwatersrand Supergroup

Sub-labile arenite is a fine-grained rock which consists primarily of quartz grains in a micaceous matrix. The bulk of the substrate is of uniform density with dispersed small high-density particles (referring to iron oxides) embedded within it. Small iron oxide particles are the brightest grains followed by progressively less bright mica and quartz. It would have been exceedingly difficult to see, and especially quantify, these small details with different techniques.

From a structural point of view, sub-labile arenites are more complex and shows a well-defined decrease in particle size and permeability (Figures 42 & 43). Sub-labile arenite exhibits a collection of discrete pores and cracks that exhibit little shape variation. Connections between the pores cannot be resolved by µCT, however, the identified pore elements agreed with the intuitive notion of a well-connected pore space, where there exists relatively small number of large well networked pores and many smaller disconnected pores. 3D volume rendering revealed that the surface of sub-labile arenite was sufficiently smoother, hence, it was characterised by a patchy covering of lichen assembladge (Figure 43). Here, lichen thalli were restricted to the upper 1mm and can be seen encrusting microdepressions irregularly and discontinuous indentations of the rock surface. No directional preference of attack by lichen thalli was discernible.

Ferruginous wacke was charactarised as a medium to coarse grained phase of rock, which consists primarily of quartz grains in a deformed matrix of muscovite and iron oxide. µCT-scanned images revealed that the bulk of the material was of less uniform-density with more high-density particles (we refer here to iron oxide) embedded within it and a series of isolated microcracks and pores (Figure 44). In µCT-scanned images, the iron oxide particles were the brightest grains followed by progressively less bright mica and quartz.

The vesicle geometry was more complex than that of sub-labile arenite, since more mineral phases are evident. Fine fractures made up the biggest portion of void space, some of which were filled with iron oxide, especially open fractures that were physically linked to the surface of the rock (Figure 44). According to SEM-EDS data (Appendix E4), such areas had a higher content of Fe with As, P, V, and Cr measured as impurities. Regions of isolated pores exhibited more shape variation and tended to be filled with iron oxide (see SEM-EDS data, Appendix E4). 3D volume rendering revealed that the surface of ferruginous wacke was characterised by a less smooth surface, with slightly deeper rock depressions (Figure 45). This provided more surface area that was easily accessible and protected from environmental extremes (e.g. gusts of wind and rain), and hence, a denser covering of lichen assembladge was noted.

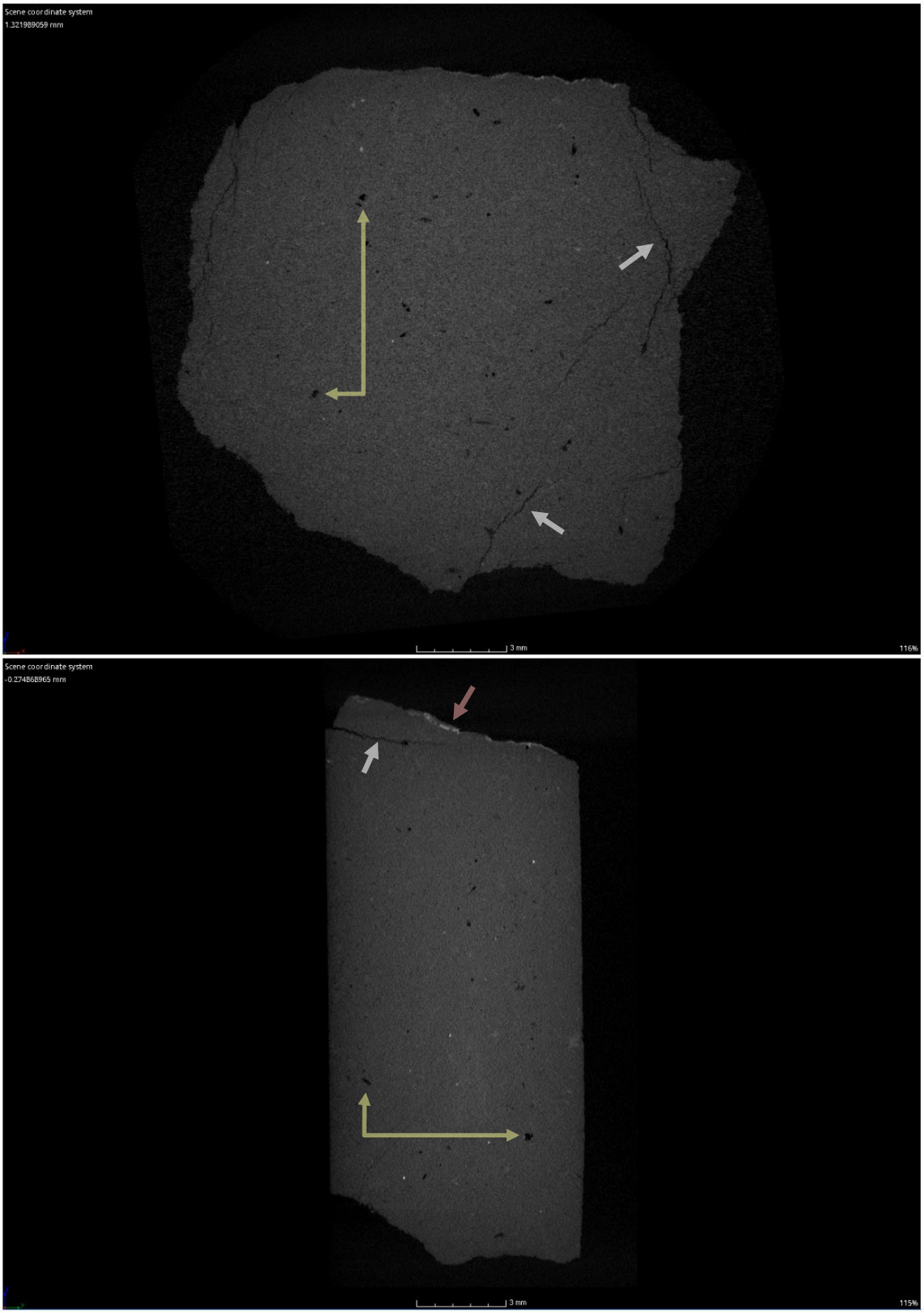


Figure 42: **Reconstructed 2D images showing the distribution of grains and void space through sub-labile arenite (sample VKB2). Note the relatively sparse distribution of pores (yellow arrows) and macrocracks (white arrows). The red arrow indicates iron staining on the surface of the rock substratum (we refer here to secondary presipitate of Fe). The brightest grains were iron oxides followed by progressively less bright mica and quartz.**

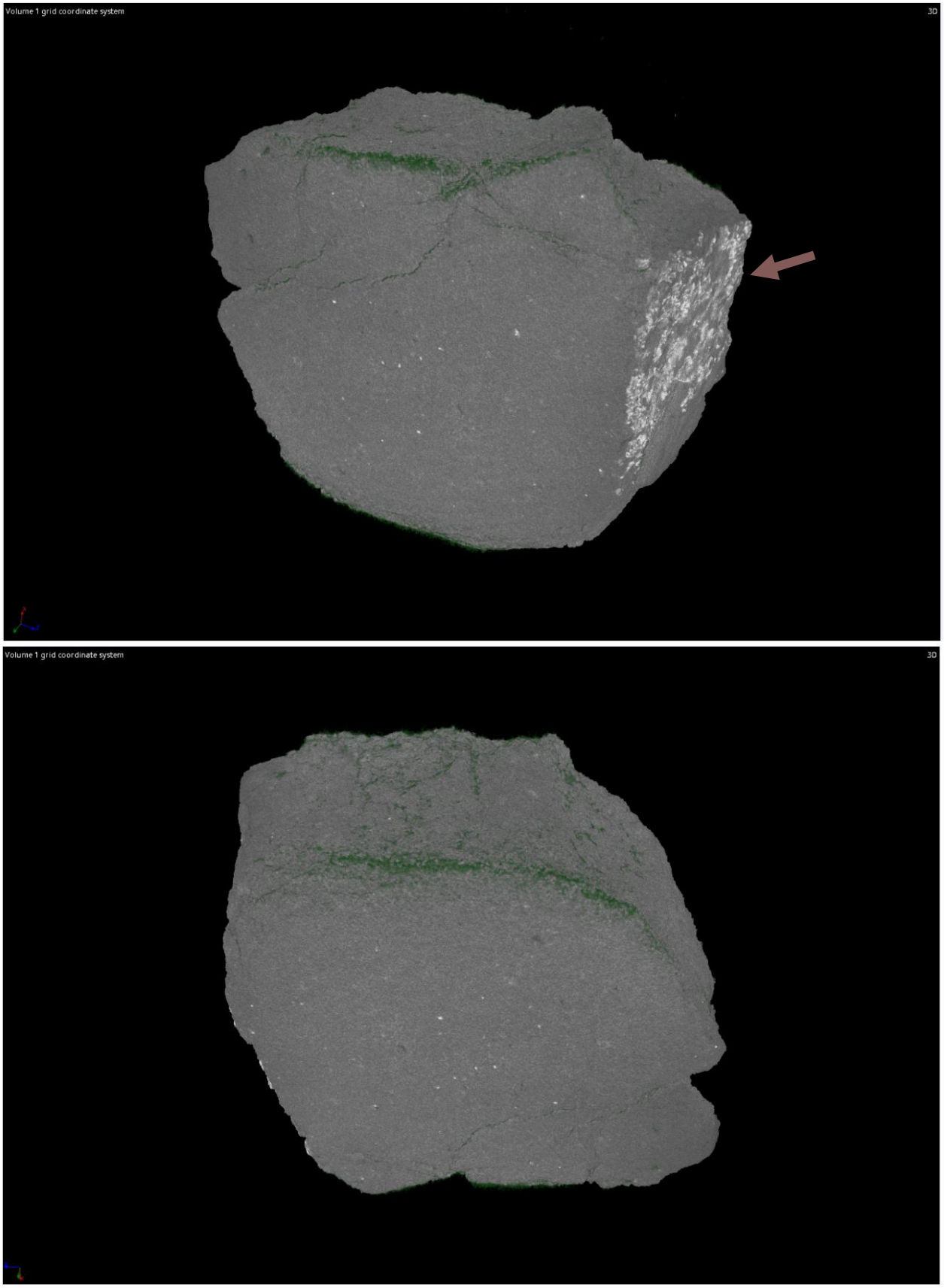


Figure 43: **Three-dimensional volume rendering of µCT data to show the distribution of *Buellia* within sub-labile arenite (sample VKB2). Matrix of lichen thalli have been rendered semi-transparent in shades of green. Red arrow = iron-stained spot.**

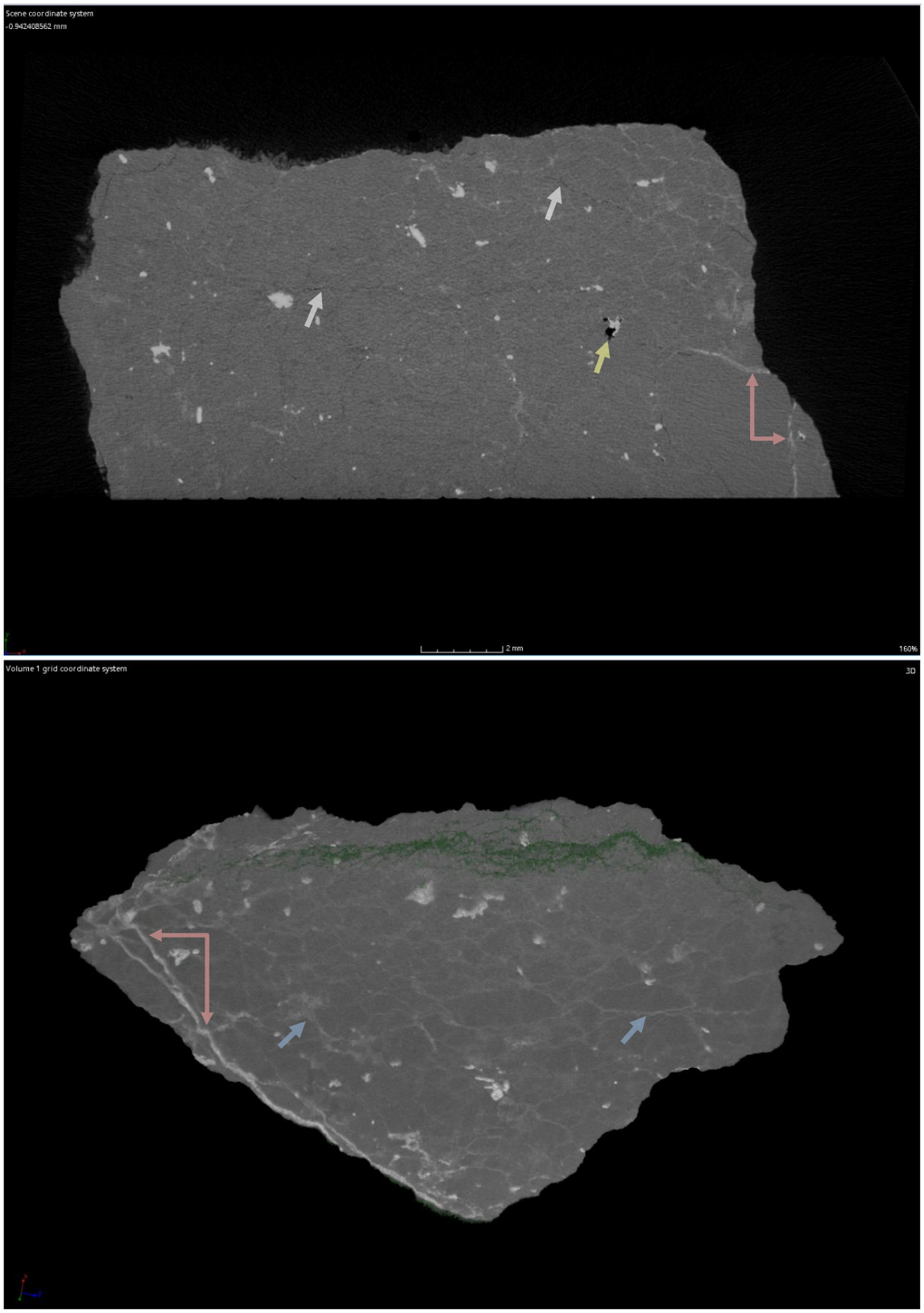


Figure 44: **Structure of ferriginous wacke as seen by µCT (sample VKD2). (A) 2D slice showing the distribution of grains and void space in ferriginous wacke. (B) 3D volume rendering of µCT data showing structural and textural relations associated with ferriginous wacke. Matrix of lichen thalli have been rendered semi-transparent in shades of green. Red arrows = Fe-rich transgranular fractures, yellow arrow = pore filled with Fe oxides, blue arrows = deformed matrix of mica.**

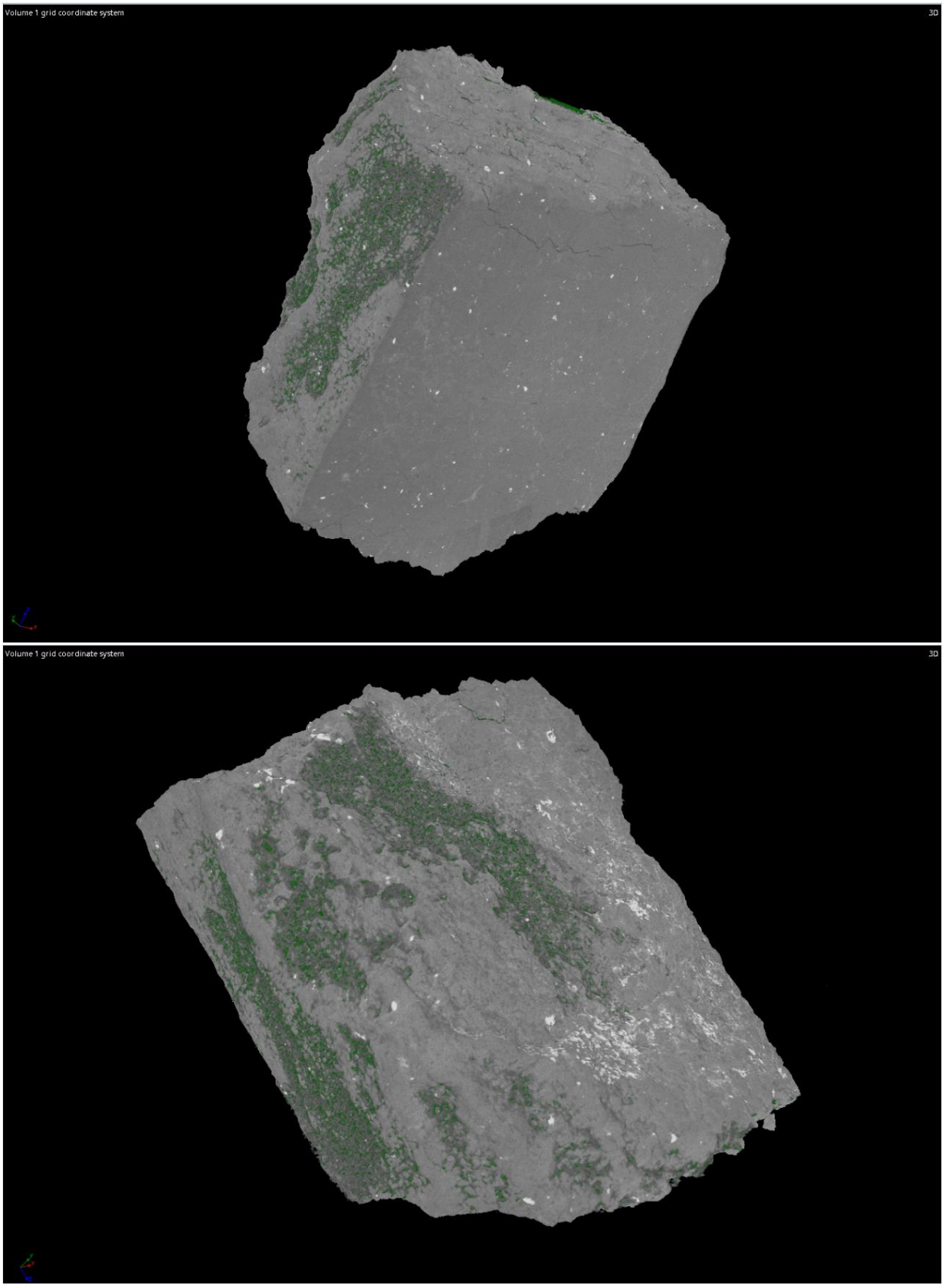


Figure 45: **Three-dimensional volume rendering of µCT data to show the distribution of *Acarospora* within ferriginous wacke (sample VKD2). Matrix of lichen thalli have been rendered semi-transparent in shades of green. Note several lichen clusters competing for space.**

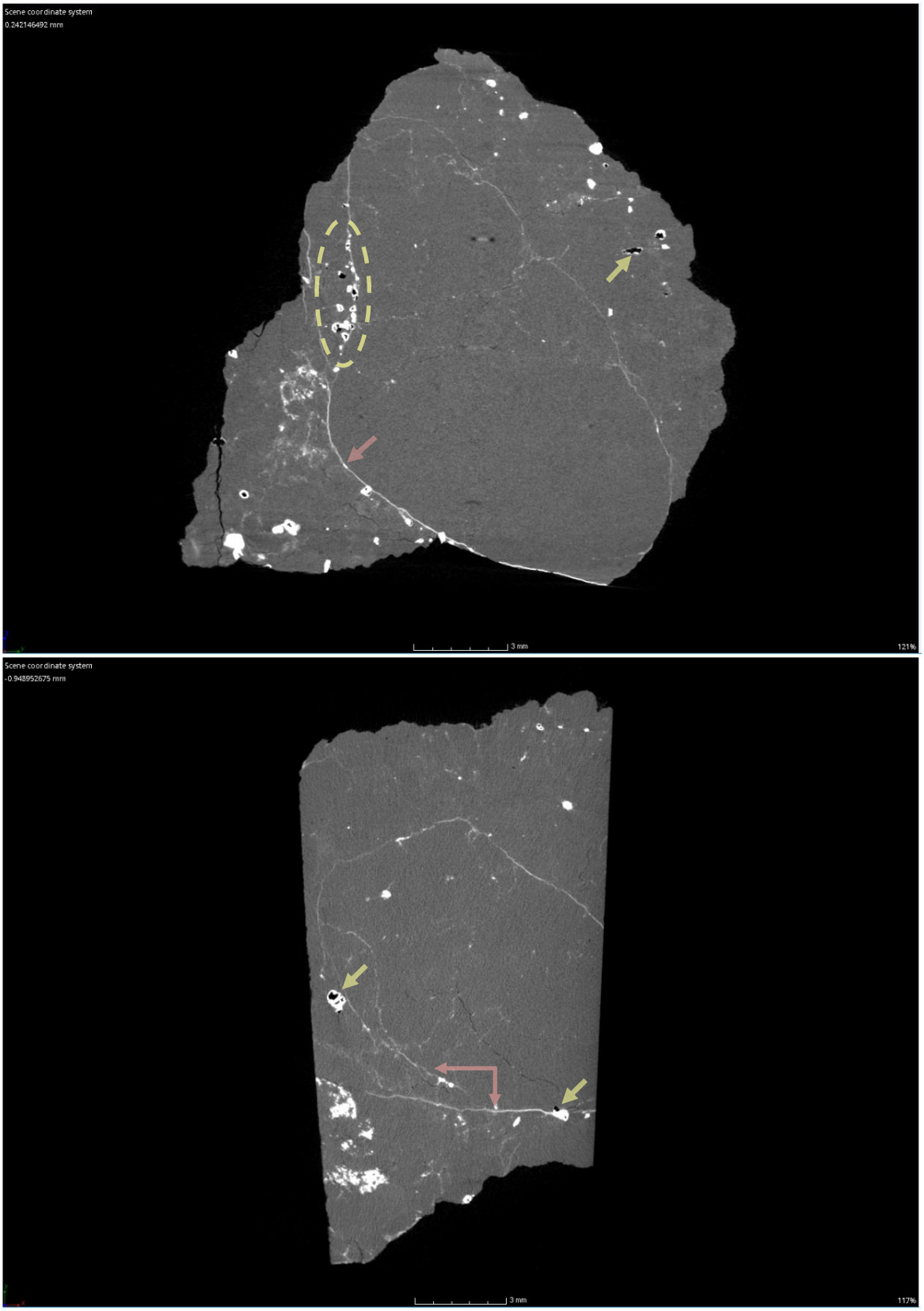


Figure 46: **Reconstructed 2D images showing the distribution of grains and void space through metaconglomerate (sample VKE1). Note the aggregation of pores along intergranular void space (yellow dashed circle). Red arrows = intergranular fractures rich in Fe, green arrow = intragranular fractures, yellow arrows = in situ pores filled with Fe.**

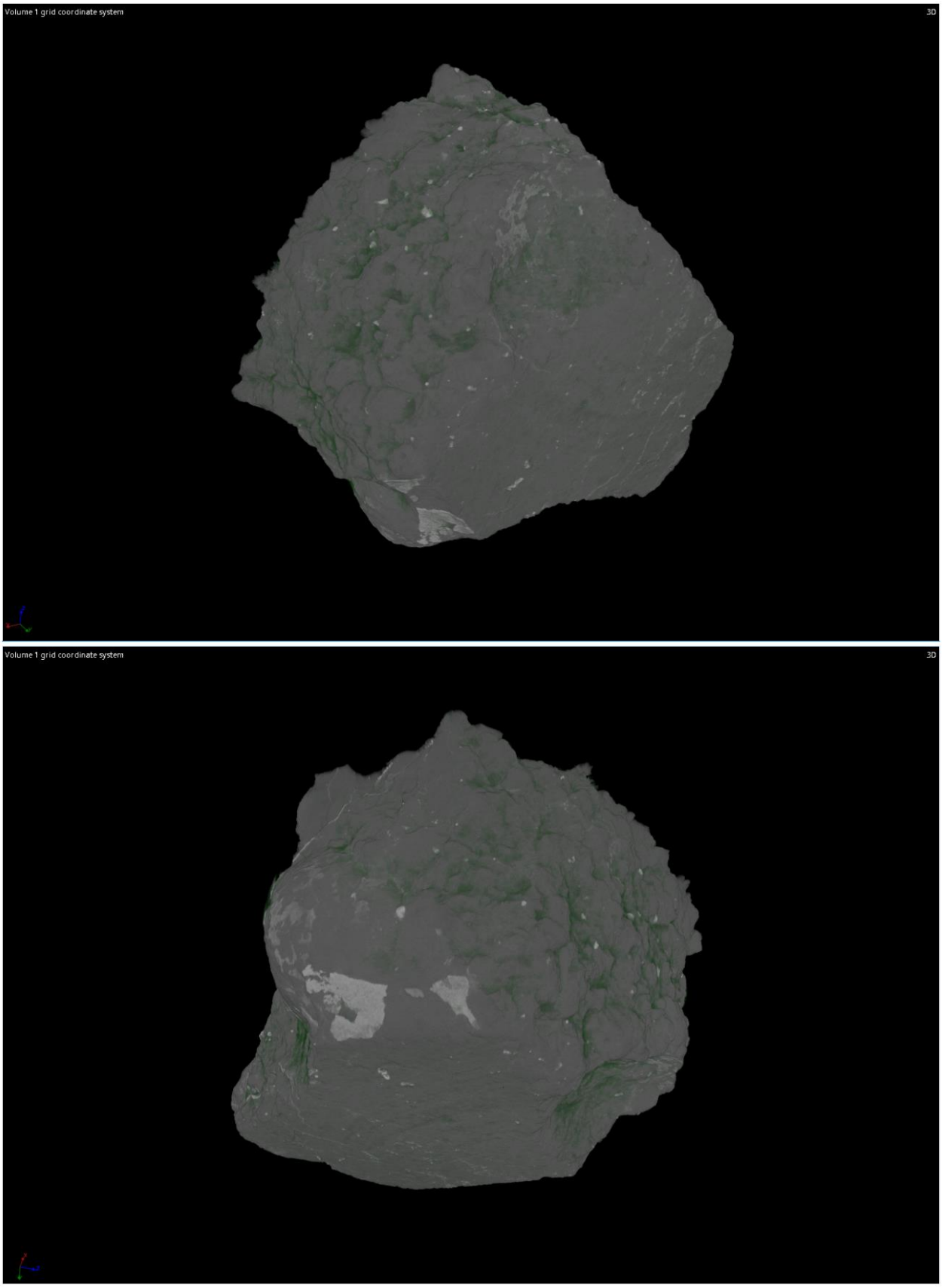


Figure 47: **Three-dimensional volume rendering of µCT data to show the distribution of *Caloplaca* within metaconglomerate (sample VKE1). Matrix of lichen thalli have been rendered semi-transparent in shades of green.**

surface of ferruginous wacke was characterised by a less smooth surface, with slightly deeper rock depressions (Figure 45). This provided more surface area that was easily accessible and protected from environmental extremes (e.g. gusts of wind and rain), and hence, a denser covering of lichen assembladge was noted.

By comparison, the metaconglomerate proofed to be a much simpler structure with regions of rounded to subangular gravel-size clasts and finer grained sediments in interstices between the clasts (Figure 46). It had a more easily resolvable pore network and intergranular fractures filled with iron derivatives were identified along grain boundaries. *In situ* pores tended to be aligned and oriented along the direction subparallel to grain bounderies. Larger pores were interconnected by smaller channels and frequently filled with iron oxides. Altogether, secondary precipitation through fractures and pores contributes to the reduction of surface area accessible to pioneer organisms. 3D volume rendering showed that the surface of metaconglomerate was characterised by the deepest rock depressions and well-developed rock indentations of the rock surface (Figure 47).

6.3 WEATHERING FEATURES AT THE LICHEN–ROCK INTERFACE

Since µCT techniques focused on observation of a wider surface area on large sample volumes, there was a need for high-resolution (nanometre to sub-nanometre) SEM to image organo-mineral associations at the lichen-rock interface. SEM imaging also provided high-resolution information of the geometry and connectivity of fractures and pores which cannot be obtained using existing µCT techniques, due to their lower contrast and resolution.

6.3.1 *Xanthoparmelia*

Xanthoparmelia sp.pl. was characterised as a foliose laciniate with apothecia (Figure 48E) and lobes, the latter of which were either radially arranged (Figure 48E) or overlapping like tiles on a roof (Figure 48F). *Xanthoparmelia* thallus ranges in thickness from 0.5 to 1.5 mm and adheres discontinuously onto the generally uneven and quite rough, alternating flat and outer surface of the substratum by means of large numbers of rhizines (Figure 48), reaching depths from some tens of microns up to 1.5 mm or more. In particular, thalli enchrouchment seemed to be localised to deep rock depressions, subcircular concavities and open fractures that are physically linked to the surface of the rock; better highlighted by µCT observations (Figures 39, 41). The major microtextural features under each lichen genus studied are summarised in Table 14.

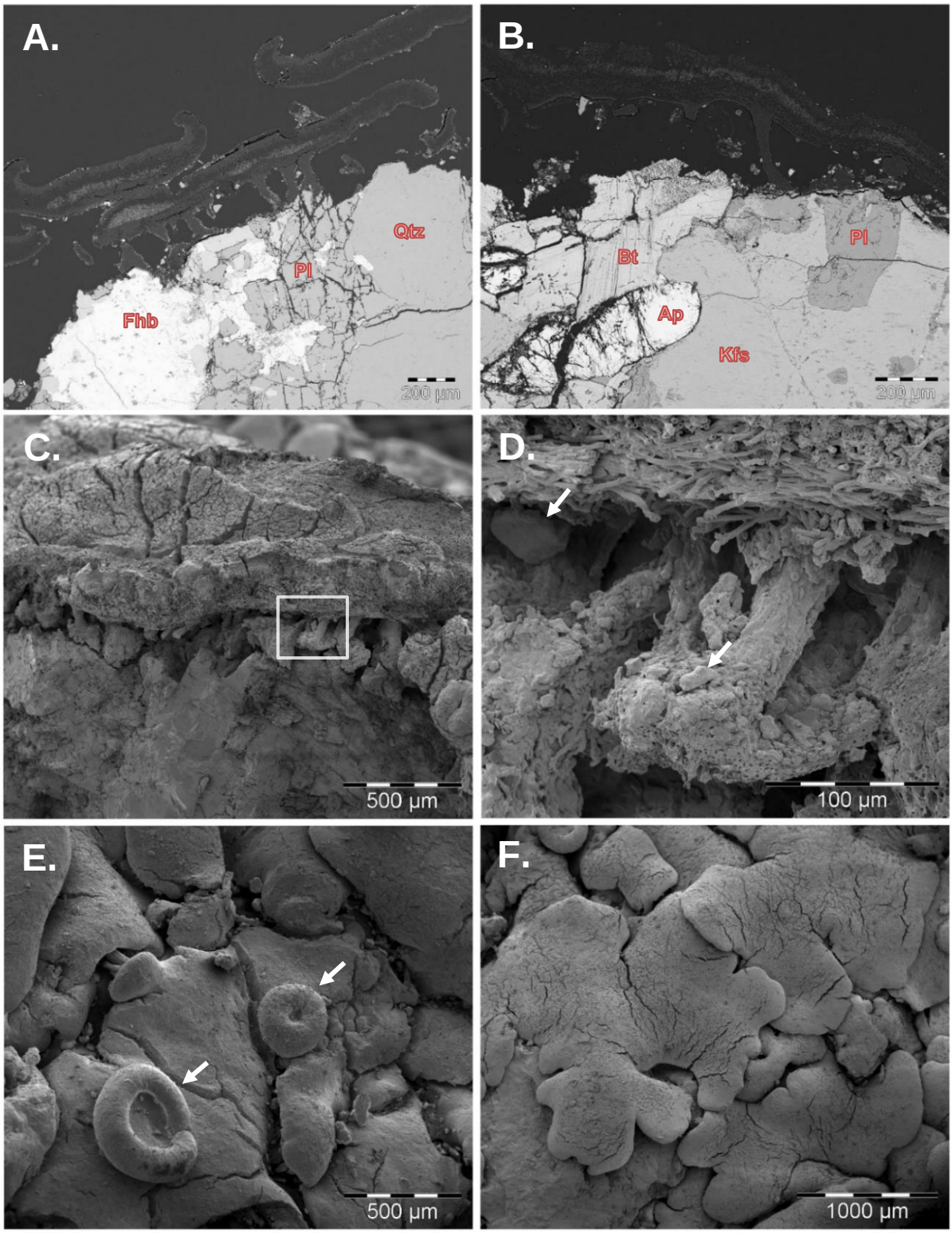


Figure 48: **Interface formed by *Xanthoparmelia* thallus and granitic outcrops: *Xanthoparmelia* encrusting alkali granite (A); *Xanthoparmelia* encrusting K-feldspar rich granite (B); bulk sample of discontinuous lichen cover attached to the rough rock surface by large numbers of rhizines (C); detail of square in C, showing the dislodgement of micro-granules (white arrows) (D); surface of *Xanthoparmelia* thallus showing apothecia (white arrows) and radially arranged lobes (E); lobes overlapping like tiles on a roof (F). Fhb=Fe-hornblende, Pl=Plagioclase, Qtz=Quartz, Bt=Biotite, Ap=Apatite, Kfs=K-feldspar.**

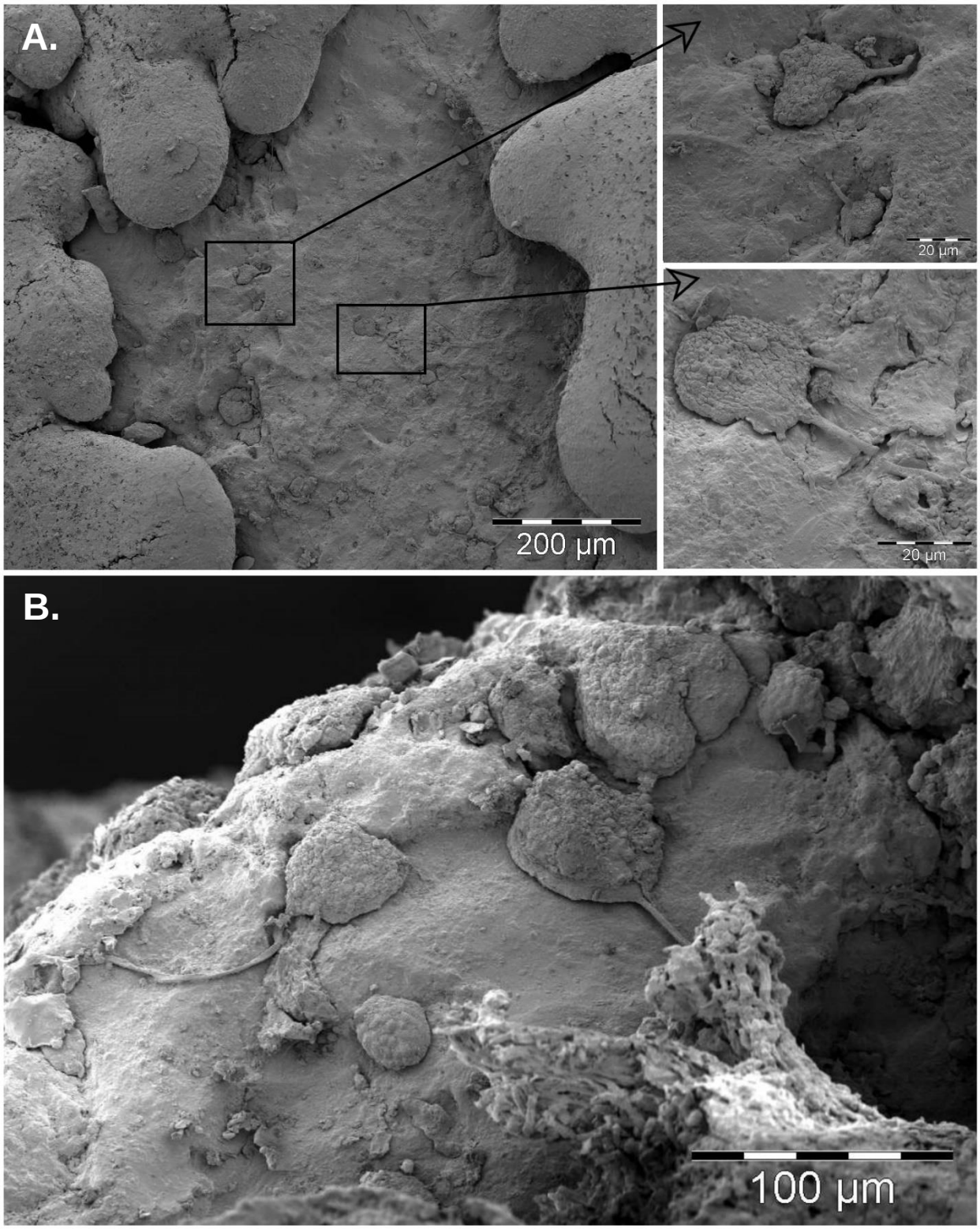


Figure 49: **Thallus ontogeny of the foliose lichen *Xanthoparmelia*. (A) SEM images of the surface of granitic rock. Insert close ups provide detail of hyphae attached to deep rock depressions and irregular rock indentations of the rough rock surface. (B) Lichen hyphae and fungal microcolonies (yellow arrows) attached to the substrate.**

Table 14: Major microtextural features under each lichen genus studied.

Lichen genus	Adhesion of thallus on substrate	Lichen-rock interface	Rock physical weathering	Rock chemical weathering	Depth of penetration	List of the supporting figures
***Xanthoparmelia* sp.pl.**	Irregular, discontinuous, adherent or attached by means of large numbers of rhizines	Uneven, alternating flat with deep depressions and indentations of the rough rock surface	Lichen penetration and fragmentation of primary minerals along points of weakness (mainly trans-, inter-, and intra-granular fractures; cavities/voids; and mineral cleavage planes), expansion and contraction of fungal hyphae	Etch pits and dissolution lines (mainly on plagioclase, biotite and Fe-hornblende), secondary precipitates (mainly mycogenic minerals and nanocrystalline alumino-silicates)	Some tens of microns up to 1.5 mm or more	Figures 38, 39, 40, 41, 48, 49, 50, 51, 52, 53, 54, 55
***Buellia* sp.pl.**	Intimate, continuous, adherent or attached by means of hyphae throughout its underside	Smooth with irregular and discontinuous microdepressions and indentations of the rock surface	Lichen penetration and fragmentation of primary minerals along points of weakness (mainly *in situ* cavities/voids connected by trans- and inter-granular fractures; microcracks parallel to rock surface (2 ranges of depths), and mineral cleavage planes), expansion and contraction of fungal hyphae	Etch pits and dissolution lines (mainly on quartz and muscovite), secondary precipitates (mainly 2:1 phyllosilicates and calcium oxalate)	Some tens of microns up to 400 microns or more	Figures 43, 56, 57, 58, 59, 60, 61
***Acarospora* sp.pl.**	Intimate, continuous, adherent or attached by means of hyphae throughout its underside	Less smooth with well-developed microdepressions and indentations of the rock surface	Lichen penetration and fragmentation of primary minerals along points of weakness (mainly trans-, inter-, and intra-granular fractures; cavities/voids; and mineral cleavage planes), expansion and contraction of fungal hyphae	Etch pits and dissolution lines (mainly on quartz, muscovite and iron oxide), secondary precipitates (mainly iron oxide accumulations and 2:1 phyllosilicates)	Some tens of microns up to 600 microns or more	Figures 44, 45, 62, 63, 64, 65, 66, 67
***Caloplaca* s. lat. sp.pl.**	Intimate, continuous, adherent or attached by means of hyphae throughout its underside	Relatively uneven with deep depressions and indentations of the rough rock surface	Lichen penetration and fragmentation of primary minerals along points of weakness (mainly inter-granular fractures; microcracks parallel to rock surface, cavities/voids, and fine-grained matrix), expansion and contraction of fungal hyphae	Etch pits and dissolution lines (mainly on scattered pebbles/clasts and the fine-grained matrix), secondary precipitates (mainly iron oxide accumulations and 2:1 phyllosilicates)	Some tens of microns up to 400 microns or more	Figures 46, 47, 68, 69, 70

The algal layer had an elevated calcium concentration compared to their surroundings (Figure 50). Higher concentrations of calcium within lichen thalli were believed to result from the breakdown of feldspar, amphibole and accessory apatite. Nevertheless, higher concentrations of calcium may also be realted to deposits of calcium oxalate which are common in species of genus *Xanthoparmelia*. Ultrastructural details of thallus ontogeny- and anatomy are shown in Figures 49 and 50 respectively.

In terms of mineral composition, *Xanthoparmelia* thalli seemed to be localised to the plagioclase, biotite, and Fe-hornblende component of the substrate. Plagioclase crystals appeared to be more fractured and weathered, with zones of diffuse etching (Figures 51 & 54A). Biotite and hornblende provide a relatively soft, Fe-rich environment for lichens and other organisms during the initiation of the weathering crust.

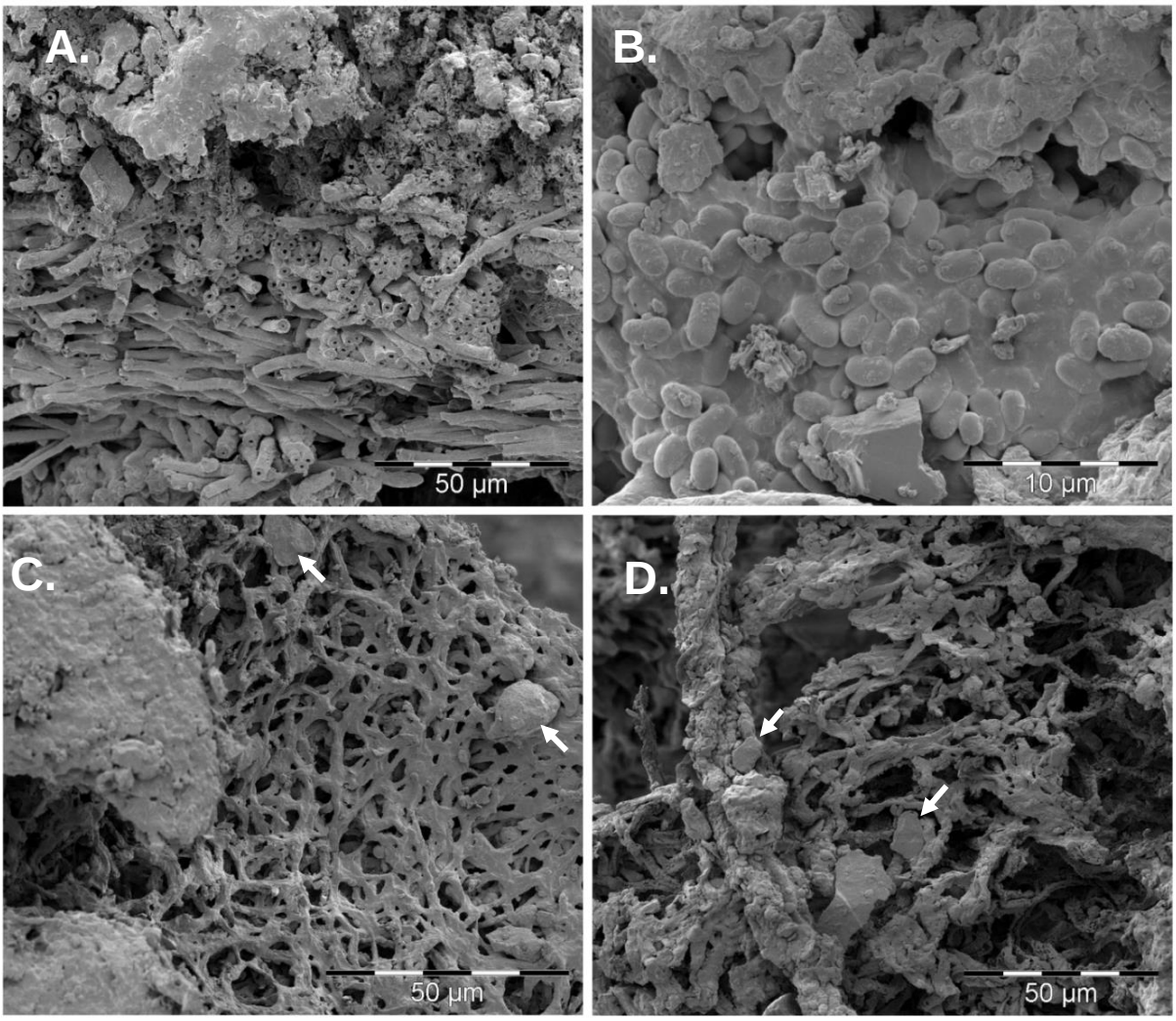


Figure 50: **Detail of thallus anatomy associated with *Xanthoparmelia*. (A) SEM close-up of lichen thalli. (B) Group of bacterial cells colonising alkali granite. (C,D) Hyphal mesh from the medulla rich in small mineral grains (white arrows) incorporated from the bedrock.**

Biotite and Fe-hornblende crystals were also altered by microcracks, leading to exfoliation along cleavage planes (Figures 52, 53, 54B). They also potentially provide a source of Mg, Ca and K. Moreover, partial fragmentation of quartz and localised apatite occur (Figures 48B & 52B), the latter providing a source P. Finally, accessory rutile provides a source of Ti as determined by EDS (Appendix E1, E3).

Initially, biomechanical breakdown of the substrate occurs through extensive penetration by thalline margins, rhizinae or hyphae, mainly along grain boundaries, cleavages and cracks. SEM analysis of individual biotite grains clearly revealed that biotite was intimately interpenetrated by hyphae, most often along basal cleavage (Figure 53B).

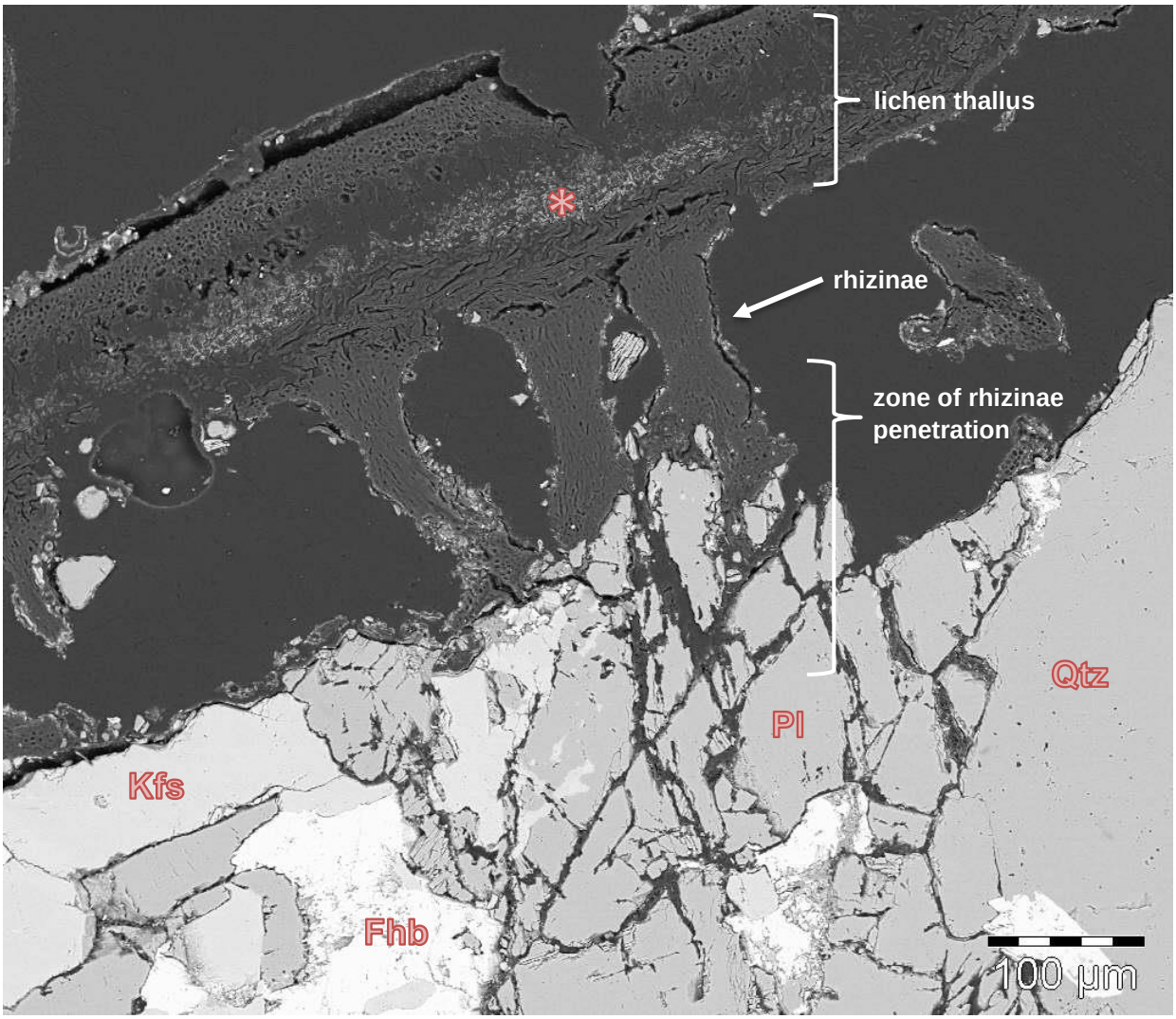


Figure 51: **SEM image of the adhesion of *Xanthoparmelia* on alkali granite. The thallus is attached to the rock surface by rhizinae, which appear incomplete in some instances because of transversal and oblique sectioning. Loose clasts disaggregated from the alkali granite by rhizinae penetration and disruption can be observed. Red asterisks show localisation of high Ca concentrations in thallus. Pl=plagioclase, Kfs=K-feldspar, Qtz=Quartz, Fhb=Fe-hornblende.**

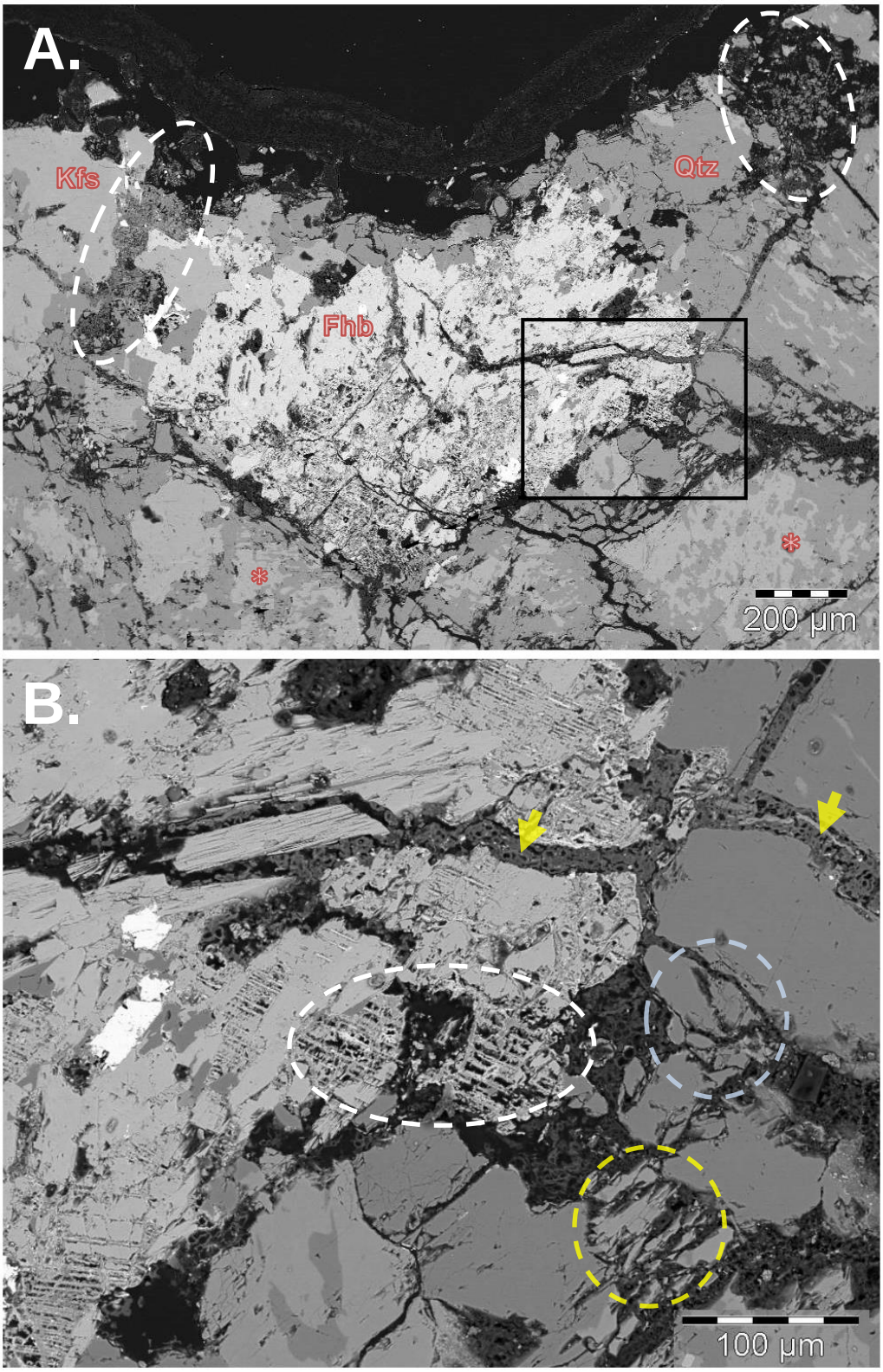


Figure 52: **Interface formed by *Xanthoparmelia* thallus and alkali granite. (A) Biological attack on alkali granite showing both physical and chemical decay. Note moldic porosity filled with a pedogenetic matrix (white dashed circles). (B) Detail of square in A; showing deep etching and bio-corrosion of Fe-hornblende (white dashed circle), quartz (blue dashed circle) and K-feldspar (yellow dashed circle) grains. Note how some fungal cells are covered with mineral crystals (yellow arrows). Red asterisks indicate antiperthite. Qtz=Quartz, Fhb=Fe-hornblende, Kfs=K-feldpsar.**

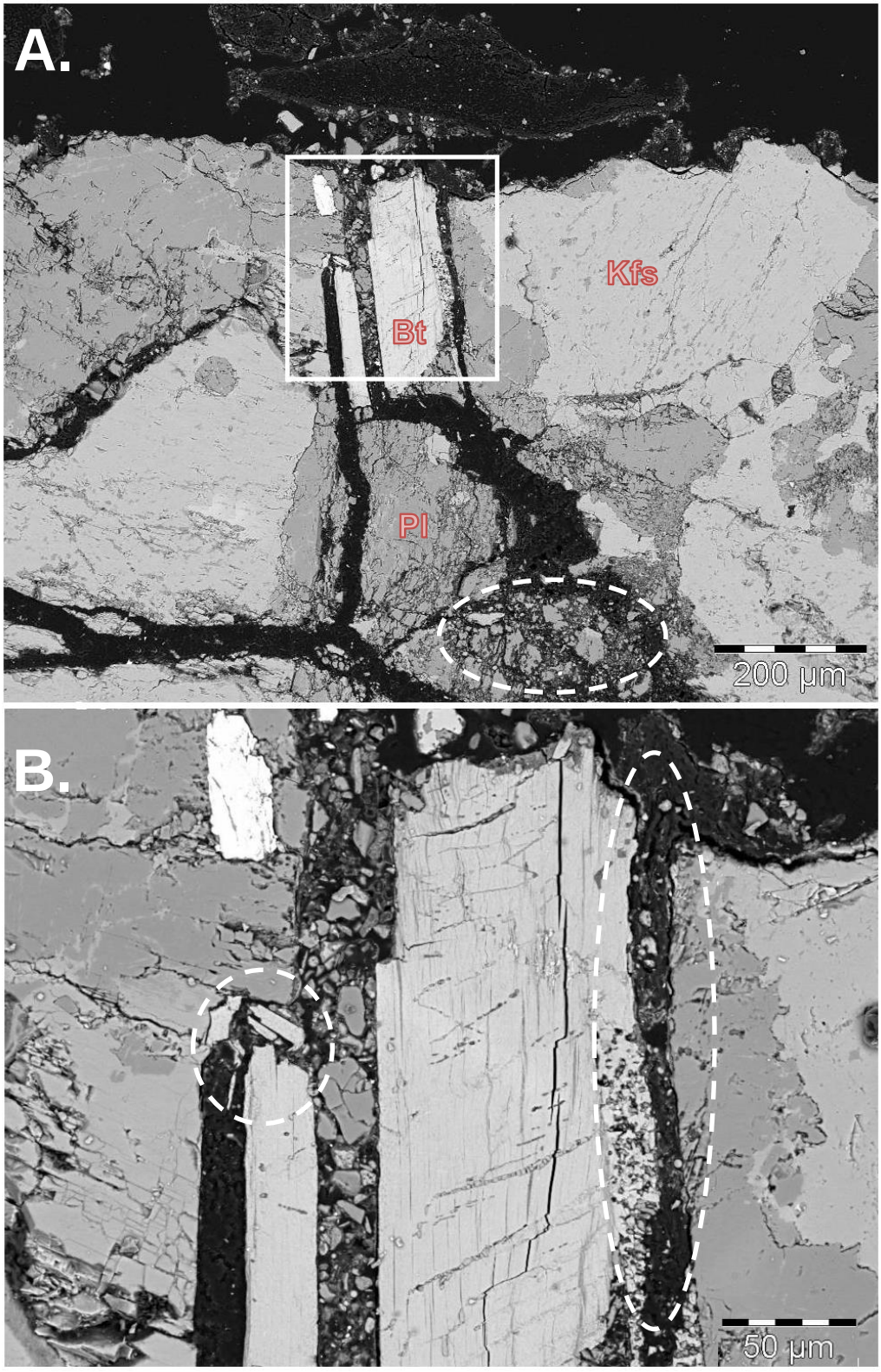


Figure 53: **Interface on K-feldspar-rich granite showing fragmentation and stripping of rock fragments, progressively incorporated into the thallus. (A) SEM image of micro-fractures radiating from a biotite grain into adjacent mineral grains, inducing rock fragmentation of plagioclase (white dashed circle) deeper down. (B) Detail of square in A, showing the distinctive patterns of etch pits and dissolution lines on biotite. Note the splitting of biotite and progressive upward incorporation of its flakes (white dashed circles) into the thallus. Note Pl=plagioclase, Kfs=K-feldspar, Bt=Biotite.**

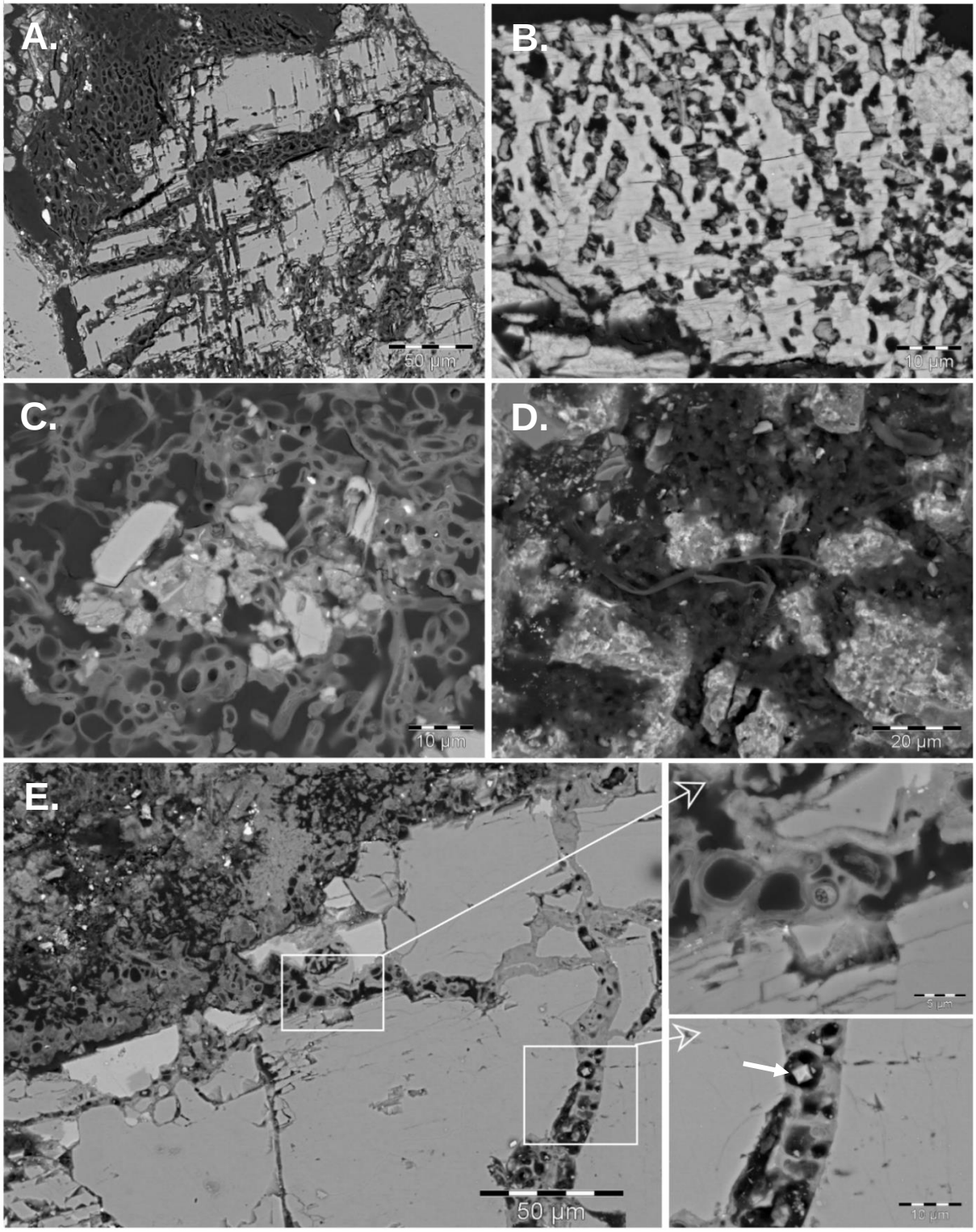


Figure 54: **Detail of mycobiont growth through intercrystalline and intracrystalline porosity. (A) Deep etching and bio-corrosion of plagioclase mineral grain. (B) Highly corroded surface of biotite showing extensive etching. (C,D) Visualization of organo-mineral associations in cavities found in alkali granite. Note how fungal cells and biofilms are covered with mineral crystals. (E) Mycobiont growth through moldic porosity (top left corner) connected by mutually interecting intracrystalline fractures of quartz. Insert SEM close ups provide detail of cylindrical hyphae covered with mineral crystals (top insert) and a pyramidal crystal of calcium dehydrate (white arrow, bottom insert) through intracrystalline porosity.**

Biomechanical attack generally proceeded from the edge of the grain and progressed towards the centre growing along cleavages. Similarly, plagioclase and Fe- hornblende represent particularly unstable constituents leading to rock disintegration along cleavage planes (Figure 54A). The breakdown of primary minerals, ultimately, induces moldic porosity (Figure 52A), which in turn poduces cavities which increases the available surface area and exposing further reactive sites.

Subsequent to the biomechanical breakdown of the substrate**,** further chemical reactions occur. For instance, primary minerals have been found to be partially dissolved in several instances by organic acid attack, manifested by a corroded aspect and the presence of distinctive etch pits and dissolution lines on the grain surfaces (figures 53B & 54B). “Etch pits are thought to represent the sites of structural dislocations in the mineral and are, consequently, regions of excess strain energy susceptible to preferential dissolution” (Jones *et al*., 1981). In other instances, weathered minerals were almost completely converted to a siliceous relic following the extraction of metal cations such as Al, Fe and Mg from its structure (see Figure 54C and EDS data in Appendix E).

New weathering products that have precipitated and crystallized at the lichen-rock interface or even within the lichen thallus itself have also been revealed by SEM. The biotic crust-mediated breakdown of granitic rocks liberates elements such as silicon and aluminium to crystallize to secondary nanocrystalline alumino-silicates (Figure 55A). Biogenic mineral formation was also evident - these minerals which commonly display distinctive morphologies indicative of the presence of microbial communities (Figure 55B).

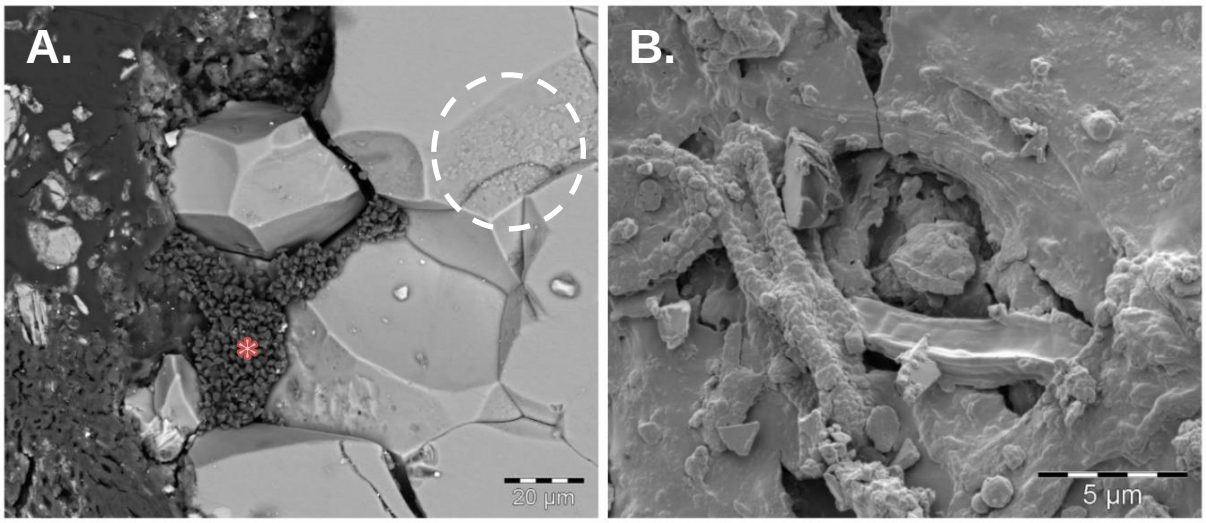


Figure 55: **Secondary weathering products on the surface of granitic rocks. (A) Secondary accumulation of nanocrystalline clay (white dashed circle) and organic matter accumulation (red asterisks) on quartz grains. (B) Mycogenic secondary mineral (white dashed circle).**

Considerable accumulation of organic matter could also be identified, especially around the hyphae or closely associated with them (Figures 58 & 60). In addition, fungal cells were sometimes also covered with secondary mineral crystals (Figures 54C & 54E). SEM-EDS analysis of the mycogenic minerals showed they were silicate minerals formed as result of oxalic acid excretion by *Xanthoparmelia* sp.pl.

6.3.2 *Buellia*

Buellia sp.pl. is a crustose lichen with a continuous thallus with mean thickness of about 100 to 200 µm (Figure 56). Moreover, *Buellia* thalli typically spread and expand radially outwards from

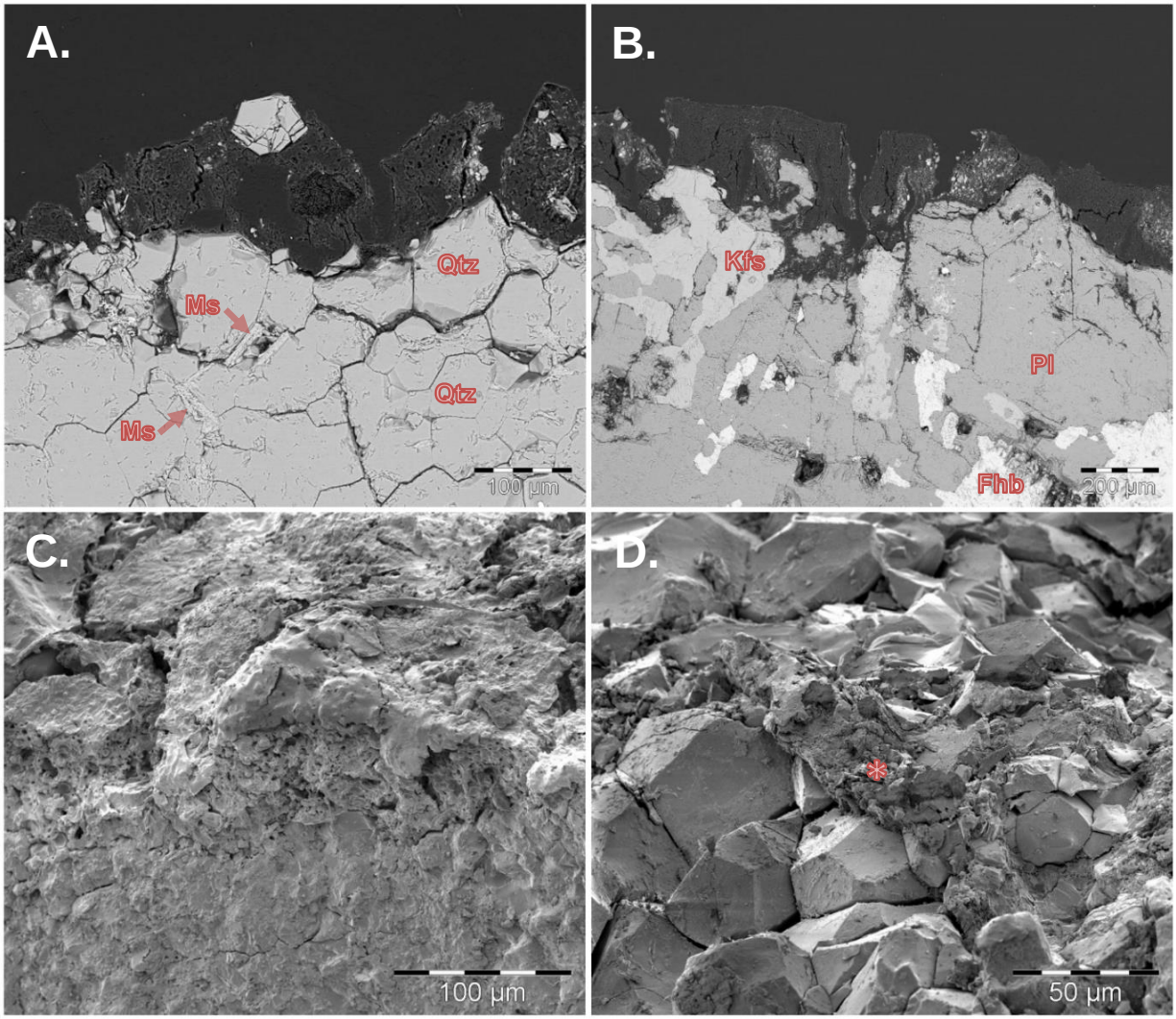


Figure 56: **Micrographs of the interface formed by the crustose *Buellia* thallus and the surface of sub-labile arenite (A) and alkali granite (B). SEM images of bulk samples of sub-labile arenite (C,D): continuous crust-like growth adherent or attached by hyphae throughout its underside (C); side view displaying a polygonal texture as well as the interstitial matrix (red asterisk) (D). Qtz=Quartz, Ms=Muscovite, Pl=Plagioclase, Kfs=K-feldspar Fhb=Fe-hornblende.**

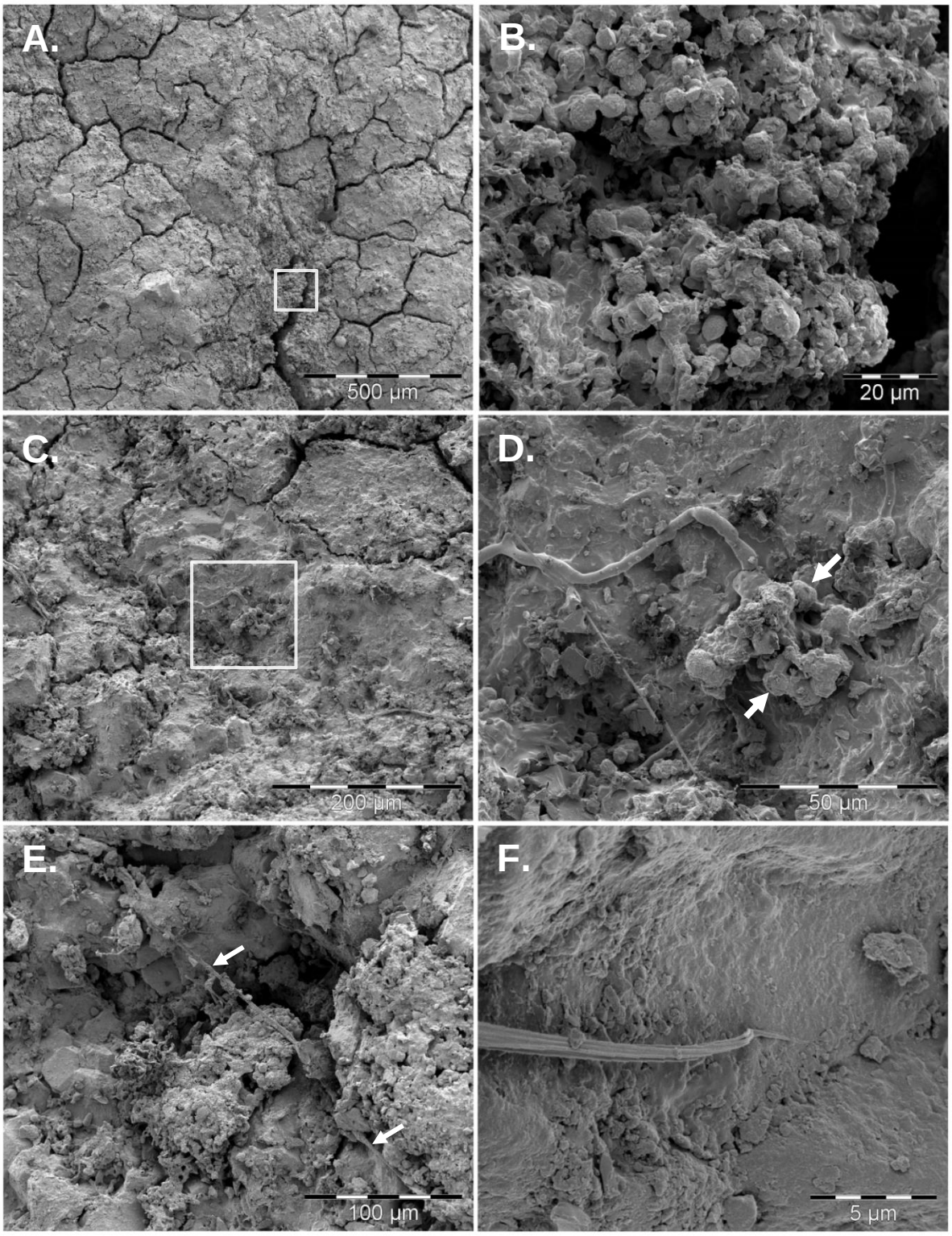


Figure 57: **SEM images of bulk samples of *Buellia* encrusting sub-labile arenite. (A) Surface of *Buellia* thallus extremely rich in small mineral grains incorporated from the bedrock. (B) Detail of square in A, showing *Buellia* thallus in close contact with a colony of algae and fungi. Thallus ontogeny associated with *Buellia* (C,D,E,F): microcolonies of fungi with branching and penetrating hyphae attached to substrate (C); detail of square in C, showing tunnelling and microcolonial fungi (white arrows) on the surface of the substrate (D); lichen hyphae (white arrow) rich in small mineral grains (white arrows) incorporated from the bedrock (E); lichen hyphae etching into quartz grain (F).**

the point of establishment, better highlighted by field relations (Figure 25). It attaches to the rock surface via the entirety of the under surface of the thallus, most often by means of a crust-like growth adherent or attached by hyphae throughout its underside (Figure 56). Ultrastructural details of thallus ontogeny and anatomy are shown in Figures 57 and 58.

Generally, hyphae invade the rock along open fractures, interfaces between grain boundaries, and cavities within the weathering crust, reaching depths from some tens of microns up to 200 µm or more (Figure 56). Additionally, occasional microcracks developed almost parallel to the contact surface at depths lower than 50 µm – these microcracks that are characterised by a marked growth of hyphae through them (Figure 59).

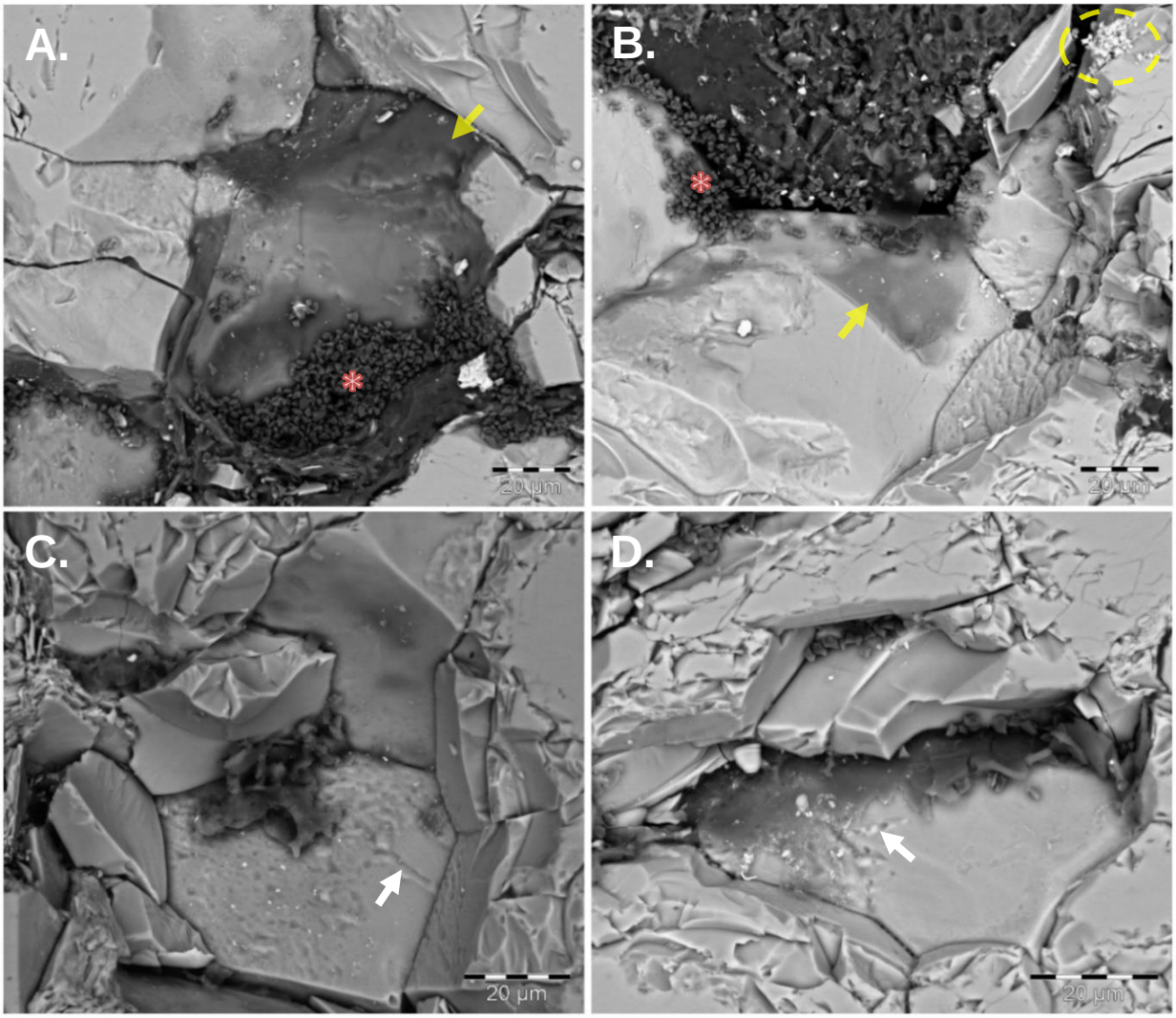


Figure 58: **Fungal growth on and in quartz grains strongly interacting with the quartzitic substrate. (A,B) Fungi (yellow arrows) and organic matter accumulation (red asterisks) along the organo-mineral interface. Also note the crystalline aggregate of calcium oxalate (yellow dashed circle). (C,D) Fungi attached to quartz grains via biologically etched pits. Note the tracks left by the hyphal growth (white arrows).**

The mechanical weathering ability of hyphae was evident through their attachment to, and growth and extension between, mineral grains (Figures 56 & 59). This highlights their ability to displace micro-granules mechanically; some fragments are incorporated into the lichen thallus. Here, matrix (i.e. a discontinuous framework) provides the most regular points of entry. The sections of rocks consisting mainly of unweathered quartz domains do not show morphology allowing the penetration of lichen hyphae and are not significantly attacked by lichen hyphae. However, where such silica-rich domains are in close contact with lichen thalli, the predominant parts consisting mainly of quartz were characterised by microscopic inter-granular void spaces (up to 200 µm or more) which surround the individual crystals and small polycrystalline aggregates.

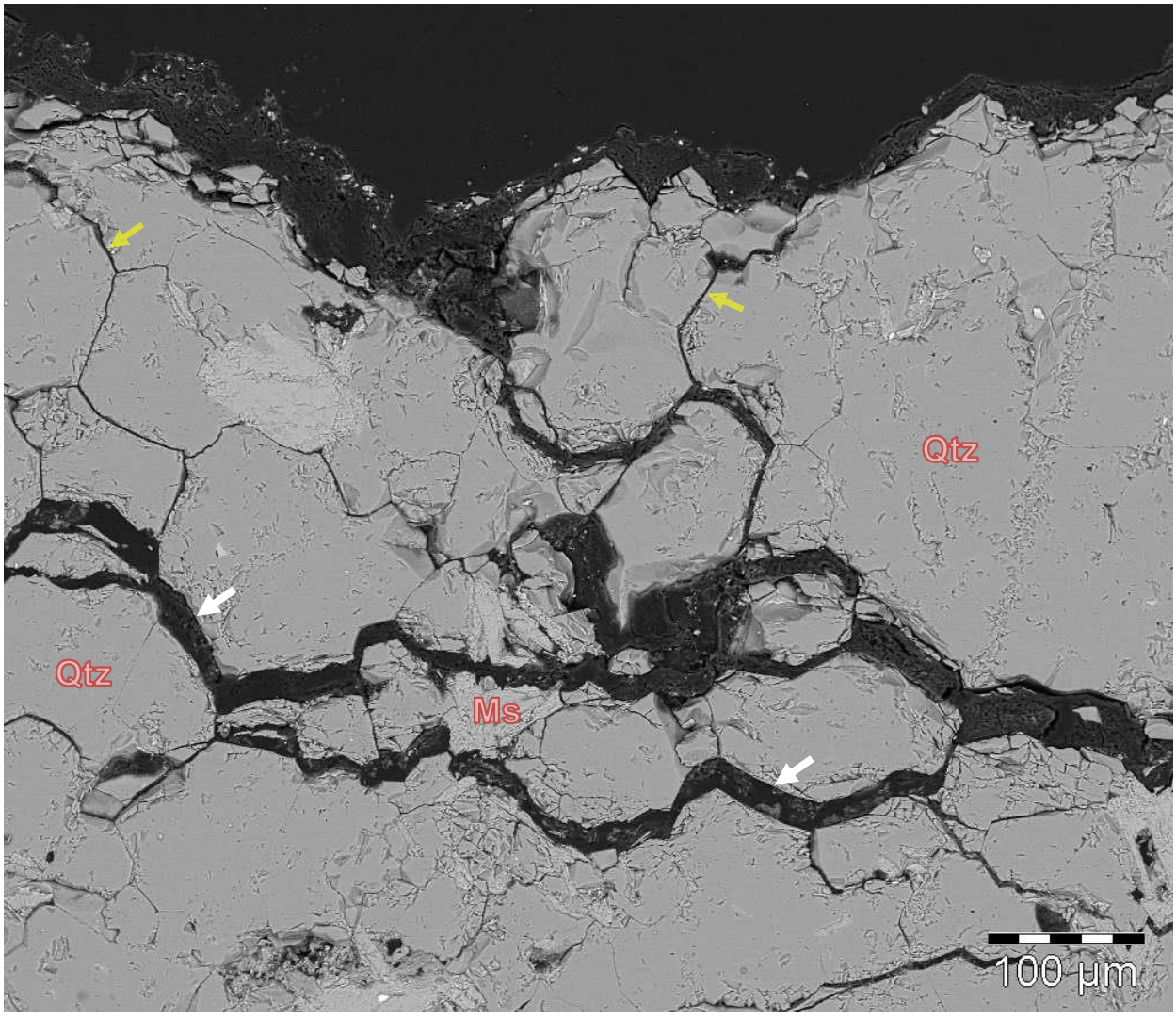


Figure 59: **SEM image of fissures in sub-labile arenite colonized by chasmoendolithic fungi. Fungal masses can be seen deeply and widely protruding into trans- (white arrows)- and inter-granular fractures (yellow arrows). Loose clasts disaggregated from the quartzite by fungal massess can be observed in the lichen thallus, mainly at its top (upper cortex). Qtz=quartz, Ms=muscovite.**

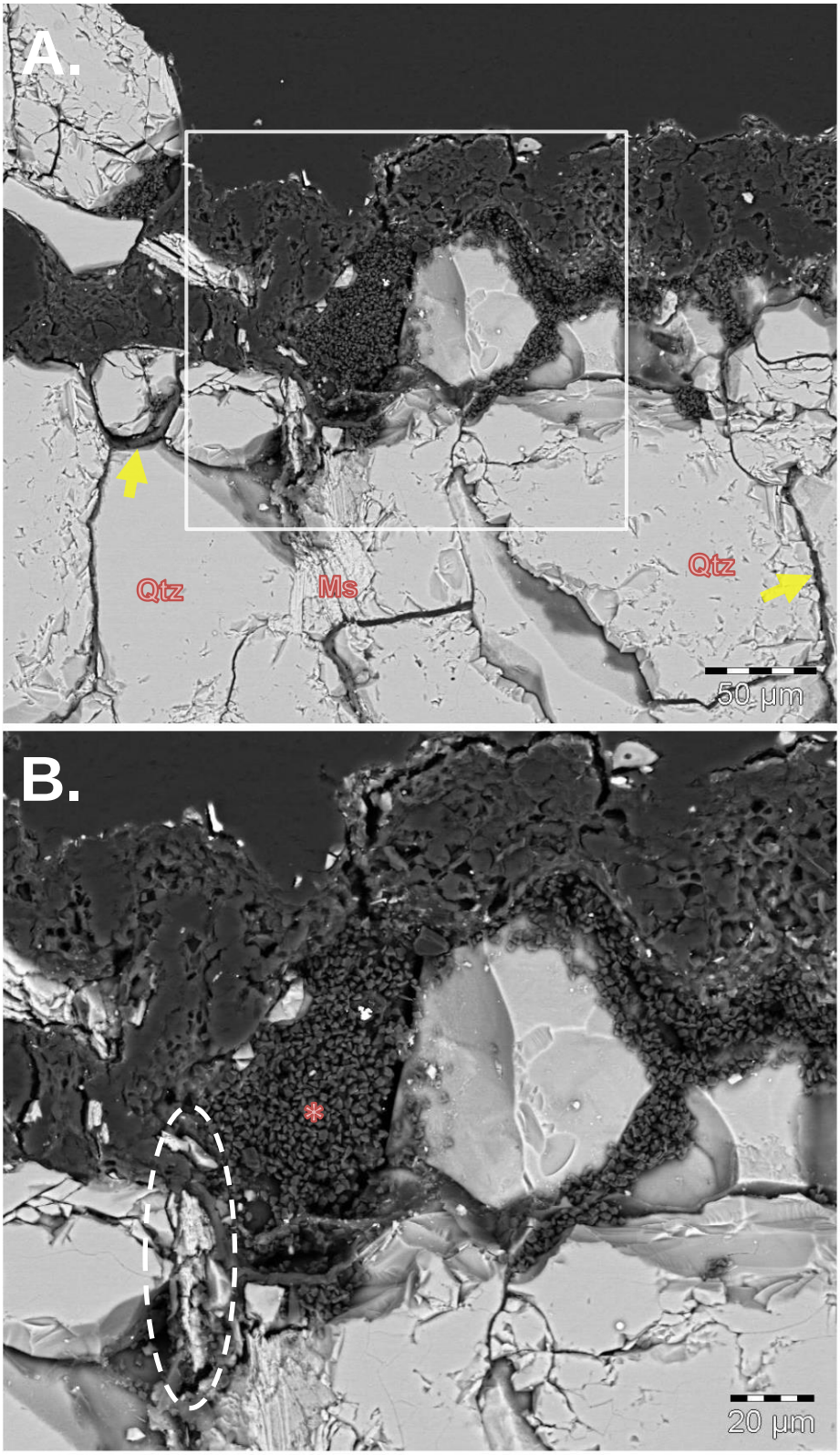


Figure 60: **Detail of the near-surface interface of *Buellia* and quartzite. (A) SEM image displaying the fragmentation and stripping of weak parts off substrate by thallus adhering action. Arrows indicate fissures associated with the points of thallus anchorage to the lithic substrate. (B) Detail of square in A, showing organic matter accumulation (red asterisks) around quartz grains. Note the splitting of muscovite (white dashed circle) and progressive upward incorporation of its flakes) into the thallus. Qtz=quartz, Ms=muscovite.**

SEM-EDS analysis (refer to Appendix E2) also confirms the presence of Fe and K depletion in biologically attacked muscovite – the dissolution of muscovite resulting in a significant release of Fe and K followed by Al with subsequent precipitation of alumino-silicate (Figures 61C & 61D) and oxalate (Figure 58B). Moreover, SEM-EDS revealed a large amount of calcium in oxalate accumulations in contrast to the silicon composition of the substratum. Hence, the oxalate deposits were classified as biominerals of calcium oxalate. Considerable accumulation of organic matter could also be identified (Figures 58 & 60). The fine minerals of alumino-silicate clays observed along intergranular porosity (Figures 61C & 61D) were likely to be the consequence of biomineralization processes. The clay plates contain 2:1 ratio of silicon to aluminium (Appendix E1) indicating the presence of 2:1 phyllosilicates. These 2:1 phyllosilicates are most likely biologically induced chemical weathering products of primary muscovite under the cover of lichen, possibly enhanced by the excretion of organic acid (Barker & Banfield, 1996; Gadd, 2017).

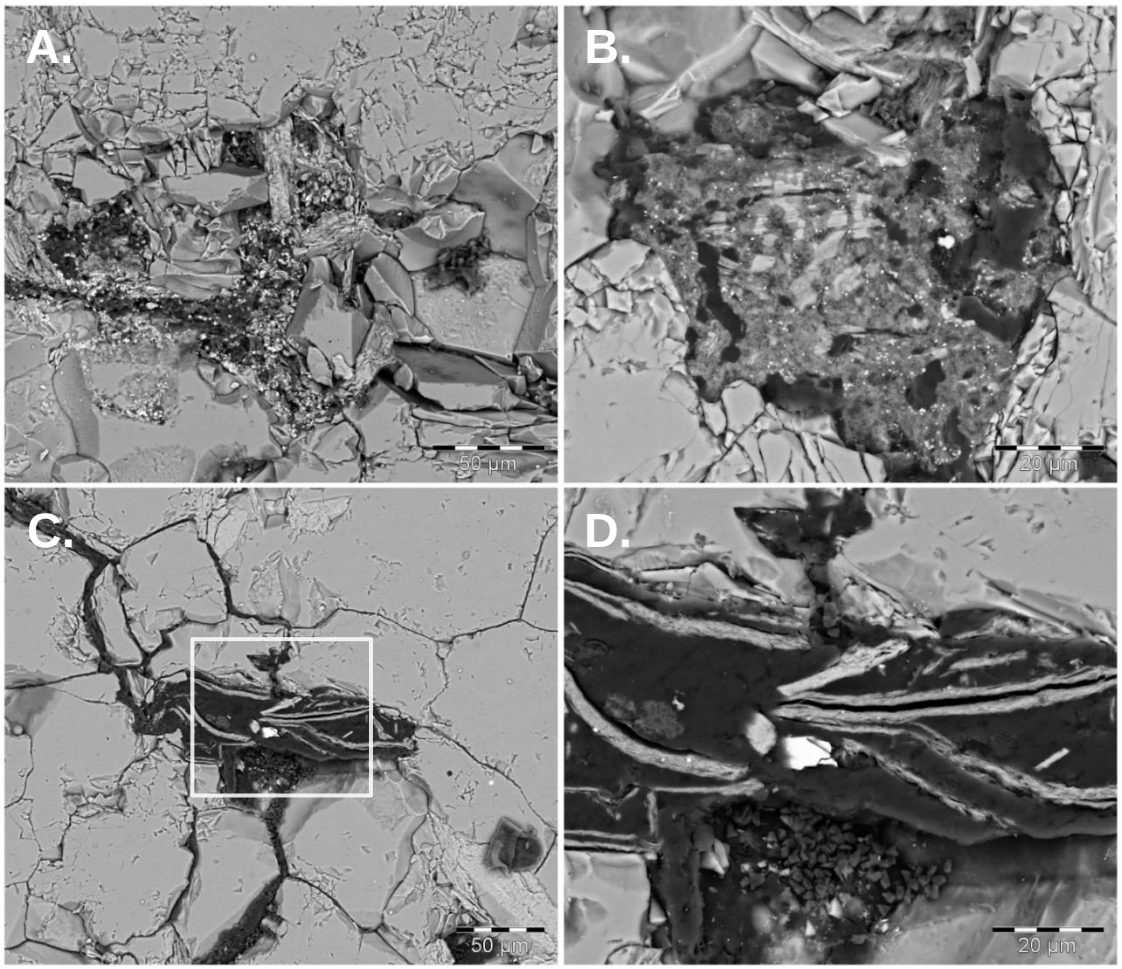


Figure 61: **Visualization of organo-mineral associations in cavities found in sub-labile arenite. (A) Close-up of groundmass composed mainly by intergranular microlitic laths of muscovite and equant mineral grains of Fe–Ti oxides dispersed into a micacious matrix. (B) Highly altered and dissolved muscovite almost totally converted to a siliceous relic following the extraction of aluminium, iron and magnesium from its structure. (C,D) Secondary accumulation of clays at a point of intersecting fractures.**

6.3.3 *Acarospora*

By comparison, the *Acarospora* thalli were slightly thicker with a maximum thickness of about 500 µm (Figure 62). Nonetheless, they were attached to the substratum by means of a crust-like growth adherent or attached by hyphae throughout its underside (Figure 62). Lichen hyphae were able to penetrate the ferrigeneous quartzite by etching their way along planes of weakness and existing open rock pore spaces (Figure 66). Algal and fungal groups without the typical thallus structure show continuity with the crustose lichen thalli (Figure 63B). The close relationship between the hyphae and the lithic substrate has also been observed deeper in the substrate, for example, where algal cells expand through deep, narrow cracks, as shown in Figure 64.

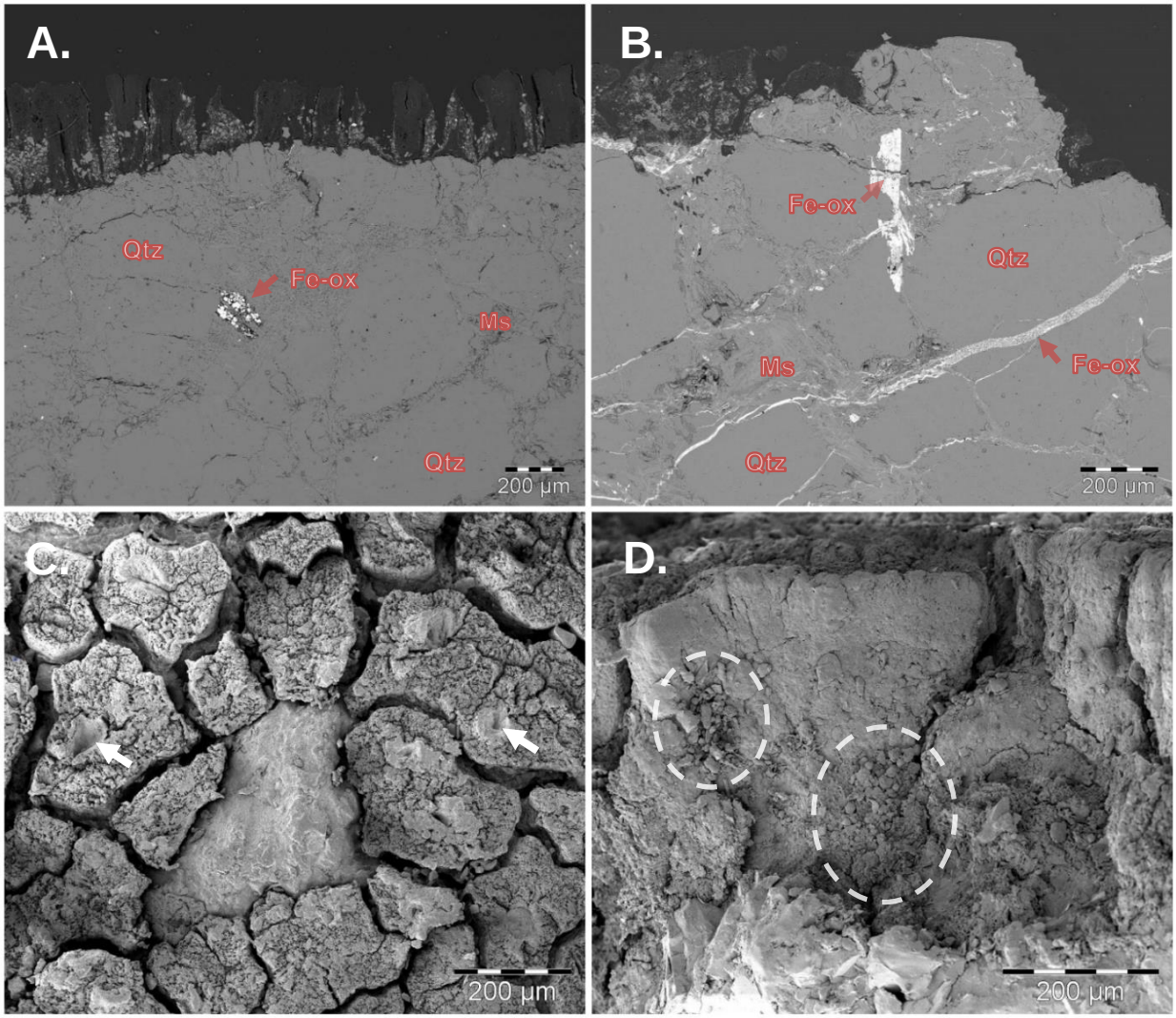


Figure 62: **Interface formed by the crustose *Acarospora* thallus and the surface of ferruginous wacke on a more silica-rich (A) and iron-rich (B) patch of the substrate. SEM images of bulk samples of *Acarospora* (C,D): surface of *Acarospora* sp.pl.' thallus showing sunken apothecia (white arrows) (C); side view displaying patches of fine matrix (white dashed circles) incorporated into the thallus (D). Qtz=Quartz, Ms=Muscovite, Fe-ox=iron oxide.**

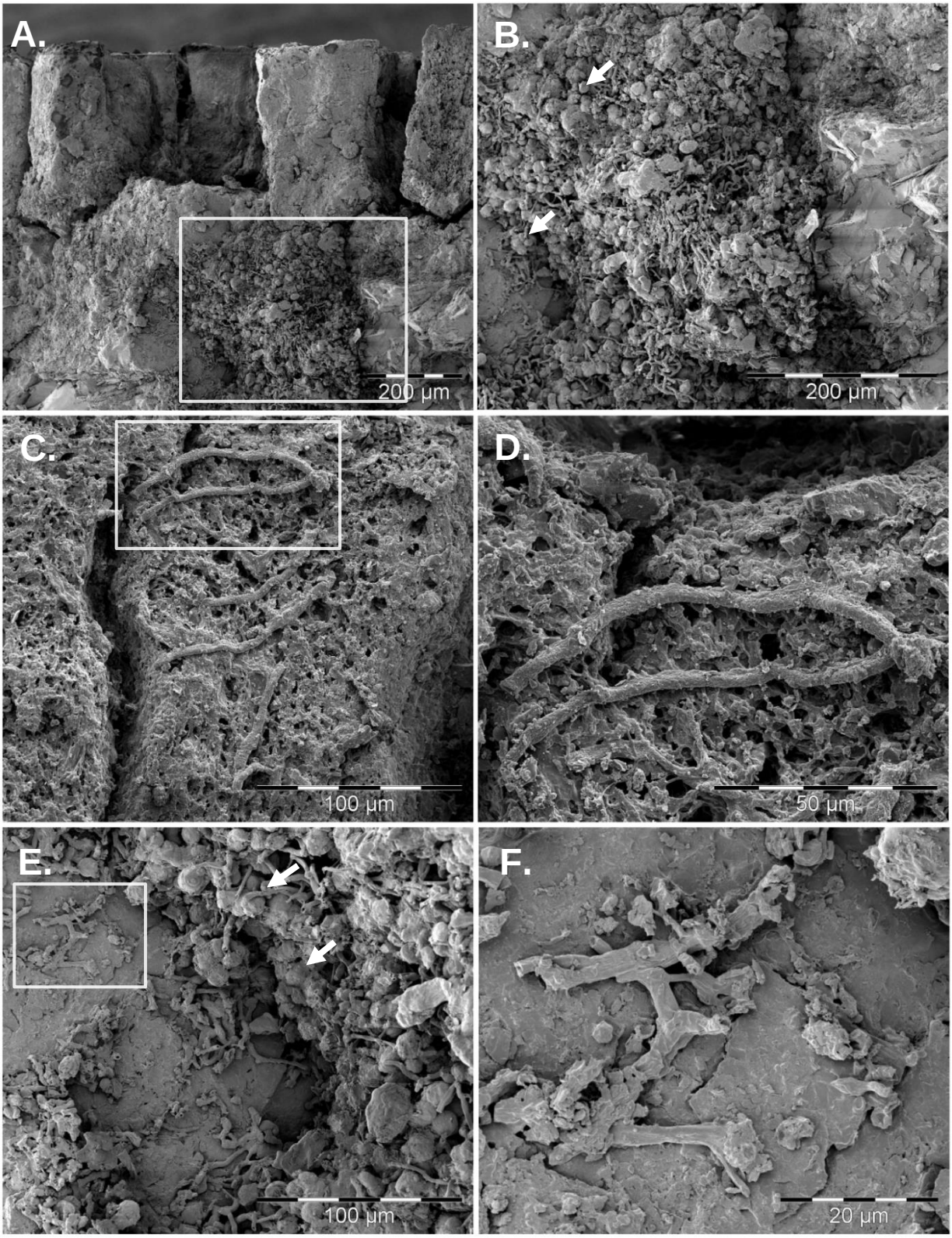


Figure 63: **Thallus ontogeny in the crustose lichen *Acarospora* (A) *Acarospora* thallus in close contact with a colony of algea and fungi. (B) Detail of square in A, showing ultrastructural details of the algal and fungal colony. (C) Surface of *Acarospora* thallus showing microcolonies of fungi with branching hyphae. (D) Detail of square in C, showing ultrastructural details of branching hyphae. (E) Colony of alga and fungi in close contact to substrate. (F) Detail of square in C, showing ultrastructural details of fungi with branching and penetrating hyphae attached to substrate**.

Ultrastructural details of thallus ontogeny and anatomy are shown in Figures 61. As the interlacing hyphae anchored themselves onto the substrate, they dislodged and displaced quartz and matrix-bearing fragments (i.e. muscovite and iron oxide) with their movement, thus contributing to mechanical weathering and erosion. As a result, high concentrations of microgranules (few microns up to few tens of microns) and patches of fine matrix (submicrons)were incorporated into the thallus close to the immediate contact area (Figures 64 & 65). The semi- quantitative chemical composition of the patches of fine matrix follows C>Si>Al with minor amounts of Fe, K, Ti, Ca, Cl and Mg (Appendix E).

Evidence of chemical decomposition was highlighted by dissolution microtextures; iron accumulation in cavities of the rock and lichen contacts and along the cracks; and neogenesis of 2:1 phyllosilicates at the expense of micas (Figures 65-67). Chemical dissolution features were sometimes also observed on the transported mineral clasts, e.g. in some instances their surfaces were covered in aluminosilicate debris with traces of Fe, K, Mg, Na, Cl, and Ti as determined by EDS (Appendix E). Furthermore, a steady decrease in Si, K and Fe content between the immediate contact area and the upper thallus portion was observed. In those cases where the hyphae were located on quartz grains a gradual decrease in silicon content in cell walls and in the matrix between the hyphae and its interface was noted. Moreover, fungal cells were also covered with mineral crystals (Figure 67C). SEM-EDS analysis of the mycogenic minerals showed they were silicate minerals formed as result of organic acid excretion by *Acarospora* sp.pl.

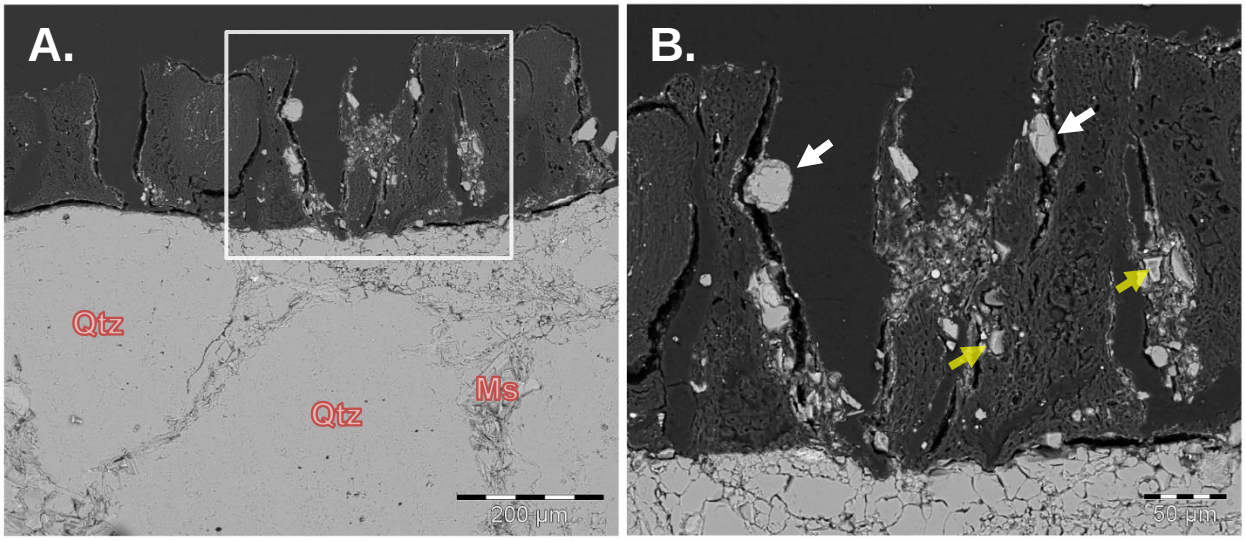


Figure 64: **Detail of the near-surface interface of *Acarospora* and ferruginous wacke. (A) SEM image displaying the fragmentation and stripping of weak parts off substrate by thallus adhering action. (B) Detail of square in A, showing ultrastructural detail of the progressive incorporation of fragmented quartz (white arrows) and muscovite (yellow arrows) grains into the thallus. Qtz=Quartz, Ms=Muscovite.**

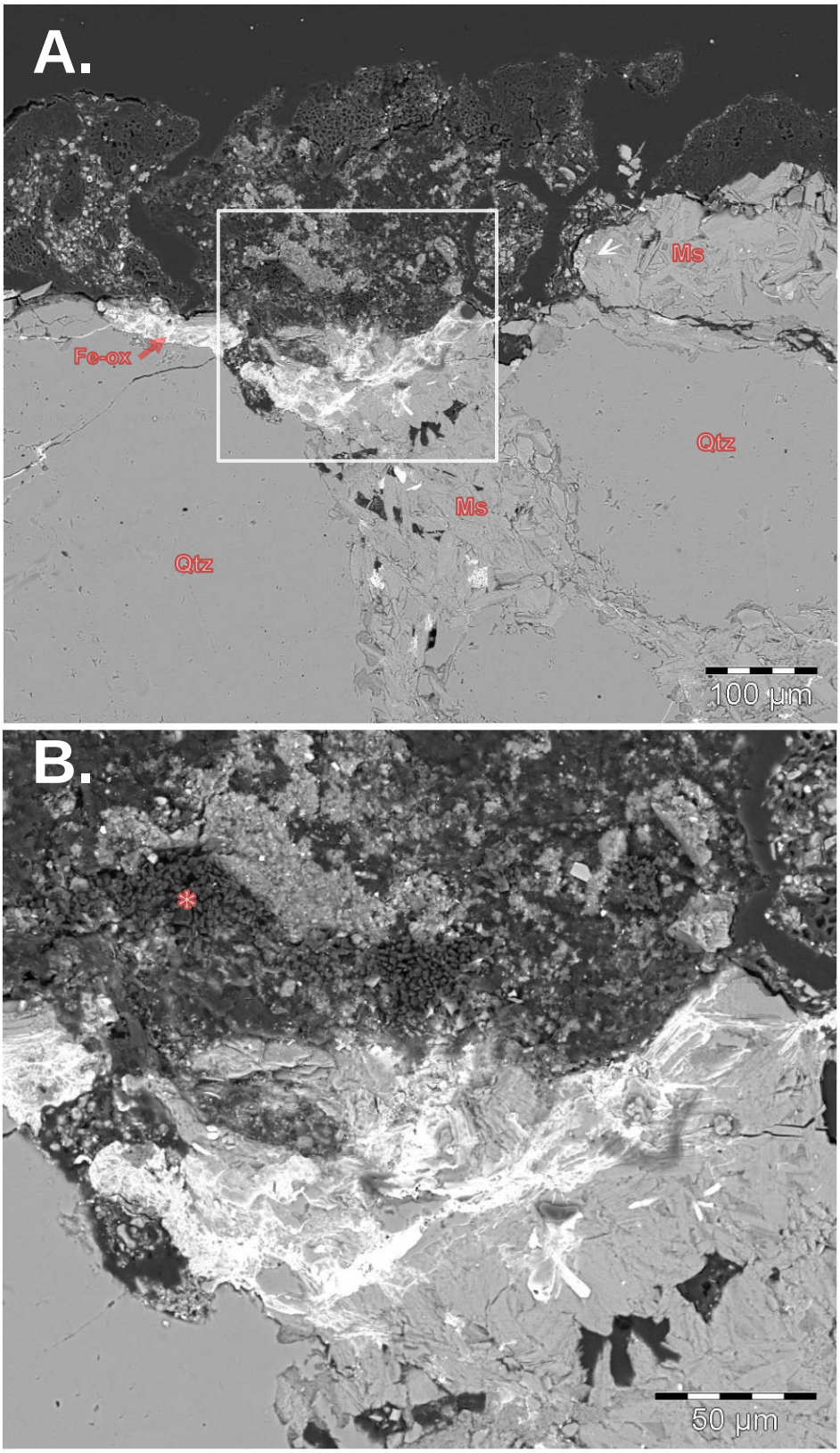


Figure 65: **Detail of the near-surface interface of *Acarospora* and ferruginous wacke. (A) SEM image displaying the fragmentation and stripping of matrix-bearing muscovite by thallus adhering action. (B) Detail of square in A, showing crystalline aggregate of iron oxide and organic matter (red asterisks) along matrix. Note the accumulation of organic matter within fungal hyphae (red asterisks). Qtz=Quartz, Ms=Muscovite, Fe-ox=iron oxide.**

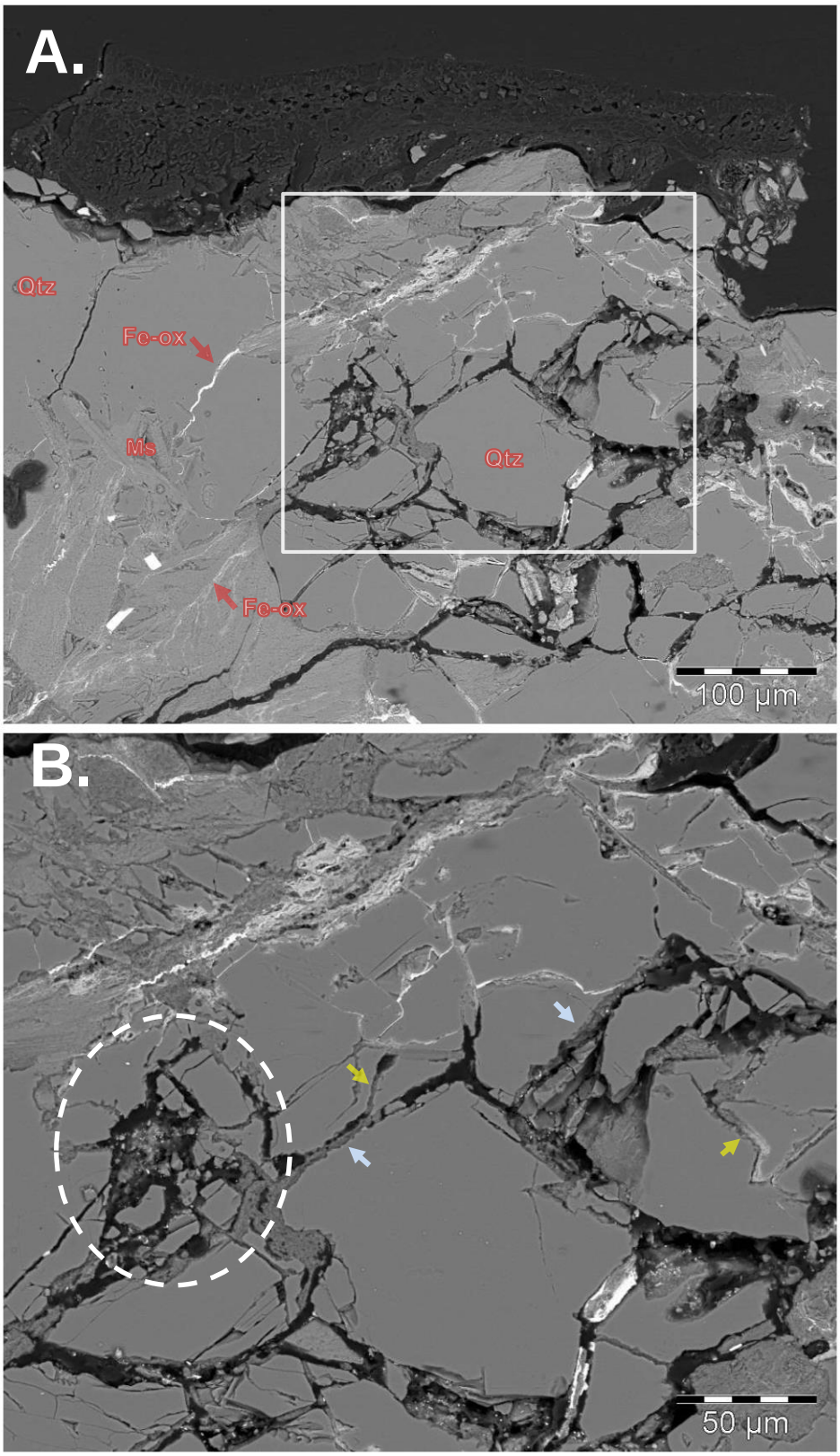


Figure 66: **Intensely fragmented substratum of ferrigineous wacke. (A) Physical penetration of mycobiont hyphae deep within the stone substrate exploiting and enlarging pre-existing fractures and porosity. (B) Detail of square in A, showing chasmoendolithic hyphae deeply and widely protruding into inter- (blue arrows), and intra-granular (yellow arrows) fractures. Note the dissolution and fragmentation of quartz (white circle) and through these layers. Qtz=Quartz, Ms=Muscovite, Fe-ox=iron oxide.**

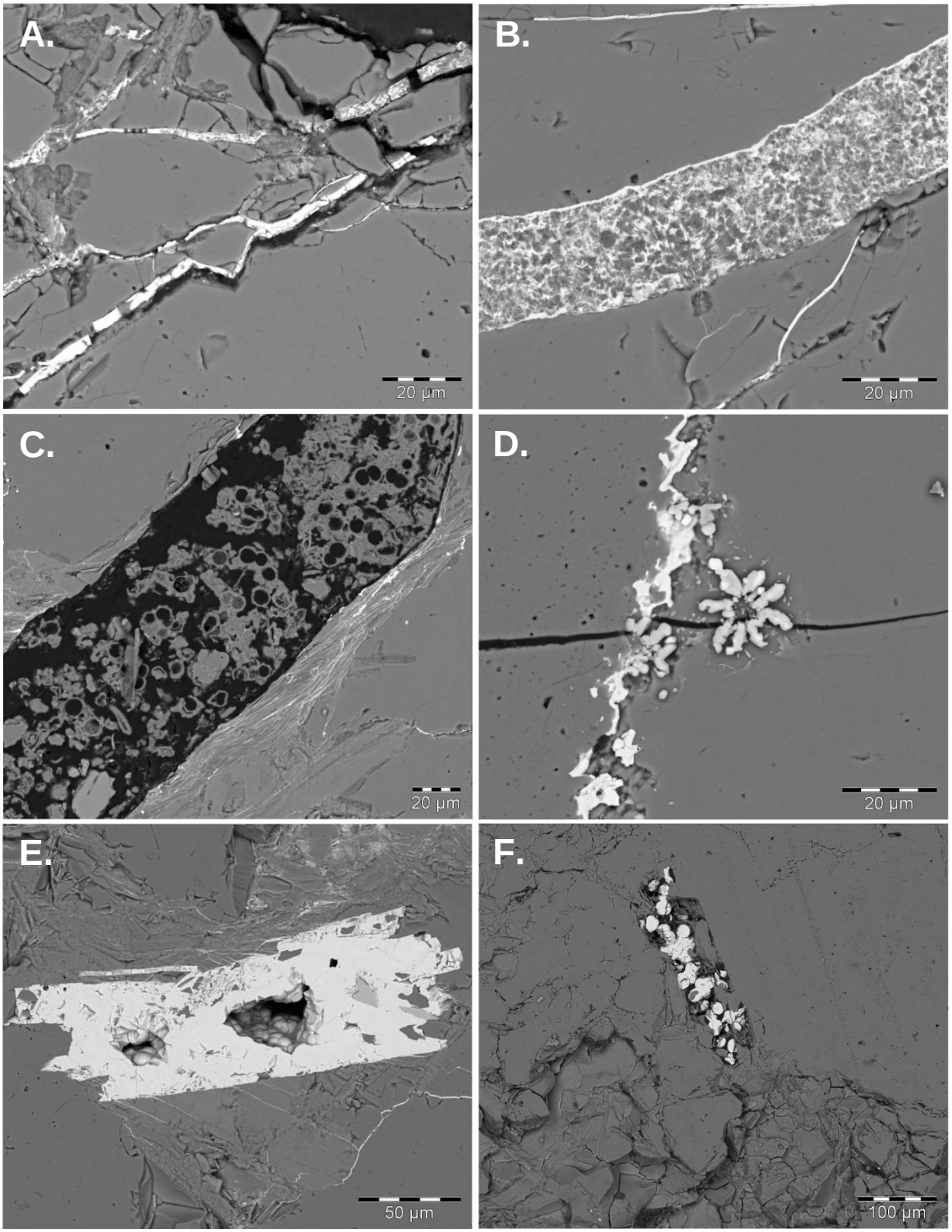


Figure 67: **Visualization of iron accumulation and organo-mineral associations in fractures and pores of ferruginous wacke. (A) Iron accumulation along transgranular fractures. (B) Dissolution of iron oxide by organic acids. (C) Endolithic fungal growth through intergranular porosity. Note how fungal cells are covered with mineral crystals. (D) Secondary iron accumulations through microfractures. (E,F) Vesicle-filling iron oxide with typical botryoidal ("bunch or cluster shaped") habit.**

6.3.4 *Caloplaca*

As was the case with *Buellia* and *Acarospora*, *Caloplaca* also showed a continuous thallus with a maximum thickness of about 200 µm (Figure 68), generally not penetrating deeply into the rock. *Caloplaca* thalli were in tight contact with the minerals in their proximity via a crust-like growth adherent or attached by hyphae throughout its underside (Figure 68). Ultrastructural details of thallus ontogeny are shown in Figure 69.

The mechanical action of *Caloplaca* thalli on the rock generally consists of an extensive disaggregation and fragmentation of the lithic surface immediately below the lichen crust with incorporation of mineral fragments into the growing biological patina (Figure 70A). Hence, its near-

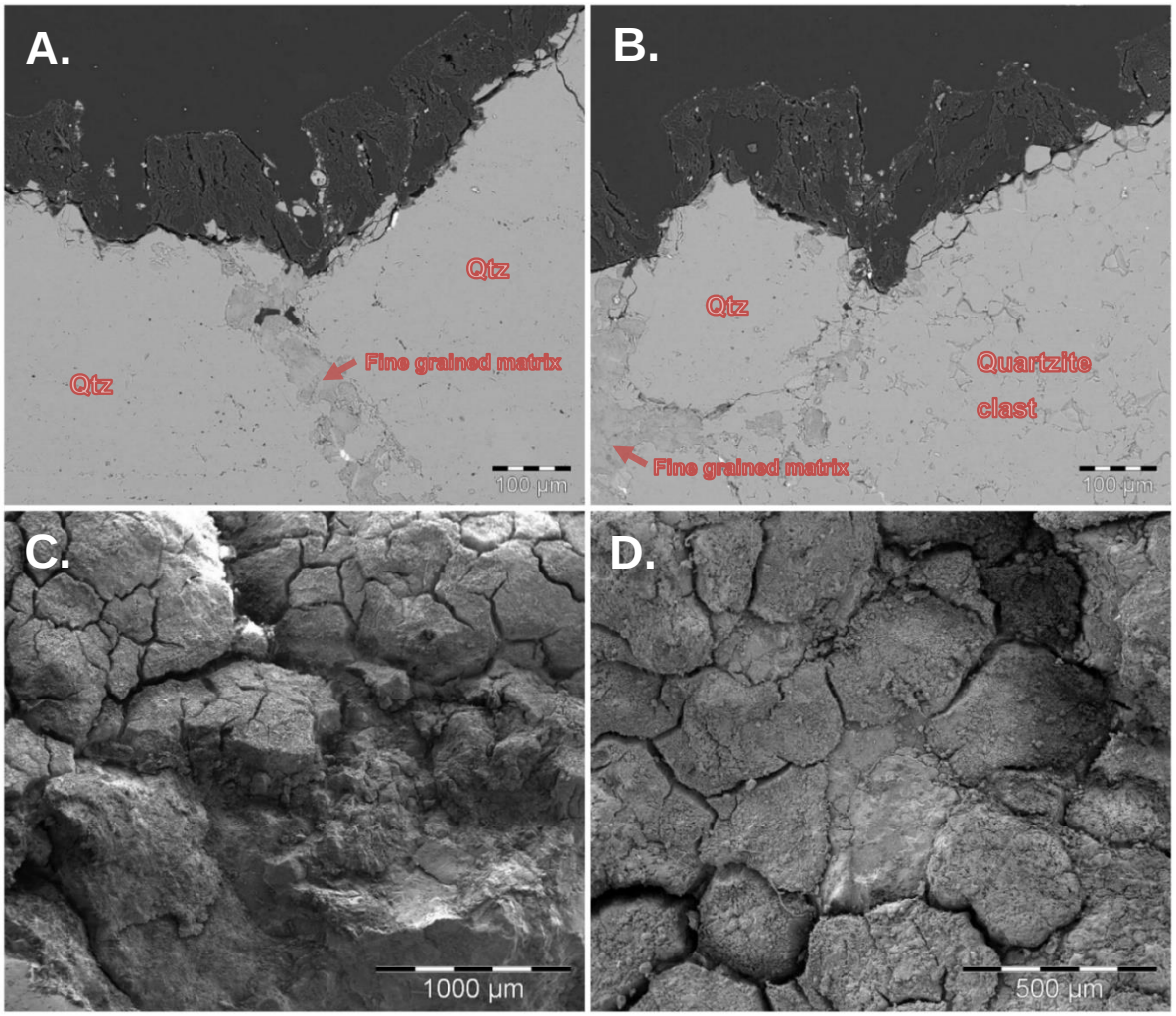


Figure 68: **Micrographs of the interface formed by the crustose *Caloplaca* thallus and the surface of metaconglomerate: lichen hyphae did not penetrate the surface of the rock but weak parts were fragmented by thallus adhering action (A,B); continuous lichen cover attached to the rock surface by hyphae (C); surface of *Caloplaca* thallus extremely rich in small mineral grains incorporated from the bedrock (D). Qtz=Quartz.**

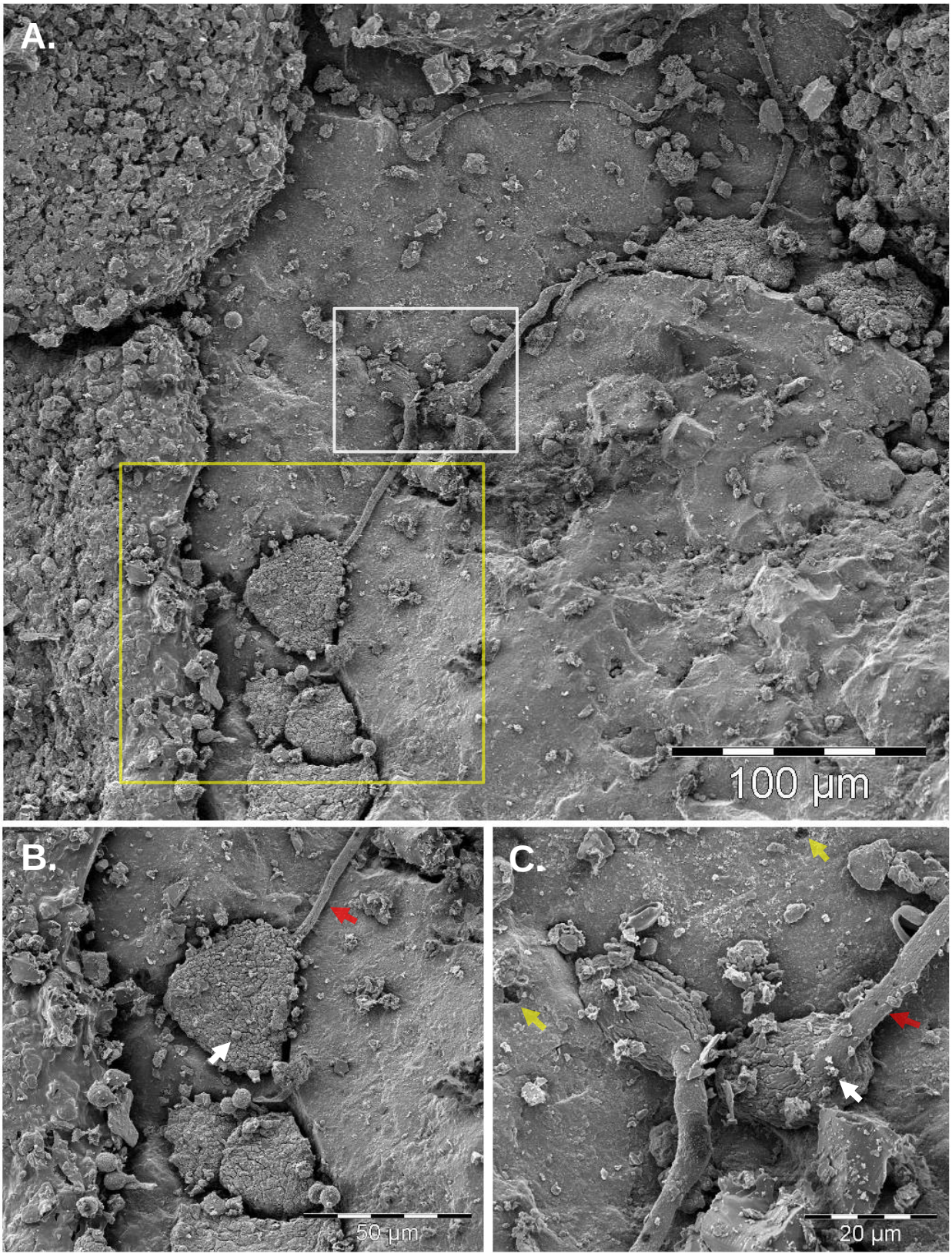


Figure 69: **Thallus ontogeny of the crustose lichen *Caloplaca*. (A) Branching and penetrating hyphae attached to substrate. (B,C) Detail of white square (B) and yellow square (C), providing evidence of hyphae attached to the surface of the substrate. Note evidence of tunnelling (red arrows), surficial holes (yellow arrows) and the dislodgement of microgranules (white arrows).**

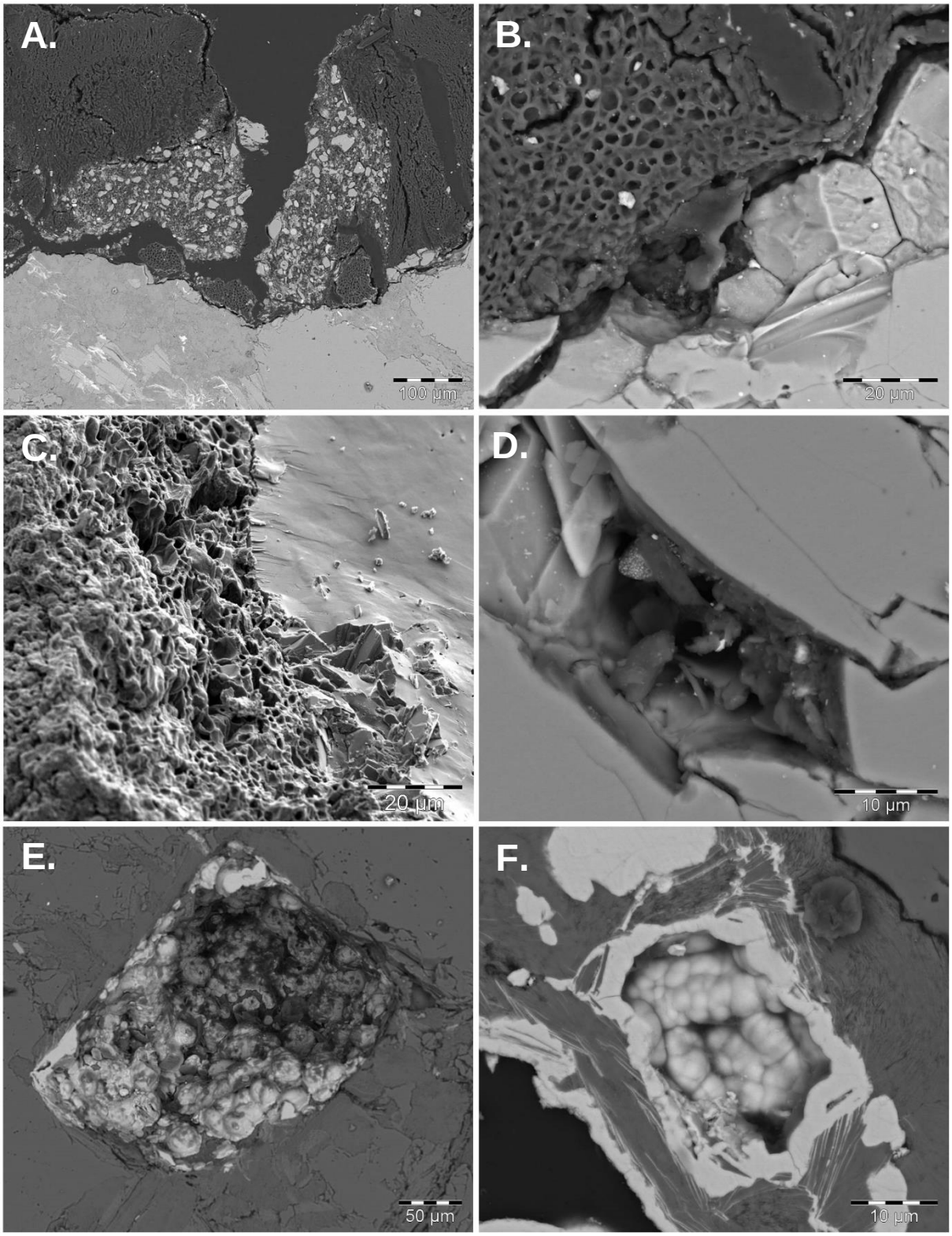


Figure 70: **Detail of the near-surface interface of *Caloplaca* and metaconglomerate. (A) Thick bio-patina with active desegregation and incorporation of mineral fragments from underlying rock substrate. (B) Detail of the near-surface interface of *Caloplaca* and metaconglomerate. (C) Traverse fracture surface of the interface between the medulla of *Caloplaca* and metaconglomerate. (D) Vesicle-filling biofilms. (E) Intragranular biological attack on iron oxide accumulation in a cavity showing both physical and chemical decay. (F) Vesicle-filling iron oxide with typical botryoidal habit.**

surface zone appeared more weathered, with dominant chemical etching features and evidence of almost parallel micrometric cracks, where lichen thallus is in contact with it (Figures 68A, 70B, 70C).

Although no directional preference of attack by mycobiont hyphaewas discernible, the fine-grained matrix seemed to have provided regular points of entry with consequent splitting of matrix-bearing muscovite and their progressive upward incorporation into the lichen thallus (Figures 68A & 68B). EDS analysis confirmed the presence of Fe and Mg depletion in biologically attacked muscovite, resulting in a significant release of Fe and K followed by Al with subsequent precipitation of poorly ordered iron oxides and secondary clays.

6.4 DISCUSSION

Impact cratering can favorably change the availability and habitability of a substrate for living organisms (e.g. lichens and microbes), which are then able to (re)colonize microfractures and pore spaces created during the impact. In doing so, these living organisms in turn weathers the rock substrate, contributing to the preliminary phases of soil formation and cation mobilization (Wierchos *et al*., 2015). In correspondence with the research aims and objectives, results were primarily focused on providing detailed documentation of the potential role of biologically mediated degradation of impact-induced silica-rich rock varieties by saxicolous lichens.

The following discussion will aim to interpret the findings of the µCT and SEM data, by describing the rock architecture (i.e. microstructural characteristics and three-dimensional textural relationships at a pore-scale level) of targeted silica-rich rock varieties, as well as identify and discuss chemical variables that correlate with changes due to lichen deterioration.

6.4.1 Rock architecture

As observed with X-ray tomography techniques, microstructural characteristics and three-dimensional textural relationships, varied significantly between targeted silica-rich rock varieties. Together, these internal structural elements (porosity, permeability, light transparency, and crystallization features) give rise to a new understanding of the features and functions relevant to the rock bioreceptive characteristics.

Amongst the silica-rich rocks studied, granitic rocks showed a particularly dense cover of saxicolous lichens (refer to section 5.2). This may be, at least partly, attributed to the fact that granitic rocks contain a greater number of fractures as well as a greater total pore surface area

for pores >1 pm in diameter, which gives granitic rocks the highest porosity among the examined silica-rich rock varieties. Such a high presence of void space provides a habitat for microorganisms and facilitate access into the rock (Ascaso & Wierzchos, 2003; de los Ríos *et al*., 2005a; Guglielmin *et al*., 2005; de los Ríos *et al*., 2007; Büdel *et al*., 2008; Archer *et al*., 2016). Granitic rocks, thus, seems to act more like a very dense soil rather than a sealed hard rock.

By comparison, the metasedminetary rock varieties had a much more complex structure with a less easily resolvable pore network. Unlike granitic rocks, the largest portion of the pore volume is hosted within isolated pores, which control bulk rock compressibility and account for the greatest fraction of the whole-rock porosity. Metasedimentary rocks showed a well-defined decrease in porosity and permeability, hence, less frequent colonisation by lichen assemblages. Referring to the stress–strain behaviour, the above observations suggest that a pore collapse occurred which reduced the number of macroscopic cracks that were accessible from the surface of the rock by pioneer organisms (Cockell & Osinski, 2007; Cockell, 2011; Pontefract *et al*., 2014. Nevertheless, metasedimentary rocks often exhibit two distinct groupings of microcracks which facilitate access into the rock, including: a) a shallower group of thin, parallel microcracks at the rock-surface, and b) a group of deeper and wider cracks in the inner rock portions (refer to section 6.3).

Based on the measured rock properties and the estimated porosities by analysing the reconstructed gray-value images from the X-ray computed tomography, the targeted silica-rich rock varieties were classified in three groups with respect to porosity and composition:

(i) Highly porous feldspar dominated (> 75% feldspar) granites, with large-sized fractures characterized by large apertures and channel structures (between 100 to 1000 µm in size). Pores between 100 to 2000 µm contribute most to volume and hence to fluid storage capacity.

(ii) Intermediate porous quartz dominated (> 75% quartz) metasedimentary rocks (we refer here to ferrugineous wacke and metaconglomerate), with medium-sized fractures of high to intermediate apertures and variable fracture geometries (between 100 to 500 µm in size) in a porous matrix. Pores between 100 to 500 µm contribute most to pore network connectivity and hence to fluid flow.

(iii) Low porous quartz dominated (> 75% quartz) metasdimentary rocks (we refer here to sub-labile arenite) with small, highly variable pores and microfractures (below 200 µm in size) in a low porous matrix. Pores below 200 µm contribute most to number.

On the whole, the pore-fracture network drives the elemental transfers in the interior of the upper 1–2 cm of the rock substratum. The fractures that were connected and physically linked to the surface of the rock represent preferential paths for microbial growth and fluid circulation, which in turn accelerate the dissolution of the clasts and concomitantly contribute to the binding of the clasts by the hyphal network (Ougier-Simonin *et al*., 2016).

I conclude that the irregularity of lichen colonization was caused by the heterogeneous nature of the targeted silica-rich rock varieties. The fractures and pores are not evenly distributed throughout the rocks because the effects of the shock caused by the impact are not homogeneous. As such, their behavior in a strain field would be different. As it is difficult to directly distinguish between impact-induced factures and tectonically induced fractures in the weathered crust I studied, it is not possible in this case to quantify the degree to which impact-induced fractures may have played a role in the rate of weathering of this material.

6.4.2 Mechanisms of rock and mineral bioweathering

Lichen growth on rock substrate promotes biomechanical and biochemical processes which influence the weathering rate of the original mineral in the rocks and the appearance of new minerals (Bjelland & Thorseth, 2002; Büdel *et al*., 2004; St. Clair & Seaward, 2004; Favero-Longo *et al*., 2011; Vingiani *et al*., 2013; Shukla *et al.,* 2014; Mitchell *et al*., 2016). The role of lichens as a weathering agent, which is characterized as one of the strongest effects on the substrate (Chen *et al*. 2000; Adamo & Violante, 2000), was demonstrated in a detailed manner.

6.4.2.1 Characteristics of the weathering crust

Within the Vredefort Dome, impacted silica-rich rocks were primarily colonized by crustose lichens (we refer here to *Acarospora* sp.pl., *Caloplaca* s. lat. sp.pl., and *Buellia* sp.pl.). Nevertheless, foliose lichens (most often *Xanthoparmelia* sp.pl.) were also encountered regularly, especially on shaded slopes where the evaporation rate is expected to be lower than in the open. In most cases foliose thallus was 1 to 1.5 mm thick whilst crustose thalli were 200 to 400 µm thick. From several points marked in Appendix E, energy spectra were made to show the distribution of constituents in the surface of a mineral grain, the surface of hyphae and matrix between hyphae. None of the elements were concentrated in the lichen thallus to a degree radically different from that present in the rock, apart from carbon and potassium. Moreover, microtextures and secondary microstructures were highly significant in determining the weathering behaviour of target lithologies.

A comparison among the specific biomechanical and biochemical attacks promoted by the four lichens under investigation showed that all of them indifferently attack any primary mineral of the targeted rock lithology without any preference. However, some of the mineral phases, such as feldspars, mica, and amphibole were more prone to fragmentation and/or flaking, to be intruded by mycobiont hyphae into crystal discontinuities and to be incorporated into the thallus. Even quartz and iron oxide were found to be colonized quite sinificantly. Both inter- and intra-granular microtextures and secondary microstructures induced by straining are highly significant in determining the weathering behaviour of these minerals.

The primary mycobiont impact on granitic rock types appears to result from biomechanical action, this being manifested by extensive hyphal penetration and tunnelling into otherwise intact mineral material, for example along fractures, crystal planes, grain boundaries, and cleavages. The process of invasive growth is facilitated by spatial exploration of the environment to locate and exploit new substrates, to acquire nutrients from solid materials (Le Pera & Sorriso-Valvo, 2000; Money, 2004; Boswell *et al*., 2003; Gadd, 2007). In terms of directional preference of penetration, the most delicate mineral components in granitic rocks appeared to be plagioclase, biotite and Fe-hornblende. Plagioclase was found to be generally more weathered than K-feldspars, possibly associated with differential dissolution due to minor variations in chemical composition (Scarciglia *et al*., 2012). Feldpsar are the repositories of most of the total content of nutrient cations and represent particularly unstable constituents (Jones *et al*., 1981). Biotite and hornblende provide a relatively soft, Fe-rich environment for lichens and other organisms during the initiation of the weathering crust.

In comparison, during a meteorite impact into a sedimentary target a proportion of the impact energy is taken up by pore collapse, which result in a well-defined decrease in particle size and permeability (Cockell *et al*., 2005; Cockell, 2011; Pontefract *et al*., 2014). This phenomenon may transform target material from one suitable for endolithic colonists to one unsuitable for endolithic colonists. Nonetheless, the metasedimentary rocks of the Vredefort Dome were transformed from one suitable for cryptoendolithic colonists to one better suited for chasmoendolithic colonists. This is in agreement with the findings of Cockell & Osinski (2007).

Only through particular mineral phases, which will be specified below, metasedimentary rocks are invaded in depth by mycobiont hyphae. Here, matrix-bearing phyllosilicates (e.g. muscovite) provide points of weakness and significantly increase susceptibility to attack. Unlike phyllosilicates, quartz and iron oxide are not affected by internal voids, hence, they appear to block penetration almost completely. In certain cases, however, quartz and iron oxide have been

found to be effectively dissolved by organic acid attack, manifested by their corroded aspect and the presence of etch pits and/or dissolution lines. Such pits presumable represent the sites of structural dislocations in the mineral and are, consequently, regions of excess strain susceptible to preferential dissolution (Banfield *et al*., 1999; Bennett *et al*., 2001).

Generally, where there are numerous lithic fragments which were included into the thallus as a result of the weathering action of lichens, organo-mineral associations can be especially well observed. Once organo-mineral associations have established themselves on the rock substrate, lichens or their mycobionts may cause disaggregation and/or dissolution of these materials, leading to the preliminary stages of fine earth formation *in situ*. Some of these fragments were probably aeolian and became entrained within the thallus; however, large grains (e.g. feldspars, mica, hornblende and quartz) deep within the thallus and the eroded appearance of these substrate around lichen-colonized zones suggest that dissolution of these components occurs.

Clay neogenesis was closely associated with fungal mass, this being manifested by discrete accumulations of clays in the organo-mineral horizons under each lichen colony. These clays are most likely biochemical weathering products of primary feldspar, micas and chlorite, probably enhanced by organic acid excretion (Scarciglia *et al*., 2012). Such clays also provide a good water storing capacity and are expected to provide preferential spots for organic matter sorption (Mergelov *et al*., 2018). Interactions between clay minerals and fungi may also alter the adsorptive properties of both clays and hyphae and may stimulate or inhibit fungal metabolism (Morley & Gadd, 1995; Fomina & Gadd, 2002).

The presence of calcium oxalate in the weathering crust of sub-labile arenite was consistent with other observations of calcium oxalate precipitation by lichens on rock substrata (Fomina *et al*., 2004; Gadd *et al*., 2007, 2014). Mycogenic secondary minerals were also identified – these minerals which display distinctive morphologies indicative of the presence of microbial communities. Secondary iron accumulations, especially in ferrigunous wacke and metaconglomerate, is indicative of the decomposition of the silicate minerals. In addition, considerable accumulation of organic matter could be identified, especially around the hyphae or closely associated with them. “The organic matter and cell excretions enable a heterotrophic bacterial population to thrive, representing a synergistic effect of the lichen thallus on weathering processes” (Chen & Blume., 2002).

On the whole, the broad range of microtextures (refer to Table 14) could be among the effective preconditioning factors that lead to the deterioration of impacted silica-rich rocks (e.g. Newsome

& Ladd, 1999; Migoń & Thomas, 2002). “The element release from rocks depends on progress of chemical weathering on microstructure properties, characterized by nearly closed, semi-open and completely open micro-systems which are interconnected by fractures or pores” (Meunier et al. 2007). Hence, the progress of solid rock weathering is affected by the initial porosity system and sensitivity of mineral associations. Moreover, the manifestation of weathering zones and initial stages of *in situ* fine earth formation emphasises the importance of organic carbon stabilization mechanisms in endolithic systems (e.g. Mergelov *et al*., 2018).

6.4.2.2 The weathering sequence

A general scheme for the weathering of the silica-rich rock varieties can be hypothesized. First, lichen propagules become established on the surface of the rock, targeting nutrient rich mineral components such as feldspar, mica and amfibole. The extension and expansion of lichenized fungi inside silica-rich rock varieties was governed by the presence and orientation of void space. “Such void space depends on the structural organization, mineralogical composition and alteration status of the lithotype” (Bjelland & Thorseth, 2002).

Initially, biomechanical breakdown of the substrate occurs through hyphal penetration and related expansion and contraction capabilities. This may increase the available surface area and expose more reactive sites, after which primary mineral components disintegrate into microgranules. The existence of greater surface energy in impact-induced rocks increases the volatility of inter-mineral contacts, thus promoting grain-by-grain disintegration of the rock substrate. Subsequently, high concentrations of microgranules and patches of fine matrix were incorporated into the thallus. In agreement with the literature on other substrata (e.g. Adamo & Violante, 2000; Chen *et al*., 2000), this microcrystalline fraction comprises (a) lithic fragments deriving from the surface disintegration of the substratum, (b) neoformation minerals deriving from the surface weathering of substrate, (c) phases deriving from biomineralization connected to lichen metabolism, and (d) fragments deriving from aeolian processes.

As soon as biomechanical breakdown progresses, further biochemical reactions occur, increasing the production of a fine matrix. “This may favour chemical attack as a prolonged interaction between mineral surfaces and the circulating soil solution is promoted” (Scarciglia *et al*., 2012). Similarly, organo-mineral associations in fractures and pores seem to induce etching of primary minerals, due to the acidic behaviour of humic substances. Highly weathered primary minerals also allow for newly formed secondary weathering products to precipitate and crystallize at the lichen rock interface or, indeed, within the lichen thallus itself.

6.5 SUMMARY

Advanced multi-scale and multi-dimensional observations were made on microstructural characteristics (pore space and microcracks) and three-dimensional textural relationships for selected samples of silica-rich rock varieties from the Vredefort Dome, South Africa. 2D and 3D datasets were collected using a combination of µCT and SEM techniques. The present findings show that fractures and pores are present in impacted silica-rich rock varieties, some of them being open, others being sealed by mineral precipitation or just closed elastically. These fractures and pores nucleate along heterogeneities initially present at all scales in the target lithology, then propagate and may connect in 3D. Whether fractures and pores were produced by internal (fracturing caused by maturation of organic matter) or external (impact shock and/or tectonic loading) loading is not possible to decipher, nor- which kind of loading controlled its formation (e.g. Ougier-Simonin *et al*., 2016; Ma *et al*., 2017).

Foliose thalli showed a mean depth of massive penetration of 1.5 mm or more; for crustose thalli, the mean values ranged from 200 to 400 µm. These results tend to be disproportional to the extent of thalli development: foliose *Xanthoparmelia* lichens, with the most developed thalli of those considered, are less invasive than the thalli of crustose lichens (200-400 µm). Amongst the silica-rich rocks under investigation, the most penetrable mineral components were feldspar (especially plagioclase), mica (especially biotite and muscovite) and amphibole (mostly Fe-hornblende). As previously alluded to, the preferential breakdown of these minerals may be attributed to their relative softness and morphology. Furthermore, their breakdown may release important nutrients that would otherwise remain bound (e.g. Mg, Ca, K and Fe). Even though quartz typically shows an exceptionally high weathering resistance, chemical weathering of silicate minerals must be significantly enhanced under biotic conditions (Büdel *et al*., 2004). This was evident as the effect of lichens on targeted silica-rich rock varieties lead to the transformation of rock silicates and iron extraction from silicates induced by organic acids.

On the whole, it is possible to accept a well-developed pore-fracture network as a prerequisite for biological weathering processes. Coexisting biotic and abiotic weathering processes were demonstrated in which the initial impact-induced pore system sets conditions for water- and hyphal penetration within the rock. Biomechanical weathering here is accompanied by local biochemical weathering, this being manifested by dissolution microtextures; iron accumulation in the micro-zones of rock and lichen contacts and along microfractures and cavities; and neogenesis of mycogenic minerals, clays, and/or alumino-silicates at the expense of primary minerals.

CHAPTER 7

CONCLUSIONS AND RECOMMENDATIONS

In order to resolve a particular lack of information regarding the potential role of saxicolous lichens in the degradation of impact-induced rock surfaces in the southern hemisphere and African ecosystems, a biogeochemical study of the Vredefort Dome was undertaken. With regards to the study aims (section 1.4), this chapter will now conclude on the findings by summarising the results of the respective chapters. Recommendations for further research and closing notes are discussed at the end of this chapter.

7.1 GEOLOGY OF THE STUDY AREA

Through the investigation of field relations and geological analysis, it could be established that the Vredefort impact event caused profound changes to target lithologies. In the case of saxicolous lichens, these effects were usually not significant because they mainly grow on the outer surfaces of rocks, where rock porosity is not a growth factor. However, by increasing either the surface area for chemical weathering or the surface area for biosphere/geosphere interaction, impacts may play a role in increasing weathering rates. In particular, impact shock may sufficiently alter the chemistry of target rocks, contributing to the fracturing of the rock, and in some instances increasing their translucence for phototrophs (Cockell *et al*., 2002, 2005, 2010). The possible extent of the effect of impact events on weathering, both chemical and biological, merits further investigation.

Saxicolous lichen assemblages were quantitatively analysed for frequency, with reference to species richness (number of selected lichen genera), growth form diversity, and associated morphological features (refer to Table 10). Two lichen growth forms, foliose and crustose, were encountered. The crustose lichens *Acarospora* sp.pl. and *Caloplaca* s. lat. sp.pl. with sunken apothecia were recorded as the dominant lichens most often associated with siliceous rocks, followed by *Buellia* sp.pl. and the foliose lichen *Xanthoparmelia* sp.pl. The latter seemed to be localised to granitic outcrops, especially alkali granite.

The results provide support in considering the geology as one of the key factors controlling species distribution and physiognomy in the dome. This was also previously noted by others (Mogg, 1961; Bezuidenhout and Bredenkamp, 1988; Mucina & Rutherford, 2006; Balkwill, 2009; Boneschans *et al*., 2015; Boneschans, 2018; Siebert *et al*., 2018).

7.2 BIOWEATHERING

Factors of biomechanical and biochemical weathering can be considered, at least in part, to be related by reciprocal cause-effect relationships at the micro- and macro-scale. Here we interpret bioweathering at the micro-scale. A detailed, multifaceted description of the 3-D spatial architecture (i.e. geometry and pore network characteristics) of targeted silica-rich rock varieties provide an improved understanding of organo-mineral interactions in silica-rich rock varieties covering a wide range of scales (section 6.2). Within the substratum, the occurrence of sufficient void space appears to be the deciding factor in allowing hyphal penetration into the substratum. Within each individual genus, this is affected locally by the nature, grain size and state of alteration of the different mineral phases.

Granitic rocks were characterized by a well-developed pore-fracture network and were generally more extensively invaded by hyphal penetration compared to metasedimentary rocks, which show a well-defined decrease in particle size and permeability, presumably related to pore collapse and/or impact-induced annealing (Cockell & Osinski, 2007; Cockell, 2011; Pontefract *et al*., 2014). The observation that foliose lichen assembladges had the most evolved thalli and the highest penetration values is consistent with the observations of Bjelland & Thorseth (2002). Here, foliose-epilithic species revealed exceptional penetration component due to a greater number of fractures and a greater total pore surface area, both of which provide shelter for endolithic organisms and facilitate access into the rock. An unforeseen, partially endolithic behavior was also revealed for crustose thalli, presumably enhanced by the existence of previously developed microcracks and increased translucence of target lithologies.

The peculiar modes of biomechanical and biochemical attacks of lichen thalli and hyphae on and into the substrate for each genus were illustrated by SEM. It could be demonstrated that biomechanical attack induces the breakdown of primary minerals, which result in the development of cavities that increase the contact surface area between the biota and the rock substratum. Biochemical weathering occurs as soon as this phase progresses, manifested by dissolution characteristics with peculiar patterns observed on crystal surfaces; iron accumulation in rock and lichen contacts micro-zones and along microfractures and cavities; and neoformed mycogenic minerals and phyllosilicate clays (and possible amorphous silica).

A comparison of the particular biomechanical and biochemical attacks promoted by lichens showed that they indifferently attack primary minerals without any preference. However, some of the mineral components, such as mica, amphibole, and plagioclase, were more susceptible to

fragmentation, to be intruded by mycobiont hyphaeinto crystal discontinuities and to be absorbed into the thallus. In addition, a positive feedback was shown between the initial accumulation of fine soil in the fissures and cavities, and the increased biophysical and biochemical influence of predominant biota production in these areas. In contrast, the vast bedrock surface between the fissures and cavities was subjected to weaker action by lichens and microorganisms.

The overall observations and analyses in this study indicate that in the initial stages of soil formation and cation mobilization, the close association between lichen taxa and impacted silica-rich rock varieties assumes considerable importance, thus facilitating colonization by higher plants. Epilithic species have shown that loose filaments and cell clusters expand in pore spaces between and around the rocks, so that even organisms such as lichens are fully embedded in the rock matrix protected by the hard surface crust. This observation is important because it shows that impact events are not only capable of increasing the abundance of lithic habitat, but can also generate entirely new, or at least rare, type of endolithic habitats.

7.3 STUDY RECOMMENDATIONS AND CLOSING NOTES

Four recurrent saxicolous lichens encrusting target silica-rich rock types were investigated to re-evaluate key factors influencing the distribution and physiognomy of lichens in the Vredefort Dome. **"**Although a range of methods are available for large-scale analysis, the development of best practices, systematic methods and ideal taxonomic approaches is an ongoing problem to ensure the consistency of data and interpretation" (Gadd, 2017). To this end, a quantitative PCR approach would allow a more exact quantification of the amounts of species present in the rock (Fryday *et al*., 2020).

The second purpose of this study was to draw attention to biologically mediated degradation of silica-rich rock types and to identify and discuss organo-mineral associations at the lichen-rock interface. This concomitantly contribute to an improved understanding of chemical variables that correlate with changes in dominant rock type**.** It is also believed that similar biogeochemical characteristics may be recognised for mafic- and ultramafic rock types and should be further examined. For example, the crustose genera *Acarospora* sp.pl. specifically illustrated a strong association with mafic rock types.

With regard to the interrelations between different lichen taxa and minerology, this study specifically focused on the breakdown of primary mineral components of granitic and metasedimentary rocks. These elements are characteristic of the weathering crust, although

relatively high values for accessory apatite, chlorite, zircon and rutile were also observed. These elements may also influence differences in substrate association for saxicolous species and require further investigation. Despite our lack of knowledge on weathering rates in impact craters, weathering of primary minerals must be considerably enhanced and accelerated under biotic conditions (Li *et al*., 2016; Smits *et al*., 2012).

Lastly, attempts should be made to not only refine our understanding of the dynamics of important biogeochemical processes in other impact craters but also to provide exact explanations for abrupt species changes across the varying lithologies within impact craters. This synthesis suggests that impact cratering must be viewed as a truly biologic process, as well as a geologic one.

REFERENCES

Adamo, P., Colombo, C. & Violante, P. 1997. Iron oxides and hydroxides in the weathering interface between *Stereocaulon vesuvianum* and volcanic rock. *Clay Minerals*, 32: 453-461.

Adamo, P. & Violante, P. 2000. Weathering of rocks and neogenesis of minerals associated with lichen activity. *Applied Clay Science*, 16:229-256.

Adams, D.G., Duggan, P.S. & Jackson, O. 2012. Cyanobacterial Symbioses. (*In* Whitton, B.A., *ed*. Ecology of Cyanobacteria II: Their Diversity in Space and Time. Dordrecht: Springer Science+Business Media. p. 593-647).

Aghamiri, R. & Schwartzman, D.W. 2002. Weathering rates of bedrock by lichens: a mini watershed study. *Chemical Geology*, 188(3-4):249-259.

Al-Thukair, A. A., Golubic, S. & Rosen, G. 1994. New euendolithic cyanobacteria from the Bahama Bank and the Arabian Gulf: *Hyella racemus* sp. nov. *Journal of Phycology*, 30:764-769.

Ames, D.E., Jonasson, I.R., Gibson, H.L. & Pope, K.O. 2006. Impact-generated hydrothermal system – constraints from large Paleoproterozoic Sudbury Crater, Canada. (*In* Cockell, C.S., Koeberl, C. & Gilmour, I., *eds*. Biological Processes Associated with Impact Craters. Heidelberg: Springer. p. 55-100).

Anhaeusser, C.R. 2004. Palaeoarchaean to Mesoproterozoic (3500-1000 Ma) ultramafic and mafic intrusions of the Kaapvaal Craton and neighbouring metamorphic belts: a review. *Information Circular – Economic Geology Research Unit*, *University of the Witwatersrand*, *Johannesburg*, 384:63.

Anhaeusser, C.R. 2006. Ultramafic and mafic intrusions of the Kaapvaal Craton. (*In* Johnsonn, M.R., Anhaeusser, C.R. & Thomas, R.J., *eds*. The Geology of South Africa. Johannesburg/Council for Geoscience. Pretoria: Geological Society of South Africa. p. 95-134).

Anhaeusser, C.R. 2014. Archaean greenstone belts and associated granitic rocks – a review. *Journal of African Earth Sciences*, 100:684-732.

Archer, S.D.J., de los Ríos, A., Lee, K.C., Niederberger, T.S., Cary, S.C. & Coyne, K.J. 2016. Endolithic microbial diversity in sandstone and granite from the McMurdo Dry Valleys, Antarctica. *Polar Biology*, 40:997-1006.

Armstrong, R. A., Compston, W., Retief, E. A., Williams, L. S. & Welke, H. J. 1991. Zircon ion microprobe studies bearing on the age and evolution of the Witwatersrand Basin. *Precambrian Research*, 53:243-266.

Armstrong, R.A., Lana, C., Reimold, W.U. & Gibson, R.L. 2006. SHRIMP Zircon age constraints on Mesoarchean crustal development in the Vredefort dome, central Kaapvaal craton, South Africa. (*In* Reimold, W.U. & Gibson, R.L. *ed.* Processes on the Early Earth. Special Paper: Geological Society of America. p. 233-253).

Arocena, J.M., Zhu, L.P. & Hall, K. 2003. Mineral accumulations induced by biological activity on granitic rocks in Qinghai Plateau, China. *Earth Surface Processes and Landforms*, 28:1429-1437.

Arocena, J.M., Siddique, T., Thring, R.W. & Kapur, S. 2007. Investigation of lichens using molecular techniques and associated mineral accumulations on a basaltic flow in a Mediterranean environment. *Catena*, 70:356-365.

Arvieu, J.C., Leprince, F. & Plassard, C. 2003. Release of oxalate and protons by ectomycorrhizal fungi in response to P-deficiency and calcium carbonate in nutrient solution. *Annals of Forest Science*, 60:815-821.

Ascaso, C. & Galvan, J. 1976. Studies on the pedogenetic action of lichen acids. *Pedobiologia*, 16:321-331.

Ascaso, C., Sancho, L.G. & Rodriguez-Pascual, C. 1990. The weathering action of saxicolous lichens in maritime Antarctica. *Polar Biology*, 11:33-39.

Ascaso, C. & Wierzchos, J. 1994. Structural aspects of the lichen–rock interface using back scattered electron imaging. *Botanica Acta*, 107(4):251-256.

Ascaso, C. & Wierzchos, J. 1995. Study of the biodeterioration zone between the lichen thallus and the substrate. *Cryptogamic Botany*, 5:270-281.

Ascaso, C. & Wierzchos, J. 2003. The search for biomarkers and microbial fossils in Antarctic rock microhabitats. *Geomicrobiology Journal*, 20(5):439-450.

Asplund, J. & Wardle, D.A. 2017. How lichens impact on terrestrial community and ecosystem properties. *Biological Reviews of the Cambridge Philosophical Society*, 92(3):1720-1738.

Avanthi Isaka, B.L., Ranjitha, P.G., Rathnaweeraa, T.D., Pereraa, M.S.A. & De Silva, V.R.S. 2019. Quantification of thermally-induced microcracks in granite using X-ray CT imaging and analysis. *Geothermics*, 81:152-167.

Bailey, A.C., Law, J.D.M., Cadle, A.B. & Phillips, G.N. 1990. The Zandfontein Quartzite Formation, a marinedeposit in the Central Rand Group, Witwatersrand Supergroup. *Suid Afrikaanse Joernaal vir Geologie*, 93(1):135-146.

Balkwill, K. 2009. Flora and fauna of the Vredefort dome: what, where and why?. (*In* Reimold, W.U. & Gibson, R.L., *eds.* Meteorite impact! The danger from space and South Africa's mega-impact: the Vredefort structure, 3rd edition. Berlin: Springer. p. 201-214).

Banfield, J.F., Barker, W.W., Welch, S.A. & Taunton, A. 1999. Biological impact on mineral dissolution: application of the lichen model to understanding mineral weathering in the rhizosphere. *Proceedings of the National Academy of Sciences of the United States of America*, 96:3404-3411.

Barker, W.W. & Banfield, J.F. 1996. Biologically versus inorganically mediated weathering reactions: relationships between minerals and extracellular microbial polymers in lithobiontic communities. *Chemical Geology*, 132:55-69.

Barker, W.W., Welch, S.A. & Banfield, J.F. 1997. Biogeochemical weathering of silicate minerals. *Reviews in Mineralogy*, 35:391-428.

Barnicoat, A.C., Henderson, I.H.C., Knipe, R.J., Yardley, B.W.D., Napier, R.W., Fox, N.P.C., Kenyon, A.K., Muntingh, D.J., Strydom, D., Winkler, K.S., Lawrence, S.R. & Cornford, C. 1997. Hydrothermal gold mineralisation in the Witwatersrand Basin. *Nature*, 386:820-824.

Bashkin, V.N. 2003. Modern biogeochemistry. Dordrecht: Kluwer Academic Publishers. 567p.

Begonha, A. 2009. Mineralogical study of the deterioration of granite stones of two Portuguese churches and characterization of the salt solutions in the porous network by the presence of diatoms. *Materials Characterization*, 60(7):621-635.

Beimforde, C. 2011. Biodeterioration of stone. (*In* Reitner, J. & Thiel, V., *ed*. Encyclopedia of geobiology. Dordrecht: Springer. p. 112-117).

Bell, R.A. 1993. Cryptoendolithic algae of hot semiarid lands and deserts. *Journal of Phycology*, 29:133-39.

Bennet, P.C., Rogers, J.R. & Choi, W.J. 2001. Silicates, silicate weathering, and microbial ecology. *Geomicrobiology Journal*, 18:3-19.

Berthelin, J. 1983. Microbial weathering processes. (*In* Krumbein, E. *ed*. Microbial Geochemistry. Blackwell: Oxford. p. 223-264).

Beukes, N.J. 1995. Stratigraphy and basin analyses of the West Rand Group with special reference to prospective areas for placer gold deposits: Johannesburg, Rand Afrikaans University Geology Department. (Unpublished Report).

Beukes, N.J. & Nelson, J. 1995. Sea-level fluctuation and basin subsidence controls on the setting of auriferous palaeoplacers in the Archaean Witwatersrand Supergroup: a genetic and sequence stratigraphic approach. pp. 860-863.

Bisschoff, A.A. 1969. The petrology of the igneous and metamorphic rocks in Vredefort dome and adjoining parts of the Potchefstroom Syncline. University of Pretoria. (Thesis - PhD).

Bisschoff, A. A. 1973. The petrology of some mafic and peralkaline intrusions in the Vredefort dome, South Africa. *Transactions of the Geological Society of South Africa,* 76:27-45.

Bisschoff, A.A., 1988. The history and origin of the Vredefort dome. *Suid Afrikaanse Tydskrif vir Wetenskap,* 84:413-417.

Bisschoff, A.A. 1999. The geology of the Vredefort dome: explanation of geological sheets 2627CA, CB, CC, CD, DA, DC and 2727AA, AB, BA (1: 50 000). Pretoria: Council for Geoscience.

Bjelland, T. & Ekman, S. 2005. Fungal diversity in rock beneath a crustose lichen as revealed by molecular markers. *Microbial Ecology*, 49:598-603.

Bjelland, T. & Thorseth, I.H. 2002. Comparative studies of the lichen–rock interface of four lichens in Vingen, western Norway. *Chemical Geology*, 192:81-98.

Boggs, S. Jr. 2010. Principles of Sedimentology and Stratigraphy. 4th ed. Upper Saddle River, NJ: Pearson Prentice Hall.

Boneschans, R.B., Coetzee, M.S., & Siebert, S.J. 2015. A geobotanical investigation of the Koedoesfontein Complex, Vredefort dome, South Africa. *Australian Journal of Botany*, 63:324-340.

Boneschans, R.B. 2018. Petrology and associated woody vegetation of the Koedoesfontein Complex in the Vredefort dome. Potchefstroom: North-West University. (Thesis – MSc)

Brady, P.V., Dorn, R.I., Brazel, A.J., Clark, J., Moore, R.B. & Glidewell, T. 1999. Direct measurement of the combined effects of lichen, rainfall, and temperature on silicate weathering. *Geochimica et Cosmochimica Acta*, 63(19–20):3293-3300.

Broadbent, N.D., 1990. Use of lichenometric and weathering rates for dating. *Norwegian Archaeological Review*, 23(1-2):3-8.

Büdel, B., Bendix, J., Bicker, F.R. & Green, T.G.A. 2008. Dewfall as a water source frequently activates the endolithic cyanobacterial communities in the granites of Taylor Valley, Antarctica. *Journal of Phycology*, 44:1415–1424.

Büdel, B. & Scheidegger, C. 2008. Thallus morphology and anatomy. (*In* Nash, T.H., *eds*. Lichen Biology, 2nd edition. Cambridge: Cambridge University Press. p. 40-68).

Büdel, B., Weber, B., Kühl, M., Pfanz, H., Sültemeyer, D. & Wessels, D. 2004. Reshaping of sandstone surfaces by cryptoendolithic cyanobacteria: bioalkalization causes chemical weathering in arid landscapes. *Geobiology*, 2:261-268.

Bungartz, F., Garvie, L.A.J. & Nash, T.H. 2004. Anatomy of the endolithic Sonoran Desert lichen *Verrucaria rubrocincta* Breuss: implications for biodeterioration and biomineralization. *The Lichenologist*, 36(1):55-73.

Burford, E.P., Kierans, M. & Gadd, G.M. 2003a. Geomycology: fungi in mineral substrata. *Mycologist*, 17:98-107.

Burford, E.P., Fomina, M. & Gadd, G.M. 2003b. Fungal involvement in bioweathering and biotransformation of rocks and minerals. *Mineralogical Magazine*, 67:127-1155.

Burford, E.P., Hillier, S. & Gadd, G.M. 2006. Biomineralization of fungal hyphae with calcite ($CaCO_3$) and calcium oxalate mono- and dihydrate in Carboniferous limestone microcosms. *Geomicrobiology Journal*, 23:599-611.

Boswell, G.P., Jacobs, H., Davidson, F.A., Gadd, G.M. & Ritz, K. 2003. Growth and function of fungal mycelia in heterogeneous environments. *Bulletin of Mathematical Biology*, 65:447-477.

Carter, N.E.A. & Viles, H.A. 2005. Bioprotection explored: the story of a little-known earth surface process. *Geomorphology*, 67:273-281.

Casarin, V., Plassard, C., Souche, G. & Arvieu, J-C. 2003. Quantification of oxalate ions and protons released by ectomycorrhizal fungi in rhizosphere soil. *Agronomie*, 23:461-469.

Catuneanu, O. 2001. Flexural partitioning in the Late Archaean Witwatersrand foreland system, South Africa. *Sedimentary Geology*, 141/142:95-112.

Chan, Y., Lacap, D.C., Lau, M.C.Y., Ha, K.Y., Warren-Rhodes, K.A., Cockell, C.S., Cowan, D.A., McKay, C.P. & Pointing, S.B. 2012. Hypolithic microbial communities: Between a rock and a hard place. *Environmental Microbiology*, 14(9):2272-2282.

Chapin, F.S. & Eviner, V.T. 2004. Biogeochemistry of Terrestrial Net Primary Production. (*In* Holland, H. & Turekian, K., *eds*. Treatise on Geochemistry, 8th edition. Amsterdam: Elsevier. p. 215-247).

Chen, J., Blume, H.P., 2002. Rock-weathering by lichens in Antarctic: patterns and mechanisms. *Journal of Geographical Sciences*, 12(4):387-396.

Chen, L., Blume, H.P. & Beyer, L. 2000. Weathering of rocks induced by lichen colonization - a review. *Catena*, 39:121-146.

Chen, M.-R., Hinkley, R.E. & Killough, J.E. 1996. Computed tomography imaging of air sparging in porous media. *Water Resources Research*, 32(10):3013-3024.

St. Clair, L.L. & Seaward, M.R.D. 2004. Biodeterioration of Stone Surfaces: Lichens and biofilms as weathering agents of rocks and Cultural Heritage. Dordrecht: Kluwer Academic Publishers. 299p.

Clarke, A.R. & Eberhardt, C.N. 2002. Microscopy techniques for materials science. Cambridge: Woodhead Publishing Limited. 482p.

Clausen, C.A. & Green, F. 2003. Oxalic acid overproduction by coppertolerant brown-rot basidiomycetes on southern yellow pine treated with copper-based preservatives. *International Biodeterioration and Biodegradation*, 51:139-144.

Cnudde, V. & Boone, M.N. 2013. High-resolution X-ray computed tomography in geosciences: a review of the current technology and applications. *Earth Science Reviews*, 123:1-17.

Cockell, C.S. 2011. Asteroid and comet impacts. (*In* Reitner, J. & Thiel, V., *ed*. Encyclopedia of geobiology. Dordrecht: Springer. p. 177-133).

Cockell, C.S., Fike, D.A., Osinski, G.R. & Lee, P. 2006. Geomicrobiology of Impact-Altered Rocks. (*In* Cockell, C.S., Koeberl, C. & Gilmour, I., *eds*. Biological Processes Associated with Impact Craters. Heidelberg: Springer. p. 21-40).

Cockell, C.S., Kennerley, N., Lindstrom, M., Watson, J., Ragnarsdottir, V., Sturkell, E., Ott, S. & Tindle, A.G. 2007. Geomicrobiology of a weathering crust from an impact crater and a hypothesis for its formation. *Geomicrobiology Journal,* 24:425-440.

Cockell, C.S. & Lee, P. 2002. The biology of impact craters - A review. *Biological Reviews*, 77:279-310.

Cockell, C.S., Lee, P., Broady, P., Lim, P.S.S. & Osinski, G.R. 2005. Effects of asteroid and comet impacts on habitats for lithophytic organisms - A synthesis. *Meteoritics & Planetary Science*, 40(12):1901-1914.

Cockell, C.S., Lee, P., Osinski, G.R., Horneck, G. & Broady, P. 2002. Impact-induced microbial endolithic habitats. *Meteoritics & Planetary Science,* 37:1287-1298.

Cockell, C.S. & Lim, D.S.S. 2005. Impact craters, water and microbial life. (*In* Tokano, T., *ed*. Water and life on Mars. Heidelberg: Springer-Verlag. p. 261-275).

Cockell, C.S., McKay, C.P., Warren-Rhodes, K. & Horneck, G. 2008. Ultraviolet radiation-induced limitation to epilithic microbial growth in arid deserts – Dosimetric experiments in the hyperarid core of the Atacama Desert. *Journal of Photochemistry and Photobiology B: Biology*, 90:79-87.

Cockell, C.S. & Osinski, G.R. 2007. Impact-induced impoverishment and transformation of a sandstone habitat for lithophytic microorganisms. *Meteoritics & Planetary Science*, 42:1985-1993.

Cockell C.S., Osinski G.R. & Lee, P. 2003. The impact crater as a habitat: Effects of impact processing of target materials. *Astrobiology*, 3:181-191.

Cockell, C.S., Osinski, G.R. & Voytek, M.A. 2013. The geomicrobiology of impact structures. (*In* Osinski, G.R. & Pierazzo, E. *ed*. Impact Cratering: Processes and Products. West Sussex: Blackwell Publishing. p. 146-156).

Cooks, J. & Fourie, Y. 1989. The influence of two epilithic lichens on the weathering of quartzite and gabbro. *Suid-Afrikaanse geograaf*, 17:24-33.

Cooks, J. & Otto, E. 1990. The weathering effects of lichen *Lecida Aff. sarcogynoides* (Koerb.) on Magaliesberg quartzite. *Earth Surface Processes and Landforms*, 15:491-500.

Cornelissen, J.H.C., Callaghan, T.V., Alatalo, J.M., Michelsen, A., Graglia, E., Hartley, A.E., Hik, D.S., Hobbie, S.E., Press, M.C., Robinson, C.H., Henry, G.H.R., Shaver, G.R., Phoneix, G.K., Gwynn Jones, D., Jonasson, S., Chapin III, F.S., Molau, U., Neill, C., Lee, J.A., J. Melillo, J.M.,

Sveinbjörnsson, B., & Aerts, R. 2001. Global Change and Arctic Ecosystems: Is Lichen Decline a Function of Increases in Vascular Plant Biomass. *Journal of Ecology*, 6:984-994.

Cornelissen, J.H.C., Lang, S.I., Soudzilovskaia, N.A., & During, H.J. 2007. Comparative cryptogam ecology: a review of bryophyte and lichen traits that drive biogeochemistry. *Annals of Botany*, 99(5):987-1001.

Cowan, D.A., Pointing, S.B., Stevens, M.I., Cary, S.C., Stomeo, F. & Tuffin, I.M. 2011. Distribution and abiotic influences on hypolithic microbial communities in an Antarctic Dry Valley. *Polar Biology*, 34:307-311.

Cowan, D.A. & Ah Tow, L. 2004. Endangered Antarctic environments. *Annual Review of Microbiology*, 58:649-690.

Coward, M.P., Spencer, R.M. & Spencer, C.E. 1995. Development of the Witwatersrand Basin, South Africa. (*In* Coward, M.P. & Ries, A.C. *eds*. Early Precambrian Processes. London: Geological Society. pp. 243-269).

Culberson, C.F. & Culberson, W.L. 2001. Future Directions in Lichen Chemistry. *The Bryologist*, 104(2):230-234.

Danell, K., Utsi, P.M., Palo, R.T. & Eriksson, O. 1994. Food plant selection by reindeer during winter in relation to plant quality. *Ecography*, 17:153-158.

Danin, A. & Caneva, G. 1990. Deterioration of limestone walls in Jerusalem and marble monuments in Rome caused by cyanobacteria and cyanophilous lichens. *International Biodeterioration*, 26:397-417.

de la Rosa, J.P.M., Warke, P.A. & Smith, B.J. 2012. Lichen-induced biomodification of calcareous surfaces: bioprotection versus biodeterioration. *Progress in Physical Geography*, 1:1-27.

de la Torre, J.R., Goebel, B.M., Friedmann, E.I. & Pace, N.R. 2003. Microbial diversity of cryptoendolithic communities from the McMurdo Dry Valleys, Antarctica. *Applied and Environmental Microbiology*, 69(7):3858-3867.

de los Ríos, A. & Ascaso, C. 2005. Contributions of in situ microscopy to the current understanding of stone biodeterioration. *International Microbiology*, 8:181-188.

de los Ríos, A., Cámara, B., del Cura, A.G., Rico, V.J., Galván, V. & Ascaso, C. 2009. Deteriorating effects of lichen and microbial colonization of carbonate building rocks in the Romanesque churches of Segovia (Spain). *Science of The Total Environment*, 407:1123-1134.

de los Ríos, A., Galván, V. & Ascaso, C. 2004. In situ microscopical diagnosis of biodeterioration processes at the convent of Santa Cruz la Real, Segovia, Spain. *International Biodeterioration & Biodegradation*, 54:113-120.

de los Ríos, A., Grube, M., Sancho, L.G. & Ascaso, C. 2007. Ultrastructural and genetic characteristics of endolithic cyanobacterial biofilms colonizing Antarctic granite rocks. *FEMS Microbiology Ecology*, 59:386-395.

de los Ríos, A., Sancho, L.G., Grube, M., Wierzchos, J. & Ascaso, C. 2005b. Endolithic growth of two *Lecidea* lichens in granite from continental Antarctica detected by molecular and microscopy techniques. *The New Phytologist*, 165:181-189.

de los Ríos, A., Wierzchos, J. & Ascaso, C. 2002. Microhabitats and chemical microenvironments under Saxicolous lichens growing on granite. *Microbial Ecology*, 43:181-188.

de los Ríos, A., Wierzchos, J. & Ascaso, C. 2014. The lithic microbial ecosystems of Antarctica's McMurdo Dry Valleys. *Antarctic Science*, 26(5):459-477.

de los Ríos, A., Wierzchos, J., Sancho, L.G. & Ascaso, C. 2003. Acid microenvironments in microbial biofilms of Antarctic endolithic microecosystems. *Environmetal Microbiology*, 5:231-237.

de los Ríos, A., Wierzchos, J., Sancho, L.G., Green, T.G.A. & Ascaso, C. 2005a. Ecology of endolithic lichens colonizing granite in continental Antarctica. *Lichenologist*, 37:383-395.

de Waal, S.A., Schweitzer, J., Graham, I., Gauert, C. & Ripley, E. 2008. A Bushveld-related high-Ti igneous suite (HITIS) derived from an alkali to transitional basaltic magma, South Africa. *South African Journal of Geology*, 111(2-3): 201-224.

Denison, C., Carlson, W.D. & Ketcham, A. 1997. Three-dimensional quantitative textural analysis of metamorphic rocks using high-resolution computed X-ray tomography: Part I. Methods and techniques. *Journal of Metamorphic Geology*, 15(1):29-44.

Dong, H. 2010. Mineral-microbe interactions: a review. *Frontiers in Earth Science*, 4(2):127-147.

Duliu, O.G. 1999. Computer axial tomography in geosciences: an overview. *Earth-Science Reviews*, 48:265-281.

Edwards, H.G.M., Jorge Villar, S.E., Seaward, M. & St. Clair, L.L. 2004. Raman spectroscopy of rock biodeterioration by the lichen *Lecidea tessellata* Flörke in a desert environment. (*In* St. Clair, L.L. & Seaward, M., *eds*. Biodeterioration of Stone Surfaces. Netherlands: Kluwer Academic Publishers. p. 229-239).

Edwards, H.G.M., Russel, N.C. & Seaward, M.R.D. 1997. Calcium oxalate in lichen biodeterioration studied using FT-Raman spectroscopy. *Spectrochimica Acta A*, 53:99-105.

Egerton, R.F. 2016. Physical principles of electron microscopy: An Introduction to TEM, SEM, and AEM. 2nd ed. Switzerland: Springer International Publishing. 203p.

Els, B.G. & Mayer, J.J. 1992. Transgressive and progradational beach and nearshore facies in the Late Archaean Turffontein Subgroup of the Witwatersrand Supergroup, Vredefort area, South Africa. South African Journal of Geology, 95:60-73.

Elsenbroek, J. H. 1991. Die struktuur en petrologie van die alkaligraniet in die Vredefortkoepel noordwes van Parys. Potchefstroom: NWU (Dissertation – M.Sc.).

Elix, J.A. & Stocker-Wörgötter, E. 2008. Biochemistry and secondary metabolites. (*In* Nash, T.H., 2nd *ed*. Lichen Biology. Cambridge: Cambridge University Press. p. 104-133).

Fandrich, R., Gu, Y., Burrows, D. & Moeller, K. 2007. Modern SEM-based mineral liberation analysis. *International Journal of Mineral Processing*, 84:310-320.

Favero-Longo, S.E., Castelli, D., Salvadori, O., Bellusob, E. & Piervittori, R. 2005. Pedogenetic action of the lichens *Lecidea atrobrunnea*, *Rhizocarpon geographicum* gr. And *Sporastatia testudinea* on serpentinized ultramafic rocks in an alpine environment. *International Biodeterioration & Biodegradation*, 56:17-27.

Favero-Longo, S.E., Gazzano, C., Girlanda, M., Castelli, D., Tretiach, M., Baiocchi, C. & Piervittori, R. 2011. Physical and chemical deterioration of silicate and carbonate rocks by meristematic microcolonial fungi and endolithic lichens (chaetothyriomycetidae). *Geomicrobiology Journal*, 28(8):732-744.

Favero-Longo, S.E. & Viles, H.A. 2020. A review of the nature, role and control of lithobionts on stone cultural heritage: weighing-up and managing biodeterioration and bioprotection. *World Journal of Microbiology and Biotechnology*, 36:100.

Fettes, D. & Desmons, J. 2007. Metamorphic rocks: a classification and glossary of terms. Cambridge: Cambridge University Press. 258p.

Fike, D.A., Cockell, C.S., Pearce, D. & Lee, P. 2003. Heterotrophic microbial colonization of the interior of impact-shocked rocks from Haughton impact structure, Devon Island, Nunavut, Canadian High Arctic. *International Journal of Astrobiology*, 1:311-323.

Fomina, M.A., Alexander, I.J., Hillier, S. & Gadd, G.M. 2004. Zinc phosphate and pyromorphite solubilization by soil plant-symbiotic fungi. *Geomicrobiology Journal*, 21:351-366.

Fomina, M.A., Burford, E.P., Hillier, S., Kierans, M. & Gadd, G.M. 2010. Rock-building fungi. *Geomicrobiology Journal*, 27:624-629.

Fomina, M.A., Gadd, G.M. 2002. Influence of clay minerals on the morphology of fungal pellets. *Mycological Research*, 106:107-117.

Frankel, J.J. 1939. The green colour of the Hospital Hill quartzites. *South African Journal of Geology*, 42(1):15-17.

French, B.M. 2004. The importance of being cratered: the new role of meteorite impact as a normal geological process. *Meteoritics and Planetary Science*, 39(2):169-197.

Friedl, T. & büdel, B. 2008. Photobionts. (*In* Nash, T.H., *ed*. Lichen Biology, 2nd edition. Cambridge: Cambridge University Press. p. 9-26).

Friedmann, E.I. 1982. Endolithic microorganisms in the antarctic cold desert. *Science*, 215:1045-1053.

Frimmel, H.E. 1997. Chlorite thermometry in the Witwatersrand Basin: Constraints on the Paleoproterozoic geotherm in the Kaapvaal Craton, South Africa. *The Journal of Geology*, 105:601-615.

Frimmel, H.E. 2005. Archaean atmospheric evolution: evidence from the Witwatersrand gold fields, South Africa. *Earth-Science Reviews*, 70:1-46.

Frimmel, H.E., Groves, D.I., Kirk, J., Ruiz, J., Chesley, J. & Minter, W.E.L. 2005. The formation and preservation of the Witwatersrand goldfields, the largest gold province in the world. *Society of Economic Geologists*, Economic Geology 100th Anniversary Volume: 769-797.

Frimmel, H.E. & Minter, W.E.L. 2002. Recent developments concerning the geologicai history and genesis of the Witwatersrand gold deposits, South Africa. *Society of Economic Geologists Special Publication*, 9:17-45.

Fryday, A.M. 2015. A new checklist of lichenised, lichenicolous and allied fungi reported from South Africa. *Bothalia*, 45(1): Art. #148.

Fryday, A.M., Medeiros, I., Siebert, S.J., Pope, N. & Rajakaruna, N. 2020. *Burrowsia*, a new genus of lichenized fungi (Caliciaceae), plus the new species *B. cataractae* and *Scoliciosporum fabisporum*, from Mpumalanga, South Africa. *South African Journal of Botany*, 132:471-481.

Fuller, A.O. 1958. A contribution to the petrology of the Witwatersrand system. *South African Journal of Geology*, 61(1):19-50.

Gadd, G.M. 2007. Geomycology: biogeochemical transformations of rocks, minerals, metals and radionuclides by fungi, bioweathering and bioremediation. *Mycological research*, 111(1):3-49.

Gadd, G.M. 2010. Metals, minerals and microbes: geomicrobiology and bioremediation. *Microbiology*, 156:609-643.

Gadd, G.M. 2011. Geomycology. (*In* Reitner, J. & Thiel, V., *eds*. Encyclopedia of geobiology. Dordrecht: Springer. p. 177-133).

Gadd, G.M. 2017a. Geomicrobiology of the built environment. *Nature Microbiology*, 2(16275):1-9.

Gadd, G.M. 2017b. Fungi, Rocks, and Minerals. *Elements*, 13:171-176.

Gadd, G.M., Bahri-Esfahani, J., Li, Q., Rhee, Y.J., Wei, Z., Fomina, M. & Liang, X. 2014. Oxalate production by fungi: significance in geomycology, biodeterioration and bioremediation. *Fungal Biology Reviews*, 28:36-55.

Gadd, G.M., Burford, E.P., Fomina, M. & Melville, K. 2007. Mineral transformations and biogeochemical cycles: a geomycological perspective. (*In* Gadd, G.M., Watkinson, S.C. & Dyer, P.S., *eds*. Fungi in the Environment. New York: Cambridge University Press. p. 77-111).

Ganor, J. & Lasaga, A.C. 1994. The effects of oxalic acid on kaolinite dissolution rate. *Mineralogical Magazine*, 58(A):315-316.

Gibbon, R.J. 2009. The fluvial history of the Lower Vaal River Catchment. University of the Witwatersrand. (Thesis – PhD).

Gibson. R.L. & Jones, M.Q.W. 2002. Late Archaean to Palaeoproterozoic geotherms in the Kaapvaal Craton, South Africa: constraints on the thermal evolution of the Witwatersrand Basin. *Basin Research*, 14:169-181.

Gibson, R.L. & Reimold, W.U. 1999. The significance of the Vredefort dome for the thermal and structural evolution of the Witwatersrand Basin, South Africa. *Mineralogy and Petrology*, 66:5-23.

Gibson, R.L. & Reimold, W.U. 2008. Geology of the Vredefort impact structure; a guide to sites of interests. Council for Geoscience South Africa: Memoir 97. 181p

Gibson, R.L. & Wallmach, T. 1995. Low pressure-high temperature metamorphism in the Vredefort dome, South Africa–anticlockwise pressure-temperature path followed by rapid decompression. *Geological Journal*, 30:121-135.

Giordani, P., Modenesi, P. & Tretiach, M. 2003. Determinant factors for the formation of the calcium oxalate minerals, weddellite and whewellite, on the surface of foliose lichens. *The Lichenologist*, 35(3):255-270.

Golubic, S., Friedmann, I. & Schneider, J. 1981. The lithobiontic ecological niche, with special reference to microorganisms. *Journal of Sedimentary Petrology*, 51(2):475-478.

Gorbushina, A.A. 2007. Life on the rocks. *Environmental Microbiology*, 9:1613-1631.

Gorbushina, A.A., Boettcher, M., Brumsack, H.J., Krumbein, W.E. & Vendrell-Saz, M. 2001. Biogenic forsterite and opal as a product of biodeterioration and lichen stromatolite formation in table mountain systems (tepuis) of Venezuela. *Geomicrobiology Journal*, 18:117-132.

Gottlieb, P., Wilkie, G., Sutherland, D., Ho-Tun, E., Suthers, S., Perera, K., Jenkins, B., Spencer, S., Butcher, A. & Rayner, A. 2000. Using quantitative electron microscopy for process mineralogy applications. *Journal of Mineralogy*, 52:24-27.

Graham, I.T., De Waal, S.A. & Armstrong, R.A. 2005. New U–Pb zircon age for the Schurwedraai alkali granite: implications for pre-impact development of the Vredefort dome and extent of Bushveld magmatism, South Africa. *Journal of African Earth Sciences*, 43, 537-548.

Guglielmin, M., Cannone, N., Strini, A. & Lewkowicz, A.G. 2005. Biotic and abiotic processes on granite weathering landforms in a cryotic environment, Northern Victoria Land, Antarctica. *Permafrost and Periglacial Processes*, 16:69-85.

Guglielmin, M., Favero-Longo, S.E., Cannone, N., Piervittori, A. & Strini, A. 2011. Role of lichens in granite weathering in cold and arid environments of continental Antarctica. *Geological Society, London, Special Publications*, 354:195-203.

Guillitte, O. 1995. Bioreceptivity: a new concept for building ecology studies. *The Science of the Total Environment*, 167:215-220.

Guy, B.M., Beukes, N.J. & Gutzmer, J. 2010. Paleoenvironmental controls on the texture and chemical composition of pyrite from non-conglomeratic sedimentary rocks of the mesoarchean Witwatersrand Supergroup, South Africa. *South African Journal of Geology*, 113(2):195-228.

Haas, J.R. & Purvis, O.W. 2006. Lichen biogeochemistry. (*In* Gadd, G.M., *ed.* Fungi in Biogeochemical Cycels. New York: Cambridge University Press. p. 344-376).

Hall, K., Arocena, J.M., Boelhouwers, J. & Liping, Z. 2005. The influence of aspect on the biological weathering of granites: observations from the Kunlun Mountains, China. *Geomorphology*, 67:171-188.

Hall, K., Guglielmin, M. & Strini, A. 2008. Weathering of granite in Antarctica: I. Light penetration into rock and implications for rock weathering and endolithic communities. *Earth Surface Processes and Landforms*, 33:295-307.

Hart, R.J., Moser D. & Andreoli, M. 1999. Archaean age for the granulite facies metamorphism near the center of the Vredefort Structure, South Africa. *Geology*, 27:1091-1094.

Hartnady, C.J.H. 2009. South Africa's gold production and reserves. *South African Journal of Science*, 105:328-329.

Huang, Y.H., Yang, S.Q., Tian, W.L., Zhao, J., Ma, D. & Zhang, C.S. 2017. Physical and mechanical behavior of granite containing pre-existing holes after high temperature treatment. *Archives of Civil and Mechanical Engineering*, 17(4):912-925.

Haynes, F.N. 1964. Lichens. *Viewpionts Biology*, 3:64-115.

Helgren, D.M. 1979. Rivers of diamonds: an alluvial history of the Lower Vaal Basin, South Africa. Chicago: University of Chicago. 389p.

Helle, T. & Aspi, J. 1983. Effects of winter grazing by reindeer on vegetation. *Oikos*, 40:337-343.

Henderson, M.E.K. & Duff, R.B. 1963. The release of metallic and silicate ions from minerals, rocks, and soils by fungal activity. *Journal of Soil Science*, 14:236-246.

Heshmatti, G.A. & Squire, V.R. 1995. Geobotany and range ecology: a convergence of thought? *Journal of Arid Environments*, 35: 395-405.

Hoffman, J.W. & De Beer, F.C. 2012. Characteristics of the micro-focus x-ray tomography facility (MIXRAD) at Necsa in South Africa, in: 18th World Conference on Nondestructive Testing, 16-20 April 2012. Durban, South Africa.

Honegger, R. 1991. Functional Aspects of the Lichen Symbiosis. *Annual Review of Plant Physiology and Plant Molecular Biology*, 42(1):553-578.

Honegger, R. 2007. Water relations in lichens. (*In* Gadd, G.M., Watkinson, S.C. & Dyer, P., *eds*. Fungi in the Environment. Cambridge: Cambridge University Press. p. 185-200).

Honegger, R. 2008. Mycobionts. (*In* Nash, T.H., *ed*. Lichen Biology, 2nd edition. Cambridge: Cambridge University Press. p. 9-26).

Honegger, R. 2009. Lichen-forming fungi and their photobionts. (*In* Deising, H.B., *ed*. The Mycota: Plant relationships V, 2nd edition. Berlin: Springer. p. 305-333).

Honegger, R. 2012. The symbiotic phenotype of lichen-forming ascomycetes and their endo- and epibionts. (*In* Hock, B., *ed*. The Mycota: Fungal Associations IX, 2nd edition. Berlin Heidelberg: Springer. p. 287-340).

Horsfield, B., Kieft, T.L. & the Geobiosphere Group. 2007. The geobiosphere. (*In* Harms, U., Koeberl, C. & Zoback, M.D., *eds*. Continental Scientific Drilling. Heidelberg: Springer. p. 163-211).

Iskandar, I.K. & Syers, J.K. 1971. Solubility of lichen compounds in water: pedogenetic implications. *Lichenologist*, 5:45-50.

Iskandar, I.K. & Syers, J.K. 1972. Metal-complex formation by lichen compounds. *Journal of Soil Science*, 23:255-265.

Jahns, H.M. 1973. Anatomy, morphology, and development. (*In* Ahmadjian, V. & Hale, M.E., *eds*. The lichens. London: Academic Press. p. 3-58).

Jie, C. & Blume, H.P. 2002. Rock-weathering by lichens in Antarctic: patterns and mechanisms. *Journal of Geographical Sciences*, 12(4):387-396.

Johnsonn, M.R., Anhaeusser, C.R. & Thomas, R.J. 2006. The Geology of South Africa. 3rd ed. Pretoria: Council for Geoscience. 691p.

Jones, D. 1988. Lichens and pedogenesis. (*In* Galun, M., *ed*. Handbook of Lichenology, 3rd edition. Boca Raton: CRC Press. p. 109-124).

Jones, D., Wilson, M.J. & McHardy, W.J. 1981. Lichen weathering of rock-forming minerals: application of scanning electron microscopy and microprobe analysis. *Journal of Microscopy*, 124:95-104.

Jorge-Villar, S.E. & Edwards, H.G.M. 2010. Lichen colonization of an active volcanic environment: a Raman spectroscopic study of extremophile biomolecular protective strategies. *Journal of Raman Spectroscopy*, 41:63-67.

Kamo, S., Reimold, W.U., Krogh, T.E. & Colliston, W.P. 1996. A 2.023 Ga age for the Vredefort impact, and a first report of shock metamorphosed zircons in the pseudotachylitic breccias and granophyre. *Earth and Planetary Science Letters*, 144: 369-388.

Kappen, L. 2000. Some aspects of the great success of lichens in Antarctica. *Antarctic Science*, 72(3): 314-324.

Kelly, L.C., Cockell, C.S., Herrera-Belaroussi, A., Piceno, Y., Andersen, G., DeSantis, T., Brodie, E., Thorsteinsson, T., Marteinsson, V., Poly, F. & LeRoux, X. 2011. Bacterial diversity of terrestrial crystalline volcanic rocks, Iceland. *Microbial Ecology*, 62:69-79.

Kenrick, P., Wellman, C.H., Schneider, H. & Edgecombe, G.D. 2012. A timeline for terrestrialization: Consequences for the carbon cycle in the Palaeozoic. *Royal Society of London Philosophical Transactions*, 367:519-536.

Kerr, S. & Zavada, M.S. 1989. The effect of the lichen *Acarospora sinopica* on the elemental composition of three sedimentary rock substrates in South Africa. *The Bryologist*, 92(3):407-410.

Ketcham, R.A. & Carlson, W.D. 2001. Acquisition, optimization and interpretation of X-ray computed tomographic imagery: applications to the geosciences. *Computers & Geosciences*, 27:381-400.

Khan, N., Tuffin, M., Stafford, W., Cary, C., Lacap, D.C., Pointing, S.B. & Cowan, D. 2011. Hypolithic microbial communities of quartz rocks from Miers Valley, McMurdo Dry Valleys, Antarctica. *Polar Biology*, 34:1657-1668.

Kidron, G.J. 2002. Causes of two patterns of lichen zonation on cobbles in the Negev Desert, Israel. *The Lichenologist*, 34(1):71-80.

Klein, C. & Dutrow, B. 2008. The manual of mineral science. 23rd ed. Hoboken, NJ: John Wiley & Sons, Inc.

Koeberl, C., Denison, C. & Ketcham, R.A. 2002. High-resolution X-ray computed tomography of impactites. *Journal of Geophysical Research*, 107(10):5089-5097.

Kojola, I., Helle, T., Niskanen, M. & Aikio, P. 1995. Effects of lichen biomass on winter diet, body mass and reproduction of semi-domesticated reindeer *Rangifer t. tarandus* in Finland. *Wildlife Biology*, 1:33-38.

Kositcin, N. & Krapež, B. 2004. Relationship between detrital zircon age-spectra and the tectonic evolution of the Late Archaean Witwatersrand Basin, South Africa. *Precambrian Research*, 129:141-168.

Kranner, I., Beckett, R., Hochman, A. & Nash, T.H. 2008. Desiccation tolerance in lichens: a review. *Bryologist*, 111:576-593.

Kurina, L.M. & Vitousek, P.M. 2001. Nitrogen fixation rates of *Stereocaulon vulcani* on young Hawaiian lava flows. *Biogeochemistry*, 55:179-194.

Lana, C., Gibson, R.L., Kisters, A. & Reimold, W.U. 2003. Archean crustal structure of the Kaapvaal craton, South Africa–evidence from the Vredefort dome. *Earth and Planetary Science Letters*, 206:133-144.

Lana, C., Reimold, W.U., Gibson, R.L. Koeberl, C. & Siegesmund, S. 2004. Nature of the Archean midcrust in the core of the Vredefort dome, Central Kaapvaal Craton, South Africa. *Geochimica et Cosmochimica Acta*, 68(3):623-642.

Lange, O.L., Büdel, B., Meyer, A. & Kilian, E. 1993. Further evidence that activation of net photosynthesis by dry cyanobacterial lichens requires liquid water. *Lichenologist*, 25:175-189.

Lange, O.L., Hahn, S.C., Meyer, A., Tenhunen, J.D. 1998. Upland tundra in the foothills of the Brooks Range, Alaska, U.S.A.: lichen long-term photosynthetic CO_2 uptake and net carbon gain. *Arctic and Alpine Research*, 30:252-261.

Larrea, M., Martig, S., Castro, S., Aliani, P. & Bjerg, E. 2010. Rock AR - A point counting application for petrographic thin sections. In 26th Spring Conference on Computer Graphics, Budmerice, Slovakia, pp. 13-15.

Law, J.D.M., Bailey, A.C., Cadle, A.B., Phillips, G.N. & Stanistreet, I.G. 1990. Reconstructive approach to the classification of Witwatersrand ‘quartzites’. *South African Journal of Geology*, 93:83-92.

Le Maitre, R.W., Streckeinsen, A., Zanettin, B., Le Bas, M.J., Bonin, B., Bateman, P., Bellieni, G., Dudek, A., Efremova, S., Keller, J., Lameyre, J., Sabine, P.A., Schmid, R. Sørensen, H. & Wooley, A.R. 2002. Igneous rocks: A classification and glossary of terms. Cambridge: Cambridge University Press. 236p.

Le Pera, E. & Sorriso-Valvo, M. 2000. Weathering, erosion and sediment composition in a high-gradient river, Calabria, Italy. *Earth Surface Processes and Landforms*, 25:277-292.

Lee, C.H. & Yi, J.E. 2007. Weathering damage evaluation of rock properties in the Bunhwangsa temple stone pagoda, Gyeongju, Republic of Korea. *Environmental Geology*, 52:1193-1205.

Lee, M.R. & Parsons, I. 1999. Biomechanical and biochemical weathering of lichen encrusted granite: textural controls on organic–mineral interactions and deposition of silica-rich layers. *Chemical Geology*, 161:385-397.

Li, Z., Liu, L., Chen, J. & Chen, H.H. 2016. Cellular dissolution at hypha- and sporemineral interfaces revealing unrecognized mechanisms and scales of fungal weathering. *Geology*, 44(4):319-322.

Lisci, M., Monte, M. & Pacini, E. 2003. Lichens and higher plants on stone: a review. *International Biodeterioration & Biodegradation*, 51:1-17.

Longton, R.E. 1997. The role of bryophytes and lichens in polar ecosystems. (*In* Woodin, S.J. & Marquiss, M., *eds*. Ecology of arctic environments. Oxford: Blackwell Science. p. 69-96).

Lücking, R., Lawrey, J.D., Sikaroodi, M., Gillevet, P.M., Chaves, J.L., Sipman, H.J.M. & Bungartz, F. 2009. Do lichens domesticate photobionts like farmers domesticate crops? Evidence from a previously unrecognized lineage of filamentous cyanobacteria. *American Journal of Botany*, 96(8):1409-1418.

Ma, L., Taylor, K.G., Doweya, P.J., Courtois, L., Gholiniad, A. & Lee, P.D. 2017. Multi-scale 3D characterisation of porosity and organic matter in shales with variable TOC content and thermal maturity: examples from the Lublin and Baltic Basins, Poland and Lithuania. *International Journal of Coal Geology*, 180:100-112.

Mahaney, W.C., Krinsley, D.H. & Allen, C.C.R. 2013. Biomineralization of weathered rock rinds: examples from the lower afroalpine zone on Mount Kenya. *Geomicrobiology Journal*, 30:411-421.

Makhalanyane, T.P., Valverde, A., Gunnigle, E., Frossard, A., Ramond, J. & Cowan, D.A. 2015. Microbial ecology of hot desert edaphic systems. *FEMS Microbiology Reviews*, 39:203-221

Mast, M.A. & Drever, J.I. 1987. The effect of oxalate on the dissolution rates of oligoclase and tremolite. *Geochimica et Cosmochimica Acta*, 51(9):2559-2568.

Maynard, J.B. & Klein, G.D. 1995. Tectonic subsidence analysis in the characterization of sedimentary ore deposits: Examples for the Witwatersrand (Au), White Opine (Cu), and Molango (Mn). *Economic Geology*, 90:37-50.

McCarthy, T.S. 2006. The Witwatersrand Supergroup. (*In* Johnsonn, M.R., Anhaeusser, C.R. & Thomas, R.J., *eds.* The Geology of South Africa. Pretoria: Geological Society of South Africa. p. 57-89).

McCarthy, T. & Rubidge, B. 2005. The story of Earth and life: A southern Africa perspective on a 4.6-billion-year journey. Cape Town: Struik Nature. 333p.

McKechnie, C., Grab, S. & Drennan, G. 2007. Documenting lichen-induced mechanical weathering of quartzitic sandstone at Kaapsehoop, Mpumalanga*. South African Journal of* Science, 103:117-120.

Mees, F., Swennen, R., Van Geet, M. & Jacobs, P. 2003. Applications of X-ray computed tomography in the geosciences. London: Geological Society - Special Publications. 250p.

Meier, D.L., Heinrich, C.A. & Watts, M.A. 2009. Mafic dikes displacing Witwatersrand gold reefs: Evidence against metamorphic-hydrothermal ore formation. *Geology*, 37:607-610.

Mengel, K. & Kirkby, E.A. 2001. Principles of plant nutrition. 5th ed. London: Kluwer Academic publishers.

Meslier, V., Casero, M.C., Dailey, M., Wierzchos, J., Ascaso, C., Artieda, O., McCullough4, P.R. & DiRuggiero, J. 2018. Fundamental drivers for endolithic microbial community assemblies in the hyperarid Atacama Desert. *Environmental Microbiology*, 20(5):1765-1781.

Meunier, A., Sardini, P., Robinet, J.C. & Prêt, D. 2007. The petrography of weathering processes: facts and outlooks. *Clay Minerology*, 42:415-435.

Meyer, F.M., Tainton, S. & Saager, R. 1990. The mineralogy and geochemistry of small-pebble conglomerates from the Promise Formation in the West Rand and Klerksdorp area. *South African Journal of Geology*, 93(1):118-134.

Migoń, P. & Lidmar-Bergstroöm, K. 2001. Weathering mantles and their significance for geomorphological evolution of central and northern Europe since the Mesozoic. *Earth-Science Review*, 56:285-324.

Migoń, P. & Thomas, M.F. 2002. Grus weathering mantles. Problems of interpretation. *Catena*, 49:5-24.

Mitchell, R.L., Cuadros, J., Duckett, J.G., Pressel, S., Mavris, C., Sykes, D., Najorka, J., Edgecombe, G.D., & Kenrick, P. 2016. Mineral weathering and soil development in the earliest land plant ecosystems. *Geology*, 44(12):1007-1010.

Mogg, A.O.D. 1961. The trees, shrubs and woody herbs of the Witwatersrand region in relation to the geology and physiography. University of the Witwatersrand. (Thesis – PhD).

Molnár, K. & Farkas, E. 2010. Current results on biological activities of lichen secondary metabolites: a review. *Biosciences*, 65(c):157-173.

Money, N.P. 2004. The fungal dining habit d a biomechanical perspective. *Mycologist*, 18:71-76.

Morley, G.F. & Gadd, G.M. 1995. Sorption of toxic metals by fungi and clay minerals. Mycological Research, 99:1429-1438.

Mucina, L. & Rutherford, M.C. ed. 2006. The vegetation of South Africa, Lesotho and Swaziland. Sterlitzia 19. Pretoria: South African National Biodiversity Institute.

Muggia, L., Vancurova, L., Skaloud, P., Peksa, O., Wedin, M. & Grube, M. 2013. The symbiotic playground of lichen thalli – a highly flexible photobiont association in rock-inhabiting lichens. *Microbiol Ecology*, 85(2):313-323.

Myers, R.E., McCarthy T.S. & Stanistreet, I.G. 1990. A tectono-sedimentary reconstruction of the development and evolution of the Witwatersrand Basin, with particular emphasis on the Central Rand group. *South African Journal of Geology*, 93:180-201.

Nakayama, H., Burns, D. M. & Kawase, T. 2011. Nondestructive microstructural analysis of porous bioceramics by microfocus X-ray computed tomography (μCT): a proposed protocol for standardized evaluation of porosity and interconnectivity between macro-pores. *Journal of Nondestructive Evaluation*, 30:71-80.

Nash, T.H. 2008. Lichen Biology. 2nd ed. Cambridge: Cambridge University Press. 498p.

Nehler, M. 2017. Evaluation of porosity and permeability estimates for rock samples based on X-ray micro-tomography. Ruhr-Universitat Bochum. (Thesis – PhD).

Nelsen, M.P., Rivas-Plata, E., Andrew, C.J., Lücking, R. & Lumbsch, H.T. 2011. Phylogenetic diversity of Trentepohlialean algae associated with lichen forming fungi. *Journal of Phycology*, 47:282-290.

Newsome, D. & Ladd, P. 1999. The use of quartz grain microtextures in the study of the origin of sand terrains in Western Australia. *Catena*, 35:1-17.

Nwaila, G. 2014. Application of HPGR and X-Ray CT to investigate the potential of Witwatersrand gold ore for heap leaching: A process mineralogy approach. Cape Town: University of Cape Town. (Thesis – MSc)

Nwaila, G., Frimmel, H.E. & Minter, W.E.L. 2017. Provenance and geochemical variations in shales of the Mesoarchean Witwatersrand Supergroup. *The Journal of Geology*, 125:399-422.

Offre, P., Spang, A. & Schleper, C. 2013. Archaea in Biogeochemical Cycles. *Annual Review of Microbiology*, 67:437-57.

Oksanen, I. 2006. Ecological and biotechnological aspects of lichens. *Applied Microbiol Biotechnology*, 73:723-734.

Omelon, C.R. 2008. Endolithic microbial communities in polar desert habitats. *Geomicrobiology Journal*, 25:404-414.

Omelon, C.R., Pollard, W.H. & Ferris, F.G. 2007. Inorganic species distribution and microbial diversity within high Arctic cryptoendolithic habitats. *Microbial Ecology*, 54:740-752.

Osinski, G.R. & Pierazzo, E. 2013. Impact Cratering: Processes and Products. West Sussex: Blackwell Publishing. 360p.

Ougier-Simonin, A., Renard, F., Boehm, C. & Vidal-Gilbert, S. 2016. Microfracturing and microporosity in shales. *Earth-Science Reviews*, 162:198-226.

Passchier, C.W. & Trouw, R.A.J. 2005. Microtectonics. 2nd ed. Berlin: Springer-Verlag. 366p.

Pegg, C.W. 1950. A contribution to the geology of the West Rand area. *Transactions of the Geological Society of South Africa*, 53:209-227.

Phillips, N.G. 1988. Widespread fluid infiltration during metamorphism of the Witwatersrand goldfields: Generation of chloritoid and pyrophyllite. *Journal of Metamorphic Geology*, 6:311-322.

Phillips, N.G. & Law, D.M. 1994. Metamorphism of the Witwatersrand goldfields: A review. *Ore Geology Reviews*, 9:1-31.

Pickersgill, A.E. 2014. Shock metamorphic effects in lunar and terrestrial plagioclase feldspar investigated by optical petrography and micro-X-ray diffraction. Ontario: The University of Western Ontario. (Thesis – DSc).

Pierazzo, E. & Melosh, H.J. 2013. Environmental effects of impact events. (*In* Osinski, G.R. & Pierazzo, E. *ed*. Impact Cratering: Processes and Products. West Sussex: Blackwell Publishing Ltd. p. 146-156).

Pointing, S.B., Büdel, B., Convey, P., Gillman, L.N., Körner, C., Leuzinger, S. & Vincent, W.F. 2015. Biogeography of photoautotrophs in the high polar biome. *Frontiers in Plant Science*, 6:692-698.

Pontefract, A., Osinski, G.R., Cockell, C.S., Moore, C.A., Moores, J.E. & Southam, G. 2014. Impact-generated endolithic habitat within crystalline rocks of the Haughton Impact Structure, Devon Island, Canada. *Astrobiology*, 14(6):522-533.

Prasad, M.N.V., Naidu, R. & Sajwan, K.S. 2006. Trace elements in the environment: biogeochemistry, biotechnology, and bioremediation. Boca Raton: Taylor & Francis Group. 706p.

Prieto, B., Silva, B., Rivas, T., Wierzchos, J. & Ascaso, C. 1997. Mineralogical transformation and neoformation in granite caused by the lichens *Tephromela atra* and *Ochrolechia parella*. *International Biodeterioration and Biodegradation*, 40:191-199.

Prieto, B., Rivas, T. & Silva, B. 1999. Environmental factors affecting the distribution of lichens on granitic monuments in the Iberian Peninsula. *The Lichenologist*, 31(3):291-305.

Purvis, W.O. 2000. Lichens. London: Smithsonian Institution Press.112p.

Purvis, O.W., Bailey, E.H., McLean, J., Kasama, T. & Williamson, B.J. 2004. Uranium biosorption by the lichen *Trapelia involuta* at a uranium mine. *Geomicrobiology Journal*, 21:159-167.

Reimold, W.U. 2006. Impact structures in South Africa. (*In* Johnsonn, M.R., Anhaeusser, C.R. & Thomas, R.J., *eds.* The Geology of South Africa. Johannesburg/Council for Geoscience, Pretoria: Geological Society of South Africa. p. 629-649).

Reimold, W.U. & Gibson, R.L. 2009. Meteorite impact! The danger from space and South Africa's mega-impact: The Vredefort structure. 3rd ed. Berlin: Springer. 338p.

Reimold, W.U., Koeberl, C., Gibson, R.L. & Dressler, B.O. 2005. Economic mineral deposits in impact structures: a review. (*In* Koeberl, C. & Henkel, H., *eds*. Impact Tectonics. Heidelberg; Springer. p. 479-552).

Reimold, W.U., Pybus, G.Q.J., Kruger, F.J., Layer, P.W. & Koeberl, C. 2000. The Anna's Rust sheet and related gabbroic intrusions in the Vredefort dome-Kibaran magmatic event on the Kaapvaal Craton and beyond. *Journal of African Earth Sciences*, 31:499-521.

Robb, L.J., Brandl, G., Anhaeusser, C.R. & Poujol, M. 2006. Archaean granitoid intrusions. (*In* Johnsonn, M.R., Anhaeusser, C.R. & Thomas, R.J., *eds.* The Geology of South Africa. Johannesburg/Council for Geoscience, Pretoria: Geological Society of South Africa. p. 57-89).

Robb, L.J. & Meyer, F.M. 1995. The Witwatersrand Basin, South Africa: Geological framework and mineralization processes. *Ore Geology Reviews*, 10:67-94.

Roering, C. 1990. The Vredefort structure: a perspective with regard to new tectonic data from adjoining terranes. *Tectonophysics*, 171:7-22.

Rossi, F. & De Philippis, R. 2015. Role of cyanobacterial exopolysaccharides in Phototrophic biofilms and in complex microbial mats. *Life*, 5:1218-1238.

Salminen, J., Pesonen, L.J., Reimold, W.U., Donadini, F. & Gibson, R.L. 2009. Paleomagnetic and rock magnetic study of the Vredefort impact structure and the Johannesburg dome, Kaapvaal Craton, South Africa—Implications for the apparent polar wander path of the Kaapvaal Craton during the Mesoproterozoic. *Precambrian Research*, 168:167-184.

Salvadori, O. & Casanova-Municchia, A. 2016. The Role of Fungi and Lichens in the Biodeterioration of Stone Monuments. *The Open Conference Proceedings Journal*, 7: 39-54.

Sand, W. 1997. Microbial mechanisms of deterioration of inorganic substrates — a general mechanistic overview. *International Biodeterioration & Biodegradation*, 40:183-190.

Scarciglia, F., Saporito, N., La Russa, M.F., Le Pera, E., Macchione, M., Puntillo, D., Crisci, G.M. & Pezzino, A. 2012. Role of lichens in weathering of granodiorite in the Sila uplands (Calabria, southern Italy). *Sedimentary Geology*, 280:119-134.

Schatz, A. 1963. Chelation in nutrition, soil microorganisms and soil chelation: the pedogenic action of lichens and lichen acids. *Agricultural and Food Chemistry*, 11(2):112-118.

Scherrer, S., Haisch, A. & Honegger, R. 2002. Characterization and expression of *XPH1*, the hydrophobin gene of the lichen-forming ascomycete *Xanthoria parietina*. *New Phytologist*, 154:175-84.

Schmitz, M.D., Bowring, S.A., de Wit, M.J. & Gartz, V. 2004. Subduction and terrane collision stabilize the western Kaapvaal craton tectosphere 2.9 billion years ago. *Earth and Planetary Science Letters*, 222(2):363-376.

Scoates, J.S. & Friedman, R.M. 2008. Precise age of the platiniferous Merensky Reef, Bushveld Complex, South Africa, by the U-Pb zircon chemical abrasion ID-TIMS technique. *Economic Geology*, 103:465-471.

Seaward, M.R.D. 1997. Major impacts made by lichens in biodeterioration processes. *International Biodeterioration & Biodegradation*, 40(2-4):269-273.

Sedia, E.G. & Ehrenfeld, J.G. 2003. Lichens and mosses promote alternate stable plant communities in the New Jersey Pinelands. *Oikos*, 100(3):447-458.

Sedia, E.G. & Ehrenfeld, J.G. 2006. Differential effects of lichens and mosses on soil enzyme activity and litter decomposition. *Biology and Fertility of Soils*, 43:177-189.

Shearer, T., Bradley, R.S., Araida Hidalgo-Bastida, L., Sherratt, M.J. & Cartmell, H. 2016. Three-dimensional visualisation of soft biological structures by X-ray computed micro-tomography. *Journal of Cell Science*, 129:2483-2492.

Shukla, V., Upreti, D.K. & Bajpai, R. 2014. Lichens to Biomonitor the Environment. New Delhi: Springer. 195p.

Siebert, S.J., Steytler, J., Boneschans, R.B., Siebert, F. & Coetzee, M.S. 2018. Manganese tolerance of *Aloe greatheadii* Schönland var. *davyana* (Schönland) Glen & D.S.Hardy

(Asphodelaceae: Alooideae) on ultramafic-peralkaline outcrops, South Africa. *Haseltonia*, 25:91-99.

Silva, B. & Prieto, B. 2004. Deteriorative effects of lichens on granite monuments. In: St. Clair, L.L., Seaward, M. (Eds.), Biodeterioration of Stone Surfaces. Kluwer Academic Publishers, Netherlands, pp. 69-77.

Silva, B., Prieto, B., Rivas, T., Sanchez-Biezma, M.J., Paz, G. & Carballal, G. 1997. Rapid biological colonization of a granitic building by lichens. *International Biodeterioration Biodegradation*, 40:263-267.

Smith, A.J.B., Beukes, N.J. & Gutzmer, J. 2013. The composition and depositional environments of Mesoarchean iron formations of the West Rand Group of the Witwatersrand Supergroup, South Africa. *Economic Geology*, 108:111-134.

Smith, D.C. 1962. The biology of lichen thalli. *Biological Reviews*, 37:537-570.

Smits, M.M., Bonneville, S., Benning, L.G., Banwart, S.A. & Leake, J.R. 2012. Plant-driven weathering of apatite – the role of an ectomycorrhizal fungus. *Geobiology*, 10:445-456.

Song, S.K. & Huang, P.M. 1988. Dynamics of potassium release from potassium-bearing minerals as influenced by oxalic and citric acids. Soil Science Society of American Journal, 52:383-390.

South African Committee for Stratigraphy. 1980. Stratigraphy of South Africa, Part 1: Randian Erathem. Pretoria: Geology Survey South Africa.

South African Committee for Stratigraphy. 2006. A revised stratigraphic framework for the Witwatersrand Supergroup. Lithostratigraphic series, 42:1-7. Pretoria: Council for Geoscience.

Souza-Egipsy, V., Valladares, F. & Ascaso, C. 2000. Water distribution in foliose lichen species: interactions between method of hydration, lichen substances and thallus anatomy. *Annals of Botany*, 86:595-601.

Souza-Egipsy, V., Wierzchos, J., García-ramos, J.V. & Ascaso, C. 2002. Chemical and ultrastructural features of the lichen–volcanic/sedimentary rock interface in a semiarid region (Almería, Spain). *Lichenologist*, 34(2):155-167.

Spiess, R., Peruzzo, L., Prior, D.J. & Wheeler, J. 2001. Development of garnet porphyroblasts by multiple nucleation, coalescence and boundary misorientation-driven rotations. *Journal of Metamorphic Geology*, 19:269-290.

Stanistreet, I.G. & McCarthy, T.S. 1991. Changing tectonosedimentary scenarios relevant to the development of the Late Archaean Witwatersrand Basin. *Journal of African Earth Sciences*, 13:65-81.

Stepto, D., 1990. The geology and gravity field in the central core of the Vredefort Structure. *Tectonophysics,* 171:75-103.

Stevens, G., Boer, R.H. & Gibson, R.L. 1997a. Metamorphism, fluid flow and gold remobilization in the Witwatersrand Basin: towards a unifying model. *South African Journal of Geology*, 100:363-375.

Stevens G., Gibson R.L. & Droop, G.T.R. 1997b. Mid-crustal granulite facies metamorphism in the Central Kaapvaal craton: The Bushveld Complex connection. *Precambrian Research*, 82:113-132.

Streckeisen, A. 1976. To each plutonic rock its proper name. *Earth Science Reviews. International Magazine for Geo-Scientists. Amsterdam*, 12:1-33.

Stretch, R.C. & Viles, H.A. 2002. The nature and rate of weathering by lichens on lava flows on Lanzarote. *Geomorphology*, 47:87-94.

Syers, J.K. 1964. A study of soil formation on carboniferous limestone with particular reference to lichens as pedogenetic agents. University of Durham. (Thesis - PhD).

Syers, J.K. & Iskander, I.K. 1973. Pedogenetic significance of lichens. (*In* Ahmadjian, V. & Hale, M.E., *eds*. The Lichens. New York: Academic Press. p. 225-248).

Tripathi, M. & Joshi, Y. 2019. Endolichenic fungi: present and future trends. New Delhi: Springer. 180p.

Tucker, R.F., Viljoen, R.P. & Viljoen, M.J. 2016. A Review of the Witwatersrand Basin - The world's greatest goldfield. *Episodes*, 39(2):105-133.

U'Ren, J.M., Lutzoni, F., Miadlikowska, J., Laetsch, A.D., & Arnold, A.E. 2012. Host and geographic structure of endophytic and endolichenic fungi at a continental scale. American journal of botany, 99(5):898-914.

Varadachari, C., Barman, A.K. & Ghosh, K. 1994. Weathering of silicate minerals by organic acids: II. Nature of residual products. *Geoderma*, 61:251-268.

Vázquez, P., Shushakova, V. & Gómez-Heras, M. 2015. Influence of mineralogy on granite decay induced by temperature increase: experimental observations and stress simulation. *Engineering Geology*, 189:58-67.

Vernon, R.H. 2019. A practical guide to rock microstructures. 2nd ed. Cambridge: Cambridge University Press. 366p.

Verrecchia, E.P., Braissant, O. & Cailleau, G. 2006. The oxalate-carbonate pathway in soil carbon storage: the role of fungi and oxalotrophic bacteria. (*In* Gadd, G.M., *ed*. Fungi in Biogeochemical Cycles. Cambridge: Cambridge University Press. p. 289-310).

Viles, H.A. 1987. A quantitative scanning electron microscope study of evidence for lichen weathering of limestone, Mendip Hills, Somerset. *Earth Surface Processes and Landforms*, 12:467-473.

Viles, H.A. 1995. Ecological perspectives on rock surface weathering: Towards a conceptual model. *Geomorphology*, 13:21-35.

Vingiani, S., Terribile, F. & Adamo, P. 2013. Weathering and particle entrapment at the rock–lichen interface in Italian volcanic environments. *Geoderma*, 207-208:244-255.

Walker, J.J. & Pace, N.R. 2007. Endolithic microbial ecosystems. *Annual Review of Microbiology*, 61:331-347.

Walraven, F. & Elsenbroek, J.H. 1991. Geochronology of the Schurwedraai alkali granite and associated nepheline syenite and implications for the origin of the Vredefort structure. *South African Journal of Geology*, 94:228-235.

Warscheid, Th. & Braams, J. 2000. Biodeterioration of stone: a review. *International Biodeterioration & Biodegradation*, 46:343-368.

Weber, B. & Büdel, B. 2011. Fungi and lichens. (*In* Reitner, J. & Thiel, V., *eds*. Encyclopedia of geobiology. Dordrecht: Springer. p. 401-411).

Weber, B., Wessels, D.C.J. & Büdel, B. 1996. Biology and ecology of cryptoendolithic cyanobacteria of a sandstone outcrop in the Northern Province, South Africa. *Algological Studies*, 83:565-579.

Wessels, D.C.J. & Büdel, B. 1989. A rock pool lichen community in northern transvaal, South Africa: composition and distribution patterns. *Lichenologist*, 21(3):259-277.

Wessels, D.C.J. & Schoeman, P. 1988. Mechanism and rate of weathering of Clarens Sandstone by an endolithic lichen. *South African Journal of Science*, 84:274-277.

Wessels, D.C.J. & Wessels, L.-A. 1991. Erosion of biogenically weathered Clarens Sandstone by lichenophagous bagworm larvae (Lepidoptera; Pyschidae). *Lichenologist*, 23(3):283-291.

Wessels, D. & Kappen, L. 1993. Photosynthetic performance of rock-colonising lichens in the Mountain Zebra National Park, South Africa. *Koedoe*, 36(1):27-48.

Wessels, D., Venter, D., Wessels, W. & Wessels, L. 1995. Experimental strain analysis of Clarens Sandstone colonised by endolithic lichens. *Koedoe*, 38(2):35-47.

Wierzchos, J. & Ascaso, C. 1994. Application of back-scattered electron imaging to the study of the lichen–rock interface. *Journal of Microscopy*, 175:54-59.

Wierzchos, J. & Ascaso, C. 1996. Morphological and chemical features of bioweathered granitic biotite induced by lichen activity. *Clays and Clay Minerals*, 44(5):652-657.

Wierzchos, J. & Ascaso, C. 2001. Life, decay and fossilisation of endolithic microorganisms from the Ross Desert, Antarctica. *Polar Biology*, 24:863-868.

Wierzchos, J., Ascaso, C., Sancho, L.G. & Green, A. 2003. Iron-rich diagenetic minerals are biomarkers of microbial activity in Antarctic rocks. *Geomicrobiology Journal*, 20:15-24.

Wierzchos, J., Cámara, B., de los Ríos, A., Davila, A.F., Sánchez Almazo, I.M., Artieda, O., Wierzchos, K., Gómez-Silva, B., McKay, C. & Ascaso, C. 2011. Microbial colonization of Ca-sulfate crusts in the hyperarid core of the Atacama Desert: implications for the search for life on Mars. *Geobiology*, 9:44-60.

Wierzchos, J., Casero, M.C., Artieda, O. & Ascaso, C. 2018. Endolithic microbial habitats as refuges for life in polyextreme environment of the Atacama Desert. *Current Opinion in Microbiology*, 43:124-131.

Wierzchos, J., Davila, A.F., Artieda, O., Cámara-Gallego, B., de los Ríos, A., Nealson, K.H., Valea, S., García-Gonzá lez, M.T. & Ascaso, C. 2013. Ignimbrite as a substrate for endolithic life

in the hyper-arid Atacama Desert: implications for the search for life on Mars. *Icarus*, 224:334-346.

Wierzchos, J., Davila, A.F., Sánchez-Almazo, I.M., Hajnos, M., Swieboda, R. & Ascaso, C. 2012a. Novel water source for endolithic life in the hyperarid core of the Atacama Desert. *Biogeosciences*, 9:2275-2286.

Wierzchos, J., de los Ríos, A. & Ascaso, C. 2012b. Microorganisms in desert rocks: the edge of life on earth. *International Microbiology*, 15:173-183.

Wierzchos, J., DiRuggiero, J., Vítek, P., Artieda, O., Souza- Egipsy, V. & Škaloud, P. 2015. Adaptation strategies of endolithic chlorophototrophs to survive the hyperarid and extreme solar radiation environment of the Atacama Desert. *Frontiers in Microbiology*, 6:934.

Wierzchos, J., Sancho, L.G. & Ascaso, C. 2005. Biomineralization of endolithic microbes in rocks from the McMurdo Dry Valleys of Antarctica: implications for microbial fossil formation and their detection. *Environmental Microbiology*, 7(4):566-575.

Williams, M.E. & Rudolph, E.D. 1974. The role of lichens and associated fungi in the chemical weathering of rock. *Mycologia*, 66:648-660.

Williamson, B.J., McLean, J. & Purvis, O.W. 1998. Application of x-ray element mapping across the lichen-rock interface. *Journal of Microscopy*, 191:91-96.

Wong, K.Y., Lacap, D.C., Lau, M.C., Aitchison, J.C., Cowan, D.A. & Pointing, S.B. 2010. Hypolithic colonization of quartz pavement in the high-altitude tundra of central Tibet. *Microbial Ecology*, 60**:**730-739.

Yahr, R., Vilgalys, R. & DePriest, P.T. 2006. Geographic variation in algal partners of *Cladonia subtenuis* (*Cladoniaceae*) highlights the dynamic nature of a lichen symbiosis. *New Phytologist*, 171:847-860.

Zambare, V.P. & Christopher, L.P. 2012. Biopharmaceutical potential of lichens. *Pharmaceutical Biology*, 50(6):778-798.

ANNEXURE

APPENDIX A: WEATHER DATA

Appendix A1: Average monthly rainfall data for the Potchefstroom station (0437104A4)…….162

Appendix A2: Average monthly temperature data for the Potchefstroom station (0437104A4)163

Appendix A3: Average monthly humidity data for the Potchefstroom station (0437104A4)…..164

APPENDIX B: ANALYTICAL EQUIPEMENT

Appendix B1: Image of the nikon eclipse 50ipol polarizing microscope…… ……165

Appendix B2: Simplified schematic diagram of a scanning electron microscope……..165

Appendix B3: Nikon xth 225 micro-focus x-ray tomography system at NECSA ……..166

APPENDIX C: GEOLOGICAL SURVEY DATA

Appendix C1: Geological survey data for the study area…… ……....167

APPENDIX D: POINT COUNT DATA

Appendix D1: Modal abundance (volume %) of the 10 rock samples…… ……168

APPENDIX E: SEM ANALYSIS RESULTS

Appendix E1: K-feldspar rich granite ……..169

Appendix E2: Sub-labile arenites ….....176

Appendix E3: Alkali granite……181

Appendix E4: Ferruginous wacke ……192

Appendix E5: Metaconglomerate……197

APPENDIX A1: AVERAGE MONTHLY RAINFALL (mm) DATA FOR THE POTCHEFSTROOM STATION - 0437104A4 FROM 1997-2017. SOUTH AFRICAN WEATHER SERVICES.

	Month											
Year	**JAN**	**FEB**	**MAR**	**APR**	**MAY**	**JUN**	**JUL**	**AUG**	**SEP**	**OKT**	**NOV**	**DEC**
1997					104	0	1,4	9,6	37,6	22,6	59.0	52,8
1998	77,2	161,4	54,6	4,4	0	0	0	0	16,2	27,4	80,6	142,2
1999	0	31.0	32	24,1	24	0,6	0	0	0	18,2	26	82,6
2000	84,2	68,2	217,4	14,2	25,8	4,2	0	0	0	64,6	38,4	88
2001	19	81,4	73,8	41,6	16,8	16,8	0,6	14,6	4,6	68	168,4	134,8
2002	2,2	7.6	23,4	0,4	3	0,6	0	47,8	3,2	28,6	6	160,2
2003	47.8	64,8	65,8	8,6	0	3	0	12	0	25.0	44	30,6
2004	53,6	144,8	80,6	54,9	0,2	1,4	1	0	0	47,4	42,2	100
2005	157,2	66,6	53,6	48,2	3	0	0	0	0	13,2	41,2	54
2006	82,4	48.8	150,8	57	3	0	0	15,8	5,2	47,6	67,8	161,6
2007	33,2	53,4	39,6	46,4	0	1,2	0	0	56	84	62,8	53.1
2008	68,6	92,8	94,2	0,2	24,2	6.8	0	0	0	37,4	71	73.8
2009	115	92,2	59,6	20,2	23,6	21,6	24,4	12,2	8,8	44,4	63,6	133
2010	119,4	44,4	106,2	47,4	19,4	0	0	0	0	0	0	76.8
2011	31.8	35.8	28,8	95,2	48,4	47,6	4,4	0	0	48,4	87,8	133,4
2012	59,4	69,6	73,4	11,6	0	14,2	1,2	2	32	35,6	31,2	173,2
2013	97,2	51	42	57,6	2,8	0	0	0	0	82,6	29	180,8
2014	61,2	85	70.6	4,4	2,8	0,8	0	6,2	8	11	75,4	83,6
2015	114,4	46	88	23,4	0,4	2,8	5,4	0	53,8	24	29,4	52,4
2016	77,4	61,8	49,6	64,4	17,8	8,8	49	0	0	47,8	79,2	157,2
2017	135	169,2	24,8	60,6	14	0	0,2	0	0			

APPENDIX A2: AVERAGE MONTHLY TEMPERATURE (°C) DATA FOR THE POTCHEFSTROOM STATION - 0437104A4 FROM 1997 - 2017. SOUTH AFRICAN WEATHER SERVICES.

Year	Month																							
	JAN		FEB		MAR		APR		MAY		JUN		JUL		AUG		SEP		OKT		NOV		DEC	
	Max	Min	Max	Min	Max	Min	Max	Min	Max	Min	Max	Min	Max	Min	Max	Min	Max	Min	Max	Min	Max	Min	Max	Min
1997									19,4	3,5	18,8	1,2	20,1	3,1	25,2	5,3	25,2	9,9	27,3	12	30.7	16.0	31,1	16,5
1998	28,6	16,1	29,1	16	29	14,9	28	10,7	23	3	22,2	-0,2	20,9	2,2	22,2	4,2	27,4	10	27,2	12,2	27,7	14,3	27,7	15,3
1999			31.1	16.7	30,6	16	28	11,2	22,9	7	21,7	2,4	21,1	3,1	23,2	3,6	25,8	8	28,3	12,3	32,2	16,5	27,9	16,4
2000	26,4	14,9	26,7	16,1	26,9	15,9	24	9,9	21,7	4,9	21,1	3,6	20	1	23,1	2,5	24,8	8,1	29,6	14,3	27,9	13,6	29,8	16,9
2001	32,6	16,7	29,9	16,9	29,3	15,2	25,1	12,8	24,2	7	22,2	3,5	19,8	1,9	24,5	4,2	26,2	8,5	29,6	15	26,3	14,6	27	14,3
2002	28,9	14,5	27	13,8	28,2	13,5	27,4	10,1	22,7	4,8	18,3	2,4	19,5	-0,2	22,9	7	25,9	8,6	28,8	11,9	28,3	11,1	26,5	14,3
2003	30.1	15.7	29,2	16,4	29,1	13,1	28,9	11,3	23,6	4,8	20,5	1,6	21,9	1,1	22,2	3,7	28,5	10,6	28	12,6	29,7	14,9	32,4	15,9
2004	30	17	28,3	16,2	25,9	14,3	24,9	9,6	23,8	4,2	19,7	0,8	18,4	-0,8	24,1	5,7	25,4	7	28,8	12,1	32,1	15,5	30	16,5
2005	30,1	17	29,5	16,2	26,3	13,3	22,6	8,6	22,6	3,1	21,2	1,4	20,7	-1,2	23,9	3,9	28,1	7,4	29,2	11,7	29,9	13,1	29,7	14,2
2006	26,6	16,3	-	-	26,6	14,8	25,6	11	21,7	3,7	21,9	0,9	23,9	3,8	22,5	5,2	28	7,7	30	13,8	29,6	15,5	30,1	17,7
2007	31,3	17	32,1	14,9	29,7	12,9	26,3	10,1	24,2	1,8	20,1	0,6	20,2	-0,8	23,7	2,1	30,3	10,4	26,1	12,2	28,4	13,4	28.8	15.1
2008	28,4	16,1	30,6	15,7	26,1	13,3	25,4	7,2	23,1	6,6	19,8	1,4	19.7	1.2	25.8	5.8	27,1	6,1	29,7	12,9	28,9	15	30,1	16,3
2009	28,7	16,8	27,1	15,8	26,6	12,9	25,5	9,3	21,4	5,4	20,4	5,1	18,5	-0,7	22,5	4,9	28,6	10,1	28,4	13,3	28	13,9	30,8	16,3
2010	27,2	17,2	29,4	16,2	28,4	15,1	24,6	12,1	23,3	6,7	19,9	-0,5	20	2,1	23,8	3,5	29,5	8,7	-	-	31.8	15.8	30.0	14.7
2011	30.2	17.1	30,8	15,7	30,2	13,9	24	9	21,6	3,9	18,6	-1,7	17,7	-3,5	22	-0,3	27,8	5,4	30	9,5	32,2	13,6	31,8	15,4
2012	33,3	16,1	32	16,3	31,5	13,6	27,3	7,7	26,9	4,9	21,5	0,7	22,5	-0,2	25,4	4,3	27	6,7	31,8	12	33,2	14,5	31	15,4
2013	33	16,7	34,7	15	31,1	14,4	27,1	8,5	25,3	4,4	23,2	0,2	22,9	2,7	24,1	2,2	29,6	6,8	31,2	11,2	31,5	13,7	28,4	15,3
2014	32,1	16,7	30	16,5	26,7	14,6	25,6	7,4	25,1	4,2	21,3	-0,5	19,6	-1,8	22,4	3,3	28,7	7,3	29,9	10,1	27,3	12,5	30	15,2
2015	31,5	15,5	32,1	13,2	28,1	13,1	26,3	8,8	26,4	4,5	19,3	0,1	20,8	1,8	26,5	4,2	26,3	9,8	32,1	13,2	31	11,7	34,6	16,9
2016	31,8	17,3	32,4	16,4	29,8	13,8	27,2	10,7	22,7	5,8	21	2,1	20,1	0	23,6	2,4	28,4	9,1	31,3	11,5	31,1	15,3	32,2	16,8
2017	29,4	16,2	28,5	16,5	30	13,3	26,6	9,6	23,6	4,2	22,7	1,7	23,1	2,5	23,9	3,2	30,1	9,1						

APPENDIX A3: AVERAGE MONTHLY HUMIDITY (%) DATA FOR THE POTCHEFSTROOM STATION - 0437104A4 FROM 1997 - 2017. SOUTH AFRICAN WEATHER SERVICES.

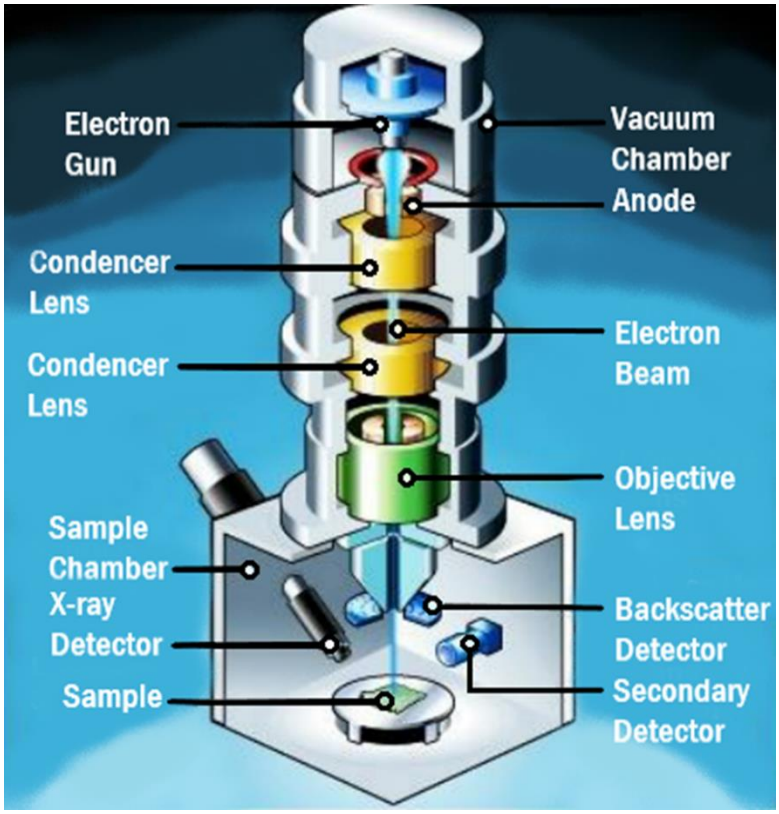
Year	Month																																						
	JAN			FEB			MAR			APR			MAY			JUN			JUL			AUG			SEP			OKT			NOV			DEC		
	08:00	14:00	20:00	08:00	14:00	20:00	08:00	14:00	20:00	08:00	14:00	20:00	08:00	14:00	20:00	08:00	14:00	20:00	08:00	14:00	20:00	08:00	14:00	20:00	08:00	14:00	20:00	08:00	14:00	20:00	08:00	14:00	20:00	08:00	14:00	20:00	08:00	14:00	20:00
1997													79	41	67	77	34	61	79	36	58	67	24	45	77	43	62	67	37	56	66	38	65	69	40	60			
1998	80	55	75	82	54	76	84	51	75	79	40	65	72	29	51	-	-	-	-	-	-	-	-	-	-	-	-	-	-	-	-	-	-	-	-			
1999	-	-	-	78	43	64	81	43	63	77	39	58	87	45	68	78	31	51	77	36	52	63	27	41	63	28	37	64	35	47	64	35	52	82	59	78			
2000	86	65	82	89	68	81	95	68	91	93	55	85	91	48	80	92	50	76	84	38	58	71	28	45	72	37	56	80	51	67	-	-	-	69	22	61			
2001	61	20	51	71	37	56	59	29	59	68	36	64	83	35	65	86	31	60	90	44	63	71	31	46	73	38	55	77	50	66	88	68	85	79	51	72			
2002	71	44	65	84	52	79	81	44	74	76	34	61	82	33	62	92	42	69	77	27	47	81	40	58	64	30	45	62	31	46	56	28	44	78	53	73			
2003	73	45	67	85	51	71	75	39	66	78	34	62	78	32	53	88	35	60	73	27	45	65	27	43	52	25	35	62	32	44	70	43	65	58	31	44			
2004	74	47	62	82	53	70	92	60	85	91	47	78	89	34	71	86	36	62	84	35	55	68	30	46	61	27	38	60	30	47	55	28	45	72	47	68			
2005	79	53	73	81	50	72	84	50	76	39	40	40	-	-	-	-	-	-	-	-	-	-	-	-	-	-	-	-	-	-	-	-	-	-	-	-	-	-	-
2006	-	-	-	-	-	87	82	51	78	71	42	67	71	25	49	71	15	42	68	18	40	62	27	46	37	15	27	48	27	48	53	34	52	66	43	63			
2007	65	36	55	27	16	24	26	28	28	76	33	62	59	16	41	76	25	53	67	19	36	52	18	29	45	18	29	75	39	66	58	33	53	73	46	71			
2008	-	69	62	-	-	-	-	-	-	-	-	-	-	-	-	-	-	-	-	-	-	7	11	11	16	20	21	20	26	26	22	28	28	68	43	55			
2009	-	-	-	-	-	-	-	-	-	-	-	-	-	-	-	-	-	-	-	-	-	-	-	-	-	-	-	-	-	-	50	26	48	66	37	65			
2010	81	59	79	75	43	68	78	45	70	86	47	75	79	35	66	45	14	28	30	11	18	25	7	13	20	6	11	-	-	-	61	37	62	69	39	63			
2011	71	47	74	71	44	70	67	42	68	78	46	78	75	35	69	70	25	56	66	26	49	56	21	41	40	15	30	47	20	40	50	26	44	62	39	57			
2012	60	35	59	69	40	68	63	31	57	64	28	59	56	19	45	65	26	52	57	18	39	48	17	32	54	24	43	49	25	47	50	25	46	65	39	67			
2013	59	40	65	-	-	-	71	49	80	63	31	55	-	-	-	-	-	-	-	-	-	-	-	-	-	-	-	-	-	-	35	26	33	-	-	-			
2014	-	-	-	-	-	-	-	-	-	-	-	-	-	-	-	-	-	-	62	20	40	55	22	37	41	16	28	47	21	36	63	38	58	65	42	59			
2015	68	38	60	59	31	49	74	42	66	71	33	62	60	21	46	69	30	51	63	25	37	46	15	27	61	32	47	42	20	33	37	18	28	48	26	41			
2016	64	38	61	65	35	57	68	37	56	73	37	63	76	36	61	78	31	55	70	27	47	56	19	32	44	19	28	44	20	27	60	36	58	64	39	56			
2017	73	50	72	80	55	79	71	37	64	78	36	63	75	31	59	72	25	47	65	22	41	56	20	34	44	16	29												

- indicates that data is unavailable

APPENDIX B1: IMAGE OF THE NIKON ECLIPSE 50IPOL POLARIZING MICROSCOPE.



APPENDIX B2: SIMPLIFIED SCHEMATIC DIAGRAM OF A SCANNING ELECTRON MICROSCOPE.



APPENDIX B3: NIKON XTH 225 MICRO-FOCUS X-RAY TOMOGRAPHY SYSTEM AT NECSA.



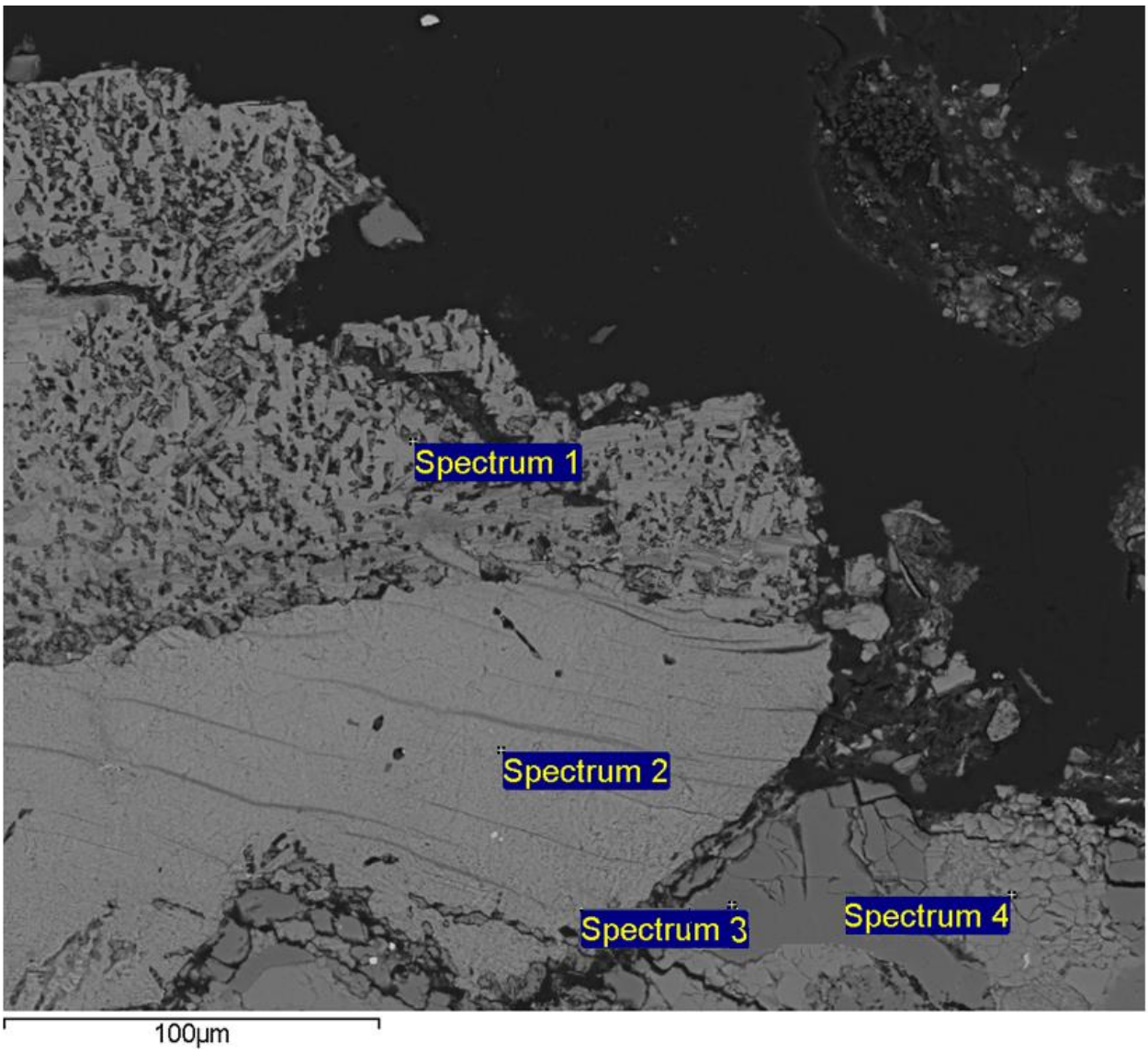
APPENDIX C1: GEOLOGICAL SURVEY DATA FOR THE STUDY AREA.

Rock sample no.	Lithology	Altitude	Approx. distance from Vaal River	Comments	Locality		Average bedding orientation	
							Strike	Dip
VKA1	K-feldspar rich granite	1373m	480m	Well sorted heterogeneous medium- to fine-grained phase of rock, extensively transected by thin, grey veinlets of pseudotachylitic breccias.	26°54'48.22"S	27°24'12.10"E	-	-
VKA2	K-feldspar rich granite	1372m	450m		26°54'48.66"S	27°24'11.10"E	-	-
VKB1	Quartzite	1342m	30m	Moderately sorted fine-grained siliceous quartzites, with minor inclusions of pale green mica which gives the rock a characteristic green tint in certain areas.	26°52'54.04"S	27°21'30.75"E	254°	58°
VKB2	Quartzite	1343m	50m		26°52'54.03"S	27°21'32.28"E	256°	62°
VKC1	Alkali Granite	1360m	100m	Well sorted heterogeneous medium-grained phase of rock, extensively transected by pseudotachylitic breccia. Alkali granite also display multiply striated joint surfaces and shatter cones.	26°51'14.99"S	27°20'15.13"E	-	-
VKC2	Alkali Granite	1355m	120m		26°51'13.54"S	27°20'13.54"E	-	-
VKD1	Ferruginous Quartzite	1446m	2780m	Poorly sorted medium- to coarse-grained phase of the rock, which often exibits scattered pebbles. The bulk of the formation weathers to brown and buff colours due to the presence of a fine clastic matrix with a variable content of iron oxides. Hence, secondary ferrous coatings are common on outcrop surfaces.	26°53'8.88"S	27°14'30.31"E	119°	56°
VKD2	Ferruginous Quartzite	1450m	2800m		26°53'6.36"S	27°14'31.94"E	117°	58°
VKE1	Metaconglomerate	1440m	2800m	Poorly sorted coarse- to fine-grained rock, which consists of a substantial fraction of rounded to subangular gravel-size clasts in a matrix of finer grained sediments.	26°52'55.35"S	27°14'38.21"E	118°	54°
VKE2	Metaconglomerate	1450m	2850m		26°52'52.67"S	27°14'37.64"E	116°	52°

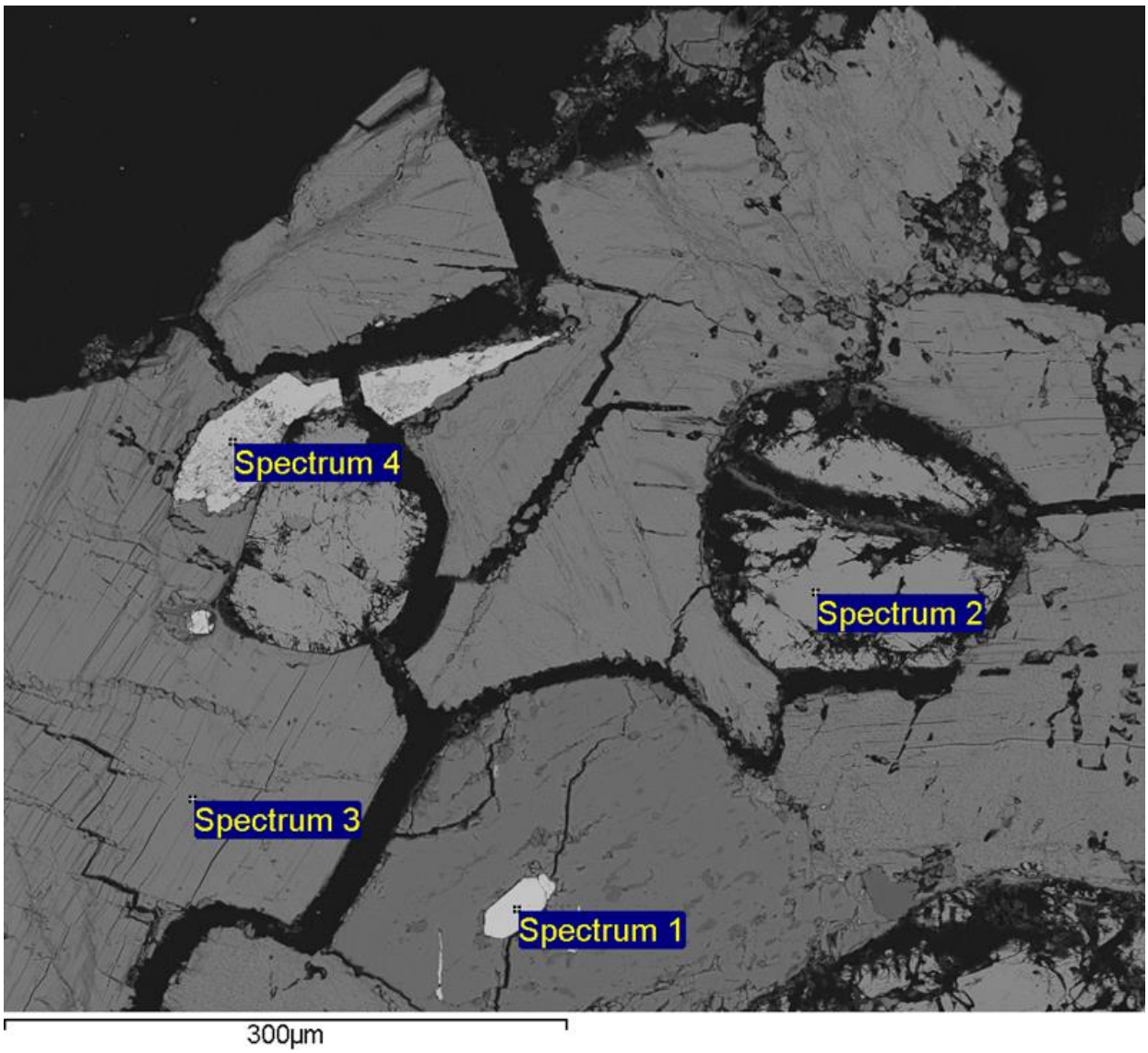
APPENDIX D1: MODAL ABUNDANCE (VOLUME %) OF THE 10 ROCK SAMPLES.

Sample	Quartz	K-feldspar	Plagioclase	Biotite	Fe-hornblende (aegerine/ardfedsonite)	Matrix component	Lithic fragments
VKA1	26	34	38	8	0	0	0
VKA2	28	36	40	6	0	0	0
VKB1	82	0	0	0	0	18	0
VKB2	83	0	0	0	0	17	0
VKC1	24	24	42	0	10	0	0
VKC2	22	26	44	0	8	0	0
VKD1	73	0	0	0	0	27	0
VKD2	71	0	0	0	0	29	0
VKE1	12	0	0	0	0	16	72
VKE2	8	0	0	0	0	18	74

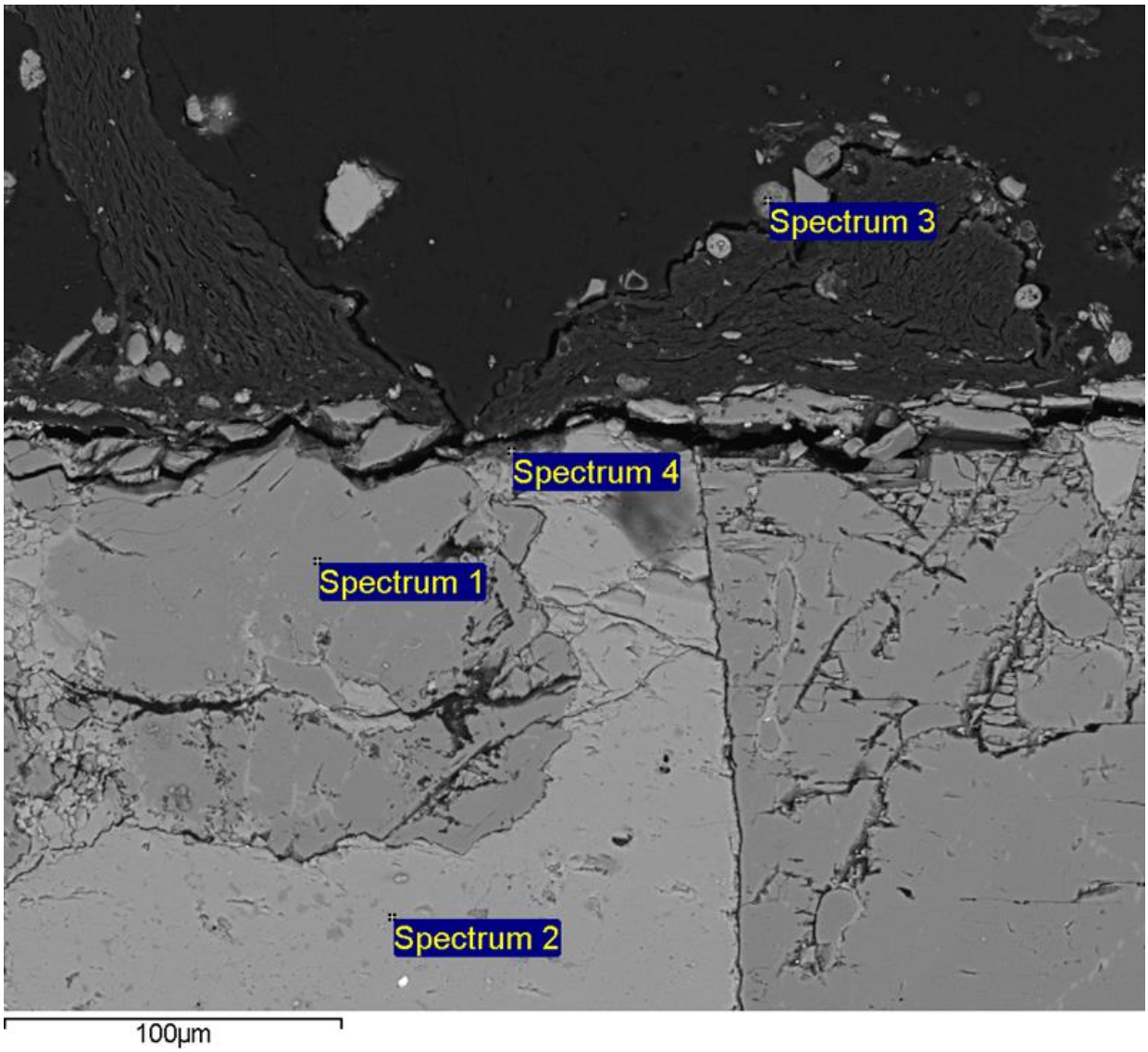
APPENDIX E1: SEM-EDS ANALYSIS RESULTS (wt. %) ON K-FELDSPAR RICH GRANITE.



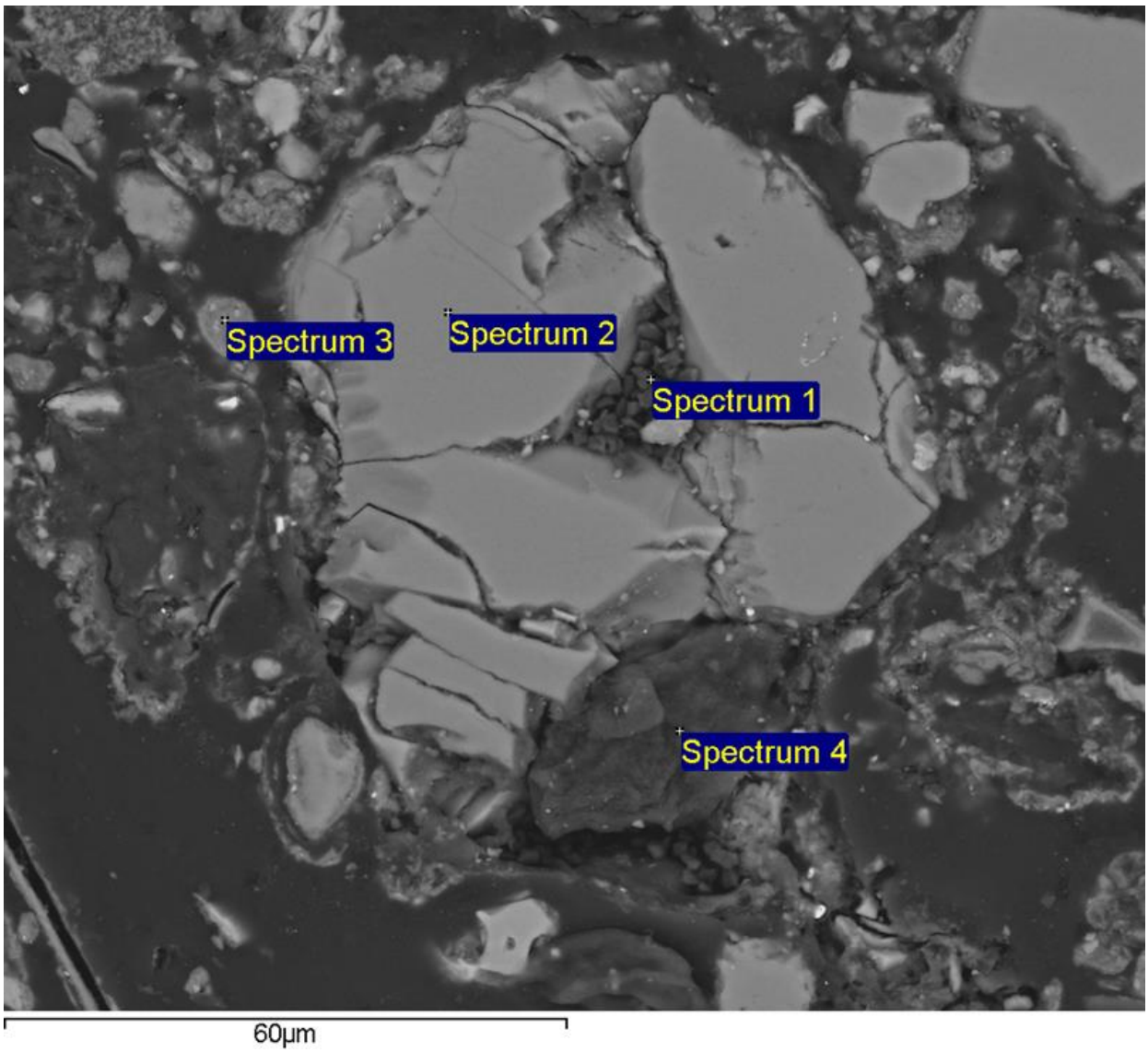
Spectrum	In stats.	C	O	Mg	Al	Si	K	Ti	Fe	Total
Spectrum 1	Yes	14,94	44,85	4,51	7,46	13,16	3,16	1,26	10,66	100
Spectrum 2	Yes	24,36	37,27	3,89	6,22	12,03	4,02	1,43	10,78	100
Spectrum 3	Yes	24,45	45,13			30,42				100
Spectrum 4	Yes	17,34	13		10,17	37,9	21,59			100



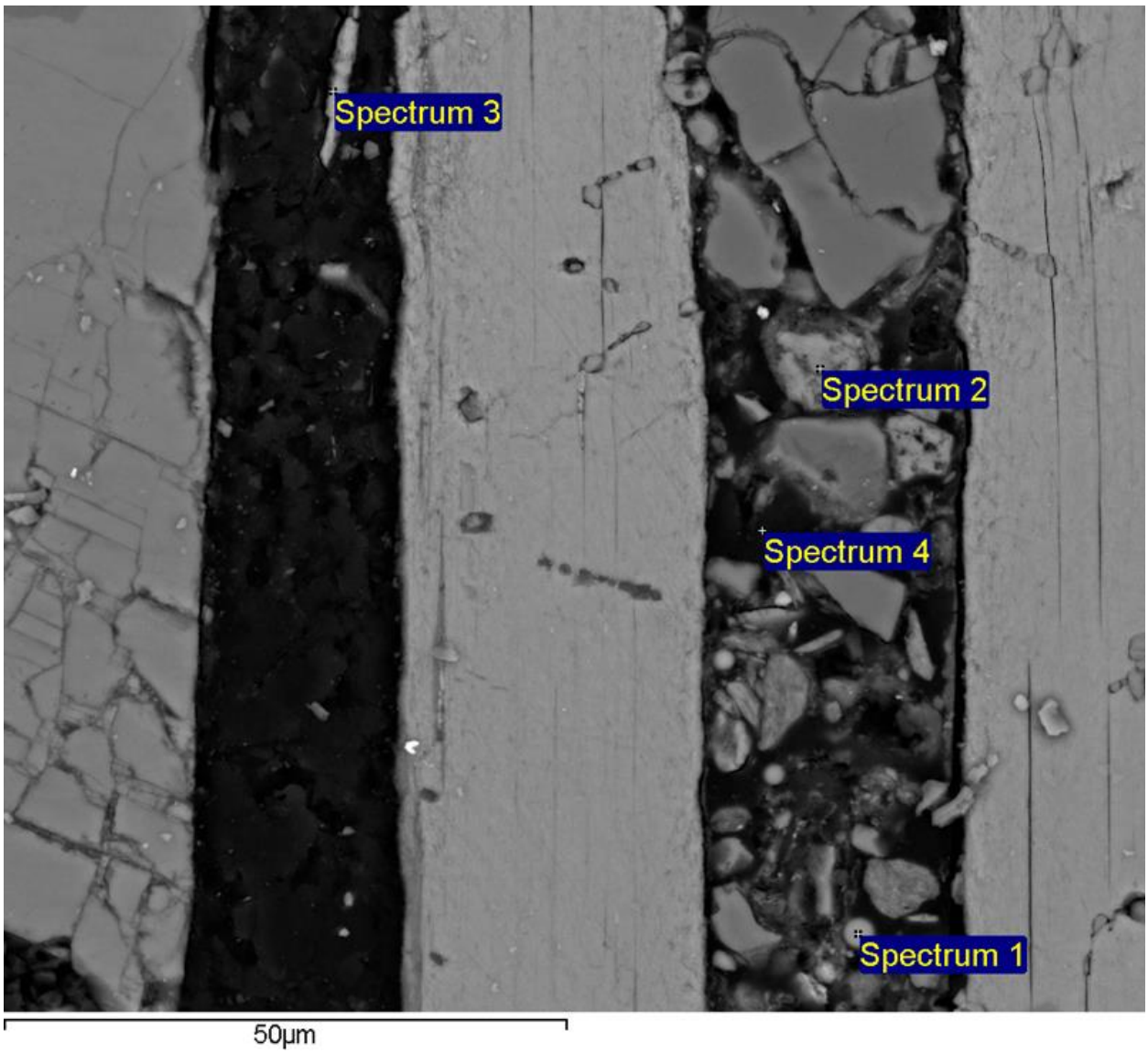
Spectrum	In stats.	C	O	F	Mg	Al	Si	P	K	Ca	Ti	Fe	Zr	Total
Spectrum 1	Yes	34,11	23,65				9,4						32,83	100
Spectrum 2	Yes	21,21	28,8	4,06				15,96		29,96				100
Spectrum 3	Yes	15,15	41,45		4,68	6,63	13,74		4,62		1,82	11,9		100
Spectrum 4	Yes	14,97	37,95								40,71	6,36		100



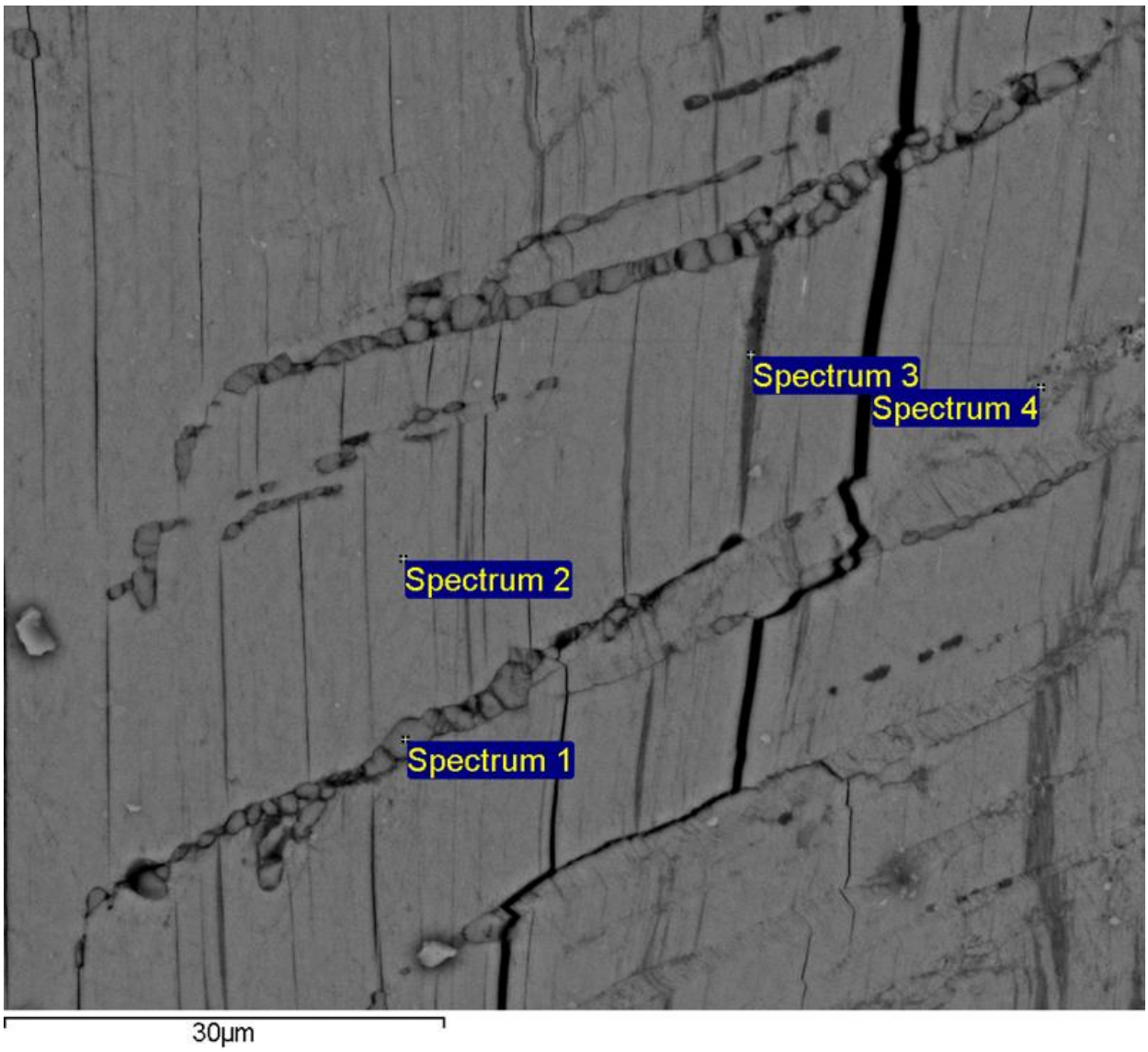
Spectrum	In stats.	C	O	Na	Al	Si	P	S	Cl	K	Ca	Ti	Fe	Total
Spectrum 1	Yes	21,31	41,83	4,93	7,74	23				0,1	1,09			100
Spectrum 2	Yes	24,12	37,08	0,32	6,9	22,67				8,78		0,13		100
Spectrum 3	Yes	34,59	32,47			32,93								100
Spectrum 4	Yes	22,91	44,68	3,89	7,1	19,79	0,22	0,11	0,09	0,43	0,31		0,46	100



Spectrum	In stats.	C	O	Na	Mg	Al	Si	P	S	Cl	K	Ca	Ti	Fe	Total
Spectrum 1	Yes	96,59	2,77	0,18			0,26		0,07	0,06	0,06				100
Spectrum 2	Yes	24,05	44,42				31,53								100
Spectrum 3	Yes	19,43	31,01		0,48	11,65	26,05			0,48	1,68		0,44	8,79	100
Spectrum 4	Yes	58,48	7,54	0,52		3,42	9,56	0,46	1,15	3,54	2,11	1,39		11,84	100



Spectrum	In stats.	C	O	Na	Mg	Al	Si	S	Cl	K	Ca	Ti	Mn	Fe	Total
Spectrum 1	Yes	28,11	42,8	0,18	0,46	9,19	14,65			0,39	2,27	0,5		1,44	100
Spectrum 2	Yes	23,92	37,56			6,85	23,16			8,06				0,45	100
Spectrum 3	Yes	36,59	41,29	0,18	2,36	3,75	7,91	0,09	0,3	1,6		0,59	0,11	5,23	100
Spectrum 4	Yes	80,63	16,38			0,28	0,46		1,88					0,37	100

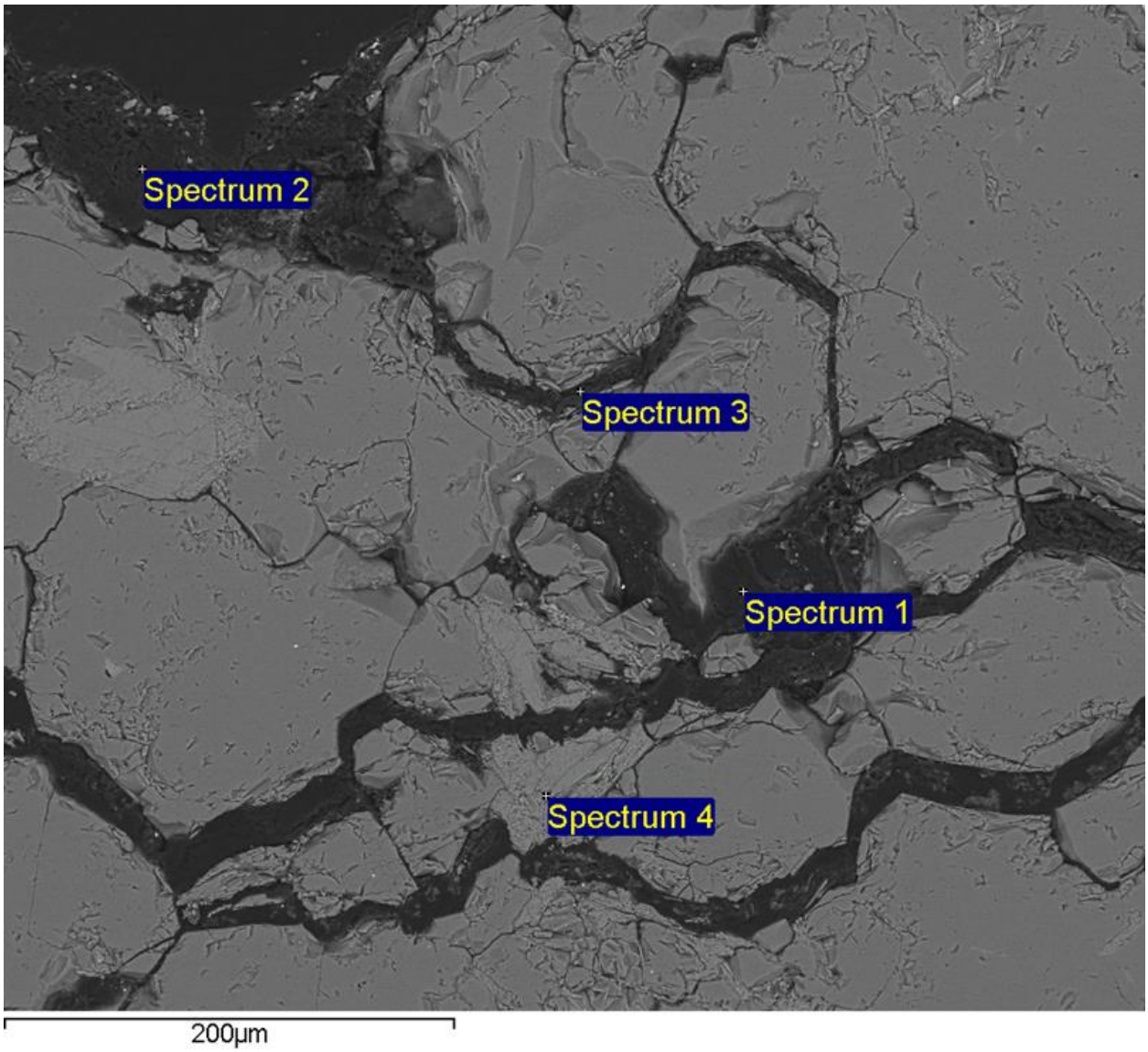


Spectrum	In stats.	C	O	Na	Mg	Al	Si	K	Ti	Fe	Total
Spectrum 1	Yes	25,69	38,83	0,54	0,19	6,25	20,5	7,42		0,59	100
Spectrum 2	Yes	21,51	36,83		4,15	6,35	12,8	4,62	1,72	12,02	100
Spectrum 3	Yes	21,79	38,81		1,84	11,08	16,46	1,79	0,81	7,41	100
Spectrum 4	Yes	13,97	39		3,8	9,09	14,09	3,84	3,16	13,05	100

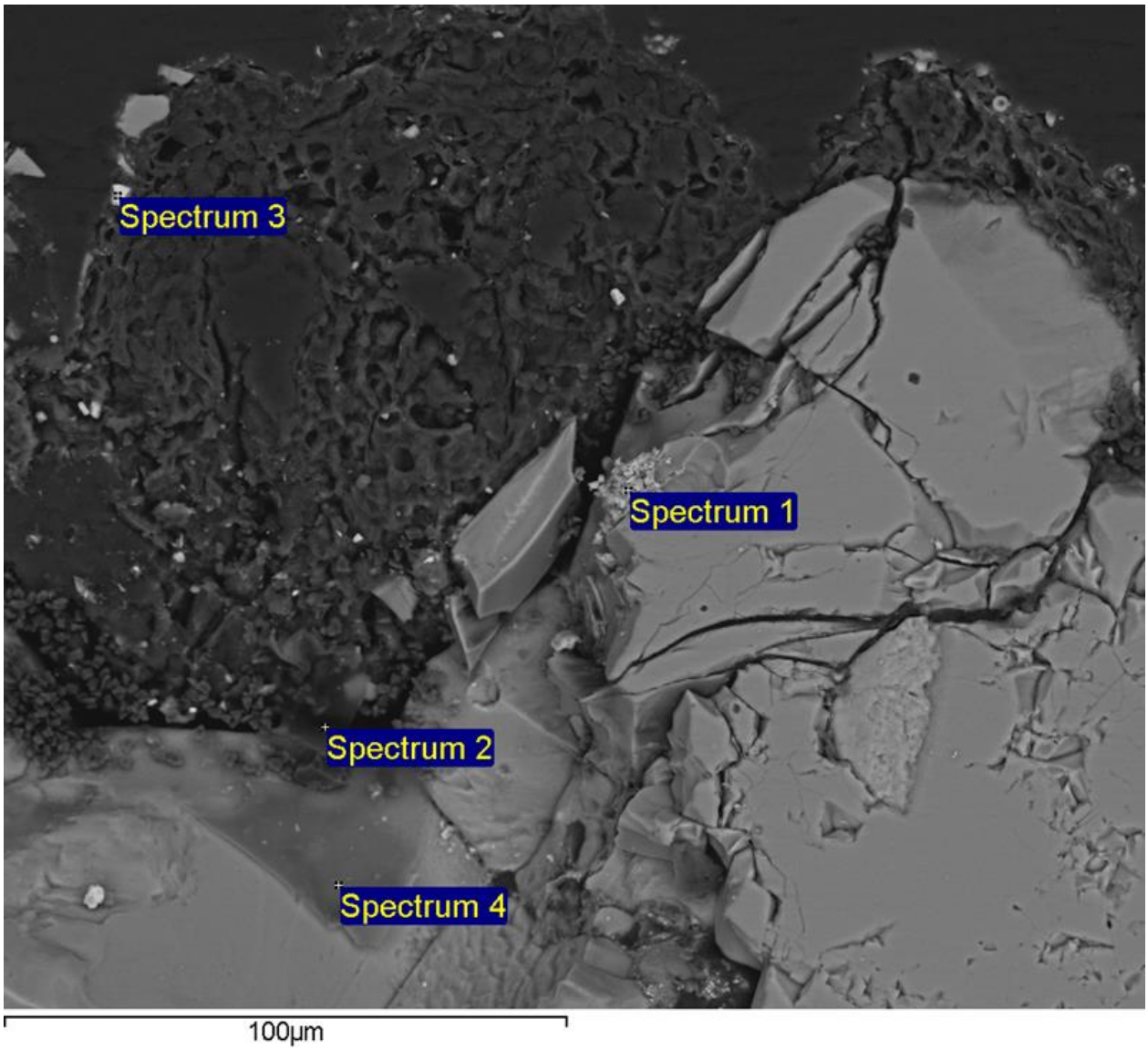


Spectrum	In stats.	C	O	Mg	Al	Si	S	Cl	K	Ca	Ti	Fe	Total
Spectrum 1	Yes	28,22	46,95		1,11	23,56						0,16	100
Spectrum 2	Yes	91,87	4,49	0,13	0,43	1,89		0,14	0,17	0,59		0,31	100
Spectrum 3	Yes	66,43	6,68	0,18	5,54	12,07	0,91		0,7	0,38	0,52	6,6	100
Spectrum 4	Yes	28	43,89			27,95						0,16	100

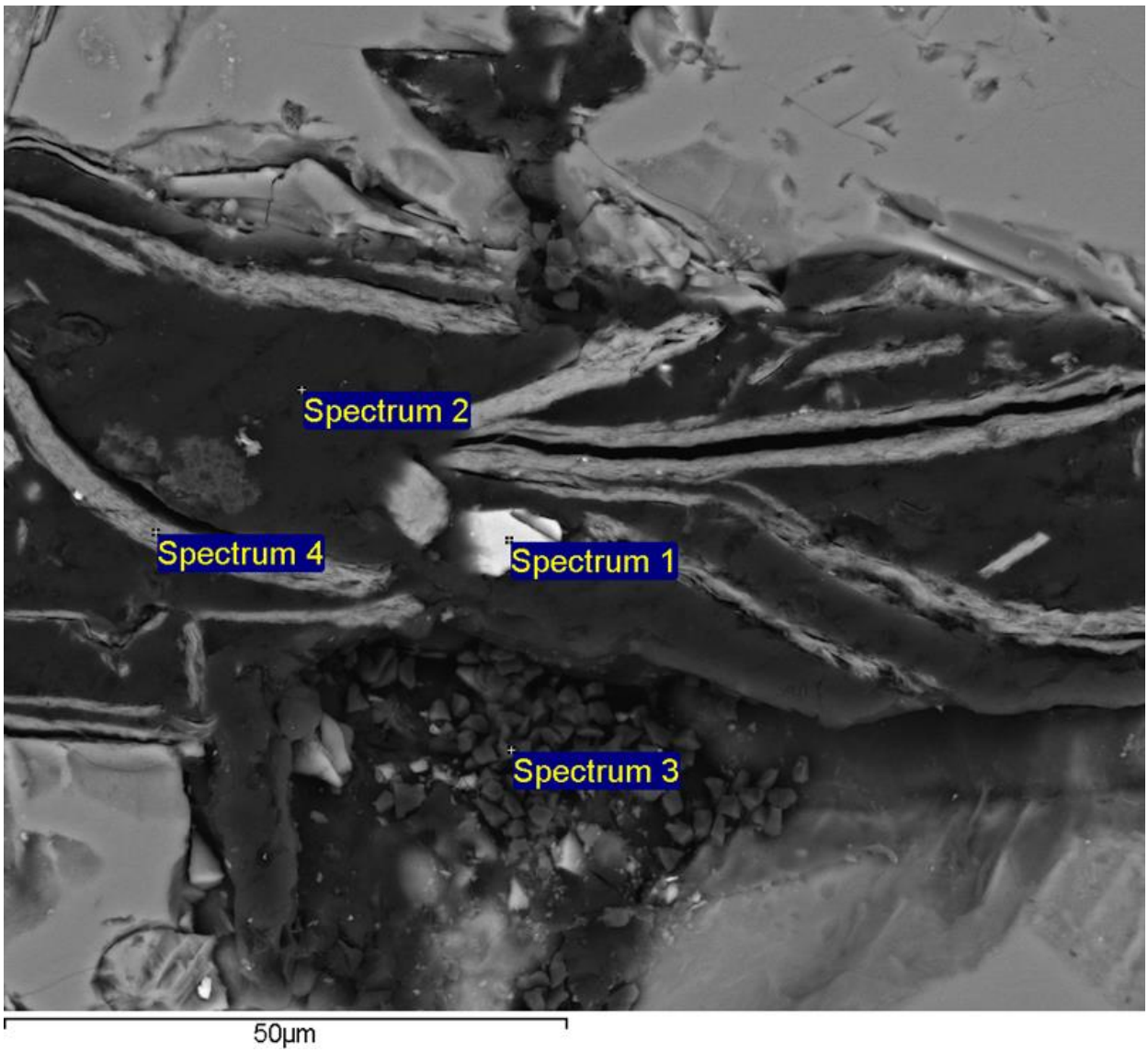
APPENDIX E2: SEM-EDS ANALYSIS (wt. %) RESULTS ON QUARTZITE.



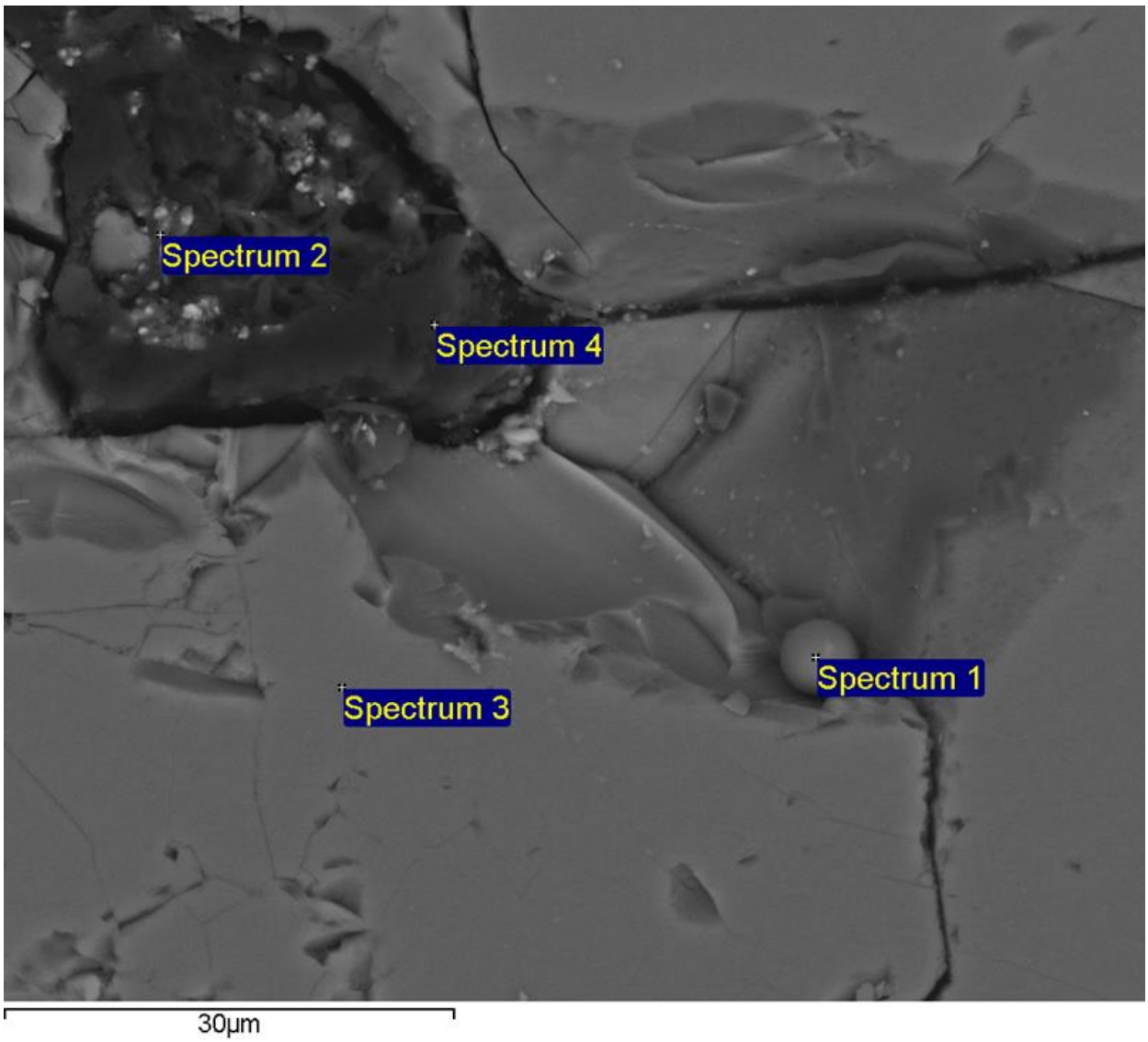
Spectrum	In stats.	C	O	Na	Mg	Al	Si	P	S	Cl	K	Ca	Ti	Fe	Total
Spectrum 1	Yes	80,45	10,95				7,15			1,45					100
Spectrum 2	Yes	79,93	18,45							1,62					100
Spectrum 3	Yes	76,9	18,95			0,17	1,83	0,23	0,49	1,13		0,3			100
Spectrum 4	Yes	17,02	44,82	0,29	0,34	13,59	17,12				5,79		0,32	0,72	100



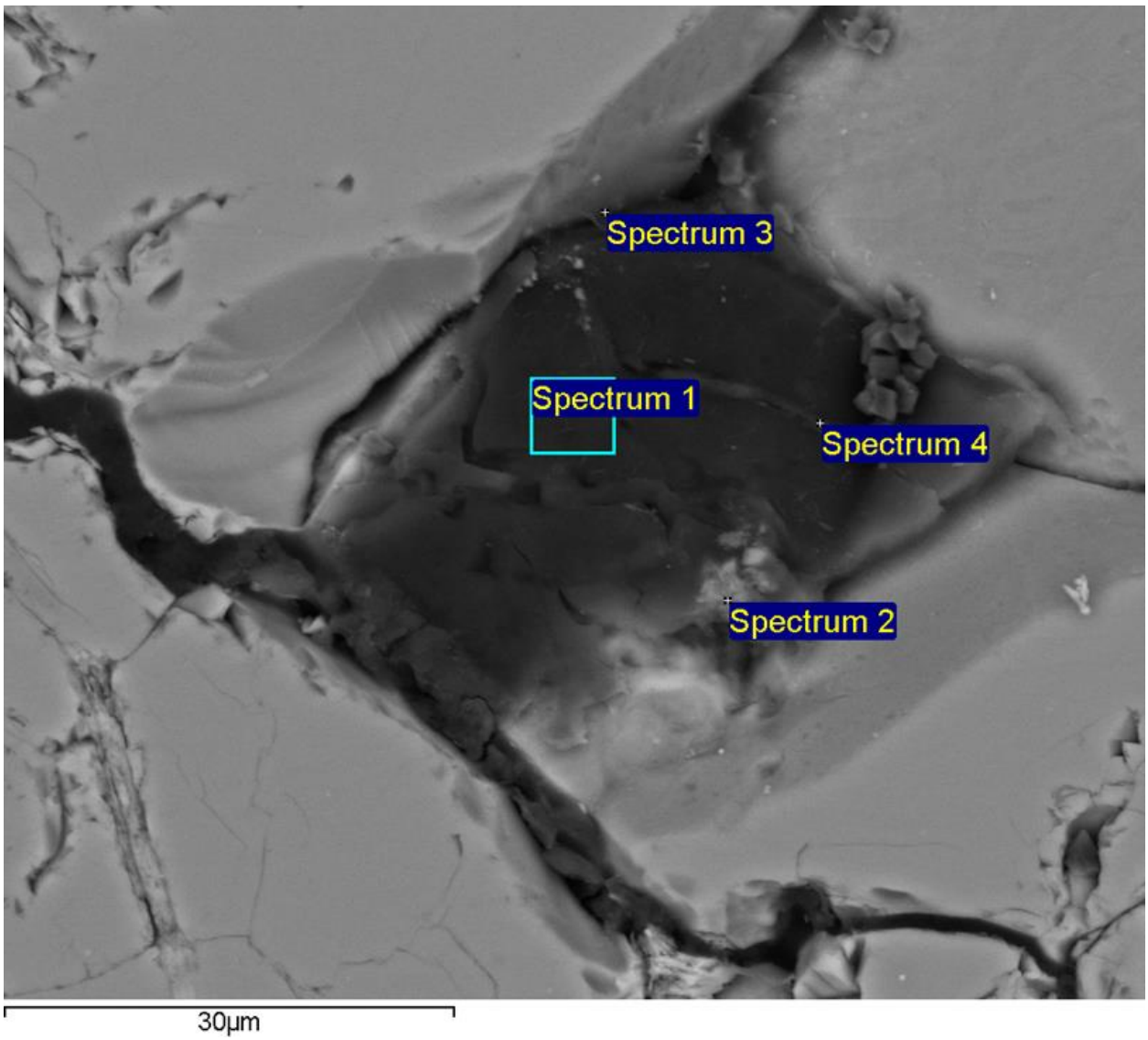
Spectrum	In stats.	C	O	Mg	Al	Si	Cl	K	Ca	Ti	Mn	Fe	Total
Spectrum 1	Yes	24,54	46,42	0,19	0,37	1,54			26,94				100
Spectrum 2	Yes	60,94	24,67		0,17	13,55	0,22	0,09	0,17			0,18	100
Spectrum 3	Yes	12,05	32,42	1,48	0,16	0,22				25,4	0,44	27,84	100
Spectrum 4	Yes	59,59	16,46			23,75	0,2						100



Spectrum	In stats.	C	O	Mg	Al	Si	Cl	Ca	Ti	Fe	Total
Spectrum 1	Yes	9,05	38,86						52,09		100
Spectrum 2	Yes	87,81	8,49				3,7				100
Spectrum 3	Yes	97,64	1,48	0,07		0,49	0,06	0,25			100
Spectrum 4	Yes	23,77	47,76		10,28	17,23		0,13		0,83	100

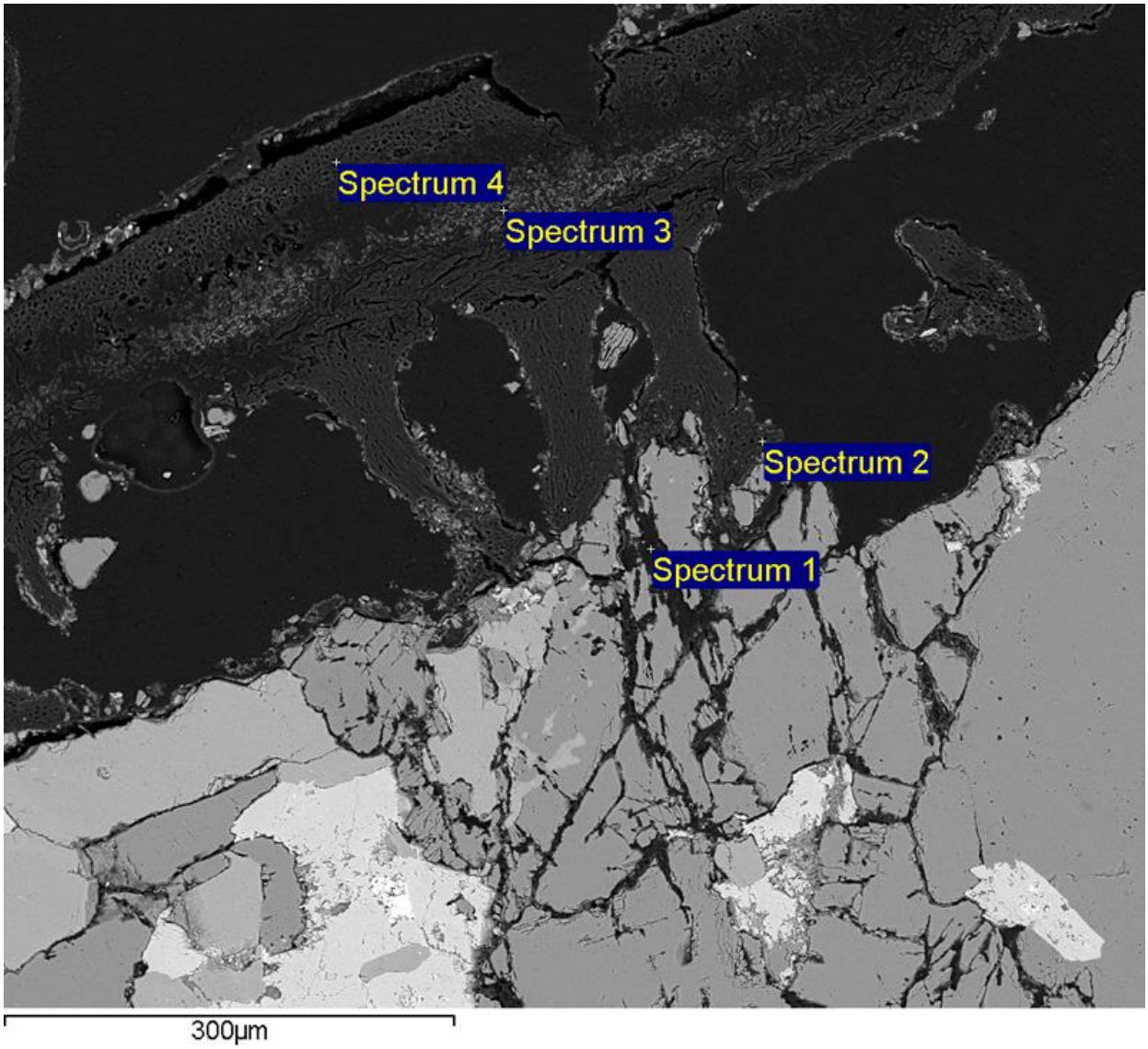


Spectrum	In stats.	C	O	Al	Si	Cl	K	Ca	Fe	Total
Spectrum 1	Yes	32,97	40,04		26,99					100
Spectrum 2	Yes	40,43	31,61	7,05	14,04	0,39	0,3	0,2	5,98	100
Spectrum 3	Yes	23,76	46,33		29,91					100
Spectrum 4	Yes	80,25	16,3		2,43	1,01				100

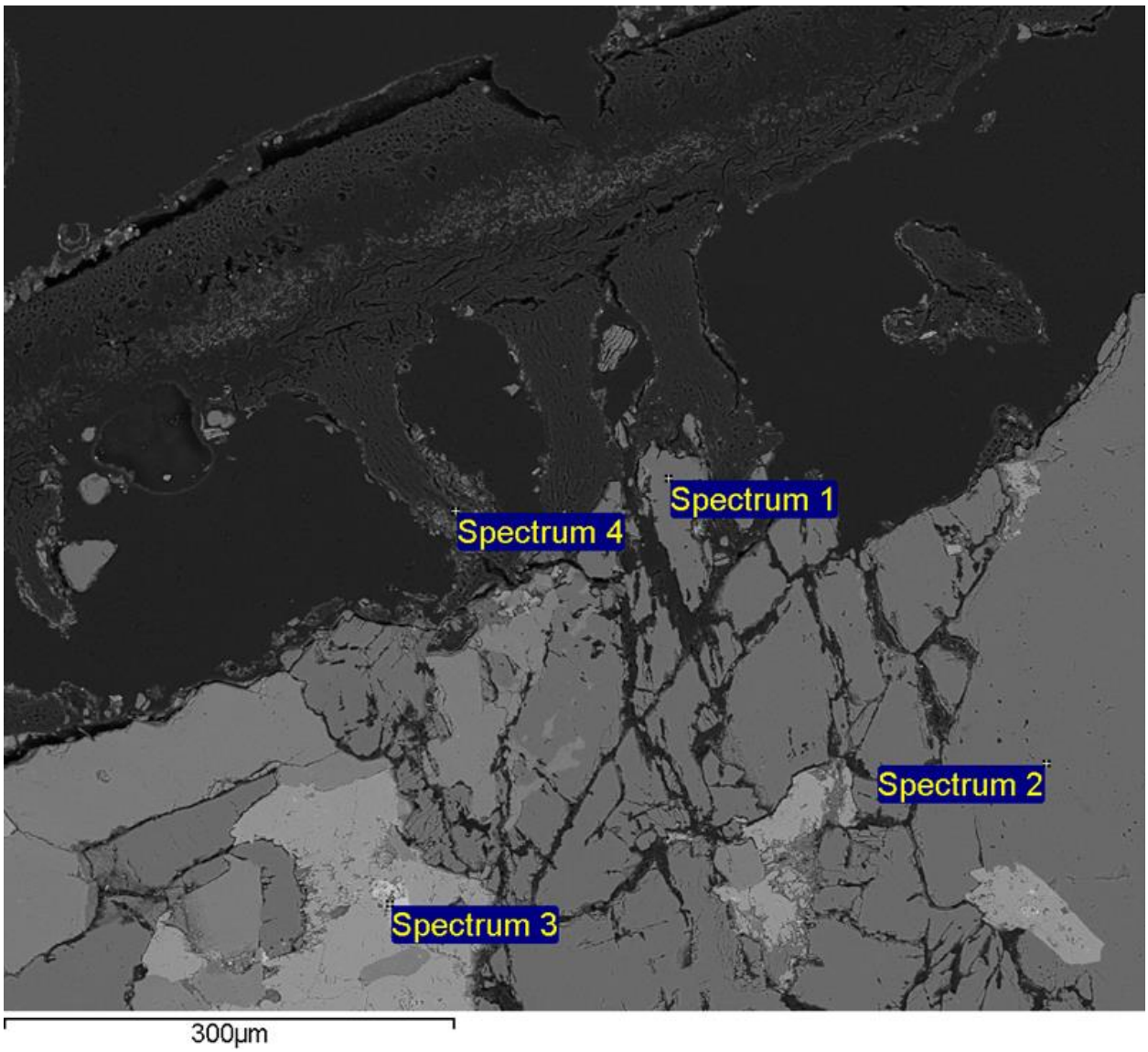


Spectrum	In stats.	C	O	Al	Si	P	S	Cl	K	Ca	Fe	Total
Spectrum 1	Yes	80,12	8,19	0,1	11,27			0,31				100
Spectrum 2	Yes	47,46	25,72	9,29	15,86			0,35	0,2	0,2	0,92	100
Spectrum 3	Yes	57,01	11,69		31,3							100
Spectrum 4	Yes	79,62	10,38	0,08	8,99	0,11	0,18	0,56		0,09		100

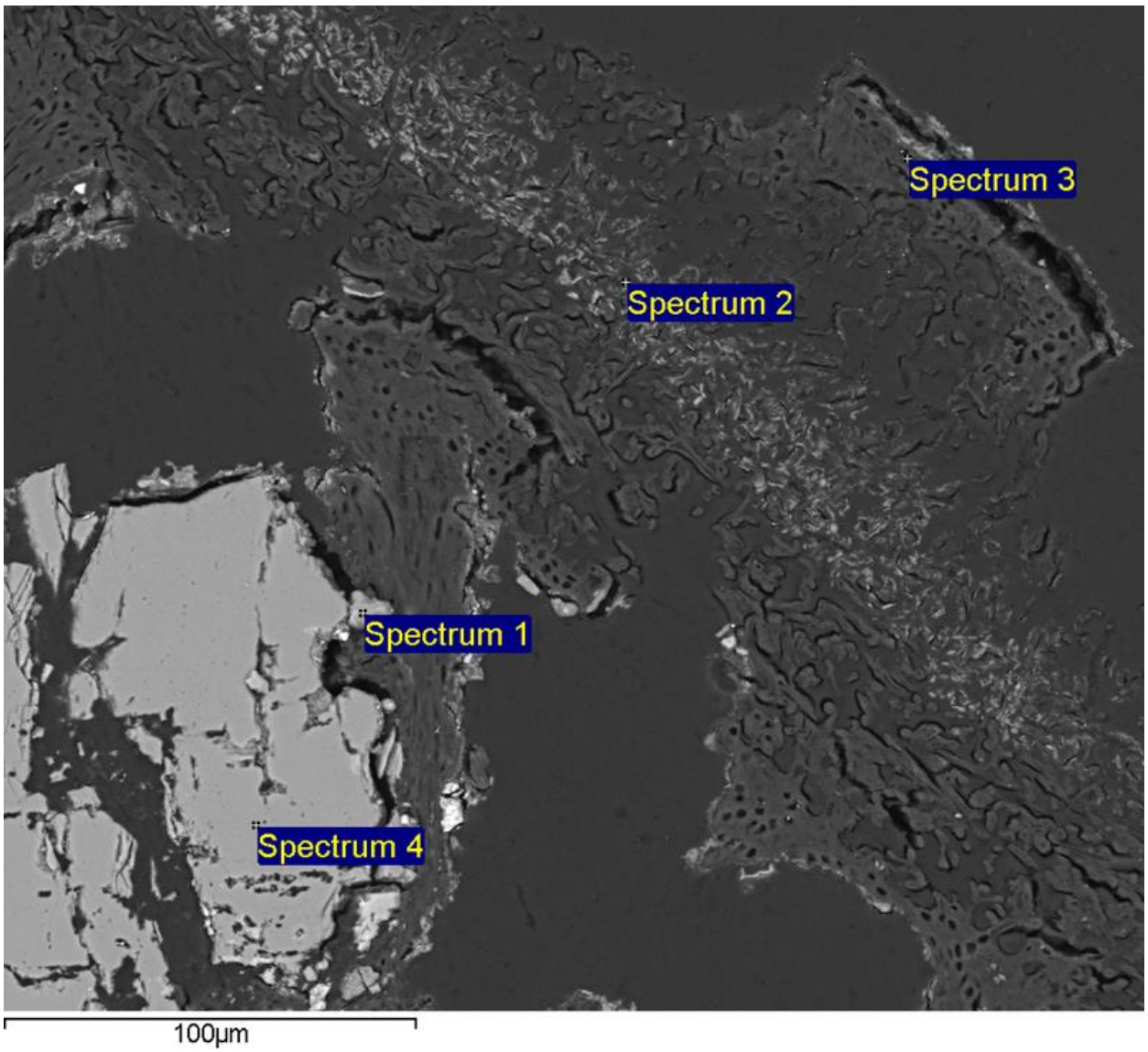
APPENDIX E3: SEM-EDS ANALYSIS (wt. %) RESULTS ON ALKALI GRANITE.



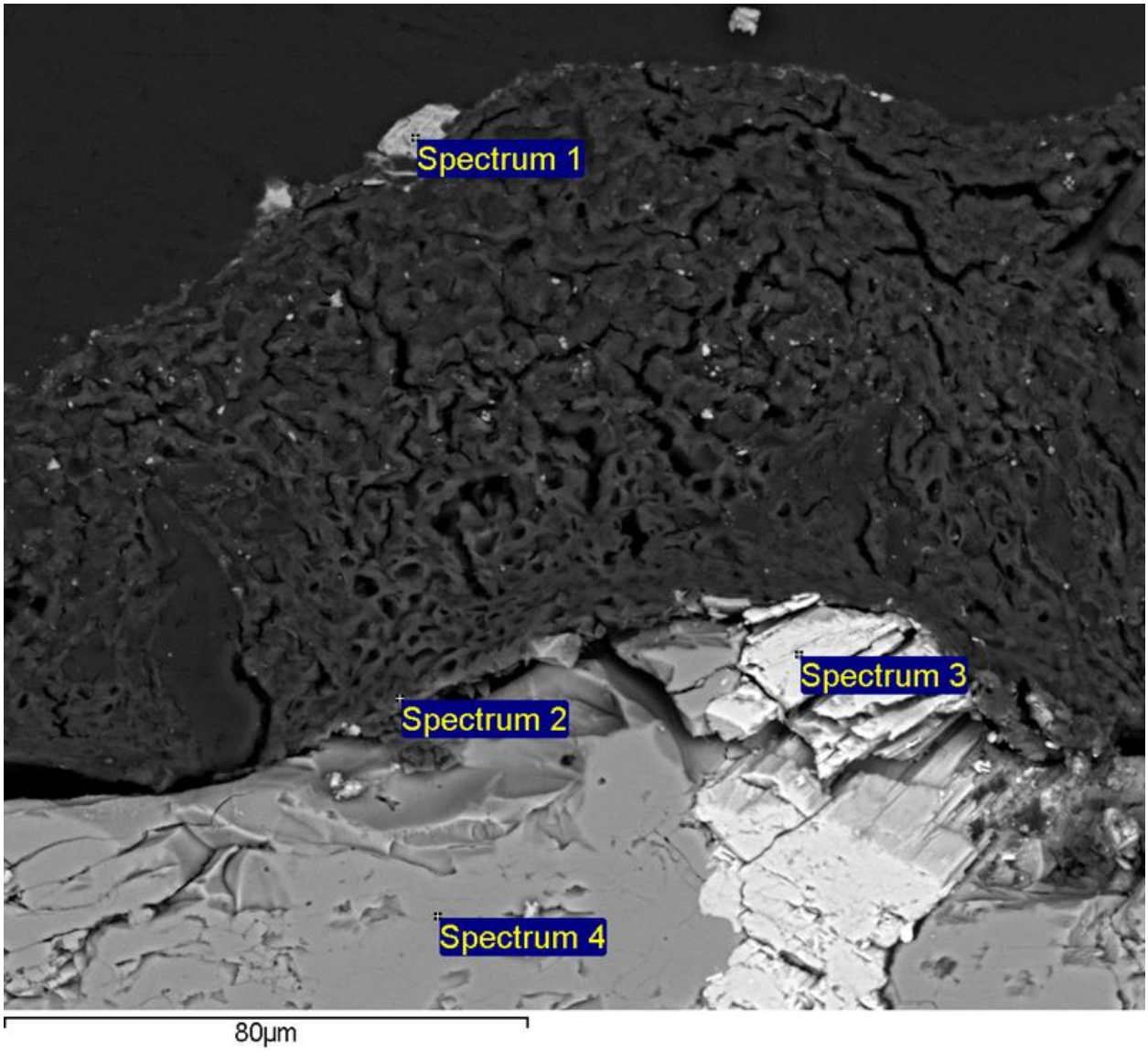
Spectrum	In stats.	C	O	Mg	Al	Si	P	S	Cl	K	Ca	Fe	Total
Spectrum 1	Yes	86,53	10,46						3,01				100
Spectrum 2	Yes	59,07	28,1	0,11	3,62	6,44		0,13	0,36	0,83	0,27	1,05	100
Spectrum 3	Yes	77,56	20,72						1,22		0,5		100
Spectrum 4	Yes	75,08	23,62				0,17	0,3	0,57		0,26		100



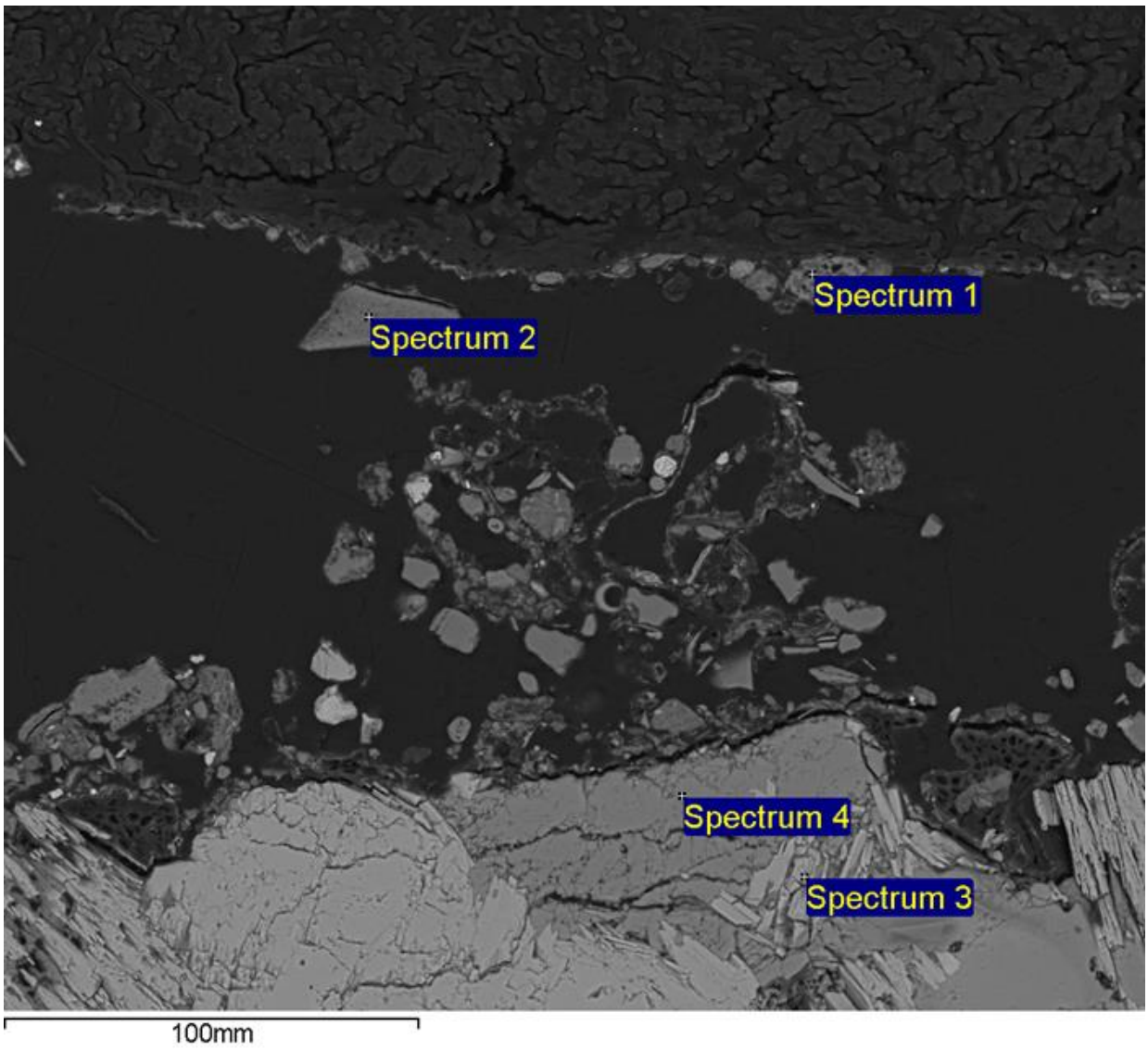
Spectrum	In stats.	C	O	Na	Mg	Al	Si	P	S	Cl	K	Ca	Ti	Mn	Fe	Total
Spectrum 1	Yes	16,41	45,64	5,41		7,47	25,08									100
Spectrum 2	Yes	15,66	49,29				35,05									100
Spectrum 3	Yes	10,58	33,89			0,9	0,73	0,4					29,83	4,47	19,2	100
Spectrum 4	Yes	52,42	10,83		0,39	6,76	11,86		0,99	0,56	1,07	0,68	0,48		13,97	100



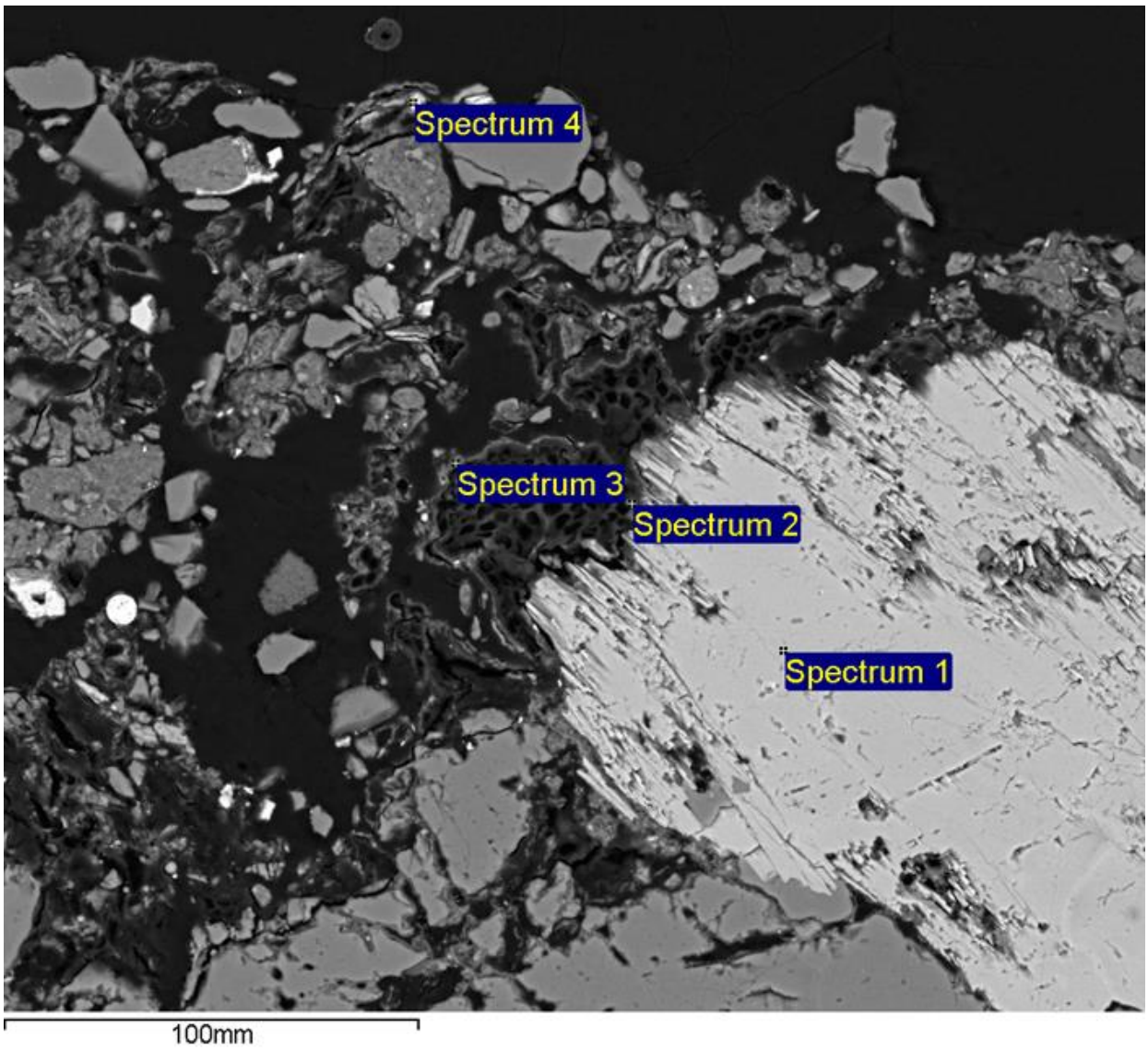
Spectrum	In stats.	C	O	Na	Al	Si	Cl	Ca	Fe	Total
Spectrum 1	Yes	38,35	43,53	0,1	0,09	17,61		0,18	0,13	100
Spectrum 2	Yes	45,5	27,54				1,16	25,8		100
Spectrum 3	Yes	76,26	20,34		0,15	0,34	2,69	0,22		100
Spectrum 4	Yes	17,13	46,69	5,18	7,29	23,71				100



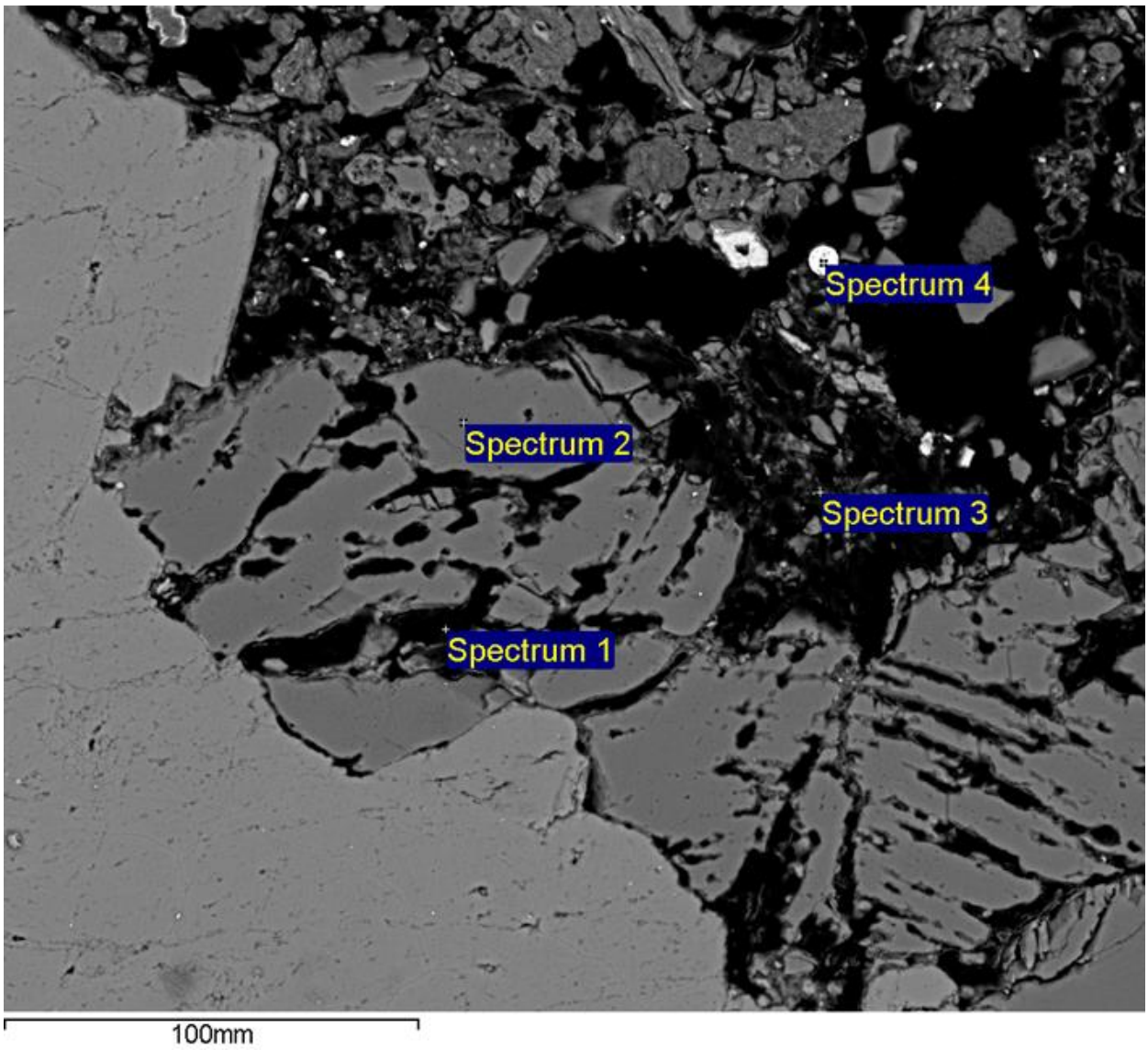
Spectrum	In stats.	C	O	Na	Mg	Al	Si	P	S	K	Ca	Mn	Fe	Total
Spectrum 1	Yes	24,17	44,23		4,55	3,82	13,09			0,32			9,82	100
Spectrum 2	Yes	81,76	12,84		0,18	0,21	1,49	0,38	2,16		0,98			100
Spectrum 3	Yes	25,21	33,48	1,79	1,41	0,31	17,38			0,43	2,45	0,38	17,16	100
Spectrum 4	Yes	23,99	44,86				31,15							100



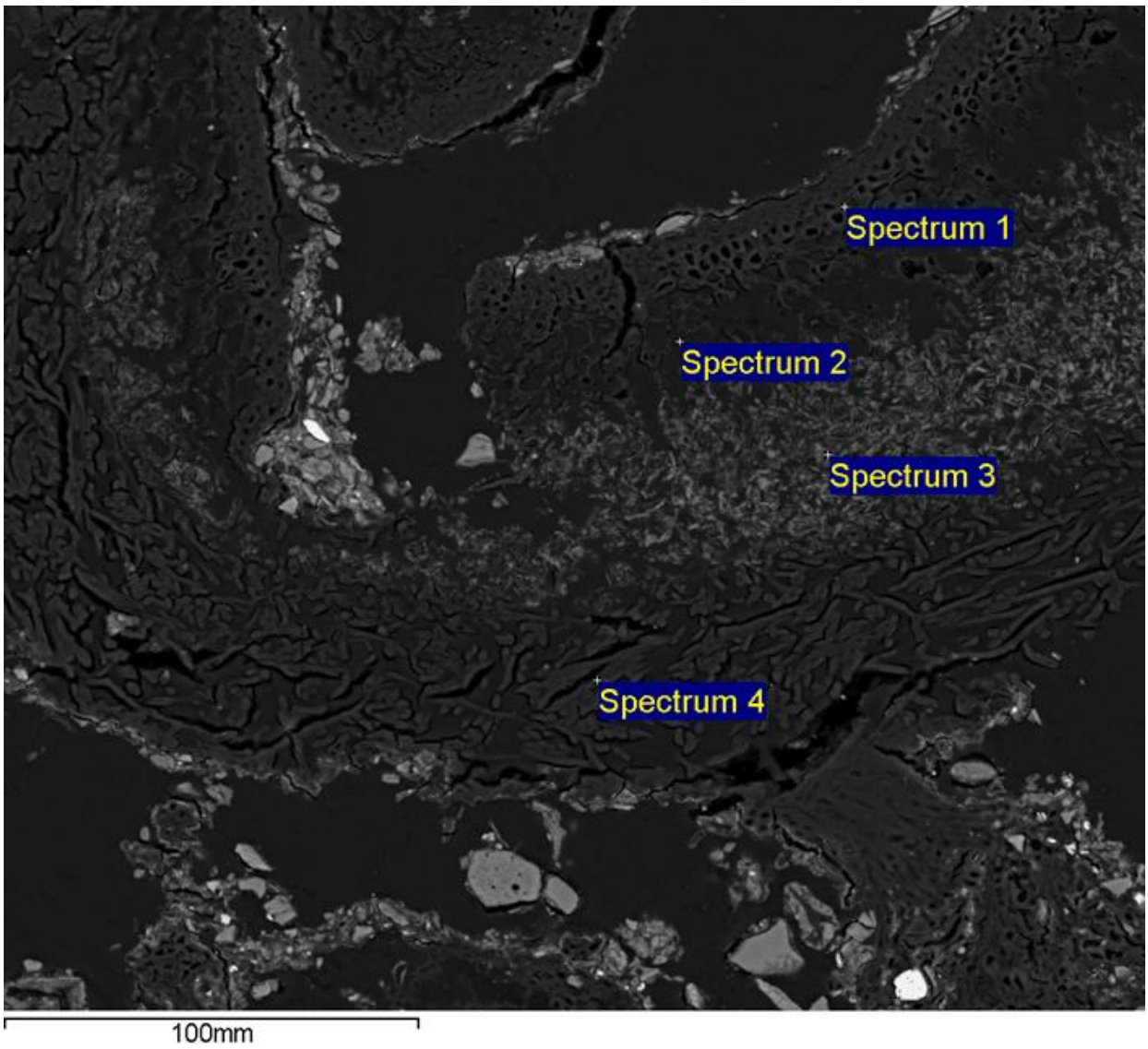
Spectrum	In stats.	C	O	Na	Mg	Al	Si	K	Ca	Mn	Fe	Total
Spectrum 1	Yes	30,11	44,94			0,28	24,46				0,2	100
Spectrum 2	Yes	33,14	37,99				28,79	0,08				100
Spectrum 3	Yes	34,31	19,93	1,64	1,13	0,24	17,78	0,75	1,21	0,6	22,42	100
Spectrum 4	Yes	26,87	36,14			6,49	21,91	8,2			0,4	100



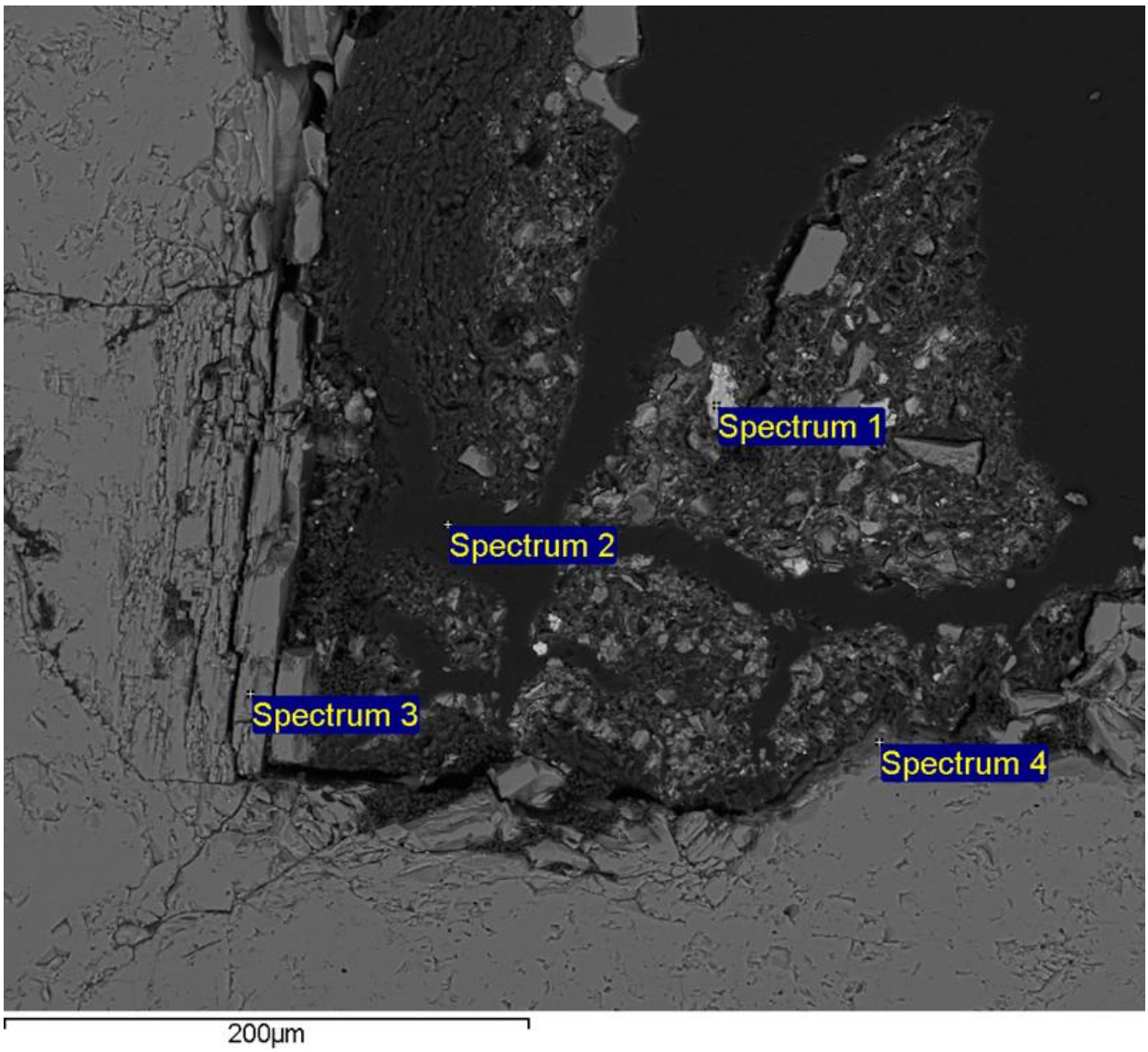
Spectrum	In stats.	C	O	Na	Mg	Al	Si	P	S	Cl	K	Ca	Ti	Mn	Fe	Total
Spectrum 1	Yes	30,45	33,73	2,51	1,61	0,23	15,69				0,56	1		0,39	13,82	100
Spectrum 2	Yes	42,04	33,12	2,21	0,71	0,46	10,88				0,11	0,18		0,2	10,08	100
Spectrum 3	Yes	60,83	19,33	0,11	0,29	5,43	8,4	0,13	0,35	0,46	0,34	0,27	0,21		3,85	100
Spectrum 4	Yes	33,19	30,52	0,35	0,3	5,06	7,32	0,15	0,14	0,13	0,38	0,1	0,15		22,22	100



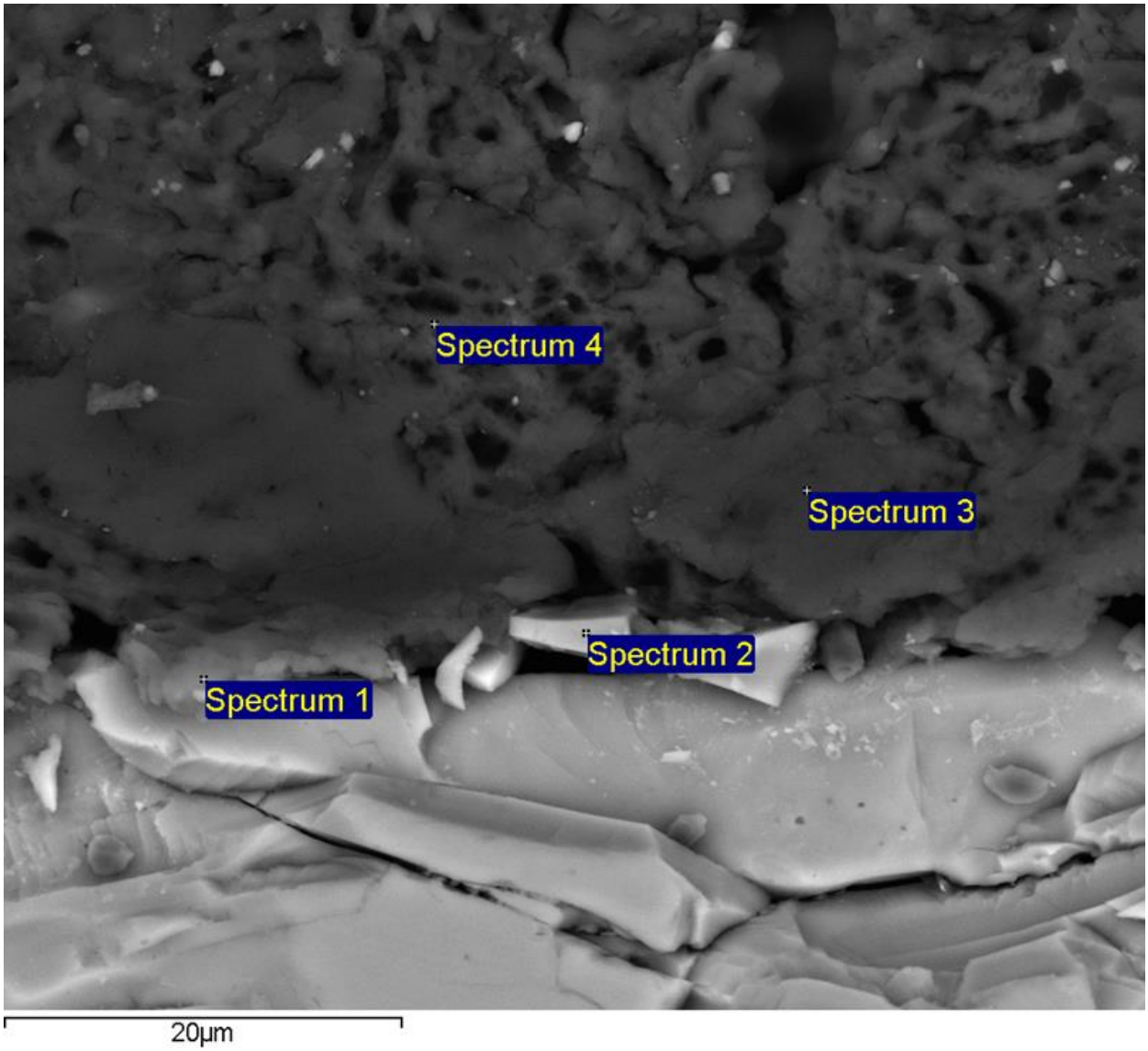
Spectrum	In stats.	C	O	Na	Al	Si	S	Cl	K	Fe	Total
Spectrum 1	Yes	81,41	12,16		0,41	4,8		1,21			100
Spectrum 2	Yes	29,81	38,44	4,66	6,1	20,75				0,25	100
Spectrum 3	Yes	56,13	21,35		1,44	5,04	0,14	0,43	0,1	15,36	100
Spectrum 4	Yes	25,42	24,51		0,91	1,21				47,95	100



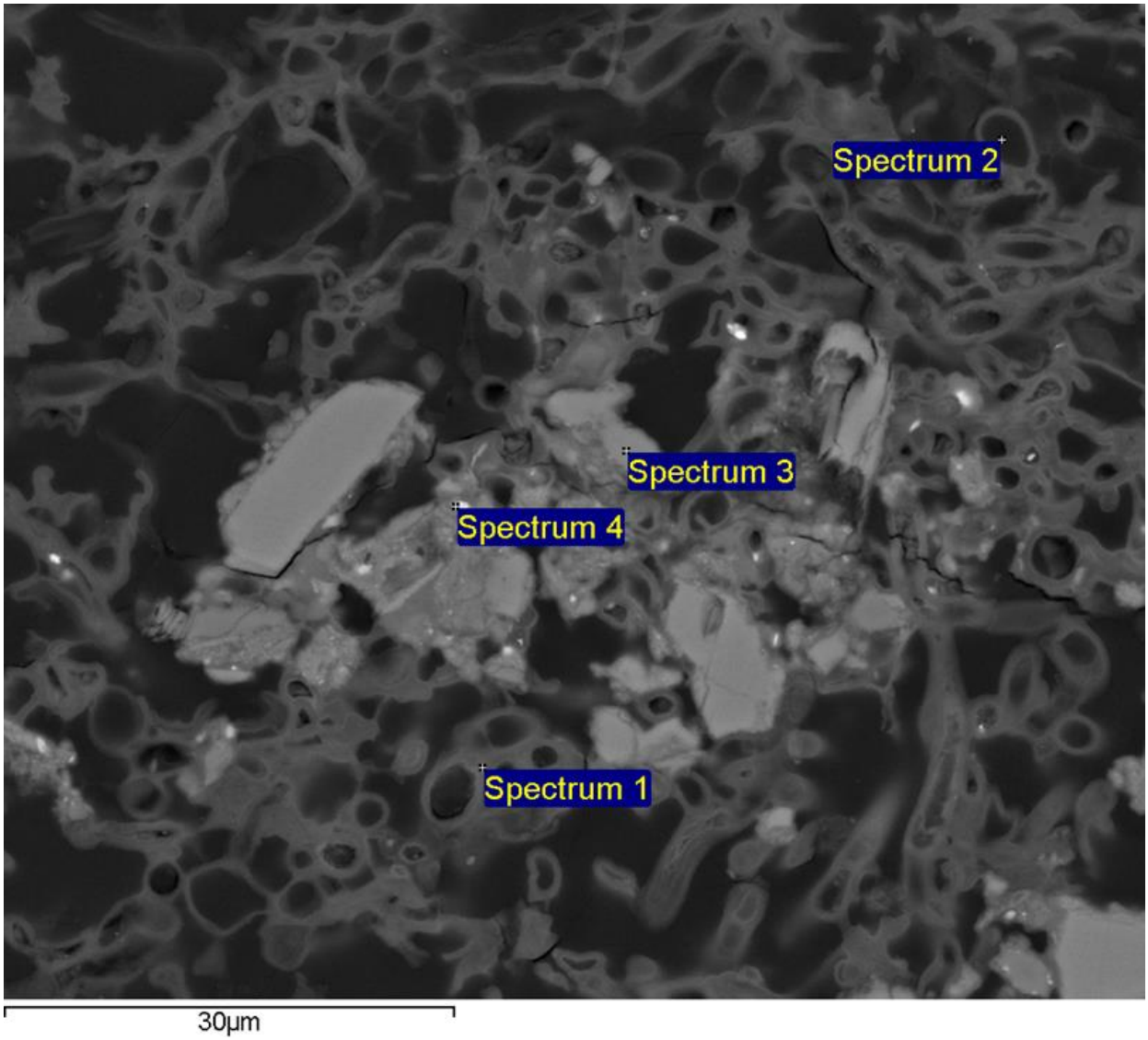
Spectrum	In stats.	C	O	Na	S	Cl	K	Ca	Total
Spectrum 1	Yes	76,14	22,04	0,16	0,24	1,09		0,32	100
Spectrum 2	Yes	84,31	13,12		0,28	2,02		0,27	100
Spectrum 3	Yes	43,39	21			1,95		33,66	100
Spectrum 4	Yes	81,44	16,68	0,24	0,35	1,02	0,26		100



Spectrum	In stats.	C	O	Na	Al	Si	Cl	K	Ca	Fe	Total
Spectrum 1	Yes	18,96	39,27		3,37	5,39				33,01	100
Spectrum 2	Yes	80,6	17,73				1,67				100
Spectrum 3	Yes	39,12	33,05	3,96	5,44	18,33		0,11			100
Spectrum 4	Yes	65,22	17,69		0,33	15,53			1,23		100

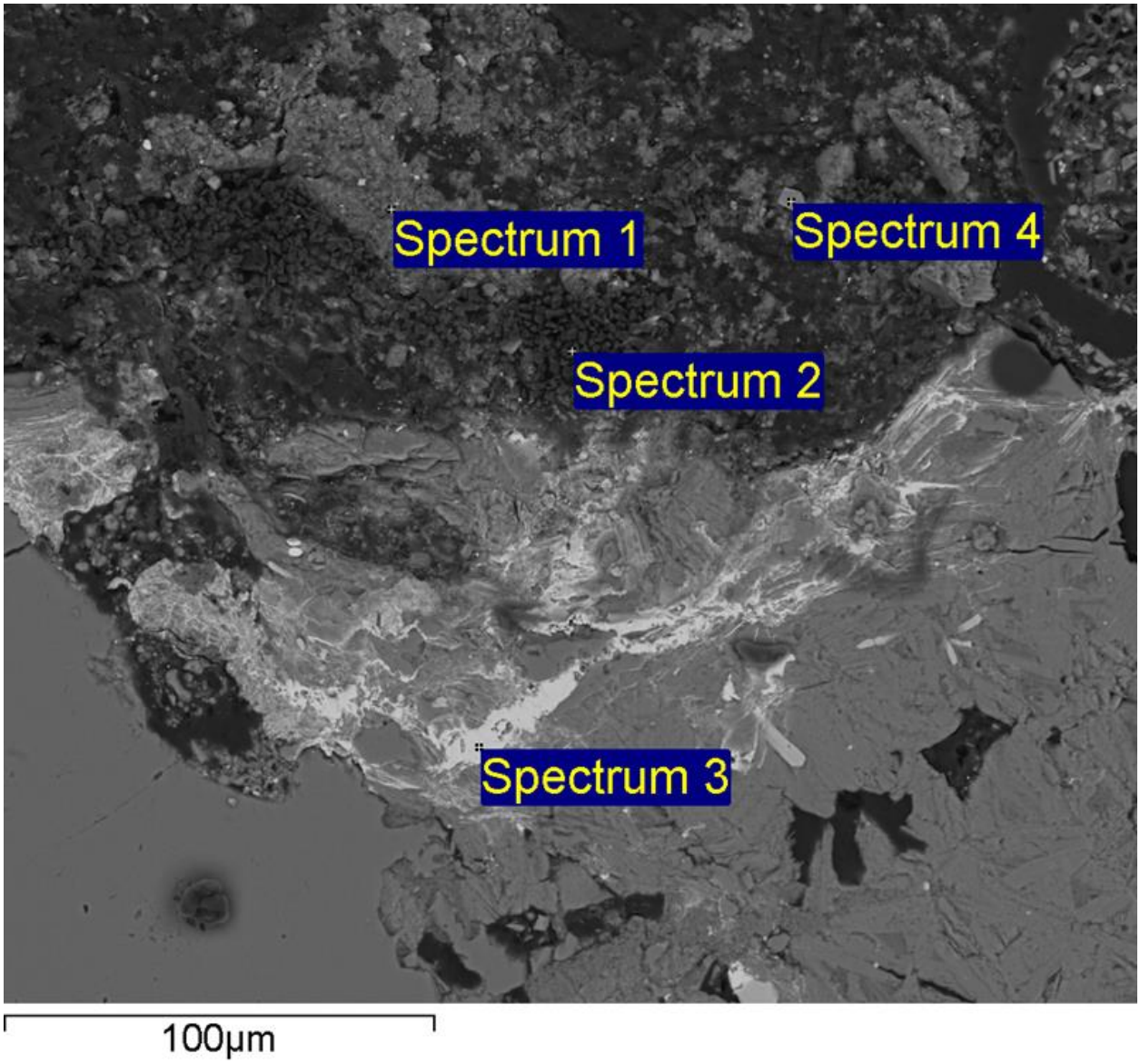


Spectrum	In stats.	C	O	Mg	Si	P	S	Cl	Ca	Mo	Total
Spectrum 1	Yes	59,02	31,05	0,12	9,07	0,12	0,31		0,31		100
Spectrum 2	Yes	29,47	47,93		22,6						100
Spectrum 3	Yes	86,05	8,73			0,66		1,42	0,7	2,44	100
Spectrum 4	Yes	81,85	14,96				1,57	1,13	0,49		100

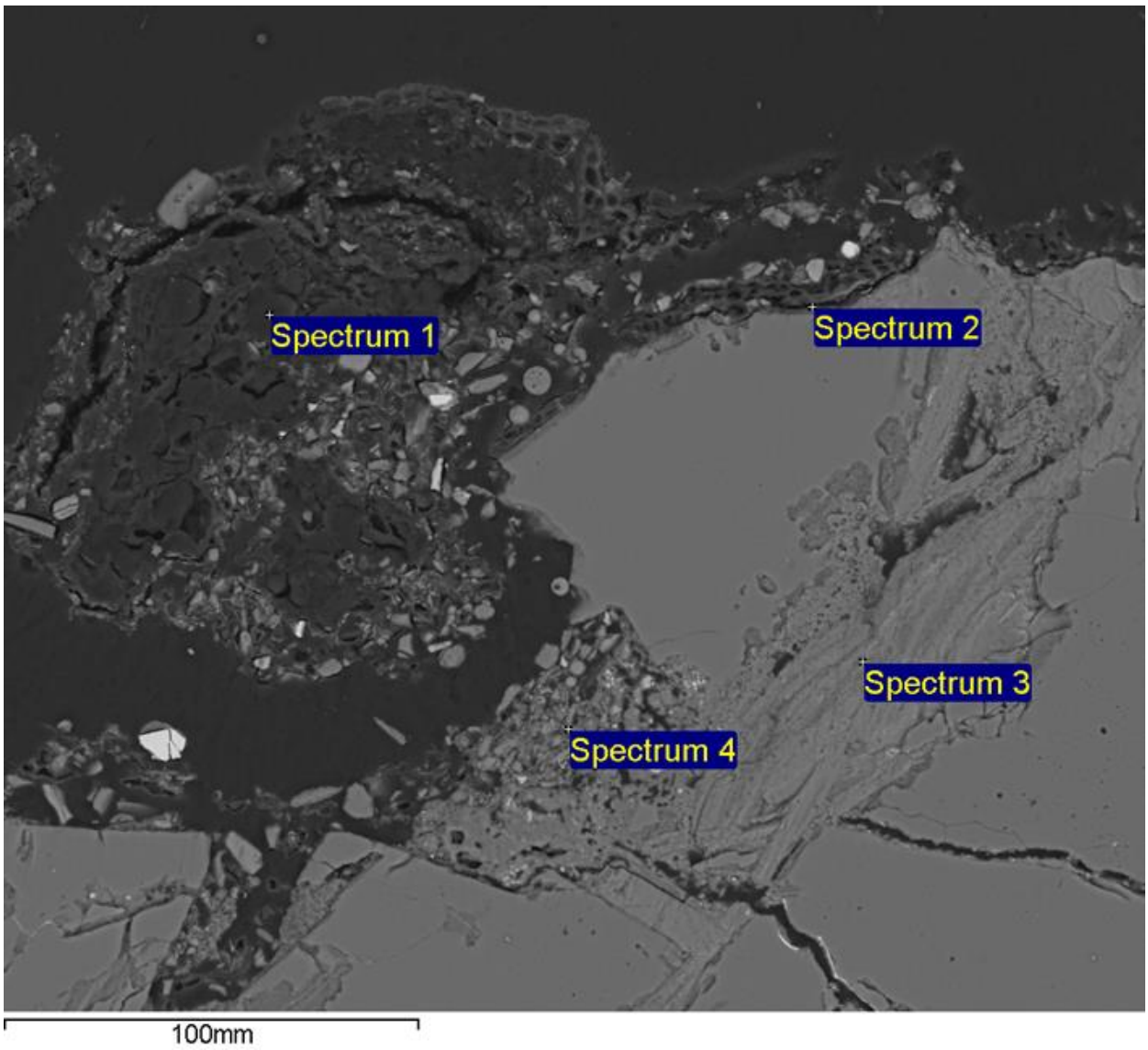


Spectrum	In stats.	C	O	Mg	Al	Si	S	Cl	K	Ca	Fe	Total
Spectrum 1	Yes	42,34	33,19		0,27	23,2	0,29	0,34	0,16	0,2		100
Spectrum 2	Yes	50,48	32,51		0,13	16,26	0,14	0,48				100
Spectrum 3	Yes	59,35	9,94		0,47	29,29		0,3	0,64			100
Spectrum 4	Yes	26,47	40,64	0,18	3,01	26,43	0,13		0,72	0,25	2,18	100

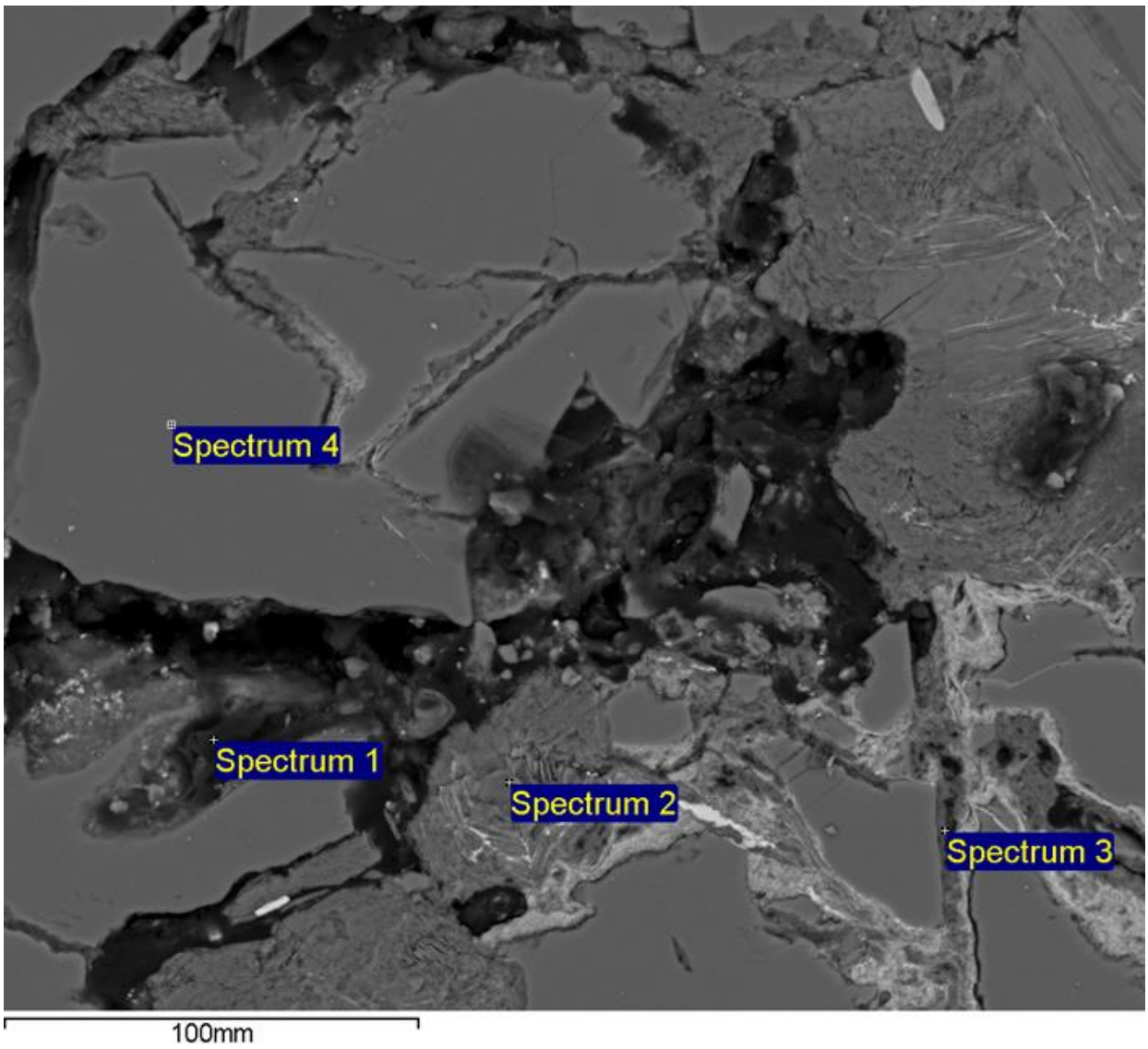
APPENDIX E4: SEM-EDS ANALYSIS (wt. %) RESULTS ON FERRUGINOUS QUARTZITE.



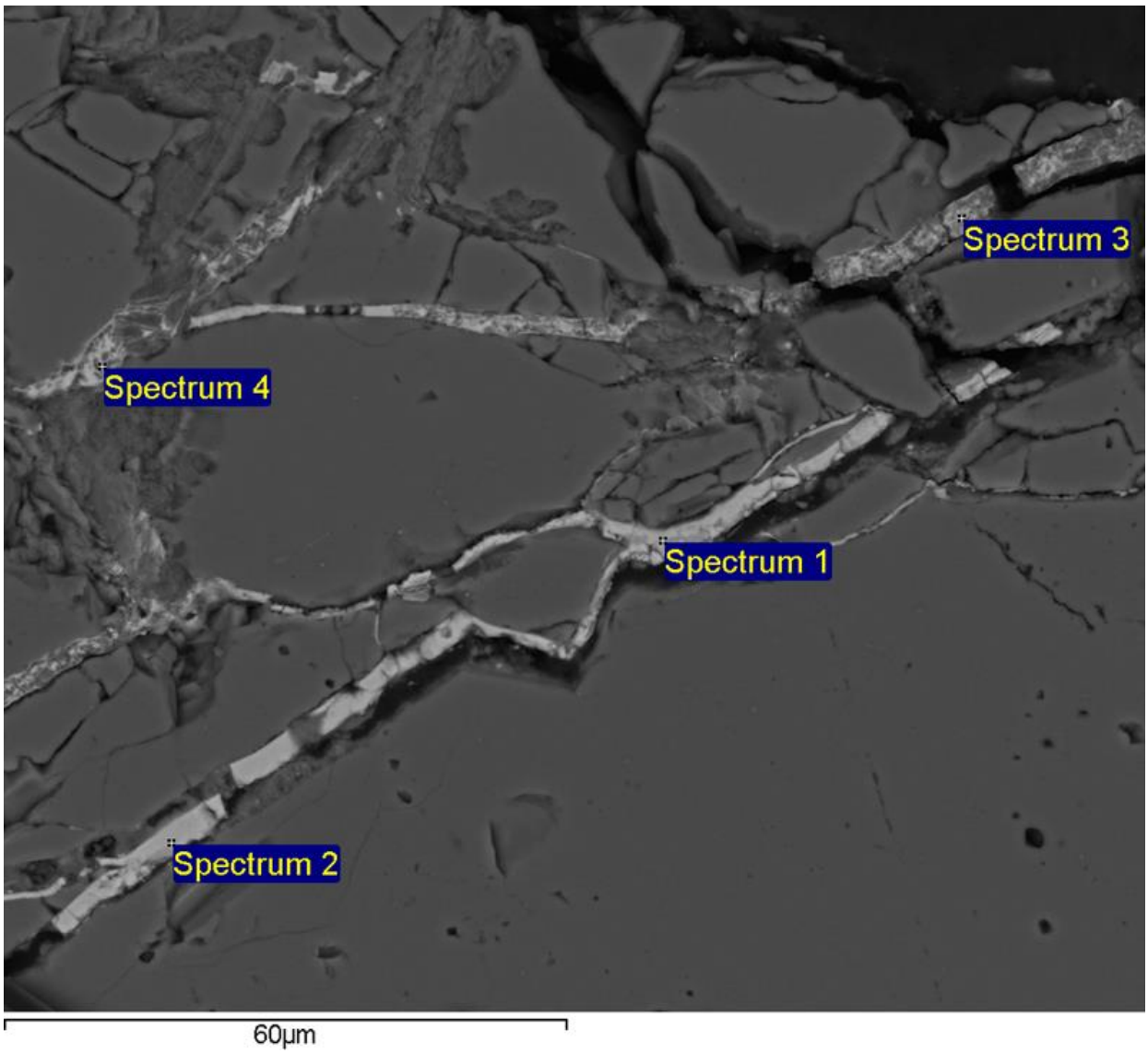
Spectrum	In stats.	C	O	Na	Mg	Al	Si	P	Cl	K	Ca	Ti	V	Cr	Fe	As	Total
Spectrum 1	Yes	35,13	39,22		0,09	2,6	21,15		0,11	0,49	0,12	0,16			0,93		100
Spectrum 2	Yes	95,99	1,02		0,08	0,87	1,36				0,34				0,33		100
Spectrum 3	Yes	23,87	29,86			0,59	0,36	0,27					0,23	0,21	44,17	0,43	100
Spectrum 4	Yes	33,55	37,51	0,33	0,11	5,35	16,73		0,13	6					0,3		100



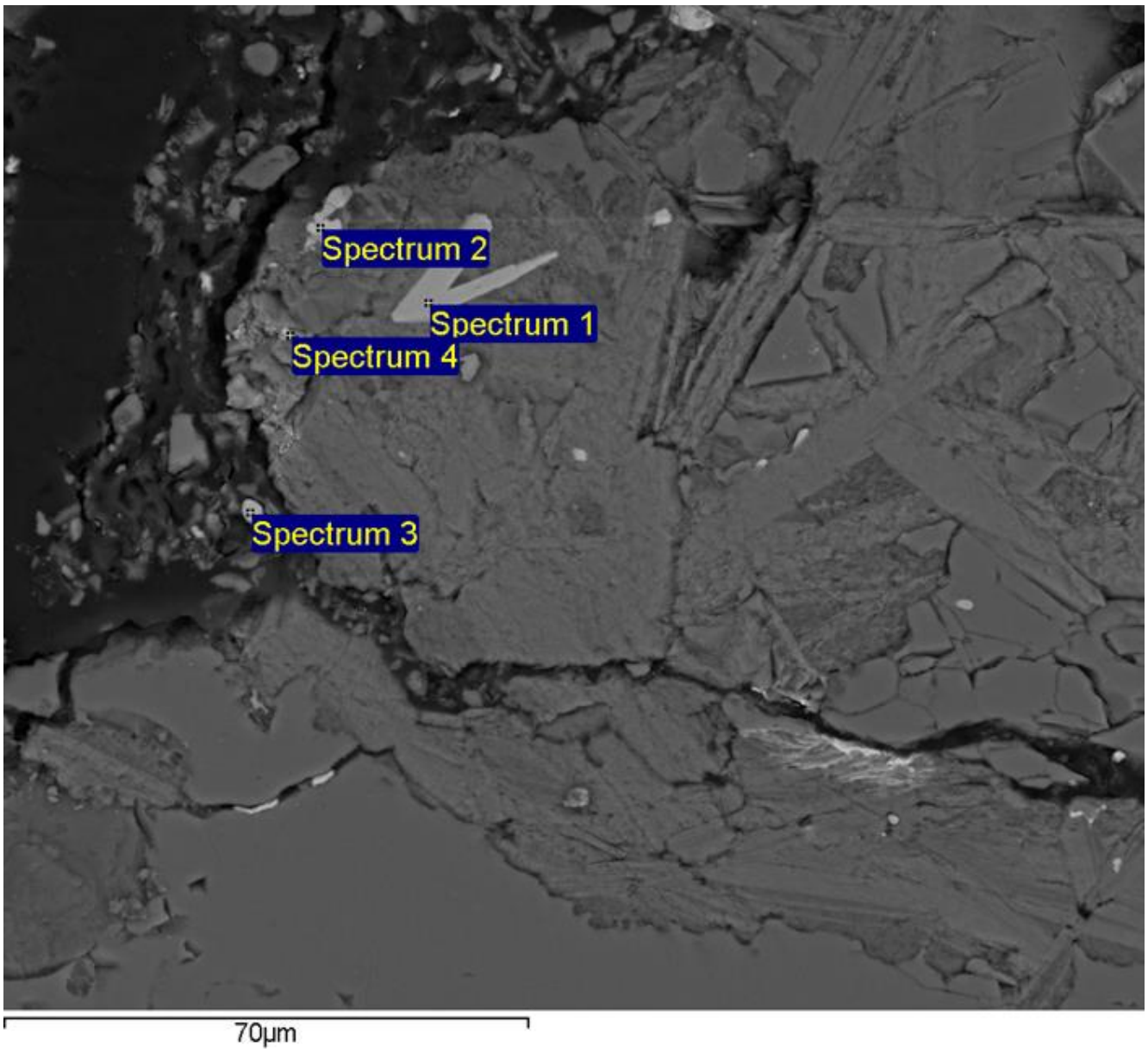
Spectrum	In stats.	C	O	Na	Mg	Al	Si	S	Cl	K	Ti	Fe	Total
Spectrum 1	Yes	88,57	7,76					0,34	3,32				100
Spectrum 2	Yes	11,09	1,42			1,53	48,02			1,23		36,71	100
Spectrum 3	Yes	21,27	44,51	0,31		13,35	14,89			2,97	0,12	2,58	100
Spectrum 4	Yes	29,83	38,81	0,12	0,15	5,94	19,26		0,19	1,46	1,15	3,1	100



Spectrum	In stats.	C	O	Na	Al	Si	Cl	K	Ti	Fe	Total
Spectrum 1	Yes	56,45	4,72	0,16	13,45	11,83	0,36	0,38	7,87	4,78	100
Spectrum 2	Yes	22,4	50,19	0,14	8,69	17,99				0,6	100
Spectrum 3	Yes	47,18	18,92		12,75	13,79	1,5			5,85	100
Spectrum 4	Yes	20,03	45,11		23,33	11,53					100

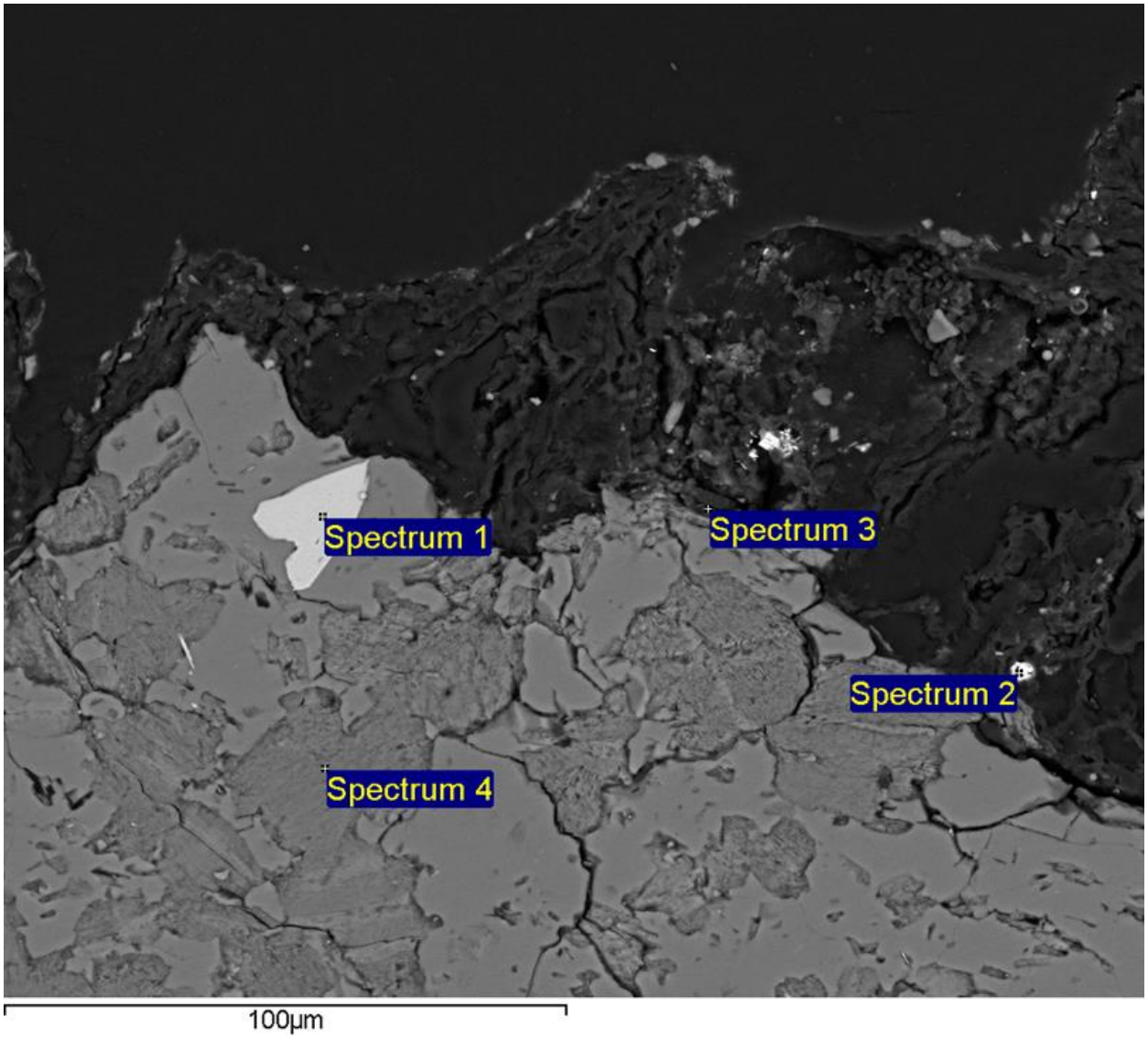


Spectrum	In stats.	C	O	Al	Si	P	Cl	V	Cr	Fe	As	Total
Spectrum 1	Yes	18,62	35,64	2,1	0,66	0,43		0,24		42,32		100
Spectrum 2	Yes	23,95	33,83	0,66	0,49	0,36		0,22	0,18	39,7	0,61	100
Spectrum 3	Yes	23,24	39,94	5,29	5,79	0,18	0,12	0,22	0,17	24,61	0,44	100
Spectrum 4	Yes	29,17	33,88	4,23	5,07	0,2			0,22	26,92	0,32	100

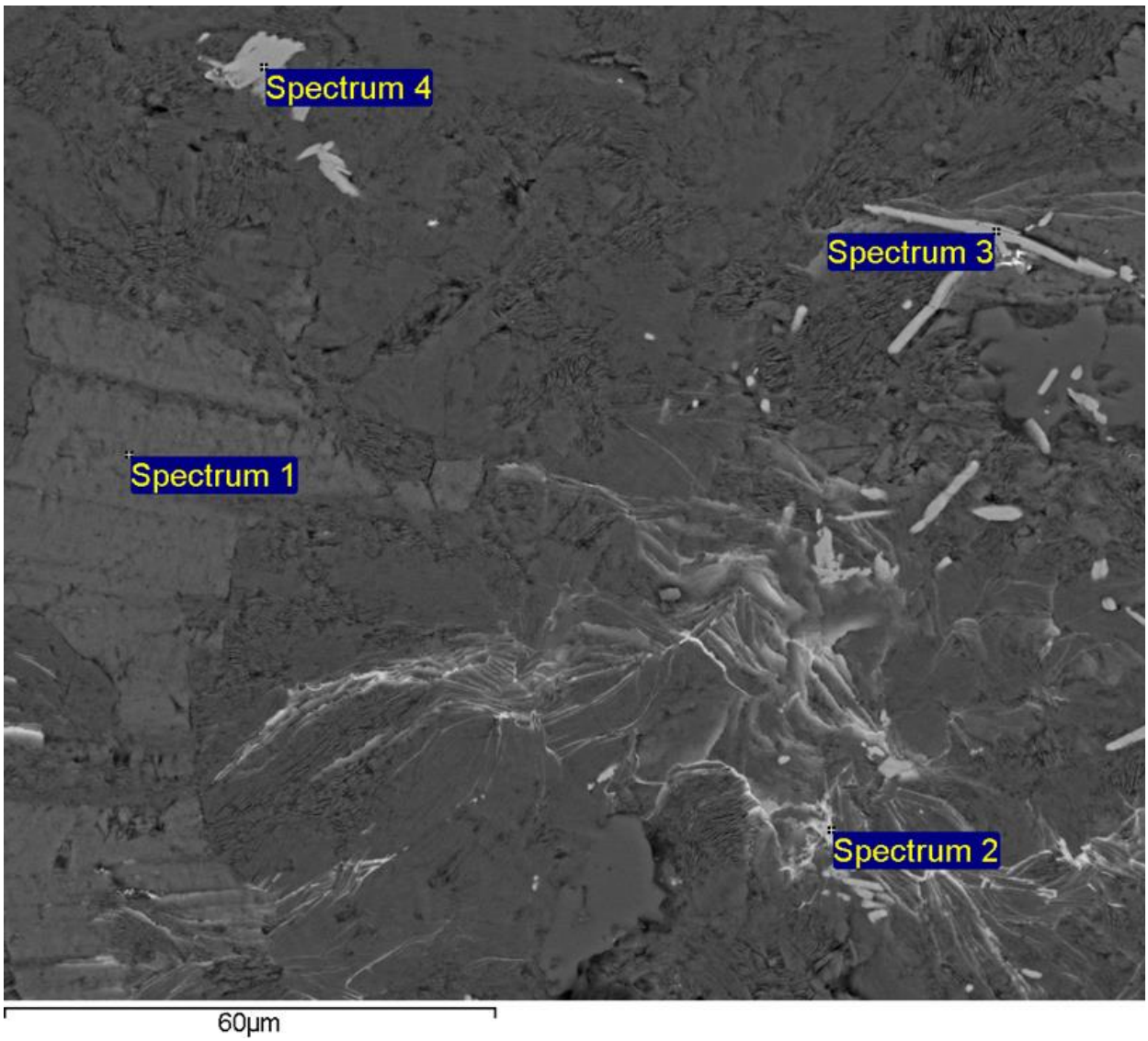


Spectrum	In stats.	C	O	F	Na	Mg	Al	Si	P	S	Cl	K	Ca	Ti	Cr	Mn	Fe	Ag	La	Ce	Nd	Total
Spectrum 1	Yes	17,06	34,69					0,14						47,73	0,38							100
Spectrum 2	Yes	21,23	42,64	0,43			11,32	1,28	8,57	0,57		0,21	0,73				1,37	0,49	2,9	6,85	1,42	100
Spectrum 3	Yes	26,55	31,22			0,49	0,23	0,74	0,2	0,16	0,32			21,97		4,36	13,76					100
Spectrum 4	Yes	31,6	27,44		0,28		15,1	17,65	0,45			6,76					0,73					100

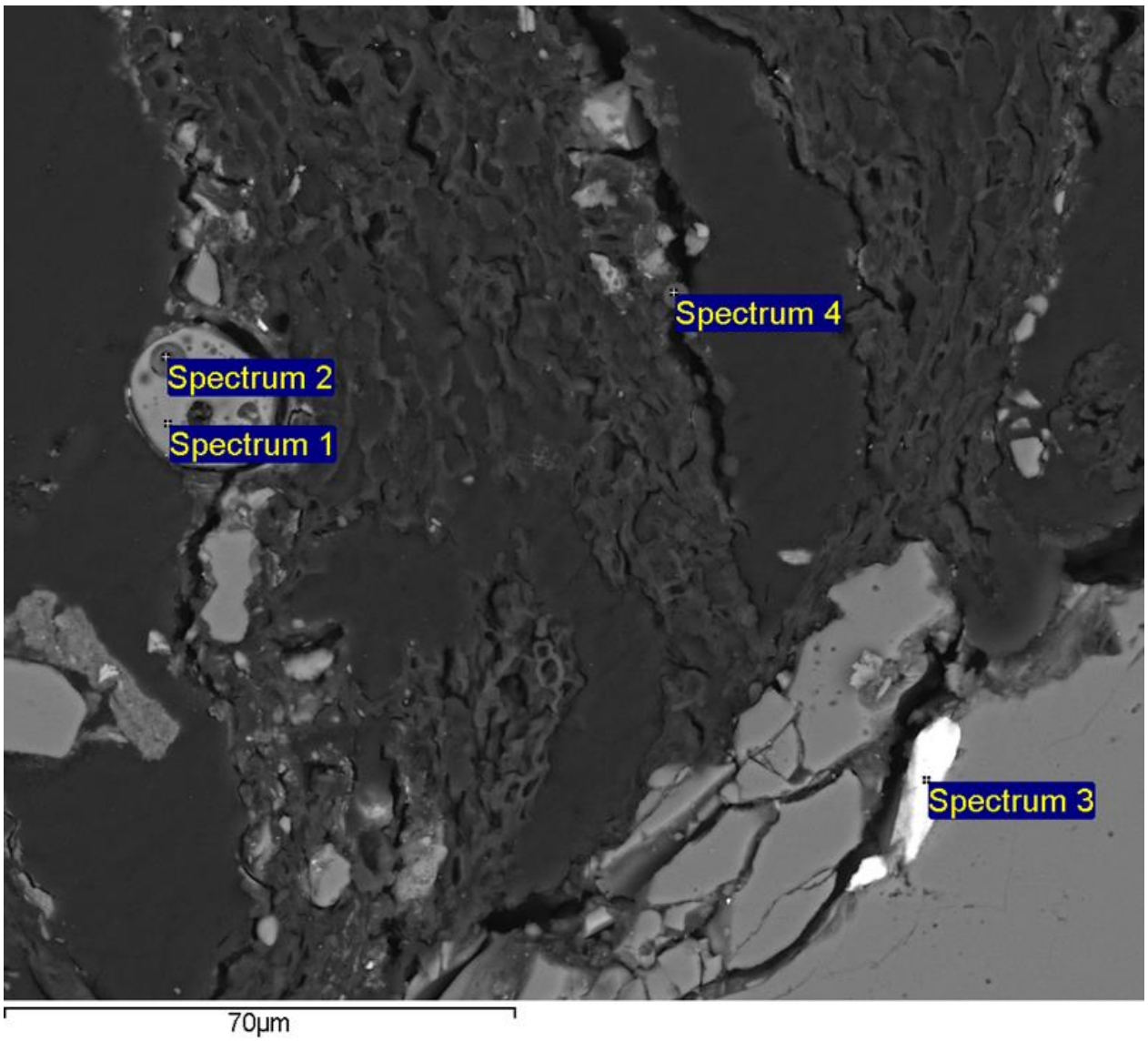
APPENDIX E5: SEM-EDS ANALYSIS (wt. %) RESULTS ON METACONGLOMERATE.



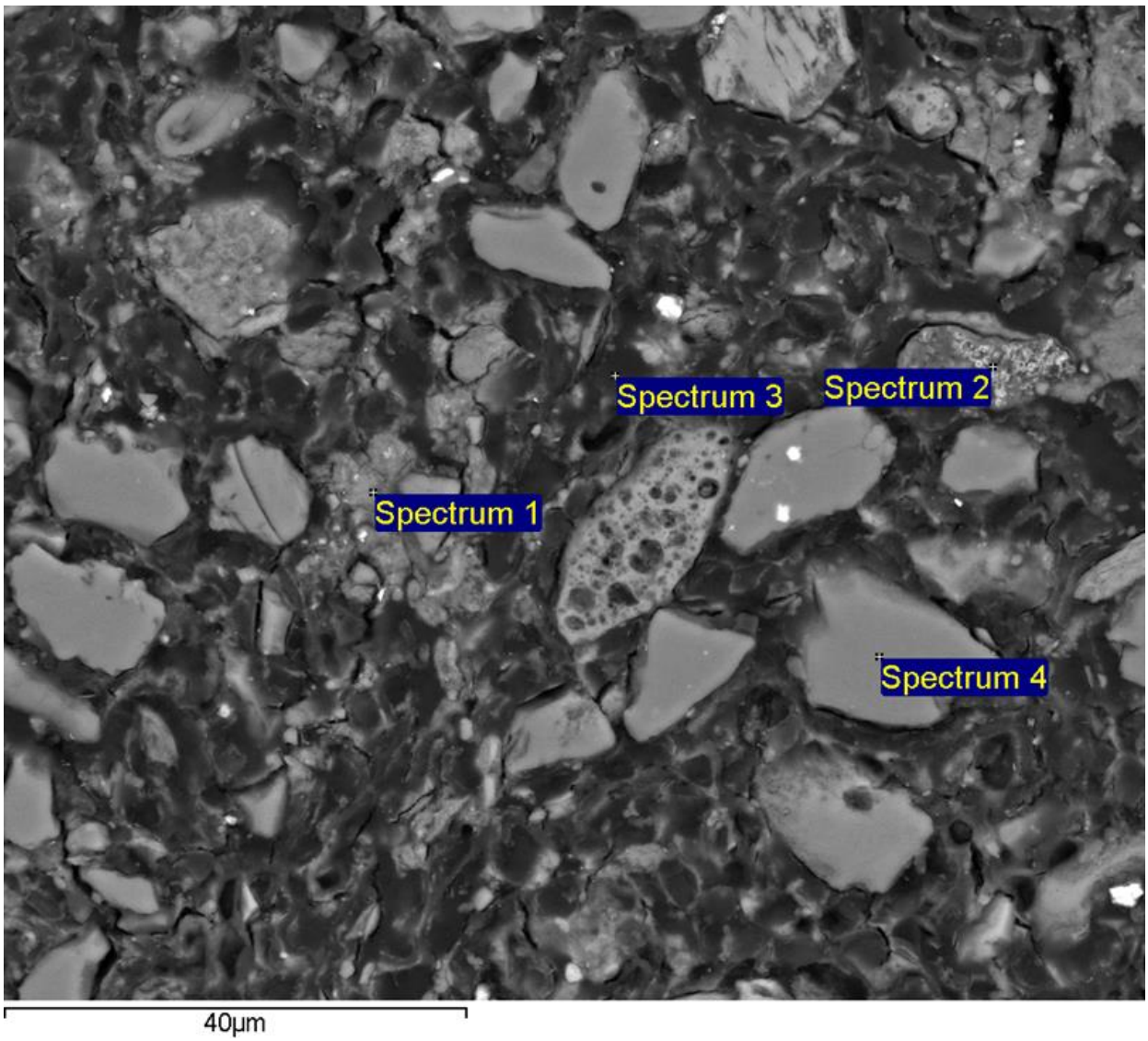
Spectrum	In stats.	C	O	Na	Al	Si	S	Cl	K	Ca	Ti	Cr	Fe	Zn	Total
Spectrum 1	Yes	7,61	39,23			0,19					52,61	0,36			100
Spectrum 2	Yes	22,77	35,53		0,47	0,93		0,24					39,51	0,55	100
Spectrum 3	Yes	60,53	8,06	0,18	3,56	24,64	0,54	0,77	0,45	0,51			0,74		100
Spectrum 4	Yes	10,73	51,05		11,95	26,26									100



Spectrum	In stats.	C	O	Na	Mg	Al	Si	P	K	Ti	Cr	Fe	As	Total
Spectrum 1	Yes	11,21	46,64	0,29	0,24	14,85	18,96		6,07	0,27		1,47		100
Spectrum 2	Yes	9,86	43,52			4,75	9,2	0,32				32	0,36	100
Spectrum 3	Yes	4,49	44,26			0,42	0,73		0,18	49,6	0,33			100
Spectrum 4	Yes	9,59	40,94				0,29			48,82	0,36			100



Spectrum	In stats.	C	O	Mg	Al	Si	P	S	Cl	K	Ca	Ti	Fe	Zr	Total
Spectrum 1	Yes	10,06	48,74	0,45	15,41	21,51				0,72	1,05	1,3	0,76		100
Spectrum 2	Yes	3,54	8,72	0,29	31,41	42,79				3,36	3,8	3,12	2,97		100
Spectrum 3	Yes	19,4	32,71			10,84								37,06	100
Spectrum 4	Yes	75,74	21,54	0,08	0,65	1,24	0,12	0,14	0,21	0,11			0,17		100



Spectrum	In stats.	C	O	Na	Mg	Al	Si	Cl	K	Ca	Ti	Mn	Fe	Total
Spectrum 1	Yes	24,37	38,82		0,1	1,27	33,63		0,22				1,6	100
Spectrum 2	Yes	24,12	32,81		5,13	7,56	12,84	0,49	0,3	0,31	0,45	0,36	15,63	100
Spectrum 3	Yes	67,4	9,82	0,12	0,37	6,95	10,09	0,57	0,79	0,14	0,36		3,39	100
Spectrum 4	Yes	10,14	52,95				36,91							100